arXiv:2509.14729v3 [cond-mat.mtrl-sci] 13 Mar 2026

High-Throughput Quantification of Altermagnetic Band Splitting

Ali Sufyan,[1,2,3] Brahim Marfoua,[4] J. Andreas Larsson,[3,5] Erik van Loon,[1,2] and Rickard Armiento[4]

[1] *NanoLund and Division of Mathematical Physics, Department of Physics, Lund University, SE-221 00 Lund, Sweden*
[2] *Wallenberg Initiative Materials Science for Sustainability, Department of Physics, Lund University, SE-221 00 Lund, Sweden*
[3] *Applied Physics, Division of Materials Science, Department of Engineering Sciences and Mathematics, Luleå University of Technology, SE-971 87 Luleå Sweden*
[4] *Department of Physics, Chemistry and Biology, Linköping University, SE-581 83 Linköping, Sweden*
[5] *Wallenberg Initiative Materials Science for Sustainability, Luleå University of Technology, SE-971 87 Luleå Sweden*

Altermagnetism represents a recently established class of collinear magnetism that combines zero net magnetization with momentum-dependent spin polarization, enabled by symmetry constraints rather than spin-orbit coupling. This distinctive behavior gives rise to sizable spin splitting even in materials composed of light, earth-abundant elements, offering promising prospects for next-generation spintronics applications. Here, we present a comprehensive high-throughput screening of the 2287 entiries comprising the MAGNDATA database, integrating symmetry analysis with spin-polarized density functional theory (DFT) calculations to identify and characterize altermagnetic candidates. Our workflow investigates the collinear structures in the data set and collinear versions of the ones reported to be non-collinear, uncovering 180 materials exhibiting significant spin splitting, spanning both metallic and semiconducting systems. Detailed results are available for all 180 materials, but we also particularly discuss UCr_2Si_2C, NbMnP, and $YRuO_3$ as representative cases with large spin splitting. Furthermore, comparison with the Computational 2D Materials Database (C2DB) and the AiiDA 2D repository gives 9 bulk altermagnets with chemically equivalent 2D counterparts linked to the same ICSD parent entry. Crucially, our momentum-resolved analysis reveals that the spin splitting varies strongly across the Brillouin zone, and that the maximal splitting tends to occur away from the high-symmetry paths, a result that directly informs and guides future photoemission experiments. By expanding the catalog of known altermagnets, this work lays a robust foundation for future experimental and theoretical advances in spintronics and quantum materials discovery.

I. INTRODUCTION

Altermagnetism has recently emerged as a distinct magnetic phase that expands beyond the traditional classifications of ferromagnetism (FM) and antiferromagnetism (AFM) [1–3]. The concept was initially introduced through theoretical predictions in rutile AFM RuO_2 in 2019 [4], and subsequently gained significant attention through systematic investigations of its distinctive characteristics in 2022, at which point the term "altermagnetism" was formally established [1, 2]. Conventional FM materials exhibit a net magnetization due to parallel alignment of spins, breaking time-reversal symmetry (TRS) uniformly throughout the crystal. In contrast, traditional AFMs have globally compensated spin arrangements with adjacent spins oriented antiparallel, thereby generating no net magnetization and typically enforcing spin degeneracy in their electronic band structure due to symmetry operations combining inversion or translational symmetry with TRS.

Altermagnets, however, possess globally compensated magnetization similar to AFMs but uniquely exhibit momentum-dependent spin polarization reminiscent of FM materials [1–12]. The essential distinction arises from the symmetry relations between their spin sublattices: in altermagnets, opposite-spin sublattices are related by rotation symmetries combined with TRS, rather than translation or inversion symmetries. This crucial difference in symmetry leads to nonrelativistic spin splitting of electronic bands, breaking Kramers degeneracy without the necessity of spin-orbit coupling (SOC) [4, 6, 7, 10, 13, 14]. In conventional AFMs, symmetry-enforced degeneracies typically prevent such splitting, while altermagnetic symmetry permits momentum-dependent spin-split bands that retain overall global spin compensation. Critically, because this spin splitting does not require SOC, altermagnetic behavior can manifest significantly even in materials composed of lighter, more earth-abundant elements like Fe and Mn. This broadens the scope for material discovery and significantly reduces reliance on heavier, expensive, or rare elements typically needed for SOC-driven phenomena [15]. Experimentally confirmed altermagnets now encompass diverse systems, from insulating compounds like CuF_2 [1], MnF_2 [7], and MnTe [14] to metallic materials such as RuO_2 [16], Mn_5Si_3 [17], and CrSb [18]. These materials have demonstrated compelling and technologically relevant phenomena, including anomalous Hall effects (AHE), spin-polarized conductivity, spin-transfer torque, tunneling magnetoresistance, and giant magnetoresistance, which are essential ingredients for future spintronic applications [2, 19–24]. Consequently, the identification and characterization of alter-

magnetic materials represent a transformative advancement in magnetism and spintronics, sparking intensive research efforts aimed at uncovering new materials, elucidating underlying physical principles, and developing practical applications for this emerging class of magnetic materials.

However, discovering new altermagnets with significant spin splitting through trial-and-error experimental approaches is inherently challenging and resource-intensive. To overcome this limitation, high-throughput computational screening, leveraging reliable first-principles density functional theory (DFT) calculations, has emerged as an efficient and powerful methodology. This approach enables the rapid and systematic exploration of large material databases for candidates exhibiting desirable characteristics. Some recent efforts have used the MAGNDATA database [25, 26] for this purpose (see Sec. V for a comparison) with a focus on specific subclasses, such as metallic altermagnets or magnonic excitations in collinear systems, or using other selection criteria [27–29]. In this present work, we undertake an exhaustive and systematic high-throughput screening of the entire MAGNDATA database, including collinear versions of the non-collinear entries, without constraints to specific classes or properties, aiming to identify and comprehensively characterize all potential altermagnetic candidates. Through this extensive computational investigation, we successfully discover numerous previously unreported altermagnetic materials, validate several known candidates, and provide robust theoretical frameworks for future experimental realizations. This comprehensive approach not only significantly enhances the current understanding of altermagnetic phenomena but also expands the available pool of materials for next-generation spintronic devices, highlighting the critical importance and novelty of this study.

II. SCREENING WORKFLOW

We present a rigorous two-stage high-throughput computational screening workflow for the systematic identification of candidate altermagnetic materials, summarized schematically in Fig. 1. In the first stage of screening (Fig. 1a), we retrieved the March 11, 2025 state of the MAGNDATA database hosted by the Bilbao Crystallographic Server [25, 26, 30]. This database contains 2287 published magnetic structures with crystal structures and magnetic configurations primarily obtained via experimental characterization.

These magnetic materials were subsequently analyzed using the recently developed computational tool amcheck [31]. Amcheck operationalizes the symmetry-based theoretical framework underpinning altermagnetism by assessing symmetry operations relating spin-up and spin-down magnetic sublattices. Specifically, the algorithm evaluates whether the magnetic sublattices can be mapped onto each other through a spatial inversion or lattice translation combined with a spin-flip operation. If such mappings are universally applicable to all magnetic atoms, the material is pure AFM since these symmetry operations guarantee spin degeneracy across the electronic band structure. Conversely, the absence of such inversion or translation symmetries, coupled with the presence of alternative symmetry operations (e.g., rotational or mirror symmetries), indicates altermagnetism. This condition implies the presence of symmetry-protected spin splitting in the band structure despite zero net magnetization. The advantage of amcheck lies in its reliance solely on crystallographic and magnetic structural information, circumventing the need for computationally intensive electronic structure calculations. Consequently, it serves as a rapid, efficient, and theoretically robust tool ideally suited to large-scale, high-throughput screenings. The symmetry analysis, both internally in amcheck and for the details we report in the supplementary materials uses Spglib [32, 33].

We used Pymatgen [34] to read the mcif files from MAGNDATA. We applied amcheck to all the collinear structures, which resulted in 157 candidate altermagnetic materials. We then applied amcheck to collinear versions of all noncollinear materials, where we aligned the spins by the algorithm used by Pymatgen when converting a magnetic moment to a scalar: the magnitude of the magnetic moment is retained and the sign assigned by projecting the moment onto a standard axis. The standard axis is arbitrarily chosen to always have the direction defined by the Cartesian vector $(x, y, z) = (1.01, 1.02, 1.03)$. Notably, the forced-collinear variants are introduced solely to enable a uniform high-throughput screening; we do not assess their energetic stability relative to the noncollinear ground state. This resulted in 131 additional candidates. Overall, we obtained a total of 288 potential AM materials from the MAGNDATA database (157 collinear and 131 noncollinear). Eliminating duplicated structures based on chemical composition and space group, the final set was 188 candidates suitable for further computational examination.

In the second screening phase (Fig. 1b), input files for spin-polarized self-consistent field (SCF) and non-self-consistent field (non-SCF) DFT calculations were systematically generated using Pymatgen and the High-throughput toolkit (*httk*) [35]. The workflow manager in *httk* provides a powerful, flexible automation framework specifically tailored for large-scale computational workflows, significantly enhancing computational efficiency. Importantly, magnetic orders and initial magnetic moments of atoms were directly extracted from MAGNDATA's mcif files, ensuring consistency with experimentally established configurations. In cases where the reported local magnetic moments were particularly small (e.g., below 1 μ_B/atom), we initialized the corresponding magnetic moments to a slightly higher value (typically 1 μ_B) to avoid artificial quenching during SCF relaxation.

The resulting spin-polarized SCF calculations, per-

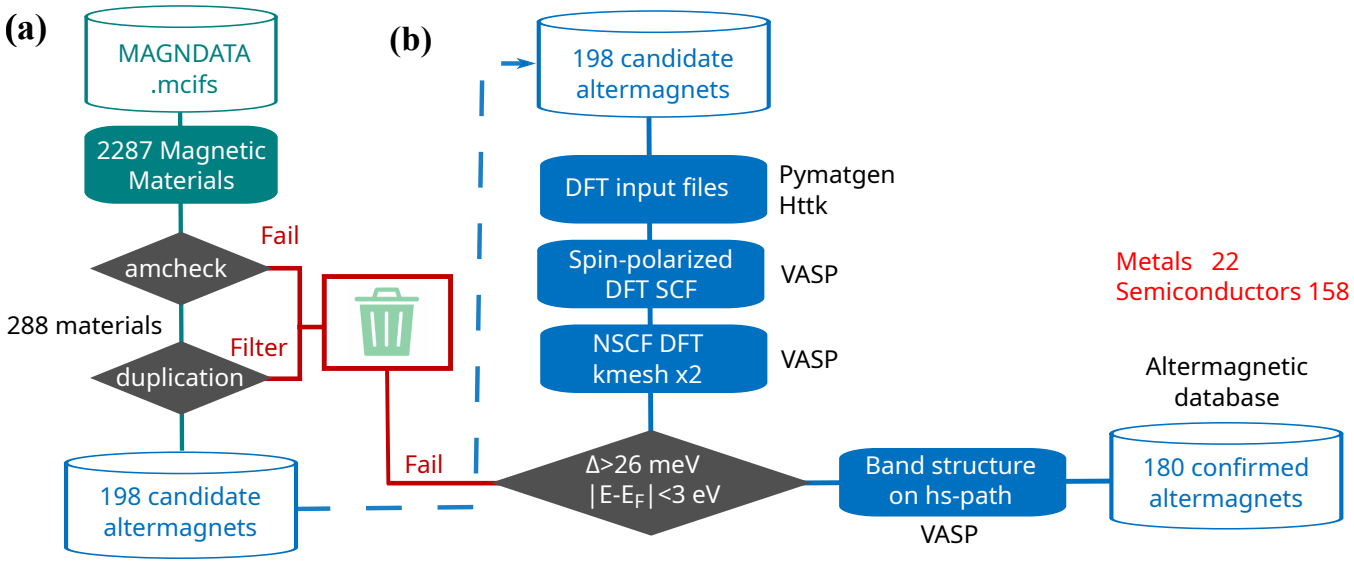


FIG. 1. **Two-stage high-throughput computational workflow to identify candidate altermagnetic materials (AMs). (a)** Initial screening selects experimentally characterized magnetic materials from the MAGNDATA database. Symmetry analysis via amcheck followed by deduplication filtering step, yielding a final set of 198 unique AM candidates. **(b)** In-depth computational verification using spin-polarized DFT calculations (VASP, pymatgen, and *httk*). Materials exhibiting spin splitting ($\geq$ 26 meV within $\pm$3 eV of E_F) are confirmed as AM and included in the final database.

formed using the Vienna Ab-initio Simulation Package (VASP) [36–38], were analyzed to identify meaningful spin-splitting. To select only robust altermagnets, a minimum spin-splitting magnitude of 26 meV was used as a selection criterion and this splitting has to occur within an energy window of $\pm$3 eV around the Fermi level. Figure S1 shows the distribution of $\Delta_{\max}$ across the screened set and supports adopting 26 meV as a physically motivated lower bound, comparable to the room-temperature thermal energy scale ($k_BT \approx 26$ meV).

Based on these criteria, 180 materials were validated as exhibiting significant spin-splitting and advanced to the final characterization step, while the remaining candidates were discarded. Detailed electronic band structure calculations were subsequently conducted for these selected 180 altermagnets, enabling direct visualization and confirmation of spin-up and spin-down band splittings. Because magnetic symmetry can enforce nodal manifolds where the nonrelativistic splitting vanishes on many high-symmetry lines/planes, we evaluate $\Delta(\mathbf{k})$ on dense Brillouin-zone meshes (and fixed-k_z slices when needed), rather than relying solely on conventional high-symmetry paths, to reliably capture $\Delta_{\max}$. In these computations, the magnetic moments were assumed to be in a collinear configuration, a commonly adopted simplification in high-throughput studies, which is sufficient for identifying the essential altermagnetic characteristics.

To further quantify the spin splitting, we computed both the average and volumetric spin-splitting metrics. The average spin splitting $\langle\Delta\rangle$ is defined as the mean of the maximum spin splitting across all $\mathbf{k}$-points with eigenstates lying within a $\pm$3 eV window around the Fermi level,

$$\langle\Delta\rangle = \frac{1}{N}\sum_{k=1}^{N} \max_{n\in W_k} \left|\varepsilon^{\uparrow}_{n,k} - \varepsilon^{\downarrow}_{n,k}\right|, \tag{1}$$

where W_k is the set of bands at $\mathbf{k}$ within the energy window, and N is the number of contributing $\mathbf{k}$-points.

The volumetric spin-splitting fraction F_Δ captures the fraction of bands and the portion of the Brillouin zone exhibiting appreciable spin splitting:

$$F_\Delta = \sum_k w_k \cdot \Theta\left(\frac{1}{M_k}\sum_{n\in W_k}\left|\varepsilon^{\uparrow}_{n,k} - \varepsilon^{\downarrow}_{n,k}\right|\right), \tag{2}$$

where w_k is the $\mathbf{k}$-point weight, M_k is the number of bands within the energy window at $\mathbf{k}$, and Θ is the Heaviside function applied with a small cutoff (e.g., 10 meV) to suppress numerical noise.

Note that the calculations are performed using the usual scalar-relativistic projector augmented-wave (PAW) pseudopotentials distributed with VASP, but we do not otherwise include spin–orbit coupling (SOC) or other relativistic corrections. This defines the nonrelativistic baseline for spin splitting in altermagnets, where the essential effect arises from exchange and crystalline symmetry rather than relativistic interactions. For compounds containing heavy 5d or 5f elements, however, SOC can strongly influence electronic phases [39] and consequently affect the magnitude of the spin splitting. The explicit inclusion of SOC in high-throughput workflows is computationally demanding and, in heavy-element systems, may also lead to convergence difficulties. Hence, in particular our results for heavy-element

compounds, which are expected to be more sensitive to these effects, may need further investigation for the contribution from SOC.

III. RESULTS AND DISCUSSION

Summarized in Table II are the key properties of the top candidate materials identified through our high-throughput screening, including their maximum, average, and volumetric spin-splitting magnitudes (ΔF), electronic band gaps, Hubbard U parameters, and minimum elemental abundances. Among these, six altermagnets, CrSb, MnTe, CrSe, RuO_2, $Ca(Al_2Fe)_4$, and UCr_2Si_2C, exhibit particularly pronounced spin-band splitting. Notably, experimental evidence for altermagnetism in CrSb [18], MnTe [40], and RuO_2 [16] has recently been presented, providing strong validation for the predictive capability of our computational framework. In the following sections, we focus on three representative cases: the metallic altermagnets UCr_2Si_2C and MnNbP, and the semiconducting altermagnet $YRuO_3$, each exhibiting spin-splitting features and serving as compelling examples of the diverse electronic characteristics accessible within the altermagnetic landscape.

A. UCr_2Si_2C

UCr_2Si_2C crystallizes in a tetragonal structure belonging to the paramagnetic space group $P4/mmm$ (No. 123), characterized by lattice parameters $a = b = 3.98$ and $c = 5.16$ [41]. The structure is composed of alternating uranium and Cr_2Si_2C layers stacked along the crystallographic c-axis. Within each Cr_2Si_2C layer, chromium atoms form planar Cr_2C networks arranged in a checkerboard motif. Magnetic moments are localized exclusively on the Cr atoms, which occupy two symmetry-inequivalent positions: Cr1 at (0.0, 0.5, 0.5) and Cr2 at (0.5, 0.0, 0.5). These moments are assumed to align antiparallel, with an estimated magnitude of approximately $0.66\mu_B$.

Under this collinear AFM configuration, UCr_2Si_2C is associated with the magnetic space group $Pm'm'm$ (No. 47.252, BNS notation), which determine its magnetic symmetry properties. This group comprises eight symmetry elements: four unitary operations that preserve spin namely, the identity $\{1\,|\,\mathbf{0}\}$, spatial inversion $\{-1\,|\,\mathbf{0}\}$, a twofold rotation about the x-axis $\{2_{100}\,|\,\mathbf{0}\}$, and a mirror reflection across the plane perpendicular to the x-axis $\{m_{100}\,|\,\mathbf{0}\}$ as well as four anti-unitary operations combining spatial transformations with time-reversal symmetry. These include the twofold rotations about the z-axis combined with time reversal $\{2'_{001}\,|\,\mathbf{0}\}$ and a twofold rotation about the y-axis combined with time reversal $\{2'_{010}\,|\,\mathbf{0}\}$, and the time-reversed mirror reflections $\{m'_{001}\,|\,\mathbf{0}\}$ and $\{m'_{010}\,|\,\mathbf{0}\}$. These operations collectively preserve the overall tetragonal crystal symmetry while accommodating a collinear antiferromagnetic configuration with Cr.

Crucially, although both inversion $\mathcal{P}$ $\{-1\,|\,\mathbf{0}\}$ and anti-unitary time revesal $\mathcal{T} = \{-1'\,|\,\mathbf{0}\}$ symmetries appear in the group, the combined operation $\mathcal{PT} = \{-1'\,|\,\mathbf{0}\}$ does not constitute a symmetry of the system. The absence of $\mathcal{PT}$ symmetry lifts the constraint that would otherwise enforce spin degeneracy, thereby permitting spin splitting even in the absence of spin–orbit coupling. Furthermore, the system lacks the combined spin-rotation and non-primitive lattice translation symmetry $U\tau$, which maps antiparallel magnetic sublattices onto one another via a 180° spin rotation coupled with a fractional lattice translation. Such symmetries are characteristic of conventional collinear antiferromagnets and protect spin degeneracy throughout the Brillouin zone. In contrast, the symmetry-inequivalent positioning of the Cr atoms in UCr_2Si_2C precludes the existence of any $U\tau$ operation. The simultaneous breaking of both $\mathcal{PT}$ and $U\tau$ symmetries thus defines the altermagnetic nature of UCr_2Si_2C.

Figure 2(c) presents the spin-polarized electronic band structure of UCr_2Si_2C along high-symmetry paths in the Brillouin zone, as defined in Fig.2(b). Spin-up and spin-down states are shown in red and blue, respectively. A prominent feature of the band structure is the coexistence of spin-degenerate and spin-split regions across momentum space, hallmarks of altermagnetic behavior. The maximum energy separation occurs near the $\Delta_{\max}$ point, where the spin splitting reaches approximately 0.72 eV. The average spin splitting across the Brillouin zone is calculated to be 0.31eV, with a volumetric splitting ratio of roughly 47%. To explicitly identify symmetry-driven spin reversals, we analyzed symmetry-equivalent paths in the reciprocal space, as shown in panel (d). Specifically, along paths such as $\Delta_{\max}$–Γ–$\Delta'_{\max}$ and R–A–R', exchanging the reciprocal-space coordinates $k_x \leftrightarrow k_y$ directly leads to inversion of the spin polarization (spin-up states become spin-down and vice versa). This momentum-dependent spin reversal arises naturally from the magnetic symmetry operations of the $Pm'm'm$ space group and it distinguishes altermagnetic systems from conventional ferromagnets or Rashba-type spin–orbit coupled systems.

To further visualize the momentum-resolved spin splitting, we plot the two-dimensional (2D) contour map of the spin splitting magnitude (ΔE) on the $k_z = 0.5$ plane in Fig. 2(e). This plane includes the maximum splitting point $\Delta_{\max} = (0.2, 0.5, 0.5)$, where the maximum spin splitting occurs. In this map, red and blue regions respectively indicate positive and negative spin splitting between spin-up and spin-down states. The most intense features appear in the vicinity of $\Delta_{\max}$, with symmetric but sign-reversed spin splitting observed on opposite sides of the Brillouin zone. This antisymmetric pattern of spin splitting, i.e., $\Delta E(\mathbf{k}) = -\Delta E(-\mathbf{k})$, is a defining signature of altermagnetic order in this material.

Figure 2(f) shows the spin-resolved Fermi surface cross-sections in the (001) plane. Spin-up and spin-down Fermi

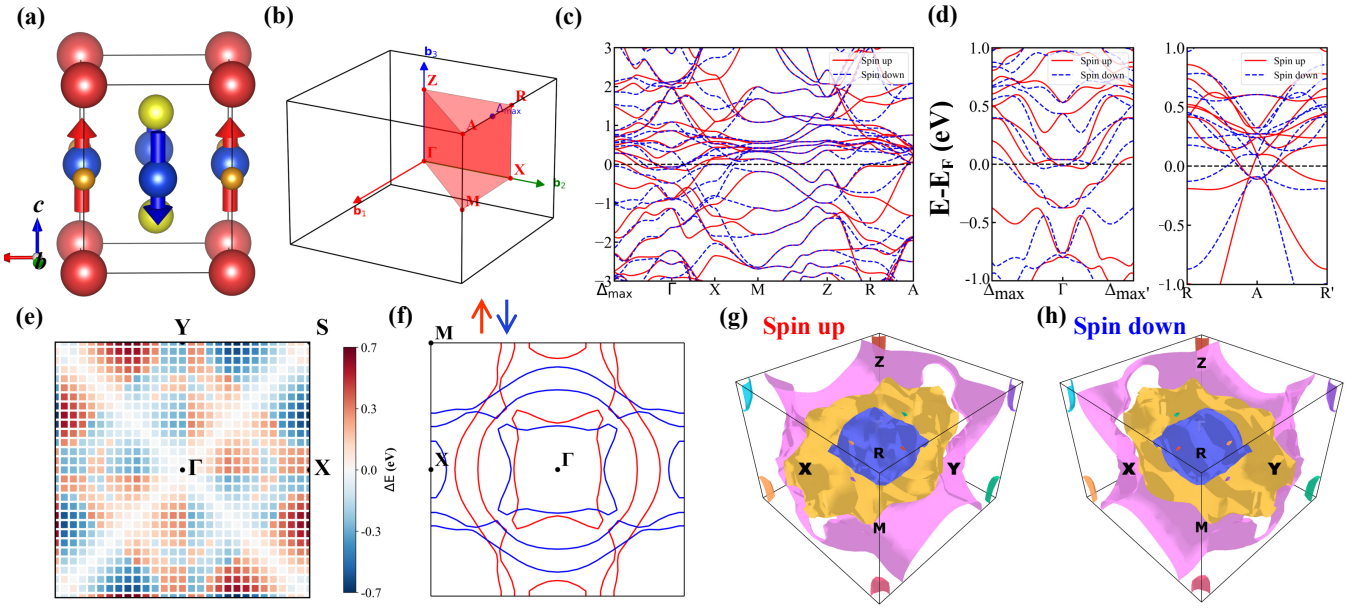


FIG. 2. **Structural, electronic, and spin-resolved properties of UCr_2Si_2C. (a)** Side view of the crystal structure of UCr_2Si_2C, illustrating the magnetic configuration with arrows representing spin orientations. **(b)** Corresponding Brillouin zone (BZ) indicating key high-symmetry points. **(c)** Spin-polarized electronic band structure along high-symmetry paths, where spin-up and spin-down bands are represented by red and blue dashed lines, respectively. **(d)** Band structures at symmetry-equivalent paths within the BZ, highlighting the inversion of spin-up and spin-down bands due to symmetry operations. **(e)** Two-dimensional contour plot of spin splitting (ΔE) at $k_z = 0.5$, showing the plane with maximal spin splitting. **(f)** The Fermi surface cut at $k_z = 0$, through the Γ−X−M plane, illustrating spin-up (red) and spin-down (blue) contributions. **(g–h)** Three-dimensional (3D) spin-resolved Fermi surfaces for **(g)** spin-up and **(h)** spin-down electronic states, emphasizing spin-dependent characteristics. Note that the absolute orientation of the collinear spin axis does not affect DFT calculations without spin-orbit coupling, hence, in our pictures the spin directions are shown as computed (in +/- z direction) rather than as reported for the respective structures.

contours are shown in red and blue, respectively. The contours are anisotropic and exhibit a clear 90° rotation between the spin channels, another hallmark of altermagnetism. To fully capture the spin-dependent topology of the Fermi surface, we plot the three-dimensional spin-resolved Fermi surfaces in Figs. 2(g) and 2(h) for the spin-up and spin-down channels, respectively. Each plot reveals four distinct Fermi surfaces corresponding to four partially occupied bands crossing the Fermi level. Notably, while the innermost Fermi surface centered at the corners of the Brillouin zone appears nearly identical for both spin channels, the remaining three Fermi sheets (colored yellow, blue, and pink) exhibit clear rotational asymmetry. The spin-down Fermi surfaces are clearly rotated by 90° relative to their spin-up counterparts, consistent with the antisymmetric spin texture expected from the symmetry constraints of the magnetic space group. Together, these observations, momentum-antisymmetric spin splitting, 90°-rotated spin-resolved Fermi surfaces, and symmetry-induced spin channel inversion, provide compelling evidence for the robust altermagnetic character of UCr_2Si_2C.

B. NbMnP

NbMnP crystallizes in the TiNiSi−type orthorhombic structure belonging to the paramagnetic space group *Pnma* (No. 62), characterized by lattice parameters $a = 6.182$, $b = 3.557$, and $c = 7.219$ [42]. Its crystal structure comprises zigzag chains of Mn atoms aligned along the b-axis, embedded within a network formed by Nb and P atoms. In this study, we consider a collinear AFM configuration as depicted in Fig. 3(a).

The magnetic symmetry properties of this AFM state are governed by magnetic space group $Pn'm'a'$ (No. 62.449, BNS notation), a type-III magnetic subgroup of the paramagnetic parent group Pnma (No. 62). This magnetic group incorporates eight symmetry elements: four unitary operations preserving spin specifically, the identity $\{1 \mid \mathbf{0}\}$, spatial inversion $\{-1 \mid \mathbf{0}\}$, mirror reflections across the yz-plane $\{m_{100} \mid \frac{1}{2}, \frac{1}{2}, \frac{1}{2}\}$, and the xz-plane $\{m_{010} \mid \frac{1}{2}, \frac{1}{2}, \frac{1}{2}\}$; and four anti-unitary operations combining spatial transformations with time reversal, including time-reversed inversion $\{-1' \mid \frac{1}{2}, 0, \frac{1}{2}\}$, a time-reversed mirror reflection across the xy-plane $\{m'_{001} \mid \frac{1}{2}, 0, \frac{1}{2}\}$, spin-flip mirror operations $\{m'_{100} \mid 0, \frac{1}{2}, 0\}$, and $\{m'_{010} \mid 0, \frac{1}{2}, 0\}$. These symmetry operations accommodate the collinear AFM order with alternating Mn spins.

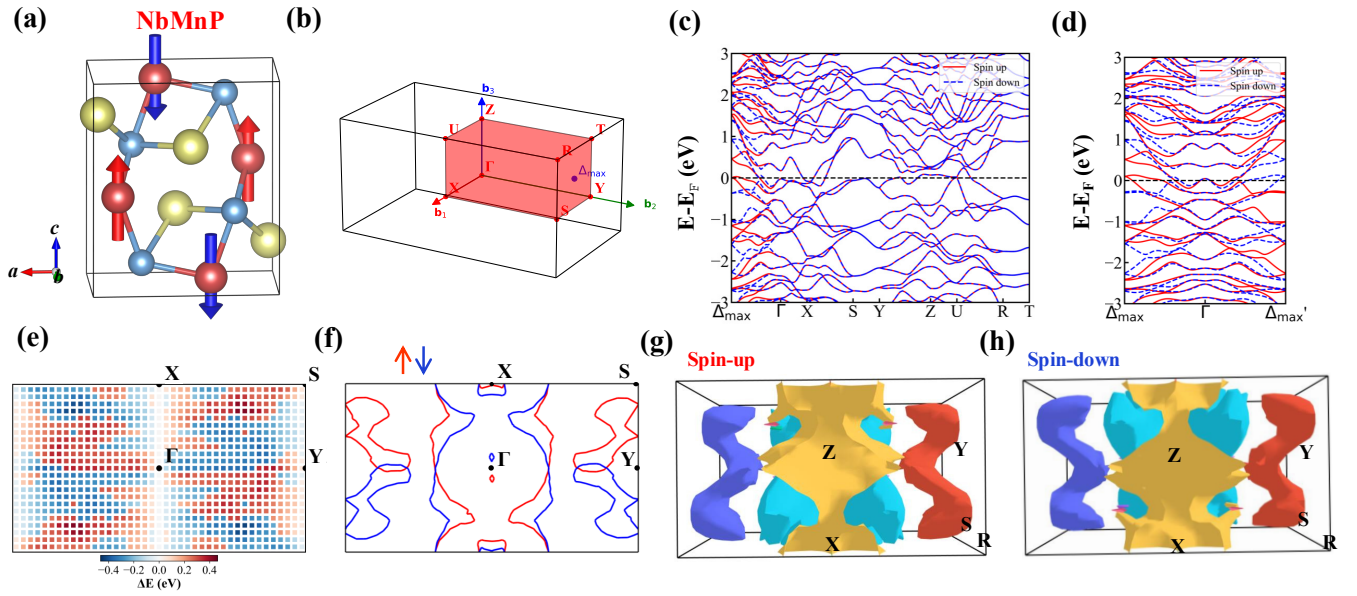


FIG. 3. **Structural, electronic, and spin-resolved properties of NbMnP.** (a) Side view of the crystal structure of NbMnP, illustrating the AFM configuration with spins aligned along the z-axis on the Mn sites. (b) Corresponding BZ indicating key high-symmetry points. (c) Spin-polarized electronic band structure along standard high-symmetry paths, with spin-up and spin-down channels represented by red and blue lines, respectively. (d) Spin-resolved band structure along the $\Delta_{max} - \Gamma - \Delta'_{max}$ path, highlighting the symmetry-enforced spin reversal. (e) 2D contour map of the spin-splitting magnitude (ΔE) on the $k_z = 0.25$ plane. (f) Spin-resolved Fermi surface cut at k_z=0.25 plane. These contours are anisotropic and exhibit a 180° rotation between the spin channels. (g) and (h) 3D spin-resolved Fermi surfaces for the spin-up and spin-down channels, respectively, showing complementary shapes related by $k_x \leftrightarrow -k_x$ and a spin flip.

Critically, both $\mathcal{PT}$ and U_τ symmetries are absent which implies that no symmetry exists to map the antiparallel Mn sublattices onto one another, thereby lifting the constraints that would typically enforce spin degeneracy in conventional antiferromagnets.

The spin-polarized electronic band structure along standard high-symmetry paths is presented in Fig. 3(c), with spin-up and spin-down channels shown in red and blue, respectively. Pronounced spin splitting regions coexist with segments of near degeneracy. The maximum spin splitting, approximately 0.46 eV, occurs near the $\Delta_{\max}$ point, whereas the BZ-averaged splitting is about 0.28 eV with a volumetric splitting ratio of 35%. To illustrate symmetry-enforced spin reversal explicitly, Fig. 3(d) displays the spin-resolved bands along the path $\Delta_{\max}$–Γ–$\Delta'_{\max}$, demonstrating symmetric spin-band exchange under the transformation $k_x \to -k_x$ across Γ.

Figure 3(e) shows the spin-splitting magnitude ΔE within the $k_z = 0.25$ plane, revealing clearly sign-reversed splitting distributions across opposite sides of the BZ. Additionally, Fig. 3(f) presents the spin-resolved Fermi surface cross-section at $k_z = 0.05$, exhibiting distinctly anisotropic contours and a clear 180° rotation between the spin channels, consistent with $k_x \leftrightarrow -k_x$ symmetry. The 3D spin-resolved Fermi surfaces shown in Figs. 3(g) and 3(h) for spin-up and spin-down channels, respectively, further highlight this 180° spin-channel rotation. Taken together, these observations robustly confirm the altermagnetic character of NbMnP.

C. $YRuO_3$

$YRuO_3$ crystallizes in the orthorhombic magnetic space group $Pn'ma'$ (No. 62.448, BNS notation), derived from the paramagnetic parent group Pnma (No. 62) [43]. The unit cell adopts lattice parameters $a = 5.839$ Å, $b = 7.523$ Å, $c = 5.192$ Å. The crystal structure can be described as a tilted perovskite framework composed of corner-sharing RuO_6 octahedra, with Y atoms occupying the interstitial positions. The magnetic ground state is G-type antiferromagnetic, with antiparallel spin alignment between neighboring Ru^{3+} sites along all three crystallographic directions. The spin moments are localized on the Ru sublattices, whereas Y and O atoms remain magnetically inactive. Addtionally, it includes standard unitary operations, such as inversion, mirror planes, and twofold rotations, along with anti-unitary operations that combine time reversal with rotations and mirrors (e.g., $2'_{001}$, m'_{100}, m'_{001}). The resulting AFM structure consists of two symmetry-inequivalent Ru sublattices with antiparallel spin orientations. This arrangement prevents any symmetry operation from mapping one sublattice onto the other via inversion–time-reversal ($\mathcal{PT}$) or spin-rotation–translation ($\mathcal{U}\tau$). This dual symmetry breaking allows for spin splitting even without spin–orbit cou-

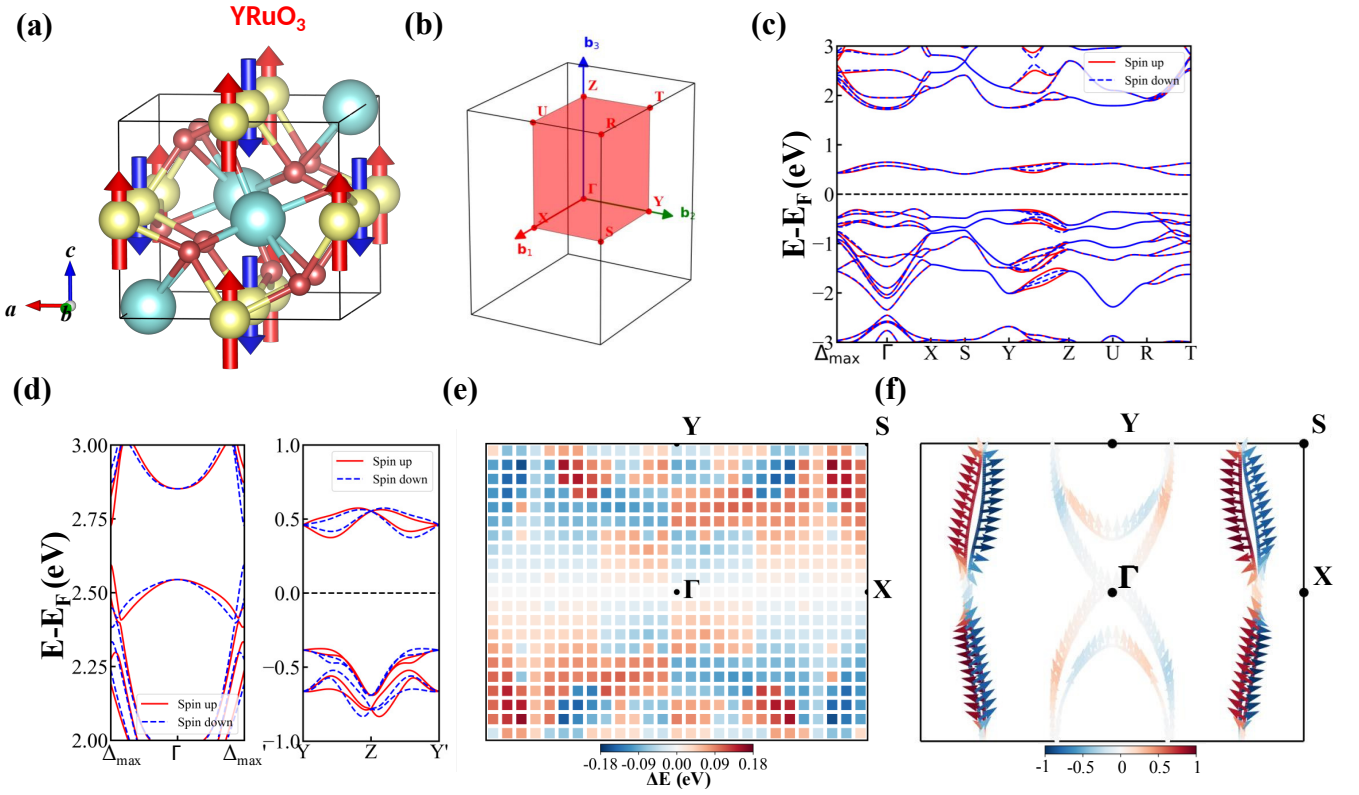


FIG. 4. **Structural, electronic, and spin-resolved properties of $YRuO_3$.** (a) Unit cell of $YRuO_3$, illustrating the atomic arrangement and the AFM spin configuration. Large light green spheres represent Y atoms, small red spheres represent O atoms, and yellow spheres represent Ru atoms. (b) Bulk Brillouin zone of $YRuO_3$ with high-symmetry points labeled. (c) Spin-polarized electronic band structure of $YRuO_3$ along high-symmetry directions. Red solid lines indicate spin-up bands, and blue dashed lines represent spin-down bands. (d) Detailed view of the spin-polarized band structure along two symmetry-equivalent paths within the BZ, highlighting the spin inversion features. (e) 2D contour plot of the spin splitting ΔE in the k_z=0.4 plane, identifying regions of maximal spin-momentum locking. (f) Spin texture visualized in the 001 plane, showing the orientation and magnitude of the spin polarization for selected states.

pling, which is what defines the altermagnetic nature of $YRuO_3$.

Figure 4(b) shows the bulk Brillouin zone BZ $YRuO_3$ with the high-symmetry points labeled according to the Pnma convention. The spin-polarized electronic band structure, computed along these high-symmetry paths, is presented in Fig. 4(c). A key feature is the coexistence of spin-degenerate and spin-split bands. The magnitude of spin splitting varies across momentum space, reaching its maximum near the $\Delta_{\max}$ point, where the energy separation between spin-up and spin-down bands is approximately 0.12 eV.

To visualize the symmetry-driven spin inversion, Fig. 4(d) compares the band dispersions along two momentum paths that are equivalent under the transformation $k_x \to -k_x$. Along these symmetry-related paths, the spin polarization reverses: spin-up states on the $\Delta_{\max}$/Y side correspond to spin-down states on the $-\Delta_{\max}$/$-$Y side, reflecting the momentum-antisymmetric spin splitting enforced by the $Pn'ma'$ magnetic group. Figure 4(e) further highlights this feature through a 2D contour map of ΔE in the $k_z = 0.1$ plane, where the splitting is maximal around $\Delta_{\max}$. Figure 4(f) illustrates the spin texture in the (001) plane from a SOC (noncollinear) calculation, showing the in-plane orientation of the spin expectation value for states near the Fermi level. The spin-up and spin-down components exhibit opposite orientations across symmetry-related k-points, indicating a momentum-dependent spin reversal that extends across the Brillouin zone rather than being localized to a specific path or point.

IV. IDENTIFICATION IN 2D DATABASES

To identify bulk altermagnetic compounds with chemically equivalent 2D counterparts, we compared the reduced formulas and ICSD IDs of all 188 bulk AM candidates with entries in two major 2D materials databases: the Computational 2D Materials Database (C2DB) [44] and the AiiDA 2D repository [45]. We only retain entries for which the ICSD ID of the bulk parent coincides with that of the corresponding 2D record. In Table I, we collect all bulk AM materials whose reduced formula

TABLE I. Bulk altermagnetic materials with an existing 2D compound of the same reduced chemical formula in the C2DB or AiiDA databases. Multiple MCIF entries with identical formulas correspond to distinct MAGNDATA models.

IDs	Chemical formula	C2DB	AiiDA
0.15	MnF_2	Yes	–
0.178, 0.334	CoF_2	Yes	–
0.335, 0.581, 1.0.33	FeF_3	Yes	–
0.36	NiF_2	Yes	–
0.607	RuO_2	Yes	–
0.800	MnTe	Yes	–
1.0.47, 1.0.48	$MnSe_2$	Yes	Yes
2.35	CrSe	Yes	–
0.65, 0.66	Fe_2O_3	–	Yes

appears in at least one of the 2D databases and indicate whether a match was found in C2DB, in AiiDA, or in both. These databases contain both experimentally synthesized and theoretically predicted monolayer compounds.

The list of bulk altermagnets with a corresponding two-dimensional compound is rather short. Indeed, the majority of compounds appearing in Table I contain transition–metal elements with partially filled d shells together with halogens (F, Cl) or chalcogens (S, Se, Te). The later help stabilizing layered or quasi-layered chemistries, while the former provide the local moments that form the basis of the magnetism.

Note that the first column of the table shows that some chemical formulas correspond to multiple MAGNDATA entries. The reason is that different experimental studies report distinct magnetic configurations, magnetic subgroup assignments, or slightly different crystallographic refinements. These duplicated entries correspond to separate magnetic models of the same material, not different compounds, and therefore belong match with a single two-dimensional material.

Table I identifies candidate bulk altermagnets which exist in 2D, but does not say that these materials are also altermagnetic as a monolayer. This question has been addressed by Sødequist and Olsen [46], who identified 7 altermagnetic monolayer candidates starting from C2DB. Crucially, they take into account the magnetic anisotropy coming from spin-orbit that is necessary to get a magnetically ordered phase in 2d, in accordance with the Mermin-Wagner theorem. Starting from C2DB, they identified which monolayers can be altermagnets, also taking into account spin-orbit coupling. The spin-orbit coupling introduces magnetic anisotropy that makes it possible to stabilize magnetism in 2d while satisfying the Mermin-Wagner theorem. Their 7 altermagnetic monolayer candidates similarly contain mostly transition metals terminated by halogens or chalcogens, although they also find two more complex compounds. Interestingly, there is zero overlap between Table I and the list in Sødequist and Olsen.

V. COMPARISON WITH OTHER STUDIES

The results reported here can be discussed in relation to two prior screenings of MAGNDATA. The high-throughput classification by Wan *et al.* relied on the absence of the antiunitary symmetries $\mathcal{PT}$ (inversion plus time reversal) and $t\mathcal{T}$ (translation plus time reversal) [27]. Moreover, they extended their candidate pool to include ferrimagnetic systems by considering their SOC-off configuration, resulting in 336 potential altermagnets. Guo *et al.* also focused on systems with $\mathcal{PT}$ symmetry [29]. They screened stoichiometric compounds with fully compensated collinear magnetic order without ferromagnetic component while avoiding some complications, including systems with magnetic order from rare-earth atoms, large unit cells, and DFT calculations difficult to converge, which resulted in 62 materials.

Our study employs the `amcheck` algorithm, which tests the same symmetry condition (absence of $\mathcal{PT}$ and $t\mathcal{T}$) to identify potential altermagnetic materials. However, `amcheck` strictly excludes ferrimagnetic states since their sublattices are completely not symmetry-related and are instead classified as "Luttinger ferrimagnets" that exhibit spin splitting but lack the required momentum-odd, nodal spin texture over the Brillouin zone. For example, Cr_2S_3, listed as "interesting" in Ref. [27], shows spin splitting in the spin–polarized DFT consistent with ferrimagnetic behavior, yet lacks the nodal spin texture and is therefore not classified as altermagnetic here. On the other hand, we find a collinear AFM with Kramers–degenerate bands for $SrMnSb_2$, and the small splittings of a few meV that appear at high energy are most likely numerical artifacts and not indicative of altermagnetism. These distinctions likely account for the smaller number of altermagnets identified in our study compared to Ref. [27], while remaining fully consistent with the symmetry–based definition of altermagnetism [1, 2]. The 59 non-metallic and 3 metallic compounds identified in Ref. [29] all appear in our list of 157 collinear entries with the right symmetries for altermagnetism (see table S2 in the supplementary materials), however, the criterion of a spin splitting threshold of 26 meV for our final list removes 10 of them.

Furthermore, we have considered a set of collinear versions of materials reported as noncollinear. This extended set of materials along with their computed spin splittings describe alternative spin configurations on otherwise stable crystal structures. They can be a valuable resource to aid the general understanding of altermagnetism. Some of them are arguably relevant due to them being very nearly collinear, shown in our analysis by the angle between the spin axes. We also speculate that for some of the ones with larger such angles, there could exist ways in practice to invoke a more aligned moments to give the altermagnetic configuration, via, e.g., external fields, stress/strain, or similar mechanisms.

TABLE II. **Top altermagnet candidate materials with respect to their spin-splitting.** Space group, max angle between spins for materials that were originally noncollinear ($\arccos(|S_i \cdot S_j|/|S_i||S_j|)$), spin-splitting metrics, band gap, wave classification, Hubbard U, and minimum elemental abundance. For more information on symmetry data, refer to the supplementary materials.

Material	Space Group	$\frac{\lvert S_i \cdot S_j \rvert}{\lvert S_i \rvert \lvert S_j \rvert}$	F_Δ (%)	Max. SS (eV)	Avg. SS (eV)	Bandgap (eV)	Wave	U Values	Min Abund.
CrSb	$P6_3/mmc$	0.0°	34.375	1.872	0.763	0	g	Cr: 3.5	2×10^3
MnTe	$P6_3/mmc$	0.0°	34.375	0.923	0.449	0.7637	g	Mn: 4.0	1×10^1
RuO_2	$P4_2/mnm$	0.0°	25.000	0.865	0.351	0	d	Ru: 2.0	1×10^1
CrSe	$P6_3/mmc$	57.79°	35.938	0.800	0.489	0	g	Cr: 3.5	5×10^2
UCr_2Si_2C	$P4/mmm$	0.0°	46.875	0.719	0.312	0	d	Cr: 3.5	3×10^4
$Ca(Al_2Fe)_4$	$I4/mmm$	8.41°	37.500	0.628	0.374	0	d	Fe: 5.3	4×10^8
CoF_2	$P4_2/mnm$	0.0°	16.667	0.479	0.223	3.3056	d	Co: 3.32	2×10^5
MnNbP	$Pnma$	86.65°	35.000	0.457	0.276	0	d	Mn: 4.0; Nb: 1.5	2×10^5
NiF_2	$P4_2/mnm$	1.72°	27.083	0.392	0.180	5.2675	d	Ni: 6.4	8×10^5
$LiFe_2F_6$	$P4_2/mnm$	0.0°	12.500	0.319	0.159	0.1679	d	Fe: 5.3	2×10^5
$Mn(C_2N_3)_2$	$Pnnm$	0.0°	20.000	0.305	0.184	4.0756	d	Mn: 4.0	2×10^5
$MnGeN_2$	$Pna2_1$	0.0°	14.583	0.305	0.145	1.5162	d	Mn: 4.0	2×10^4
$FeSO_4F$	$C2/c$	0.0°	28.906	0.301	0.158	2.4510	d	Fe: 5.3	4×10^6
$NiCO_3$	$R\text{-}3c$	0.0°	20.833	0.301	0.167	4.1969	g	Ni: 6.4	8×10^5
MnF_2	$P4_2/mnm$	0.0°	18.750	0.294	0.156	3.5754	d	Mn: 4.0	6×10^6
$CrVO_4$	$Cmcm$	0.0°	28.571	0.292	0.158	2.8766	d	Cr: 3.5; V: 3.5	1×10^6
$Sr_4Fe_4O_{11}$	$Cmmm$	0.0°	29.808	0.289	0.150	0.1756	d	Fe: 5.3	4×10^6
La_2CoIrO_6	$P2_1/c$	89.27°	24.107	0.272	0.121	0	d	La: 6.0; Co: 3.32; Ir: 2.0	1×10^1
$TbFeO_3$	$Pnma$	0.0°	26.786	0.271	0.133	2.8257	d	Tb: 6.7; Fe: 5.3	1×10^4
Fe_2WO_6	$Pbcn$	37.39°	29.688	0.270	0.173	1.4648	d	Fe: 5.3	1×10^4
$Er_2Ru_2O_7$	$Fd\text{-}3m$	0.0°	20.312	0.268	0.266	0.4121	d	Er: 6.0; Ru: 2.0	1×10^1
$FeBO_3$	$R\text{-}3c$	0.0°	29.688	0.262	0.177	2.6602	g	Fe: 5.3	1×10^5
$DyFeO_3$	$Pnma$	33.4°	26.786	0.251	0.133	2.8605	d	Dy: 6.7; Fe: 5.3	5×10^4
$HoFeO_3$	$Pnma$	90.0°	25.000	0.250	0.125	2.7346	d	Ho: 6.0; Fe: 5.3	1×10^4
$TlCrO_3$	$Pnma$	0.0°	24.107	0.246	0.146	0.6254	d	Cr: 3.5	8×10^3

VI. CONCLUSION

In this work, we have established a comprehensive and symmetry-aware high-throughput framework for the discovery and characterization of altermagnetic materials. We systematically screened more than 2,000 experimentally verified magnetic structures from the MAGNDATA database using a two-stage workflow. This approach, built on the magnetic symmetry diagnostic tool amcheck and the High-Throughput Toolkit, identified 180 candidate materials exhibiting significant momentum-dependent spin splitting. These include both metallic and semiconducting systems, many of which had not been previously reported as altermagnets. Notably, our approach recovers experimentally confirmed compounds such as CrSb, MnTe, and RuO_2, and highlights previously overlooked materials like UCr_2Si_2C, MnNbP, and $YRuO_3$ that display robust symmetry-protected spin splitting even in the absence of spin–orbit coupling. Furthermore, by cross-referencing our bulk AM candidates with the C2DB and AiiDA 2D repository, we identify nine materials with chemically equivalent 2D counterparts.

Crucially, our momentum-resolved analysis reveals that spin splitting varies strongly across the Brillouin zone, often away from high-symmetry paths, providing actionable insights for future spin and angle-resolved photoemission spectroscopy (ARPES) measurements. The open-access database generated through this effort offers a valuable resource for guiding experimental exploration and materials design in spintronics. More broadly, this study establishes a scalable and transferable blueprint for accelerating the discovery of unconventional magnetic phases and paves the way for targeted development of altermagnetic materials with desirable symmetry and transport properties.

VII. ACKNOWLEDGEMENTS

This work was partially supported by the Wallenberg Initiative Materials Science for Sustainability (WISE) funded by the Knut and Alice Wallenberg Foundation. R.A. acknowledges financial support from the Swedish e-Science Research Centre (SeRC). EvL acknowledges support from the Swedish Research Council (Vetenskapsrådet, VR) under grant 2022-03090, from the Royal Physiographic Society in Lund and by eSSENCE, a strategic research area for e-Science, grant number eSSENCE@LU 9:1. J.A.L thank the Kempe-stiftelserna, Sweden and Swedish Research Council under grant no. 2023-03894 for financial support. B.M. acknowledge the financial support of Olle Engkvists stiftelse, project 207-

0582. The computations were enabled by resources provided by the National Academic Infrastructure for Supercomputing in Sweden (NAISS), partially funded by the Swedish Research Council through grant agreement no. 2022-06725.

Appendix A: Computational Details

Density functional theory (DFT) calculations were carried out using the Vienna *Ab initio* Simulation Package (VASP) [37, 38], employing the projector augmented-wave (PAW) method and the generalized gradient approximation (GGA) with the Perdew–Burke–Ernzerhof (PBE) functional to describe exchange-correlation effects [36, 47]. Electron correlation was treated using the rotationally invariant DFT+U approach [48], with the effective Hubbard U_{eff} parameters taken from Pymatgen (Materials Project) [49] and supplemented by Wang *et al.* [50] where needed. The magnitude of the spin splitting depends on the value of U via the magnitude of the magnetic moments [51], whereas the structure of the splitting in the Brillouin Zone is expected to be weakly dependent on the value of U. Consistent with this, recalculations with U scaled by $\pm 10\%$ for all metallic candidates show that the altermagnetic classification is unchanged and sizable splittings persist; the variations are mainly quantitative and not strictly monotonic, with only $Co_2Mo_3O_8$ turning insulating at U+10% (Table S4).

For all simulations, the plane-wave energy cutoff was automatically set to 1.3 times the maximum ENMAX value among the elements present in the system, following VASP's recommended settings and the electronic self-consistency loop was converged to within 10^{-6} eV. K-point meshes for SCF calculations were automatically generated by Pymatgen, targeting a density of approximately 1000 k-points per reciprocal atom. For NSCF calculations, the k-point mesh was manually doubled along each reciprocal axis to ensure accurate Brillouin zone sampling for spin-splitting analysis. Although canted magnetic configurations occur in many materials, for computational efficiency we approximated their magnetic structures using collinear spin arrangements to identify signatures of altermagnetism.

High-throughput calculations were managed using *httk* [35]. High-symmetry **k**-paths were constructed using Pymatgen [34], and magnetic space groups were identified using the Spglib library [32, 33]. Fermi surfaces and spin textures were visualized using the `IFermi` package [52].

The elemental abundance values, expressed in parts per million (ppm) with respect to the Earth's crust, were obtained using the `mendeleev` [53] Python library and are reported in the table.

[1] L. Šmejkal, J. Sinova, and T. Jungwirth, Beyond conventional ferromagnetism and antiferromagnetism: A phase with nonrelativistic spin and crystal rotation symmetry, Physical Review X **12**, 031042 (2022).

[2] L. Šmejkal, J. Sinova, and T. Jungwirth, Emerging research landscape of altermagnetism, Physical Review X **12**, 040501 (2022).

[3] I. Mazin and PRX editors, Altermagnetism—a new punch line of fundamental magnetism (2022).

[4] K.-H. Ahn, A. Hariki, K.-W. Lee, and J. Kuneš, Antiferromagnetism in RuO2 as d-wave Pomeranchuk instability, Physical Review B **99**, 184432 (2019).

[5] M. Naka, S. Hayami, H. Kusunose, Y. Yanagi, Y. Motome, and H. Seo, Spin current generation in organic antiferromagnets, Nature communications **10**, 4305 (2019).

[6] L. Šmejkal, R. González-Hernández, T. Jungwirth, and J. Sinova, Crystal time-reversal symmetry breaking and spontaneous hall effect in collinear antiferromagnets, Science advances **6**, eaaz8809 (2020).

[7] L.-D. Yuan, Z. Wang, J.-W. Luo, E. I. Rashba, and A. Zunger, Giant momentum-dependent spin splitting in centrosymmetric low-z antiferromagnets, Physical Review B **102**, 014422 (2020).

[8] S. Hayami, Y. Yanagi, and H. Kusunose, Bottom-up design of spin-split and reshaped electronic band structures in antiferromagnets without spin-orbit coupling: Procedure on the basis of augmented multipoles, Physical Review B **102**, 144441 (2020).

[9] H.-Y. Ma, M. Hu, N. Li, J. Liu, W. Yao, J.-F. Jia, and J. Liu, Multifunctional antiferromagnetic materials with giant piezomagnetism and noncollinear spin current, Nature communications **12**, 2846 (2021).

[10] I. I. Mazin, K. Koepernik, M. D. Johannes, R. González-Hernández, and L. Šmejkal, Prediction of unconventional magnetism in doped FeSb2, Proceedings of the National Academy of Sciences **118**, e2108924118 (2021).

[11] P. Liu, J. Li, J. Han, X. Wan, and Q. Liu, Spin-group symmetry in magnetic materials with negligible spin-orbit coupling, Physical Review X **12**, 021016 (2022).

[12] S. Rooj, S. Saxena, and N. Ganguli, Altermagnetism in the orthorhombic P nma structure through group theory and DFT calculations, Physical Review B **111**, 014434 (2025).

[13] S. Hayami, Y. Yanagi, and H. Kusunose, Momentum-dependent spin splitting by collinear antiferromagnetic ordering, journal of the physical society of japan **88**, 123702 (2019).

[14] J. Krempaskỳ, L. Šmejkal, S. D'souza, M. Hajlaoui, G. Springholz, K. Uhlířová, F. Alarab, P. Constantinou, V. Strocov, D. Usanov, *et al.*, Altermagnetic lifting of kramers spin degeneracy, Nature **626**, 517 (2024).

[15] C.-C. Wei, E. Lawrence, A. Tran, and H. Ji, Crystal chemistry and design principles of altermagnets, ACS Organic & Inorganic Au **4**, 604 (2024).

[16] O. Fedchenko, J. Minár, A. Akashdeep, S. W. D'Souza, D. Vasilyev, O. Tkach, L. Odenbreit, Q. Nguyen, D. Kutnyakhov, N. Wind, *et al.*, Observation of time-reversal symmetry breaking in the band structure of altermagnetic ruo2, Science advances **10**, eadj4883 (2024).

[17] H. Reichlova, R. Lopes Seeger, R. González-Hernández,

I. Kounta, R. Schlitz, D. Kriegner, P. Ritzinger, M. Lammel, M. Leiviskä, A. Birk Hellenes, *et al.*, Observation of a spontaneous anomalous Hall response in the Mn5Si3 d-wave altermagnet candidate, Nature Communications **15**, 4961 (2024).

[18] S. Reimers, L. Odenbreit, L. Šmejkal, V. N. Strocov, P. Constantinou, A. B. Hellenes, R. Jaeschke Ubiergo, W. H. Campos, V. K. Bharadwaj, A. Chakraborty, *et al.*, Direct observation of altermagnetic band splitting in CrSb thin films, Nature Communications **15**, 2116 (2024).

[19] L. Šmejkal, A. H. MacDonald, J. Sinova, S. Nakatsuji, and T. Jungwirth, Anomalous Hall antiferromagnets, Nature Reviews Materials **7**, 482 (2022).

[20] R. Gonzalez Betancourt, J. Zubáč, R. Gonzalez-Hernandez, K. Geishendorf, Z. Šobáň, G. Springholz, K. Olejník, L. Šmejkal, J. Sinova, T. Jungwirth, *et al.*, Spontaneous anomalous Hall effect arising from an unconventional compensated magnetic phase in a semiconductor, Physical Review Letters **130**, 036702 (2023).

[21] L. Šmejkal, A. B. Hellenes, R. González-Hernández, J. Sinova, and T. Jungwirth, Giant and tunneling magnetoresistance in unconventional collinear antiferromagnets with nonrelativistic spin-momentum coupling, Physical Review X **12**, 011028 (2022).

[22] R. González-Hernández, L. Šmejkal, K. Výborný, Y. Yahagi, J. Sinova, T. Jungwirth, and J. Železný, Efficient electrical spin splitter based on nonrelativistic collinear antiferromagnetism, Physical Review Letters **126**, 127701 (2021).

[23] H. Bai, Y. Zhang, Y. Zhou, P. Chen, C. Wan, L. Han, W. Zhu, S. Liang, Y. Su, X. Han, *et al.*, Efficient spin-to-charge conversion via altermagnetic spin splitting effect in antiferromagnet RuO2, Physical review letters **130**, 216701 (2023).

[24] A. Bose, N. J. Schreiber, R. Jain, D.-F. Shao, H. P. Nair, J. Sun, X. S. Zhang, D. A. Muller, E. Y. Tsymbal, D. G. Schlom, *et al.*, Tilted spin current generated by the collinear antiferromagnet ruthenium dioxide, Nature Electronics **5**, 267 (2022).

[25] S. V. Gallego, J. M. Perez-Mato, L. Elcoro, E. S. Tasci, R. M. Hanson, K. Momma, M. I. Aroyo, and G. Madariaga, MAGNDATA: towards a database of magnetic structures. I. the commensurate case, Journal of Applied Crystallography **49**, 1750–1776 (2016).

[26] S. V. Gallego, J. M. Perez-Mato, L. Elcoro, E. S. Tasci, R. M. Hanson, M. I. Aroyo, and G. Madariaga, Magndata: towards a database of magnetic structures. ii. the incommensurate case, Applied Crystallography **49**, 1941 (2016).

[27] X. Wan, S. Mandal, Y. Guo, and K. Haule, High-throughput search for metallic altermagnets by embedded dynamical mean field theory, arXiv preprint arXiv:2412.10356 (2024).

[28] X. Chen, Y. Liu, P. Liu, Y. Yu, J. Ren, J. Li, A. Zhang, and Q. Liu, Unconventional magnons in collinear magnets dictated by spin space groups, Nature , 1 (2025).

[29] Y. Guo, H. Liu, O. Janson, I. C. Fulga, J. van den Brink, and J. I. Facio, Spin-split collinear antiferromagnets: A large-scale ab-initio study, Materials Today Physics **32**, 100991 (2023).

[30] M. I. Aroyo, J. M. Perez-Mato, C. Capillas, and H. Wondratschek, The Bilbao crystallographic server, in *International Tables for Crystallography* (International Union of Crystallography, 2011) p. 57–69.

[31] A. Smolyanyuk, L. Šmejkal, and I. I. Mazin, A tool to check whether a symmetry-compensated collinear magnetic material is antiferro-or altermagnetic, SciPost Physics Codebases , 030 (2024).

[32] K. S. Atsushi Togo and I. Tanaka, Spglib: a software library for crystal symmetry search, Sci. Technol. Adv. Mater., Meth. **4**, 2384822 (2024).

[33] K. Shinohara, A. Togo, and I. Tanaka, Algorithms for magnetic symmetry operation search and identification of magnetic space group from magnetic crystal structure, Acta Cryst. A **79**, 390 (2023).

[34] S. P. Ong, W. D. Richards, A. Jain, G. Hautier, M. Kocher, S. Cholia, D. Gunter, V. L. Chevrier, K. A. Persson, and G. Ceder, Python materials genomics (pymatgen): A robust, open-source python library for materials analysis, Computational Materials Science **68**, 314 (2013).

[35] R. Armiento, B. Kozinsky, G. Pizzi, *et al.*, High-throughput toolkit (httk), `https://httk.org/` (2016), python package for high-throughput calculations.

[36] P. E. Blöchl, Projector augmented-wave method, Phys. Rev. B **50**, 17953 (1994).

[37] G. Kresse and J. Furthmüller, Efficient iterative schemes for ab initio total-energy calculations using a plane-wave basis set, Phys. Rev. B **54**, 11169 (1996).

[38] G. Kresse and D. Joubert, From ultrasoft pseudopotentials to the projector augmented-wave method, Phys. Rev. B **59**, 1758 (1999).

[39] S. Picozzi, Spin–orbit coupling in quantum materials: Emergent phenomena, their modelling and examples from 2d magnets, EPJ Quantum Technology **12**, 1 (2025).

[40] Z. Liu, M. Ozeki, S. Asai, S. Itoh, and T. Masuda, Chiral split magnon in altermagnetic mnte, Physical Review Letters **133**, 156702 (2024).

[41] P. Lemoine, A. Verniere, M. Pasturel, G. Venturini, and B. Malaman, Unexpected magnetic ordering on the Cr substructure in UCr2Si2C and structural relationships in quaternary U-Cr-Si-C compounds, Inorganic Chemistry **57**, 2546 (2018).

[42] M. Matsuda, D. Zhang, Y. Kuwata, Q. Zhang, T. Sakurai, H. Ohta, H. Sugawara, K. Takeda, J. Hayashi, and H. Kotegawa, Noncollinear spin structure with weak ferromagnetism in nbmnp, Physical Review B **104**, 174413 (2021).

[43] K. Ji, A. Paul, E. Solana-Madruga, A. M. Arevalo-Lopez, U. V. Waghmare, and J. P. Attfield, YRuO3: A quantum weak ferromagnet, Physical Review Materials **4**, 091402 (2020).

[44] S. Haastrup, M. Strange, M. Pandey, T. Deilmann, P. Schmidt, H. Hernández, A. Rubio, and K. Thygesen, The computational 2d materials database: high-throughput modeling and discovery of atomically thin crystals, 2D Materials **5**, 042002 (2018).

[45] G. Pizzi, A. Cepellotti, R. Sabatini, N. Marzari, and B. Kozinsky, Aiida: automated interactive infrastructure and database for computational science, Computational Materials Science **111**, 218 (2016).

[46] J. Sødequist and T. Olsen, Two-dimensional altermagnets from high throughput computational screening: Symmetry requirements, chiral magnons, and spin-orbit effects, Applied Physics Letters **124**, 182409 (2024).

[47] J. P. Perdew, K. Burke, and M. Ernzerhof, Generalized

gradient approximation made simple, Physical review letters **77**, 3865 (1996).

[48] V. I. Anisimov, J. Zaanen, and O. K. Andersen, Band theory and Mott insulators: Hubbard U instead of Stoner I, Physical Review B **44**, 943 (1991).

[49] A. Jain, S. P. Ong, G. Hautier, *et al.*, Commentary: The materials project: A materials genome approach to accelerating materials innovation, APL Materials **1**, 011002 (2013).

[50] L. Wang, T. Maxisch, and G. Ceder, Oxidation energies of transition metal oxides within the GGA+U framework, Physical Review B **73**, 195107 (2006).

[51] M. Roig, A. Kreisel, Y. Yu, B. M. Andersen, and D. F. Agterberg, Minimal models for altermagnetism, Phys. Rev. B **110**, 144412 (2024).

[52] A. M. Ganose, A. Searle, A. Jain, and S. M. Griffin, IFermi: A python library for Fermi surface generation and analysis, Journal of Open Source Software **6**, 3089 (2021).

[53] Łukasz Mentel, mendeleev: A python resource for properties of chemical elements, ions and isotopes, `https://pypi.org/project/mendeleev/` (2014).

Supplemental Material for

High-Throughput Quantification of Altermagnetic Band Splitting

Ali Sufyan,[1,2,3] Brahim Marfoua,[4] J. Andreas Larsson,[3,5] Erik van Loon,[1,2] and Rickard Armiento[4]

[1]NanoLund and Division of Mathematical Physics, Department of Physics, Lund University, SE-221 00 Lund, Sweden
[2]Wallenberg Initiative Materials Science for Sustainability, Department of Physics, Lund University, SE-221 00 Lund, Sweden
[3]Applied Physics, Division of Materials Science, Department of Engineering Sciences and Mathematics, Luleå University of Technology, SE-971 87 Luleå, Sweden
[4]Department of Physics, Chemistry and Biology, Linköping University, SE-581 83 Linköping, Sweden
[5]Wallenberg Initiative Materials Science for Sustainability, Luleå University of Technology, SE-971 87 Luleå, Sweden

Table S1: **High-throughput screening results for candidate altermagnets.** The table lists the MAGNDATA ID(s), material, space group, spin-splitting metrics (F_Δ, Max SS, Avg SS), band gap, and minimum elemental crustal abundance, and is ordered by decreasing Max SS. When multiple MAGNDATA IDs are listed for the same material/space group, the first ID corresponds to the record with the largest Max SS and the values reported in the remaining columns, while the other listed IDs are also identified as altermagnets with Max SS > 26 meV.

MAGNDATA ID	Material	Space group	F_Δ (%)	Max SS	Avg SS	Bandgap	Min abund. (ppm)
0.528	CrSb	$P6_3/mmc$	34.375	1.872	0.763	0.000	2.000×10^{-1}
0.8	MnTe	$P6_3/mmc$	34.375	0.923	0.449	0.764	1.000×10^{-3}
0.607	RuO_2	$P4_2/mnm$	25.000	0.865	0.351	0.000	1.000×10^{-3}
2.35	CrSe	$P6_3/mmc$	35.938	0.800	0.489	0.000	5.000×10^{-2}
0.499	UCr_2Si_2C	P4/mmm	46.875	0.719	0.312	0.000	2.700
0.236	$Ca(Al_2Fe)_4$	I4/mmm	37.500	0.628	0.374	0.000	4.150×10^{4}
0.296, 0.295	Cu_2O_3Cl	$P2_1/c$	35.417	0.553	0.233	0.000	6.000×10^{1}
0.178	CoF_2	$P4_2/mnm$	16.667	0.479	0.223	3.306	2.500×10^{1}
0.803	MnNbP	Pnma	35.000	0.457	0.276	0.000	2.000×10^{1}
0.36	NiF_2	$P4_2/mnm$	27.083	0.392	0.180	5.268	8.400×10^{1}
0.131	$Mn(C_2N_3)_2$	Pnnm	16.250	0.348	0.156	3.742	1.900×10^{1}
0.501	$LiFe_2F_6$	$P4_2/mnm$	12.500	0.319	0.159	0.168	2.000×10^{1}
0.1065	$MnGeN_2$	$Pna2_1$	14.583	0.305	0.145	1.516	1.500
0.113	$NiCO_3$	R-3c	20.833	0.301	0.167	4.197	8.400×10^{1}
0.128	$FeSO_4F$	C2/c	28.906	0.301	0.158	2.451	3.500×10^{2}
0.15	MnF_2	$P4_2/mnm$	18.750	0.294	0.156	3.575	5.850×10^{2}
1.522	$CrVO_4$	Cmcm	28.571	0.292	0.158	2.877	1.020×10^{2}
0.402	$Sr_4Fe_4O_{11}$	Cmmm	29.808	0.289	0.150	0.176	3.700×10^{2}
0.99, 0.991, 0.992, 0.993, 0.994	$HoFeO_3$	Pnma	25.893	0.283	0.126	2.835	1.300
0.375	La_2CoIrO_6	$P2_1/c$	24.107	0.272	0.121	0.000	1.000×10^{-3}
0.351	$TbFeO_3$	Pnma	26.786	0.271	0.133	2.826	1.200
0.813, 0.81, 0.811, 0.812	Fe_2WO_6	Pbcn	29.688	0.270	0.173	1.465	1.250
0.154	$Er_2Ru_2O_7$	Fd-3m	20.313	0.268	0.266	0.412	1.000×10^{-3}
0.112	$FeBO_3$	R-3c	29.688	0.262	0.177	2.660	1.000×10^{1}
0.837, 0.836, 0.841, 0.84, 0.838, 0.839, 0.1, 0.11	$DyFeO_3$	Pnma	26.786	0.261	0.134	2.863	5.200
0.309	$TlCrO_3$	Pnma	24.107	0.246	0.146	0.625	8.500×10^{-1}
0.1049	$CoH_6(CO_3)_2$	$P2_1/c$	14.773	0.245	0.132	1.908	2.500×10^{1}
0.1067, 0.1066	$MnSiN_2$	$Pna2_1$	18.750	0.245	0.114	2.733	1.900×10^{1}
0.76	$FeHSO_5$	C2/c	26.563	0.242	0.156	2.625	3.500×10^{2}
0.103, 0.101, 0.102	Mn_2GeO_4	Pnma	23.125	0.239	0.127	0.594	1.500
0.66, 0.65	Fe_2O_3	R-3c	28.977	0.237	0.152	2.566	5.630×10^{4}
0.59, 0.591	$ErCrO_3$	Pnma	21.875	0.234	0.108	3.143	3.500
0.308	$CrInO_3$	Pnma	20.536	0.232	0.132	1.886	2.500×10^{-1}
0.758, 0.759, 0.757	$CeFeO_3$	Pnma	27.679	0.227	0.121	2.818	6.650×10^{1}
0.307	$ScCrO_3$	Pnma	20.536	0.227	0.127	2.987	2.200×10^{1}
0.475	Sr_2TbIrO_6	$P2_1/c$	27.083	0.226	0.114	0.139	1.000×10^{-3}
0.698, 0.697	$SmCrO_3$	Pnma	20.536	0.222	0.095	3.115	7.050
0.586, 0.947	$YCrO_3$	Pnma	21.429	0.221	0.115	3.121	3.300×10^{1}
0.379	$SmFeO_3$	Pnma	27.679	0.215	0.124	2.843	7.050
0.261	$FeNiPO_5$	Pnma	24.375	0.207	0.121	2.694	8.400×10^{1}

continued on next page

Table S1 (continued).

MAGNDATA ID	Material	Space group	F_Δ (%)	Max SS	Avg SS	Bandgap	Min abund. (ppm)
0.609, 0.288, 0.37	$NdMnO_3$	Pnma	19.643	0.206	0.143	1.420	4.150×10^{1}
0.592, 2.64, 2.63	$DyCrO_3$	Pnma	20.833	0.206	0.103	3.079	5.200
0.587	$TmCrO_3$	Pnma	25.000	0.202	0.117	3.141	5.200×10^{-1}
0.983, 0.982	$TmVO_3$	$P2_1/c$	18.750	0.200	0.100	1.739	5.200×10^{-1}
0.392	$Fe_3P_2(HO_5)_2$	$P2_1/c$	23.611	0.197	0.126	2.051	1.050×10^{3}
0.1085	$PrFeO_3$	Pnma	28.571	0.197	0.120	2.822	9.200
0.26	$CuFePO_5$	Pnma	27.500	0.194	0.119	1.955	6.000×10^{1}
0.25	$NaOsO_3$	Pnma	22.917	0.193	0.082	0.119	1.500×10^{-3}
0.336, 0.337	$NdFeO_3$	Pnma	27.679	0.192	0.122	2.833	4.150×10^{1}
0.1071	Fe_2SiO_4	Pnma	17.361	0.192	0.132	2.940	5.630×10^{4}
0.642, 0.1	$LaMnO_3$	Pnma	20.536	0.188	0.106	1.283	3.900×10^{1}
0.354, 2.62	$TbCrO_3$	Pnma	23.958	0.188	0.098	3.114	1.200
0.114	$CoCO_3$	R-3c	25.000	0.188	0.125	2.766	2.500×10^{1}
0.1021, 0.1022	$TmFeO_3$	Pnma	22.321	0.188	0.124	0.762	5.200×10^{-1}
0.295	$Cu_2H_3ClO_3$	$P2_1/c$	23.125	0.186	0.055	1.749	6.000×10^{1}
0.896	$CrNiO_4$	Cmcm	31.250	0.186	0.109	2.000	8.400×10^{1}
0.315	$ZrMn_2(GeO_3)_4$	P4/nbm	14.423	0.184	0.105	2.309	1.500
0.323, 0.417	$LaCrO_3$	Pnma	20.536	0.182	0.097	3.105	3.900×10^{1}
1.0.47	$MnSe_2$	Pa-3	45.833	0.178	0.133	0.983	5.000×10^{-2}
0.608	$PrMnO_3$	Pnma	21.429	0.176	0.107	0.896	9.200
0.298	$BaNa_2V_2FeO_8$	C2/c	20.956	0.174	0.102	2.710	1.200×10^{2}
0.5	$TiMnO_3$	R3c	25.000	0.173	0.101	2.470	9.500×10^{2}
0.21	$NiPbO_3$	R3c	26.136	0.170	0.111	0.561	1.400×10^{1}
0.314	$ZrCo_2(GeO_3)_4$	P4/nbm	17.788	0.170	0.110	2.628	1.500
0.788	YVO_3	$P2_1/c$	20.833	0.168	0.067	2.043	3.300×10^{1}
0.792, 0.794, 0.793	Sr_2HoRuO_6	$P2_1/c$	22.321	0.166	0.084	1.031	1.000×10^{-3}
0.589	$NdCrO_3$	Pnma	19.643	0.165	0.107	3.079	4.150×10^{1}
0.105, 0.104	$ErVO_3$	Pnma	18.750	0.165	0.082	1.971	3.500
0.262	$CoFePO_5$	Pnma	26.875	0.164	0.103	2.399	2.500×10^{1}
0.115	$MnCO_3$	R-3c	19.531	0.161	0.112	4.015	2.000×10^{2}
0.712	Nb_3VS_6	$P6_{322}$	31.250	0.161	0.057	0.000	2.000×10^{1}
1.0.33	FeF_3	$P6_3/m$	31.250	0.159	0.080	3.764	5.850×10^{2}
0.714	$Li_2Ni(SO_4)_2$	$P2_1/c$	20.536	0.158	0.077	4.565	2.000×10^{1}
0.1068	$LuCrO_3$	Pnma	19.792	0.158	0.125	3.192	8.000×10^{-1}
0.116	$FeCO_3$	R-3c	17.361	0.157	0.110	3.688	2.000×10^{2}
0.747	$Ba_3CoIr_2O_9$	C2/c	29.167	0.156	0.124		1.000×10^{-3}
0.334	CoF_3	R-3c	31.250	0.155	0.095	1.825	2.500×10^{1}
0.937, 0.301	Sr_2CoTeO_6	$P2_1/c$	29.167	0.155	0.088	2.154	1.000×10^{-3}
0.1036	$CoTa_4Se_8$	$P6_3/mmc$	36.719	0.154	0.126	0.000	5.000×10^{-2}
0.575	$ZnFeH_4O_2F_5$	Imm2	23.438	0.154	0.074	3.124	7.000×10^{1}
0.984	$LuVO_3$	Pnma	18.750	0.153	0.073	1.991	8.000×10^{-1}
1.0.26	$RbCoBr_3$	$P6_3/mmc$	24.432	0.150	0.100	0.000	2.400
0.189	$CeMn_2Ge_4O_{12}$	P4/nbm	18.269	0.149	0.117	0.000	1.500
0.6	$YMnO_3$	$P6_3cm$	21.875	0.145	0.092	1.305	3.300×10^{1}
0.204	Ca_2MnReO_6	$P2_1/c$	11.458	0.145	0.076	0.000	7.000×10^{-4}
0.218, 0.219	Co_2SiO_4	Pnma	22.222	0.144	0.101	2.506	2.500×10^{1}
0.148	$LiLa_2RuO_6$	$P2_1/c$	26.042	0.142	0.093	1.221	1.000×10^{-3}
0.755	$Mn_2SeO_3F_2$	Pnma	21.250	0.141	0.095	3.889	5.000×10^{-2}
0.581, 0.335	FeF_3	R-3c	32.813	0.141	0.094	4.342	5.850×10^{2}
0.722	$Mn_4Nb_2O_9$	Cc	21.250	0.140	0.078	1.270	2.000×10^{1}
0.681	Ce_4Sb_3	I-43d	47.500	0.139	0.058	0.000	2.000×10^{-1}
0.79	Sr_2DyRuO_6	$P2_1/c$	23.214	0.138	0.081	1.114	1.000×10^{-3}

continued on next page

Table S1 (continued).

MAGNDATA ID	Material	Space group	F_Δ (%)	Max SS	Avg SS	Bandgap	Min abund. (ppm)
0.513	$YRuO_3$	Pnma	18.750	0.138	0.067	0.569	1.000×10^{-3}
0.121	$Li_2Co(SO_4)_2$	$P2_1/c$	20.536	0.136	0.088	3.224	2.000×10^{1}
0.83	$LiFeP_2O_7$	$P2_1$	22.917	0.136	0.085	2.958	2.000×10^{1}
0.1008	Sr_2ErRuO_6	$P2_1/c$	22.321	0.134	0.075	1.009	1.000×10^{-3}
0.795	Sr_2YRuO_6	$P2_1/c$	22.321	0.134	0.075	1.012	1.000×10^{-3}
0.263	Fe_2PO_5	Pnma	22.500	0.134	0.102	2.086	1.050×10^{3}
0.31, 0.32, 0.33	$HoMnO_3$	$P6_3cm$	25.000	0.134	0.084	1.310	1.300
0.98, 0.981, 0.979	$TmVO_3$	Pnma	19.792	0.133	0.068	2.050	5.200×10^{-1}
0.999, 0.1	Fe_4O_5	Cmcm	13.942	0.132	0.076	0.000	5.630×10^{4}
0.1059	$BaPrMn_2O_6$	$Pmc2_1$	23.214	0.132	0.054	0.000	9.200
0.117	$LuFeO_3$	$P6_3cm$	24.375	0.131	0.077	1.795	8.000×10^{-1}
0.67, 0.669	Sr_2YbRuO_6	$P2_1/c$	22.321	0.131	0.072	0.982	1.000×10^{-3}
0.671	Sr_2TmRuO_6	$P2_1/c$	22.321	0.129	0.070	0.978	1.000×10^{-3}
0.24	$Er_2Cu_2O_5$	$Pna2_1$	23.558	0.129	0.071	1.732	3.500
3.4	$MgCr_2O_4$	Fd-3m	39.338	0.127	0.093	1.545	1.020×10^{2}
0.241	$Y_2Cu_2O_5$	$Pna2_1$	21.635	0.127	0.070	1.704	3.300×10^{1}
0.416	$LaCrO_3$	R-3c	19.375	0.124	0.098	3.194	3.900×10^{1}
0.791	Sr_2TbRuO_6	$P2_1/c$	24.107	0.122	0.079	1.044	1.000×10^{-3}
0.168	$Fe_2H_4NF_6$	Pnma	6.250	0.121	0.065	1.828	1.900×10^{1}
0.45	La_2NiO_4	$P4_2/ncm$	24.375	0.121	0.076	2.313	3.900×10^{1}
0.787	YVO_3	Pnma	19.792	0.120	0.061	2.037	3.300×10^{1}
0.948	$CaNi_3P_4O_{14}$	$P2_1/c$	23.958	0.120	0.075	4.464	8.400×10^{1}
0.934	Sr_2NiTeO_6	$P2_1/c$	28.125	0.119	0.053	2.343	1.000×10^{-3}
0.42	Sr_2LuRuO_6	$P2_1/c$	21.429	0.119	0.078	0.958	1.000×10^{-3}
0.122	$Li_2Mn(SO_4)_2$	$P2_1/c$	20.833	0.118	0.051	5.101	2.000×10^{1}
0.108	$Ca_2Fe_2O_5$	Pnma	22.917	0.116	0.080	1.373	4.150×10^{4}
0.708	$CrNb_4S_8$	$P6_3/mmc$	37.500	0.112	0.056	0.000	2.000×10^{1}
0.165	$SrMnVHO_5$	$P2_{12121}$	21.250	0.108	0.073	2.356	1.200×10^{2}
0.7, 0.8	$ScMnO_3$	$P6_3cm$	20.625	0.107	0.076	1.400	2.200×10^{1}
0.582, 2.61	$Fe_3H_4(OF_4)_2$	C2/m	22.917	0.106	0.065	2.686	5.850×10^{2}
0.802	$CuFeS_2$	I-42d	28.571	0.105	0.081	1.043	6.000×10^{1}
0.1082	$LuCrWO_6$	$Pna2_1$	26.136	0.104	0.067	2.347	8.000×10^{-1}
0.748	$Ba_3NiRu_2O_9$	$P6_3/mmc$	19.375	0.104	0.071	1.062	1.000×10^{-3}
0.192	$RbFe_2F_6$	Pnma	5.729	0.104	0.064	1.744	9.000×10^{1}
1.0.39	$BaMnO_3$	$P6_3/mmc$	26.250	0.103	0.061	2.613	4.250×10^{2}
0.936	Sr_2MnTeO_6	$P2_1/c$	20.833	0.103	0.060	1.792	1.000×10^{-3}
0.368	$CoH_9C_4NO_6$	Pnma	20.192	0.101	0.062	3.236	1.900×10^{1}
0.41, 0.40	Mn_2O_3	Pbca	20.602	0.101	0.084	0.946	9.500×10^{2}
0.294	$Cu_4H_6BrO_6F$	Pnma	21.053	0.100	0.072	1.714	2.400
0.229	$Ba_2MnSi_2O_7$	$P\text{-}42_1m$	15.179	0.098	0.062	3.349	4.250×10^{2}
0.79	$CaIrO_3$	Cmcm	29.167	0.096	0.066	0.038	1.000×10^{-3}
0.1018, 0.1019	$SrMnO_3$	$C222_1$	25.481	0.095	0.063	1.873	3.700×10^{2}
0.967	$BaMn_2V_2O_8$	$I4_1cd$	25.781	0.095	0.064	2.087	1.200×10^{2}
0.292	$NiTe_2O_5$	Pnma	26.389	0.095	0.067	2.766	1.000×10^{-3}
0.917	Sr_2ScOsO_6	$P2_1/c$	16.964	0.094	0.045	0.000	1.500×10^{-3}
0.785, 0.786	$NdVO_3$	Pnma	18.750	0.093	0.056	1.676	4.150×10^{1}
0.1013	Ba_2NdRuO_6	$P2_1/c$	25.893	0.092	0.042	1.026	1.000×10^{-3}
0.726, 0.727	$CsMn_2F_6$	Pnma	13.021	0.090	0.054	1.529	3.000
0.715, 0.716	$HoCrWO_6$	$Pna2_1$	26.136	0.090	0.063	2.398	1.250
0.404	$NaSr_3RuO_6$	R-3c	25.625	0.089	0.064	1.564	1.000×10^{-3}
0.316	$DyCrWO_6$	$Pna2_1$	26.705	0.087	0.059	1.912	1.250
0.361	Sr_3LiRuO_6	R-3c	24.063	0.086	0.067	1.553	1.000×10^{-3}
0.434, 0.553	K_2ReI_6	$P2_1/c$	34.375	0.084	0.043	1.483	7.000×10^{-4}

continued on next page

Table S1 (continued).

MAGNDATA ID	Material	Space group	F_Δ (%)	Max SS	Avg SS	Bandgap	Min abund. (ppm)
0.552	$Mn(PbO_2)_2$	P-42$_1$c	24.063	0.083	0.064	1.458	1.400×10^{1}
0.191	$BaCuF_4$	Cmc2$_1$	22.222	0.083	0.039	2.208	6.000×10^{1}
0.431	CuB_2O_4	I-42d	21.023	0.081	0.052	2.137	1.000×10^{1}
0.724	$BaCoSiO_4$	P6$_3$	25.000	0.079	0.054	3.079	2.500×10^{1}
0.329	$RbMnF_4$	P2$_1$/c	17.188	0.076	0.040	1.926	9.000×10^{1}
0.62	$SrMn_2V_2O_8$	I4$_1$cd	24.219	0.076	0.054	2.760	1.200×10^{2}
0.239	$LiCa_3RuO_6$	R-3c	26.042	0.074	0.062	1.495	1.000×10^{-3}
0.955	$Na_2MnH_8(C_3O_5)_2$	Pbca	15.461	0.074	0.053	3.726	2.000×10^{2}
0.21	Sr_2CoOsO_6	C2/c	23.558	0.073	0.043	0.000	1.500×10^{-3}
1.0.35	$CsMnBr_3$	P6$_3$/mmc	26.875	0.071	0.057	3.828	2.400
0.331	$Fe_2Mo_3O_8$	P6$_3$mc	17.361	0.069	0.042	0.000	1.200
1.0.9, 1.0.38	$CsCoCl_3$	P6$_3$/mmc	18.750	0.069	0.054	0.000	3.000
0.3	$LiCa_3OsO_6$	R-3c	17.014	0.068	0.060	0.813	1.500×10^{-3}
0.56	$Ba_2CoGe_2O_7$	P-42$_1$m	17.969	0.068	0.047	2.592	1.500
0.398	Ca_2RuO_4	Pbca	18.056	0.067	0.041	0.664	1.000×10^{-3}
0.13	$Cu_3Mo_2O_9$	Pnma	18.438	0.064	0.045	1.236	1.200
0.134	$Mn_3B_7IO_{13}$	Pca2$_1$	18.750	0.063	0.043	4.319	4.500×10^{-1}
0.13	Ca_3MnCoO_6	R-3c	18.750	0.063	0.051	2.003	2.500×10^{1}
0.1014	$CsNiC_3(SN)_3$	P2$_1$/c	14.205	0.060	0.037	2.844	3.000
0.405	$CsCoF_4$	I-4c2	28.205	0.059	0.045	0.053	3.000
0.106	$MnH_6(CO_2)_3$	Pca2$_1$	19.318	0.059	0.043	3.660	2.000×10^{2}
1.0.46	$Ba_3MnSb_2O_9$	C2/c	9.821	0.057	0.045	2.075	2.000×10^{-1}
2.88	UGaNi	P-62m	2.371	0.057	0.028	0.000	2.700
0.332	$Co_2Mo_3O_8$	P6$_3$mc	20.139	0.057	0.035	0.000	1.200
0.254, 0.255	$CuH_9C_4(NO_2)_3$	Pna2$_1$	17.500	0.056	0.034	2.201	1.900×10^{1}
0.303	$BaCrF_5$	P2$_{12121}$	23.611	0.049	0.030	4.241	1.020×10^{2}
1.0.44	$Ba_3CoSb_2O_9$	P6$_3$/mmc	24.750	0.044	0.038	2.439	2.000×10^{-1}
0.1063	$Fe_2H_6(SeO_4)_3$	R3c	14.732	0.043	0.040		5.000×10^{-2}
1.0.31, 1.0.32	$Eu(InAs)_2$	P6$_3$/mmc	2.083	0.041	0.026		2.500×10^{-1}
0.425	$Na_2CoP_2O_7$	Pna2$_1$	15.750	0.040	0.032	3.327	2.500×10^{1}
0.849	$Er_5(In_2Pd)_2$	Pbam	2.500	0.036	0.021	0.000	1.500×10^{-2}
0.658	$BaCu(TeO_3)_2$	P4$_{132}$	13.603	0.032	0.023	1.921	1.000×10^{-3}
1.0.4	$CsNiCl_3$	P6$_3$/mmc	16.369	0.032	0.025	3.837	3.000
0.109	CrH_4NF_3	P4$_2$/mbc	1.442	0.032	0.017	2.835	1.900×10^{1}
0.53	$SrCu(TeO_3)_2$	P4$_{132}$	5.147	0.026	0.019	1.974	1.000×10^{-3}

Table S2: Symmetry data for 157 collinear entries in MAGNDATA identified as potential altermagnets. Rows are identified by their MAGNDATA *ID*. For materials where the detected symmetries depend on the precision used for symmetry identification, values of the spglib `symprec` setting ranging from 10^{-5} to 10^{-1} were tested, and when the results differ, multiple rows are included in the table. The column *SP* shows the lowest value (i.e., the most precise symmetry matching) in this range that gives the respective result. The wave classification is made by matching the Laue classes of the parent spacegroup G and an identified halving subgroup H with Fig. 2 in [PRX 12, 031042 (2022)]. The identified phases are: *AM* = Altermagnet, *FiM* = Ferrimagnet. Materials are included as long as one choice of symmetry precision resulted in altermagnetism (i.e., gave a positive result from the amcheck `is_altermagnet` function). The *BNS* symbols and numbers are the ones in the MAGNDATA mcif files, whereas the (nonmagnetic) parent spacegroup (*Parent SG*) is shown as detected by `spglib`.

ID	ICSD	Chemical formula	SP	BNS (mcif)	Parent SG	Phase	G	H	Wave
0.1	.	$LaMnO_3$	10^{-5}	Pn′ma′ (62.448)	Pnma (62)	AM	mmm	2/m	d
0.3	.	Ca_3LiOsO_6	10^{-5}	C2′/c′ (15.89)	R$\bar{3}$c (167)	AM	-3m	-3	g
0.13	93775	Ca_3Co_2−xMnxO_6	10^{-5}	R3c (161.69)	R3c (161)	AM	-3m	-3	g
0.13	93775	Ca_3Co_2−xMnxO_6	10^{-4}	R3c (161.69)	R$\bar{3}$c (167)	AM	-3m	-3	g
0.15	68735	MnF_2	10^{-5}	$P4_2'/mnm'$ (136.499)	$P4_2/mnm$ (136)	AM	4/mmm	mmm	d
0.21	.	$PbNiO_3$	10^{-5}	R3c (161.69)	R3c (161)	AM	-3m	-3	g
0.23	55666	$Ca_3Mn_2O_7$	10^{-5}	Cm′c$2_1'$ (36.174)	$Cmc2_1$ (36)	AM	mmm	2/m	d
0.25	.	$NaOsO_3$	10^{-5}	Pn′ma′ (62.448)	Pnma (62)	AM	mmm	2/m	d
0.45	69753	La_2NiO_4	10^{-5}	Pc′c′n (56.369)	$P4_2/ncm$ (138)	AM	mmm	2/m	d
0.50	.	$MnTiO_3$	10^{-5}	Cc′ (9.39)	R3c (161)	AM	-3m	-3	g
0.56	.	$Ba_2CoGe_2O_7$	10^{-5}	Cm′m2′ (35.167)	P2 (3)	FiM	2/m	2/m	s
0.56	.	$Ba_2CoGe_2O_7$	10^{-3}	Cm′m2′ (35.167)	P$\bar{4}2_1$m (113)	AM	4/mmm	4/m	g
0.62	182224	$SrMn_2V_2O_8$	10^{-5}	Ib′a2′ (45.237)	$I4_1$cd (110)	AM	4/mmm	mmm	d
0.65	.	Fe_2O_3−alpha	10^{-5}	C2′/c′ (15.89)	R$\bar{3}$c (167)	AM	-3m	-3	g
0.66	.	Fe_2O_3−alpha	10^{-5}	P$\bar{1}$ (2.4)	R$\bar{3}$c (167)	AM	-3m	-3	g
0.79	160816	$CaIrO_3$	10^{-5}	Cm′cm′ (63.464)	Cmcm (63)	AM	mmm	2/m	d
0.83	95751	$LiFeP_2O_7$	10^{-5}	$P2_1$ (4.7)	$P2_1$ (4)	AM	2/m	-1	d
0.105	185838	$ErVO_3$	10^{-5}	$P2_1/c$ (14.75)	Pnma (62)	AM	2/m	-1	d
0.112	34474	$FeBO_3$	10^{-5}	C2′/c′ (15.89)	R$\bar{3}$c (167)	AM	-3m	-3	g
0.113	173985	$NiCO_3$	10^{-5}	C2/c (15.85)	R$\bar{3}$c (167)	AM	-3m	-3	g
0.114	61066	$CoCO_3$	10^{-5}	C2/c (15.85)	R$\bar{3}$c (167)	AM	-3m	-3	g
0.115	.	$MnCO_3$	10^{-5}	C2/c (15.85)	R$\bar{3}$c (167)	AM	-3m	-3	g
0.116	100678	$FeCO_3$	10^{-5}	R$\bar{3}$c (167.103)	R$\bar{3}$c (167)	AM	-3m	-3	g
0.118	99371	$Ba_5Co_5ClO_{13}$	10^{-5}	$P6_3'/m'm'c$ (194.268)	$P6_3/mmc$ (194)	AM	6/mmm	-3m	g
0.128	182945	$FeSO_4F$	10^{-5}	C2′/c′ (15.89)	C2/c (15)	AM	2/m	-1	d
0.131	.	$Mn(N(CN_2))_2$	10^{-5}	Pnn′m′ (58.398)	Pnnm (58)	AM	mmm	2/m	d
0.137	.	$Cu_2V_2O_7$	10^{-5}	Fd′d′2 (43.227)	Fdd2 (43)	AM	mmm	2/m	d
0.148	97488	La_2LiRuO_6	10^{-5}	$P2_1/c$ (14.75)	$P2_1/c$ (14)	AM	2/m	-1	d
0.154	97533	$Er_2Ru_2O_7$	10^{-5}	$I4_1'/am'd$ (141.554)	Fd$\bar{3}$m (227)	AM	4/mmm	mmm	d
0.178	98786	CoF_2	10^{-5}	$P4_2'/mnm'$ (136.499)	$P4_2/mnm$ (136)	AM	4/mmm	mmm	d
0.189	.	$CeMn_2Ge_4O_{12}$	10^{-5}	P4′/nbm′ (125.367)	P4/nbm (125)	AM	4/mmm	mmm	d
0.229	.	$Ba_2MnSi_2O_7$	10^{-5}	P$\bar{4}2_1$m (113.267)	P$\bar{4}2_1$m (113)	AM	4/mmm	4/m	g
0.239	96219	Ca_3LiRuO_6	10^{-5}	C2′/c′ (15.89)	R$\bar{3}$c (167)	AM	-3m	-3	g
0.241	79429	$Y_2Cu_2O_5$	10^{-5}	$Pna2_1$ (33.144)	$Pna2_1$ (33)	AM	mmm	2/m	d
0.254	248006	$[C(ND_2)_3]Cu(DCOO)_3$	10^{-5}	$Pna2_1$ (33.144)	$Pna2_1$ (33)	AM	mmm	2/m	d
0.255	248006	$[C(ND_2)_3]Cu(DCOO)_3$	10^{-5}	Pn′a′2_1 (33.148)	$Pna2_1$ (33)	AM	mmm	2/m	d
0.260	93582	$CuFePO_5$	10^{-5}	Pnma (62.441)	Pnma (62)	AM	mmm	2/m	d
0.261	93581	$NiFePO_5$	10^{-5}	Pnma (62.441)	Pnma (62)	AM	mmm	2/m	d
0.263	32641	Fe_2PO_5	10^{-5}	Pnma (62.441)	Pnma (62)	AM	mmm	2/m	d
0.301	195658	Sr_2CoTeO_6	10^{-5}	$P2_1/c$ (14.75)	$P2_1/c$ (14)	AM	2/m	-1	d
0.303	31705	$BaCrF_5$	10^{-5}	$P2_1'2_1'2_1$ (19.27)	$P2_12_12_1$ (19)	AM	mmm	2/m	d
0.307	.	$ScCrO_3$	10^{-5}	Pnma (62.441)	Pnma (62)	AM	mmm	2/m	d
0.308	.	$InCrO_3$	10^{-5}	Pnma (62.441)	Pnma (62)	AM	mmm	2/m	d
0.309	.	$TlCrO_3$	10^{-5}	Pnma (62.441)	Pnma (62)	AM	mmm	2/m	d
0.315	257623	$ZrMn_2Ge_4O_{12}$	10^{-5}	P4′/nbm′ (125.367)	P4/nbm (125)	AM	4/mmm	mmm	d
0.323	180183	$LaCrO_3$	10^{-5}	Pnma (62.441)	Pnma (62)	AM	mmm	2/m	d

continued on next page

Table S2 (continued).

ID	ICSD	Chemical formula	SP	BNS (mcif)	Parent SG	Phase	G	H	Wave
0.329	73587	$RbMnF_4$	10^{-5}	$P\bar{1}$ (2.4)	$P2_1/c$ (14)	AM	2/m	-1	d
0.331	4182	$Fe_2Mo_3O_8$	10^{-5}	$P6'_3m'c$ (186.205)	$P6_3mc$ (186)	AM	6/mmm	-3m	g
0.332	10143	$Co_2Mo_3O_8$	10^{-5}	$P6'_3m'c$ (186.205)	$P6_3mc$ (186)	AM	6/mmm	-3m	g
0.334	.	CoF_3	10^{-5}	$R\bar{3}c$ (167.103)	$R\bar{3}c$ (167)	AM	-3m	-3	g
0.335	.	FeF_3	10^{-5}	$C2'/c'$ (15.89)	$R\bar{3}c$ (167)	AM	-3m	-3	g
0.336	153441	$NdFeO_3$	10^{-5}	$Pn'ma'$ (62.448)	Pnma (62)	AM	mmm	2/m	d
0.345	74663	Tb_2C_3	10^{-5}	$Fd'd2'$ (43.226)	$I\bar{4}3d$ (220)	AM	mmm	2/m	d
0.351	22311	$TbFeO_3$	10^{-5}	$Pn'ma'$ (62.448)	Pnma (62)	AM	mmm	2/m	d
0.354	.	$TbCrO_3$	10^{-5}	$Pn'm'a$ (62.446)	Pnma (62)	AM	mmm	2/m	d
0.358	258572	$CaFe_5O_7$	10^{-5}	$P2'_1/m'$ (11.54)	$P2_1/m$ (11)	AM	2/m	-1	d
0.361	.	Sr_3LiRuO_6	10^{-5}	$C2'/c'$ (15.89)	$R\bar{3}c$ (167)	AM	-3m	-3	g
0.379	252077	$SmFeO_3$	10^{-5}	$Pn'm'a$ (62.446)	Pnma (62)	AM	mmm	2/m	d
0.380	252078	$SmFeO_3$	10^{-5}	$Pn'ma'$ (62.448)	Pnma (62)	AM	mmm	2/m	d
0.392	91881	$Fe_3(PO_4)_2(OH)_2$	10^{-5}	$P2_1/c$ (14.75)	$P2_1/c$ (14)	AM	2/m	-1	d
0.402	190551	$Sr_4Fe_4O_{11}$	10^{-5}	$Cmm'm'$ (65.486)	Cmmm (65)	AM	mmm	2/m	d
0.404	.	Sr_3NaRuO_6	10^{-5}	$C2'/c'$ (15.89)	C2/c (15)	AM	2/m	-1	d
0.404	.	Sr_3NaRuO_6	10^{-4}	$C2'/c'$ (15.89)	$R\bar{3}c$ (167)	AM	-3m	-3	g
0.405	86430	$CsCoF_4$	10^{-5}	$I\bar{4}'$ (82.41)	$I\bar{4}c2$ (120)	AM	4/mmm	mmm	d
0.416	.	$LaCrO_3$	10^{-5}	$R\bar{3}c$ (167.103)	$R\bar{3}c$ (167)	AM	-3m	-3	g
0.417	.	$LaCrO_3$	10^{-5}	$Pn'ma'$ (62.448)	Pnma (62)	AM	mmm	2/m	d
0.420	202867	Sr_2LuRuO_6	10^{-5}	$P2_1/c$ (14.75)	$P2_1/c$ (14)	AM	2/m	-1	d
0.432	31498	$KMnF_3$	10^{-5}	$Pn'ma'$ (62.448)	Pnma (62)	AM	mmm	2/m	d
0.433	.	$KMnF_3$	10^{-5}	I4/mcm (140.541)	I4/mcm (140)	AM	4/mmm	4/m	g
0.434	235193	K_2ReI_6	10^{-5}	$P2_1/c$ (14.75)	$P2_1/c$ (14)	AM	2/m	-1	d
0.448	.	Ce_4Ge_3	10^{-5}	$I\bar{4}2d$ (122.333)	$I\bar{4}3d$ (220)	AM	4/mmm	4/m	g
0.475	90499	Sr_2TbIrO_6	10^{-5}	$P2_1/c$ (14.75)	$P2_1/c$ (14)	AM	2/m	-1	d
0.499	432804	UCr_2Si_2C	10^{-5}	$Pm'm'm$ (47.252)	P4/mmm (123)	AM	4/mmm	mmm	d
0.501	28244	$LiFe_2F_6$	10^{-5}	$P4'_2/mnm'$ (136.499)	$P4_2/mnm$ (136)	AM	4/mmm	mmm	d
0.513	.	$YRuO_3$	10^{-5}	$Pn'ma'$ (62.448)	Pnma (62)	AM	mmm	2/m	d
0.528	626689	CrSb	10^{-5}	$P6'_3/m'm'c$ (194.268)	$P6_3/mmc$ (194)	AM	6/mmm	-3m	g
0.553	235193	K_2ReI_6	10^{-5}	$P2_1/c$ (14.75)	$P2_1/c$ (14)	AM	2/m	-1	d
0.575	202194	$ZnFeF_5(H_2O)_2$	10^{-5}	Imm2 (44.229)	Imm2 (44)	AM	mmm	2/m	d
0.581	41120	FeF_3	10^{-5}	$C2'/c'$ (15.89)	$R\bar{3}c$ (167)	AM	-3m	-3	g
0.582	.	$Fe_3F_8(H_2O)_2$	10^{-5}	$C2'/m'$ (12.62)	C2/m (12)	AM	2/m	-1	d
0.586	251107	$YCrO_3$	10^{-5}	$Pn'ma'$ (62.448)	Pnma (62)	AM	mmm	2/m	d
0.587	251103	$TmCrO_3$	10^{-5}	$Pn'ma'$ (62.448)	Pnma (62)	AM	mmm	2/m	d
0.591	28487	$ErCrO_3$	10^{-5}	$Pn'ma'$ (62.448)	Pnma (62)	AM	mmm	2/m	d
0.592	16506	$DyCrO_3$	10^{-5}	$Pn'm'a$ (62.446)	Pnma (62)	AM	mmm	2/m	d
0.607	.	RuO_2	10^{-5}	$P4'_2/mnm'$ (136.499)	$P4_2/mnm$ (136)	AM	4/mmm	mmm	d
0.608	15718	$PrMnO_3$	10^{-5}	$Pn'ma'$ (62.448)	Pnma (62)	AM	mmm	2/m	d
0.609	15719	$NdMnO_3$	10^{-5}	$P2_1/m$ (11.50)	Pnma (62)	AM	mmm	2/m	d
0.642	16281	$LaMnO_3$	10^{-5}	$Pn'ma'$ (62.448)	Pnma (62)	AM	mmm	2/m	d
0.671	55715	Sr_2TmRuO_6	10^{-5}	$P2_1/c$ (14.75)	$P2_1/c$ (14)	AM	2/m	-1	d
0.681	162009	Ce_4Sb_3	10^{-5}	$I\bar{4}'2d'$ (122.336)	$I\bar{4}3d$ (220)	AM	4/mmm	mmm	d
0.706	.	$Tb_2Ir_3Ga_9$	10^{-5}	$Cm'cm'$ (63.464)	Cmcm (63)	AM	mmm	2/m	d
0.708	42657	$CrNb_4S_8$	10^{-5}	$P6'_3/m'm'c$ (194.268)	C2/c (15)	AM	2/m	-1	d
0.708	42657	$CrNb_4S_8$	10^{-4}	$P6'_3/m'm'c$ (194.268)	$P6_3/mmc$ (194)	AM	6/mmm	-3m	g
0.712	42650	VNb_3S_6	10^{-5}	$C2'2'2_1$ (20.33)	$C222_1$ (20)	AM	mmm	2/m	d
0.712	42650	VNb_3S_6	10^{-5}	$C2'2'2_1$ (20.33)	$P6_322$ (182)	AM	6/mmm	-3m	g
0.714	.	$Li_2Ni(SO_4)_2$	10^{-5}	$P2_1/c$ (14.75)	$P2_1/c$ (14)	AM	2/m	-1	d
0.722	.	$Mn_4Nb_2O_9$	10^{-5}	Cc (9.37)	Cc (9)	AM	2/m	-1	d
0.747	.	$Ba_3CoIr_2O_9$	10^{-5}	C2/c (15.85)	C2/c (15)	AM	2/m	-1	d
0.748	69091	$Ba_3NiRu_2O_9$	10^{-5}	$P6'_3/m'm'c$ (194.268)	$P6_3/mmc$ (194)	AM	6/mmm	-3m	g
0.755	.	$Mn_2SeO_3F_2$	10^{-5}	$Pn'ma'$ (62.448)	Pnma (62)	AM	mmm	2/m	d
0.757	.	$CeFeO_3$	10^{-5}	$Pn'ma'$ (62.448)	Pnma (62)	AM	mmm	2/m	d

continued on next page

Table S2 (continued).

ID	ICSD	Chemical formula	SP	BNS (mcif)	Parent SG	Phase	G	H	Wave
0.758	.	$CeFeO_3$	10^{-5}	Pnma (62.441)	Pnma (62)	AM	mmm	2/m	d
0.760	.	$FeOHSO_4$	10^{-5}	C2′/c′ (15.89)	C2/c (15)	AM	2/m	-1	d
0.784	153431	$NdCoO_3$	10^{-5}	Pnma (62.441)	Pnma (62)	AM	mmm	2/m	d
0.786	185834	$NdVO_3$	10^{-5}	$P2_1'/m'$ (11.54)	Pnma (62)	AM	mmm	2/m	d
0.787	155476	YVO_3	10^{-5}	Pn′m′a (62.446)	Pnma (62)	AM	mmm	2/m	d
0.790	188479	Sr_2DyRuO_6	10^{-5}	$P2_1'/c'$ (14.79)	$P2_1/c$ (14)	AM	2/m	-1	d
0.792	90654	Sr_2HoRuO_6	10^{-5}	$P2_1/c$ (14.75)	$P2_1/c$ (14)	AM	2/m	-1	d
0.793	90655	Sr_2HoRuO_6	10^{-5}	$P2_1/c$ (14.75)	$P2_1/c$ (14)	AM	2/m	-1	d
0.795	.	Sr_2YRuO_6	10^{-5}	$P2_1/c$ (14.75)	$P2_1/c$ (14)	AM	2/m	-1	d
0.800	43541	MnTe	10^{-5}	Cmcm (63.457)	Cmcm (63)	AM	mmm	2/m	d
0.800	43541	MnTe	10^{-4}	Cmcm (63.457)	$P6_3/mmc$ (194)	AM	6/mmm	-3m	g
0.802	2518	$CuFeS_2$	10^{-5}	$I\bar{4}2d$ (122.333)	$I\bar{4}2d$ (122)	AM	4/mmm	4/m	g
0.811	1147	Fe_2WO_6	10^{-5}	Pbc′n′ (60.423)	Pbcn (60)	AM	mmm	2/m	d
0.813	.	Fe_2WO_6	10^{-5}	Pbc′n′ (60.423)	Pbcn (60)	AM	mmm	2/m	d
0.823	98066	Sr_2MnGaO_5	10^{-5}	Im′a2′ (46.243)	Ima2 (46)	AM	mmm	2/m	d
0.825	51464	Ca_2MnGaO_5	10^{-5}	Pnm′a′ (62.447)	Pnma (62)	AM	mmm	2/m	d
0.836	.	$DyFeO_3$	10^{-5}	Pn′ma′ (62.448)	Pnma (62)	AM	mmm	2/m	d
0.837	.	$DyFeO_3$	10^{-5}	Pn′ma′ (62.448)	Pnma (62)	AM	mmm	2/m	d
0.838	.	$DyFeO_3$	10^{-5}	Pn′ma′ (62.448)	Pnma (62)	AM	mmm	2/m	d
0.839	.	$DyFeO_3$	10^{-5}	Pn′ma′ (62.448)	Pnma (62)	AM	mmm	2/m	d
0.840	.	$DyFeO_3$	10^{-5}	Pnma (62.441)	Pnma (62)	AM	mmm	2/m	d
0.841	.	$DyFeO_3$	10^{-5}	Pnma (62.441)	Pnma (62)	AM	mmm	2/m	d
0.896	23493	$NiCrO_4$	10^{-5}	Cmcm (63.457)	Cmcm (63)	AM	mmm	2/m	d
0.904	.	Nd_2PdGe_6	10^{-5}	Cm′c′a (64.474)	Cmce (64)	AM	mmm	2/m	d
0.917	253172	Sr_2ScOsO_6	10^{-5}	$P2_1/c$ (14.75)	$P2_1/c$ (14)	AM	2/m	-1	d
0.927	.	Nd_2PdGe_6	10^{-5}	Cm′c′a (64.474)	Cmce (64)	AM	mmm	2/m	d
0.934	241466	Sr_2NiTeO_6	10^{-5}	$P2_1/c$ (14.75)	$P2_1/c$ (14)	AM	2/m	-1	d
0.936	.	Sr_2MnTeO_6	10^{-5}	$P2_1/c$ (14.75)	$P2_1/c$ (14)	AM	2/m	-1	d
0.937	.	Sr_2CoTeO_6	10^{-5}	$P2_1/c$ (14.75)	$P2_1/c$ (14)	AM	2/m	-1	d
0.947	.	$YCrO_3$	10^{-5}	Pn′ma′ (62.448)	Pnma (62)	AM	mmm	2/m	d
0.955	.	$Na_2Mn(H_2C_3O_4)_2(H_2O)_2$	10^{-5}	Pbca (61.433)	Pbca (61)	AM	mmm	2/m	d
0.967	.	$BaMn_2V_2O_8$	10^{-5}	Ib′a2′ (45.237)	$I4_1cd$ (110)	AM	4/mmm	mmm	d
0.979	.	$TmVO_3$	10^{-5}	Pn′m′a (62.446)	Pnma (62)	AM	mmm	2/m	d
0.980	.	$TmVO_3$	10^{-5}	Pn′m′a (62.446)	Pnma (62)	AM	mmm	2/m	d
0.982	.	$TmVO_3$	10^{-5}	$P2_1/c$ (14.75)	$P2_1/c$ (14)	AM	2/m	-1	d
0.982	.	$TmVO_3$	10^{-1}	$P2_1/c$ (14.75)	Pnma (62)	AM	mmm	2/m	d
0.983	.	$TmVO_3$	10^{-5}	$P2_1/c$ (14.75)	$P2_1/c$ (14)	AM	2/m	-1	d
0.983	.	$TmVO_3$	10^{-1}	$P2_1/c$ (14.75)	Pnma (62)	AM	mmm	2/m	d
0.984	185841	$LuVO_3$	10^{-5}	Pn′m′a (62.446)	Pnma (62)	AM	mmm	2/m	d
0.991	.	$HoFeO_3$	10^{-5}	Pn′ma′ (62.448)	Pnma (62)	AM	mmm	2/m	d
0.999	.	Fe_4O_5	10^{-5}	$Cm'c2_1'$ (36.174)	Cmcm (63)	AM	mmm	2/m	d
0.1008	.	Sr_2ErRuO_6	10^{-5}	$P2_1/c$ (14.75)	$P2_1/c$ (14)	AM	2/m	-1	d
0.1013	.	Ba_2NdRuO_6	10^{-5}	$P\bar{1}$ (2.4)	$P2_1/c$ (14)	AM	2/m	-1	d
0.1018	157936	$SrMnO_3$	10^{-5}	$C22'2_1'$ (20.34)	$C222_1$ (20)	AM	mmm	2/m	d
0.1019	157936	$SrMnO_3$	10^{-5}	$C22'2_1'$ (20.34)	$C222_1$ (20)	AM	mmm	2/m	d
0.1021	27283	$TmFeO_3$	10^{-5}	Pn′ma′ (62.448)	Pnma (62)	AM	mmm	2/m	d
0.1022	27283	$TmFeO_3$	10^{-5}	Pn′m′a (62.446)	Pnma (62)	AM	mmm	2/m	d
0.1036	.	$CoTa_4Se_8$	10^{-5}	$P6_3'/m'm'c$ (194.268)	$P6_3/mmc$ (194)	AM	6/mmm	-3m	g
0.1059	.	$PrBaMn_2O_6$	10^{-5}	$Pmc'2_1'$ (26.69)	$Pmc2_1$ (26)	AM	mmm	2/m	d
0.1065	23592	$MnGeN_2$	10^{-5}	$Pn'a2_1'$ (33.146)	$Pna2_1$ (33)	AM	mmm	2/m	d
0.1066	200019	$MnSiN_2$	10^{-5}	$Pn'a2_1'$ (33.146)	$Pna2_1$ (33)	AM	mmm	2/m	d
0.1071	.	Fe_2SiO_4	10^{-5}	Pnma.1 (62.441)	Pnma (62)	AM	mmm	2/m	d
0.1080	.	$Ca_2Fe_2O_5$	10^{-5}	Pn′m′a (62.446)	Pnma (62)	AM	mmm	2/m	d
0.1082	.	$LuCrWO_6$	10^{-5}	$Pna2_1$ (33.144)	$Pna2_1$ (33)	AM	mmm	2/m	d
0.1085	63645	$PrFeO_3$	10^{-5}	Pn′ma′ (62.448)	Pnma (62)	AM	mmm	2/m	d

continued on next page

Table S2 (continued).

ID	ICSD	Chemical formula	SP	BNS (mcif)	Parent SG	Phase	G	H	Wave
0.1090	.	NH_4CrF_3	10^{-5}	Ccc′m′ (66.496)	$P4_2/mbc$ (135)	AM	4/mmm	mmm	d
1.0.9	27511	$CsCoCl_3$	10^{-5}	$P6'_3/m'cm'$ (193.259)	$P6_3/mcm$ (193)	AM	6/mmm	-3m	g
1.0.9	27511	$CsCoCl_3$	10^{-4}	$P6'_3/m'cm'$ (193.259)	$P6_3/mmc$ (194)	AM	6/mmm	-3m	g
1.0.26	.	$RbCoBr_3$	10^{-5}	$P6'_3/m'cm'$ (193.259)	$P6_3/mcm$ (193)	AM	6/mmm	-3m	g
1.0.26	.	$RbCoBr_3$	10^{-4}	$P6'_3/m'cm'$ (193.259)	$P6_3/mmc$ (194)	AM	6/mmm	-3m	g
1.0.38	27511	$CsCoCl_3$	10^{-5}	$P6'_3/m'cm'$ (193.259)	$P6_3/mcm$ (193)	AM	6/mmm	-3m	g
1.0.38	27511	$CsCoCl_3$	10^{-4}	$P6'_3/m'cm'$ (193.259)	$P6_3/mmc$ (194)	AM	6/mmm	-3m	g
1.0.39	10332	$BaMnO_3$	10^{-5}	$P6'_3/m'cm'$ (193.259)	$P6_3/mcm$ (193)	AM	6/mmm	-3m	g
1.0.39	10332	$BaMnO_3$	10^{-3}	$P6'_3/m'cm'$ (193.259)	$P6_3/mmc$ (194)	AM	6/mmm	-3m	g
1.0.47	12959	$MnSe_2$	10^{-5}	Pbca (61.433)	Pbca (61)	AM	mmm	2/m	d
1.0.47	12959	$MnSe_2$	10^{-3}	Pbca (61.433)	$Pa\bar{3}$ (205)	AM	mmm	2/m	d
1.0.48	12959	$MnSe_2$	10^{-5}	$Pca'2'_1$ (29.102)	$Pca2_1$ (29)	AM	mmm	2/m	d
1.0.48	12959	$MnSe_2$	10^{-3}	$Pca'2'_1$ (29.102)	$Pa\bar{3}$ (205)	AM	mmm	2/m	d
1.0.48	12959	$MnSe_2$	10^{-4}	$Pca'2'_1$ (29.102)	Pbca (61)	AM	mmm	2/m	d
1.522	27508	$CrVO_4$	10^{-5}	$P\bar{1}$ (2.4)	Cmcm (63)	AM	mmm	2/m	d
2.88	106739	UNiGa	10^{-5}	$P\bar{6}'2m'$ (189.224)	$P\bar{6}2m$ (189)	AM	6/mmm	-3m	g

Table S3: Symmetry data for 131 noncollinear entries in MAGNDATA converted into collinear systems and then identified as potential altermagnets. A measure of how much the spins were changed is provided by the highest value of $\arccos(|S_i \cdot S_j|/|S_i||S_j|)$ (i.e., 0° means all spins are aligned, 90° means that the original structure contains orthogonal spin directions). Rows are identified by their MAGNDATA *ID*. For materials where the detected symmetries depend on the precision used for symmetry identification, values of the spglib `symprec` setting ranging from 10^{-5} to 10^{-1} were tested, and when the results differ, multiple rows are included in the table. The column *SP* shows the lowest value (i.e., the most precise symmetry matching) in this range that gives the respective result. The wave classification is made via the Laue classes of the parent spacegroup G and an identified halving subgroup H that are matched with Fig. 2 in [PRX 12, 031042 (2022)]. The identified phases are: AM = Altermagnet, FiM = Ferrimagnet. Materials are included as long as one choice of symmetry precision resulted in altermagnetism (i.e., gave a positive result from the amcheck `is_altermagnet` function). The *BNS* symbols and numbers are the ones in the MAGNDATA mcif files, whereas the (nonmagnetic) parent spacegroup (*Parent SG*) is shown as detected by `spglib`.

ID	ICSD	Chemical formula	SP	BNS (mcif)	Parent SG	$\frac{\lvert S_i \cdot S_j \rvert}{\lvert S_i \rvert \lvert S_j \rvert}$	Phase	G	H	Wave
0.6	.	$YMnO_3$	10^{-5}	$P6_3cm$ (185.197)	$P6_3cm$ (185)	60°	AM	mmm	2/m	d
0.7	50694	$ScMnO_3$	10^{-5}	$P6_3c'm'$ (185.201)	$P6_3cm$ (185)	60°	AM	mmm	2/m	d
0.8	50694	$ScMnO_3$	10^{-5}	$P6_3$ (173.129)	$P6_3cm$ (185)	60°	AM	mmm	2/m	d
0.10	280091	$DyFeO_3$	10^{-5}	$P2_12_12_1$ (19.25)	Pnma (62)	33.4°	AM	mmm	2/m	d
0.11	280091	$DyFeO_3$	10^{-5}	$Pn'a'2_1$ (33.148)	Pnma (62)	33.4°	AM	mmm	2/m	d
0.29	24152	$Er_2Ti_2O_7$	10^{-5}	$I4_1'/am'd$ (141.554)	$Fd\bar{3}m$ (227)	70.53°	AM	4/mmm	mmm	d
0.31	92838	$HoMnO_3$	10^{-5}	$P6_3c'm'$ (185.201)	$P6_3cm$ (185)	60°	AM	mmm	2/m	d
0.32	92838	$HoMnO_3$	10^{-5}	$P6_3cm$ (185.197)	$P6_3cm$ (185)	60°	AM	mmm	2/m	d
0.33	92838	$HoMnO_3$	10^{-5}	$P6_3cm$ (185.197)	$P6_3cm$ (185)	90°	AM	2/m	-1	d
0.36	.	NiF_2	10^{-5}	$Pnn'm'$ (58.398)	$P4_2/mnm$ (136)	1.72°	AM	4/mmm	mmm	d
0.40	.	Mn_2O_3−alpha	10^{-5}	Pbca (61.433)	Pbca (61)	66.62°	AM	mmm	2/m	d
0.41	.	Mn_2O_3−alpha	10^{-5}	Pbca (61.433)	Pbca (61)	62.66°	AM	mmm	2/m	d
0.47	84753	$Gd_2Sn_2O_7$	10^{-5}	$I4_1'/amd'$ (141.555)	$Fd\bar{3}m$ (227)	90°	AM	4/mmm	mmm	d
0.69	.	$Co_4(OH)_2(C_{10}H_{16}O_4)_3$	10^{-5}	$P2_1'/c'$ (14.79)	$P2_1/c$ (14)	75.19°	AM	2/m	-1	d
0.90	.	$Rb_2Fe_2O(AsO_4)_2$	10^{-5}	Pnma (62.441)	Pnma (62)	50.9°	AM	mmm	2/m	d
0.101	.	Mn_2GeO_4	10^{-5}	$Pn'm'a$ (62.446)	Pnma (62)	15.19°	AM	mmm	2/m	d
0.102	.	Mn_2GeO_4	10^{-5}	Pnma (62.441)	Pnma (62)	62.44°	AM	mmm	2/m	d
0.103	.	Mn_2GeO_4	10^{-5}	$P2_1/c$ (14.75)	Pnma (62)	11.65°	AM	mmm	2/m	d
0.104	185838	$ErVO_3$	10^{-5}	$P2_1'/m'$ (11.54)	Pnma (62)	14.47°	AM	mmm	2/m	d
0.107	161912	$Ho_2Ge_2O_7$	10^{-5}	$P4_12_12$ (92.111)	$P4_12_12$ (92)	90°	AM	mmm	2/m	d
0.117	183152	$LuFeO_3$	10^{-5}	$P6_3c'm'$ (185.201)	$P6_3cm$ (185)	60°	AM	mmm	2/m	d
0.121	.	$Li_2Co(SO_4)_2$	10^{-5}	$P2_1'/c'$ (14.79)	$P2_1/c$ (14)	4.13°	AM	2/m	-1	d
0.122	290292	$Li_2Mn(SO_4)_2$	10^{-5}	$P2_1/c$ (14.75)	$P2_1/c$ (14)	0.5°	AM	2/m	-1	d
0.129	173779	$Cu_3Mo_2O_9$	10^{-5}	$P2_1'2_1'2_1$ (19.27)	Pnma (62)	90°	AM	mmm	2/m	d
0.130	.	$Cu_3Mo_2O_9$	10^{-5}	$Pm'c2_1'$ (26.68)	Pnma (62)	54.03°	AM	mmm	2/m	d
0.132	.	$Fe(N(CN_2))_2$	10^{-5}	$Pnn'm'$ (58.398)	Pnnm (58)	28.41°	AM	mmm	2/m	d
0.134	84319	$Mn_3B_7O_{13}I$	10^{-5}	$Pc'a2_1'$ (29.101)	$Pca2_1$ (29)	77.96°	AM	2/m	-1	d
0.165	.	$SrMn(VO_4)(OH)$	10^{-5}	$P2_1$ (4.7)	$P2_1$ (4)	17.33°	AM	2/m	-1	d
0.165	.	$SrMn(VO_4)(OH)$	10^{-1}	$P2_1$ (4.7)	$P2_12_12_1$ (19)	17.33°	AM	mmm	2/m	d
0.168	.	$NH_4Fe_2F_6$	10^{-5}	Pnma (62.441)	Pnma (62)	75.98°	AM	2/m	-1	d
0.175	.	$Ca_2CoSi_2O_7$	10^{-5}	$P2_12_1'2'$ (18.19)	$P2_12_12$ (18)	2.87°	AM	mmm	2/m	d
0.191	9930	$BaCuF_4$	10^{-5}	$Cm'c'2_1$ (36.176)	$Cmc2_1$ (36)	8.14°	AM	mmm	2/m	d
0.192	186748	$RbFe_2F_6$	10^{-5}	Pnma (62.441)	Pnma (62)	90°	AM	2/m	-1	d
0.204	.	Ca_2MnReO_6	10^{-5}	$P2_1/c$ (14.75)	$P2_1/c$ (14)	81.26°	AM	2/m	-1	d
0.207	.	$TlFe_1 \cdot {}_6Se_2$	10^{-5}	I4/m (87.75)	I4/m (87)	90°	AM	2/m	-1	d
0.210	.	Sr_2CoOsO_6	10^{-5}	C2/c (15.85)	C2/c (15)	0.7°	AM	2/m	-1	d
0.218	260092	Co_2SiO_4	10^{-5}	Pnma (62.441)	Pnma (62)	31.39°	AM	mmm	2/m	d
0.219	260092	Co_2SiO_4	10^{-5}	Pnma (62.441)	Pnma (62)	40.1°	AM	mmm	2/m	d
0.236	.	$CaFe_4Al_8$	10^{-5}	$I4'/mmm'$ (139.535)	I4/mmm (139)	8.41°	AM	4/mmm	mmm	d
0.237	84749	$Er_2Sn_2O_7$	10^{-5}	$I4_1'/amd'$ (141.555)	$Fd\bar{3}m$ (227)	90°	AM	4/mmm	mmm	d
0.238	.	$Er_2Pt_2O_7$	10^{-5}	$I4_1'/amd'$ (141.555)	$Fd\bar{3}m$ (227)	90°	AM	4/mmm	mmm	d
0.240	79430	$Er_2Cu_2O_5$	10^{-5}	$Pna2_1$ (33.144)	$Pna2_1$ (33)	56.95°	AM	mmm	2/m	d

continued on next page

Table S3 (continued).

ID	ICSD	Chemical formula	SP	BNS (mcif)	Parent SG	$\frac{\lvert S_i \cdot S_j \rvert}{\lvert S_i \rvert \lvert S_j \rvert}$	Phase	G	H	Wave
0.262	93580	$CoFePO_5$	10^{-5}	Pnm′a′ (62.447)	Pnma (62)	25.81°	AM	mmm	2/m	d
0.288	.	$NdMnO_3$	10^{-5}	Pn′ma′ (62.448)	Pnma (62)	42.18°	AM	mmm	2/m	d
0.292	.	$NiTe_2O_5$	10^{-5}	Pnma (62.441)	Pnma (62)	20.14°	AM	mmm	2/m	d
0.294	.	$Cu_4(OD)_6FBr$	10^{-5}	Pn′m′a (62.446)	Pnma (62)	55.52°	AM	mmm	2/m	d
0.295	163214	$Cu_2(OD)_3Cl$	10^{-5}	$P2_1/c$ (14.75)	$P2_1/c$ (14)	80.16°	AM	2/m	-1	d
0.296	153644	$Cu_2(OD)_3Cl$	10^{-5}	$P2_1/c$ (14.75)	$P2_1/c$ (14)	31.92°	AM	2/m	-1	d
0.298	254516	$Na_2BaFe(VO_4)_2$	10^{-5}	C2′/c′ (15.89)	C2/c (15)	81.26°	AM	2/m	-1	d
0.314	257626	$ZrCo_2Ge_4O_{12}$	10^{-5}	Pb′an′ (50.282)	P4/nbm (125)	69.25°	AM	4/mmm	mmm	d
0.316	.	$DyCrWO_6$	10^{-5}	$P2_1$ (4.7)	$Pna2_1$ (33)	75.71°	AM	2/m	-1	d
0.324	.	$CdYb_2S_4$	10^{-5}	$I4_1/amd$ (141.551)	$Fd\bar{3}m$ (227)	90°	AM	4/mmm	mmm	d
0.325	.	$CdYb_2Se_4$	10^{-5}	$I4_1/amd$ (141.551)	$Fd\bar{3}m$ (227)	90°	AM	4/mmm	mmm	d
0.337	153442	$NdFeO_3$	10^{-5}	$P2_1'/c'$ (14.79)	Pnma (62)	90°	AM	2/m	-1	d
0.342	56035	Tb_3Ge_5	10^{-5}	Fdd2 (43.224)	Fdd2 (43)	43.93°	AM	mmm	2/m	d
0.353	22311	$TbFeO_3$	10^{-5}	$P2_1'2_1'2_1$ (19.27)	Pnma (62)	80.54°	AM	mmm	2/m	d
0.357	258571	$CaFe_5O_7$	10^{-5}	$P2_1/m$ (11.50)	$P2_1/m$ (11)	53.13°	AM	2/m	-1	d
0.368	.	$(CH_3NH_3)(Co(COOH)_3$	10^{-5}	Pn′ma′ (62.448)	Pnma (62)	29.29°	AM	mmm	2/m	d
0.370	163728	$NdMnO_3$	10^{-5}	Pn′ma′ (62.448)	Pnma (62)	53.9°	AM	mmm	2/m	d
0.375	.	La_2CoIrO_6	10^{-5}	$P2_1/c$ (14.75)	$P2_1/c$ (14)	89.27°	AM	2/m	-1	d
0.398	.	Ca_2RuO_4	10^{-5}	Pbca (61.433)	Pbca (61)	11.42°	AM	mmm	2/m	d
0.419	.	$Er_2Ge_2O_7$	10^{-5}	$P4_12_12'$ (92.113)	$P4_12_12$ (92)	60.02°	AM	4/mmm	mmm	d
0.425	251081	$Na_2CoP_2O_7$	10^{-5}	$Pn'a2_1'$ (33.146)	$Pna2_1$ (33)	43.82°	AM	mmm	2/m	d
0.431	191850	CuB_2O_4	10^{-5}	P1 (1.1)	$I\bar{4}2d$ (122)	89.43°	AM	2/m	-1	d
0.440	.	$SrCuTe_2O_6$	10^{-5}	$P4_132$ (213.63)	$P4_132$ (213)	90°	AM	2/m	-1	d
0.530	.	$SrCuTe_2O_6$	10^{-5}	$P4_132$ (213.63)	$P4_132$ (213)	90°	AM	2/m	-1	d
0.552	159208	Pb_2MnO_4	10^{-5}	$P\bar{4}'2_1c'$ (114.278)	$P\bar{4}2_1c$ (114)	90°	AM	mmm	2/m	d
0.589	28488	$NdCrO_3$	10^{-5}	$P2_1/m$ (11.50)	Pnma (62)	90°	AM	2/m	-1	d
0.590	28487	$ErCrO_3$	10^{-5}	$P2_1/m$ (11.50)	Pnma (62)	90°	AM	2/m	-1	d
0.658	.	$BaCuTe_2O_6$	10^{-5}	$P4_132'$ (213.65)	$P4_132$ (213)	90°	AM	2/m	-1	d
0.669	55716	Sr_2YbRuO_6	10^{-5}	$P2_1/c$ (14.75)	$P2_1/c$ (14)	0.01°	AM	2/m	-1	d
0.670	55716	Sr_2YbRuO_6	10^{-5}	$P2_1/c$ (14.75)	$P2_1/c$ (14)	0.19°	AM	2/m	-1	d
0.697	.	$SmCrO_3$	10^{-5}	Pn′m′a (62.446)	Pnma (62)	86.12°	AM	2/m	-1	d
0.698	.	$SmCrO_3$	10^{-5}	Pbn′m′ (62.446)	Pnma (62)	86.16°	AM	2/m	-1	d
0.707	.	$Tb_2Ir_3Ga_9$	10^{-5}	Cm′cm′ (63.464)	Cmcm (63)	13.2°	AM	mmm	2/m	d
0.715	.	$HoCrWO_6$	10^{-5}	$Pna2_1$ (33.144)	$Pna2_1$ (33)	82.46°	AM	2/m	-1	d
0.716	.	$HoCrWO_6$	10^{-5}	$Pna2_1$ (33.144)	$Pna2_1$ (33)	82.25°	AM	2/m	-1	d
0.724	.	$BaCoSiO_4$	10^{-5}	$P6_3$ (173.129)	$P6_3$ (173)	60°	AM	2/m	-1	d
0.726	.	$CsMn_2F_6$	10^{-5}	Pnm′a′ (62.447)	Pnma (62)	84.11°	AM	2/m	-1	d
0.727	.	$CsMn_2F_6$	10^{-5}	$P2_1/c$ (14.75)	Pnma (62)	22.82°	AM	2/m	-1	d
0.759	.	$CeFeO_3$	10^{-5}	Pnma (62.441)	Pnma (62)	90°	AM	2/m	-1	d
0.785	185834	$NdVO_3$	10^{-5}	$P2_1'/m'$ (11.54)	Pnma (62)	57.97°	AM	mmm	2/m	d
0.788	155478	YVO_3	10^{-5}	$P\bar{1}$ (2.4)	$P2_1/c$ (14)	32.9°	AM	2/m	-1	d
0.788	155478	YVO_3	10^{-1}	$P\bar{1}$ (2.4)	Pnma (62)	32.9°	AM	mmm	2/m	d
0.791	290794	Sr_2TbRuO_6	10^{-5}	$P2_1/c$ (14.75)	$P2_1/c$ (14)	0.04°	AM	2/m	-1	d
0.794	164512	Sr_2HoRuO_6	10^{-5}	$P2_1/c$ (14.75)	$P2_1/c$ (14)	0.02°	AM	2/m	-1	d
0.803	.	NbMnP	10^{-5}	$Pm'n2_1'$ (31.125)	Pnma (62)	86.65°	AM	mmm	2/m	d
0.810	1147	Fe_2WO_6	10^{-5}	Pbc′n′ (60.423)	Pbcn (60)	37.39°	AM	mmm	2/m	d
0.812	.	Fe_2WO_6	10^{-5}	Pn′c2′ (30.113)	Pbcn (60)	47.1°	AM	mmm	2/m	d
0.849	.	$Er_5Pd_2In_4$	10^{-5}	Pb′am′ (55.358)	Pbam (55)	45.93°	AM	mmm	2/m	d
0.850	.	$Er_5Pd_2In_4$	10^{-5}	Pb′am′ (55.358)	Pbam (55)	39.49°	AM	mmm	2/m	d
0.851	.	$C_7H_{14}NFeCl_4$	10^{-5}	$P2_1'2_1'2_1$ (19.27)	Pbca (61)	59.01°	AM	mmm	2/m	d
0.854	.	$Gd_2Pt_2O_7$	10^{-5}	$I4_1'/amd'$ (141.555)	$Fd\bar{3}m$ (227)	90°	AM	4/mmm	mmm	d
0.903	.	Pr_2PdGe_6	10^{-5}	Cm′c′a (64.474)	Cmce (64)	60.6°	AM	mmm	2/m	d
0.912	.	$Ho_5Ni_2In_4$	10^{-5}	$P2_1/c$ (14.75)	Pbam (55)	10.71°	AM	mmm	2/m	d
0.926	.	Pr_2PdGe_6	10^{-5}	Cm′c′a (64.474)	Cmce (64)	60.6°	AM	mmm	2/m	d
0.942	19241	$Er_2Ge_2O_7$	10^{-5}	$P4_1'2_12'$ (92.113)	$P4_12_12$ (92)	47.86°	AM	4/mmm	mmm	d

continued on next page

Table S3 (continued).

ID	ICSD	Chemical formula	SP	BNS (mcif)	Parent SG	$\frac{\lvert S_i \cdot S_j \rvert}{\lvert S_i \rvert \lvert S_j \rvert}$	Phase	G	H	Wave
0.948	4626	$CaNi_3P_4O_{14}$	10^{-5}	$P2_1/c$ (14.75)	$P2_1/c$ (14)	13.08°	AM	2/m	-1	d
0.951	189421	$LaYbO_3$	10^{-5}	$Pn'ma'$ (62.448)	Pnma (62)	40.19°	AM	mmm	2/m	d
0.981	.	$TmVO_3$	10^{-5}	Pnma (62.441)	Pnma (62)	90°	AM	2/m	-1	d
0.990	239903	$HoFeO_3$	10^{-5}	$Pn'm'a$ (62.446)	Pnma (62)	90°	AM	2/m	-1	d
0.992	.	$HoFeO_3$	10^{-5}	$Pn'm'a$ (62.446)	Pnma (62)	89.66°	AM	2/m	-1	d
0.993	.	$HoFeO_3$	10^{-5}	$Pn'ma'$ (62.448)	Pnma (62)	18.79°	AM	mmm	2/m	d
0.994	.	$HoFeO_3$	10^{-5}	$Pn'm'a$ (62.446)	Pnma (62)	90°	AM	2/m	-1	d
0.1000	.	Fe_4O_5	10^{-5}	$P2_1'$ (4.9)	Cmcm (63)	65.81°	AM	mmm	2/m	d
0.1014	.	$CsNi(NCS)_3$	10^{-5}	$P2_1/n$ (14.75)	$P2_1/c$ (14)	58.76°	AM	2/m	-1	d
0.1043	432631	$NdPt_6Al_3$	10^{-5}	$C2/c.1$ (15.85)	$R\bar{3}c$ (167)	30.1°	AM	-3m	-3	g
0.1049	.	$Co(DCOO)_2(D_2O)_2$	10^{-5}	$P2_1/c.1$ (14.75)	$P2_1/c$ (14)	50.11°	AM	2/m	-1	d
0.1060	.	$C_3H_6MnO_6$	10^{-5}	$Pc'a2_1'$ (29.101)	$Pca2_1$ (29)	1.33°	AM	mmm	2/m	d
0.1063	.	$Fe_2(SeO_3)_3(H_2O)_3$	10^{-5}	Cc (9.37)	R3c (161)	42.56°	AM	-3m	-3	g
0.1067	.	$MnSiN_2$	10^{-5}	Pc' (7.26)	Pc (7)	0.18°	FiM	2/m	2/m	s
0.1067	.	$MnSiN_2$	10^{-1}	Pc' (7.26)	$Pna2_1$ (33)	0.18°	AM	mmm	2/m	d
0.1068	.	$LuCrO_3$	10^{-5}	$Pn'm'a$ (62.446)	Pnma (62)	8.35°	AM	mmm	2/m	d
1.0.3	.	$CsCoBr_3$	10^{-5}	$Cm'c2_1'$ (36.174)	$Cmc2_1$ (36)	19.42°	AM	mmm	2/m	d
1.0.3	.	$CsCoBr_3$	10^{-5}	$Cm'c2_1'$ (36.174)	Ama2 (40)	19.42°	AM	mmm	2/m	d
1.0.3	.	$CsCoBr_3$	10^{-3}	$Cm'c2_1'$ (36.174)	$P6_3/mmc$ (194)	19.42°	AM	6/mmm	-3m	g
1.0.4	59371	$CsNiCl_3$	10^{-5}	$C22'2_1'$ (20.34)	Cmcm (63)	59.49°	AM	mmm	2/m	d
1.0.4	59371	$CsNiCl_3$	10^{-3}	$C22'2_1'$ (20.34)	$P6_3/mmc$ (194)	59.49°	AM	mmm	2/m	d
1.0.31	260109	$EuIn_2As_2$	10^{-5}	$C2'2'2_1$ (20.33)	Cmcm (63)	79.49°	AM	mmm	2/m	d
1.0.31	260109	$EuIn_2As_2$	10^{-4}	$C2'2'2_1$ (20.33)	$P6_3/mmc$ (194)	79.49°	AM	6/mmm	-3m	g
1.0.31	260109	$EuIn_2As_2$	10^{-3}	$C2'2'2_1$ (20.33)	$P6_3/mmc$ (194)	79.49°	AM	6/mmm	-3m	g
1.0.32	260109	$EuIn_2As_2$	10^{-5}	$P6_122'2'$ (178.159)	$P6_122$ (178)	60°	AM	mmm	2/m	d
1.0.32	260109	$EuIn_2As_2$	10^{-4}	$P6_122'2'$ (178.159)	$P6_3/mmc$ (194)	60°	AM	6/mmm	-3m	g
1.0.33	.	FeF_3	10^{-5}	$P6_3/m$ (176.143)	$P6_3/m$ (176)	60°	AM	2/m	-1	d
1.0.34	60261	$RbNiCl_3$	10^{-5}	$Cm'c2_1'$ (36.174)	$Cmc2_1$ (36)	65.04°	AM	2/m	-1	d
1.0.34	60261	$RbNiCl_3$	10^{-3}	$Cm'c2_1'$ (36.174)	$P6_3/mmc$ (194)	65.04°	AM	6/mmm	-3m	g
1.0.34	60261	$RbNiCl_3$	10^{-5}	$Cm'c2_1'$ (36.174)	Cmcm (63)	65.04°	AM	mmm	2/m	d
1.0.35	2782	$CsMnBr_3$	10^{-5}	$P\bar{6}2'm'$ (189.225)	Pm (6)	60°	AM	2/m	-1	d
1.0.35	2782	$CsMnBr_3$	10^{-5}	$P\bar{6}2'm'$ (189.225)	$P\bar{6}$ (174)	60°	AM	2/m	-1	d
1.0.35	2782	$CsMnBr_3$	10^{-3}	$P\bar{6}2'm'$ (189.225)	$P6_3/mmc$ (194)	60°	AM	6/mmm	-3m	g
1.0.36	15952	$CsMnI_3$	10^{-5}	$Cm'c2_1'$ (36.174)	$Cmc2_1$ (36)	79.86°	AM	2/m	-1	d
1.0.36	15952	$CsMnI_3$	10^{-3}	$Cm'c2_1'$ (36.174)	$P6_3/mmc$ (194)	79.86°	AM	6/mmm	-3m	g
1.0.36	15952	$CsMnI_3$	10^{-5}	$Cm'c2_1'$ (36.174)	Cmcm (63)	79.86°	AM	mmm	2/m	d
1.0.37	15951	$CsMnI_3$	10^{-5}	$Cm'c2_1'$ (36.174)	$Cmc2_1$ (36)	81.79°	AM	2/m	-1	d
1.0.37	15951	$CsMnI_3$	10^{-3}	$Cm'c2_1'$ (36.174)	$P6_3/mmc$ (194)	81.79°	AM	6/mmm	-3m	g
1.0.37	15951	$CsMnI_3$	10^{-5}	$Cm'c2_1'$ (36.174)	Cmcm (63)	81.79°	AM	mmm	2/m	d
1.0.41	60261	$RbNiCl_3$	10^{-5}	$C22'2_1'$ (20.34)	Cmcm (63)	60°	AM	mmm	2/m	d
1.0.41	60261	$RbNiCl_3$	10^{-3}	$C22'2_1'$ (20.34)	$P6_3/mmc$ (194)	60°	AM	6/mmm	-3m	g
1.0.42	60262	$CsNiCl_3$	10^{-5}	$C22'2_1'$ (20.34)	Cmcm (63)	60°	AM	mmm	2/m	d
1.0.42	60262	$CsNiCl_3$	10^{-3}	$C22'2_1'$ (20.34)	$P6_3/mmc$ (194)	60°	AM	6/mmm	-3m	g
1.0.44	151442	$Ba_3CoSb_2O_9$	10^{-5}	$Cm'c2_1'$ (36.174)	Cmcm (63)	60°	AM	mmm	2/m	d

continued on next page

Table S3 (continued).

ID	ICSD	Chemical formula	SP	BNS (mcif)	Parent SG	$\frac{\lvert S_i \cdot S_j \rvert}{\lvert S_i \rvert \lvert S_j \rvert}$	Phase	G	H	Wave
1.0.44	151442	$Ba_3CoSb_2O_9$	10^{-2}	$Cm'c2'_1$ (36.174)	$P6_3/mmc$ (194)	60°	AM	6/mmm	-3m	g
1.0.45	151442	$Ba_3CoSb_2O_9$	10^{-5}	$P\bar{6}2m$ (189.221)	P1 (1)	60°	FiM	-1	-1	s
1.0.45	151442	$Ba_3CoSb_2O_9$	10^{-4}	$P\bar{6}2m$ (189.221)	$P\bar{6}2m$ (189)	60°	AM	mmm	2/m	d
1.0.45	151442	$Ba_3CoSb_2O_9$	10^{-3}	$P\bar{6}2m$ (189.221)	$P6_3/mmc$ (194)	60°	AM	6/mmm	-3m	g
1.0.46	151441	$Ba_3MnSb_2O_9$	10^{-5}	C2 (5.13)	C2/c (15)	60.05°	AM	2/m	-1	d
1.0.46	151441	$Ba_3MnSb_2O_9$	10^{-3}	C2 (5.13)	C2/c (15)	60.05°	AM	2/m	-1	d
1.0.49	.	$BaCoSiO_4$	10^{-5}	$P6_3$ (173.129)	$P6_3$ (173)	60°	AM	2/m	-1	d
2.35	626717	CrSe	10^{-5}	P31m′ (157.55)	Pm (6)	57.79°	AM	2/m	-1	d
2.35	626717	CrSe	10^{-5}	P31m′ (157.55)	$P6_3/mmc$ (194)	57.79°	AM	6/mmm	-3m	g
2.61	.	$Fe_3F_8(H_2O)_2$	10^{-5}	C2′/m′ (12.62)	C2/m (12)	72.73°	AM	2/m	-1	d
2.62	.	$TbCrO_3$	10^{-5}	$Pm'n'2_1$ (31.127)	Pnma (62)	90°	AM	mmm	2/m	d
2.63	16507	$DyCrO_3$	10^{-5}	$P2'_1/m'$ (11.54)	Pnma (62)	90°	AM	2/m	-1	d
2.64	28248	$DyCrO_3$	10^{-5}	$P2'_1/m'$ (11.54)	Pnma (62)	90°	AM	2/m	-1	d
3.4	.	$MgCr_2O_4$	10^{-5}	$P\bar{4}2'm'$ (111.255)	$Fd\bar{3}m$ (227)	70.53°	AM	4/mmm	mmm	d

Table S1. Sensitivity of the band gap E_g, maximum splitting $\Delta_{\max}$, and average splitting Δ_{avg} to ±10% variations of the Hubbard U values (relative to the reference values used in the main text). Band gaps are reported with two decimal places.

	E_g (eV)		$\Delta_{\max}$ (meV)		Δ_{avg} (meV)	
Material	$U-10\%$	$U+10\%$	$U-10\%$	$U+10\%$	$U-10\%$	$U+10\%$
$Ba_3CoIr_2O_9$	0.00	0.00	258.6	221.0	172.69	151.41
Ca_2MnReO_6	0.00	0.00	145.8	143.2	77.69	75.11
$CaFe_4Al_8$	0.00	0.00	606.8	612.3	368.73	382.87
Ce_4Sb_3	0.00	0.00	152.2	152.2	34.21	34.21
$CeMn_2Ge_4O_{12}$	0.00	0.00	140.4	164.1	115.22	121.32
$Co_2Mo_3O_8$	0.00	1.65	72.3	72.7	37.81	45.18
$CoTa_4Se_8$	0.00	0.00	158.1	148.8	126.14	127.04
$CrNb_4S_8$	0.00	0.00	113.2	111.5	61.36	55.54
CrSb	0.00	0.00	1797.6	1921.0	736.97	782.25
CrSe	0.00	0.00	813.7	787.2	494.50	485.39
Cu_2O_3Cl	0.00	0.00	146.6	157.3	84.62	104.85
La_2CoIrO_6	0.00	0.00	269.5	269.7	124.47	121.21
NbMnP	0.00	0.00	439.8	478.4	271.28	278.59
$PrBaMn_2O_6$	0.00	0.00	115.2	133.8	52.98	54.41
$RbCoBr_3$	0.00	0.00	144.5	152.6	94.97	90.57
RuO_2	0.00	0.00	865.9	969.4	344.38	356.02
Sr_2CoOsO_6	0.00	0.00	67.0	67.6	41.90	41.59
Sr_2ScOsO_6	0.00	0.00	94.0	94.0	45.34	45.34
UCr_2Si_2C	0.00	0.00	409.1	925.7	217.15	369.64
UNiGa	0.00	0.00	47.4	41.3	24.18	22.36
VNb_3S_6	0.00	0.00	154.1	169.1	59.18	60.86

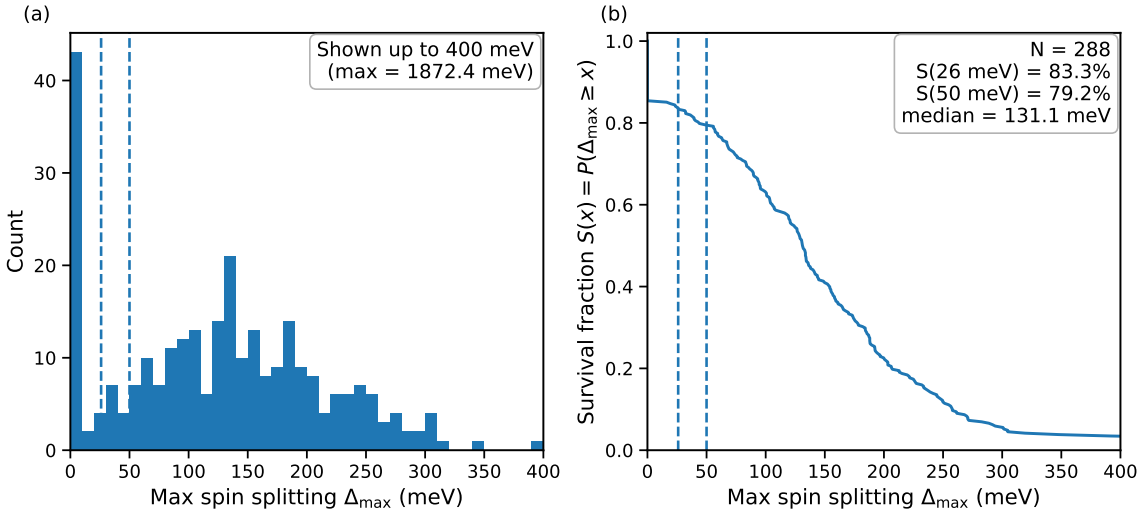
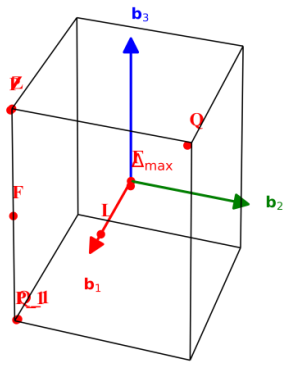
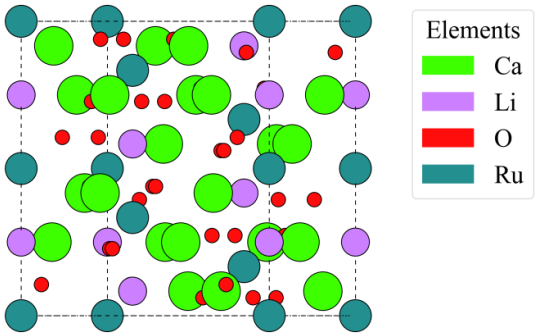


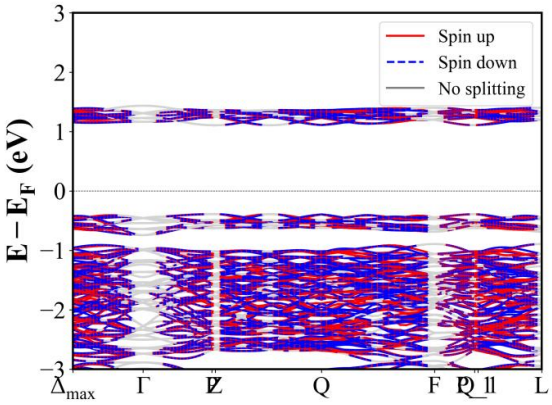
FIG. S1. (a) Histogram of the maximal altermagnetic spin splitting $\Delta_{\max}$ across the screened set ($N = 288$), shown up to 800 meV for clarity (outliers extend to 1872.4 meV). (b) Survival distribution $S(x) = P(\Delta_{\max} \geq x)$ with dashed lines marking 26 meV ($k_B T$ at 300 K) and the screening threshold 50 meV.

LiCa3RuO6 (R-3c) | Band Gap = 1.495 eV

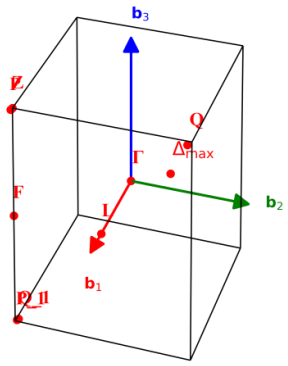


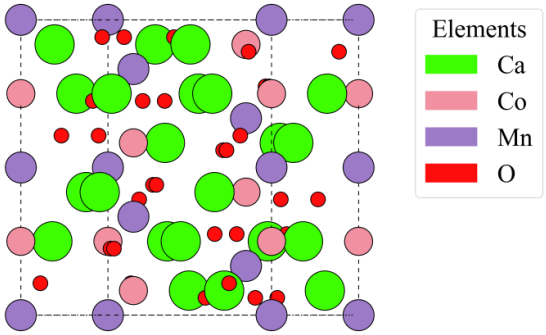


Δ_{max}: (0.500, 0.167, 0.250)

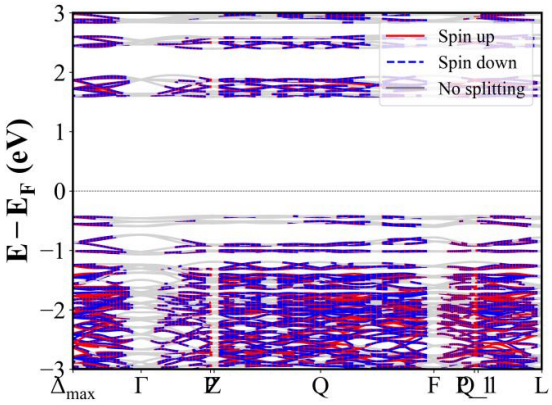


Ca3MnCoO6 (R-3c) | Band Gap = 2.003 eV

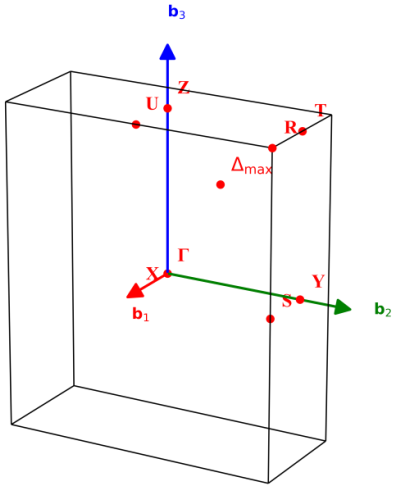


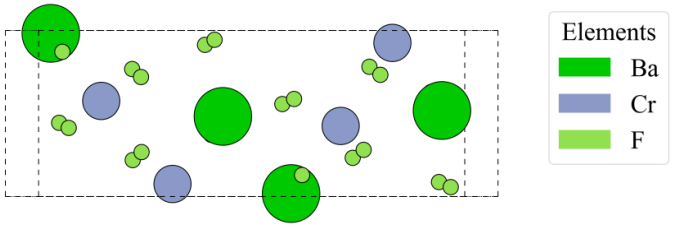


Δ_{max}: (0.333, 0.333, 0.250)

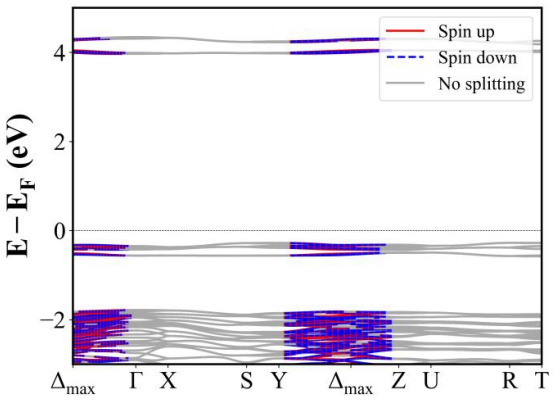


BaCrF5 (P2_12_12_1) | Band Gap = 4.241 eV

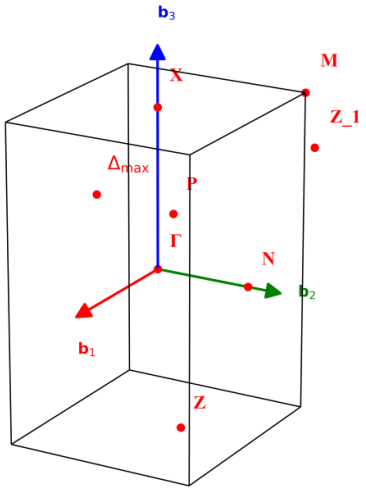


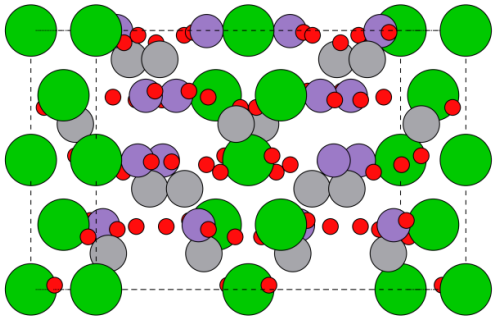


Δ_{max}: (0.000, 0.200, 0.300)



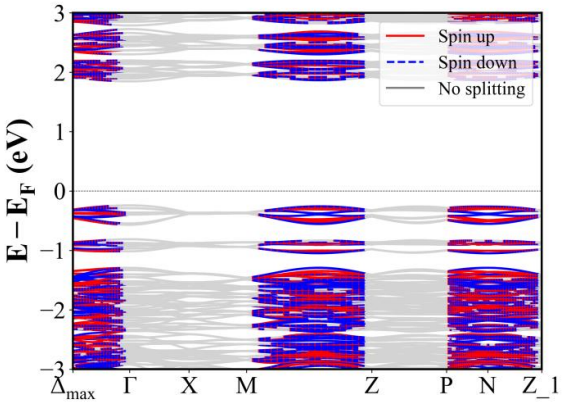
BaMn2V2O8 (I4_1cd) | Band Gap = 2.087 eV



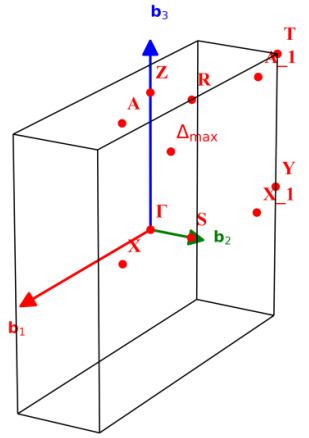


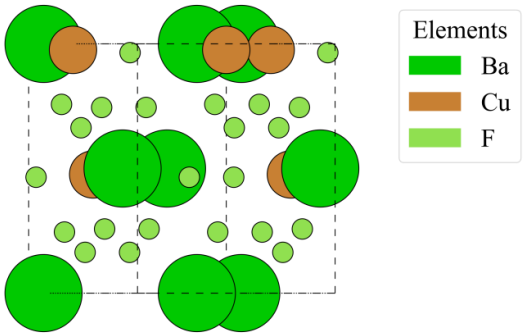


Δ_{max}: (0.500, 0.000, 0.333)

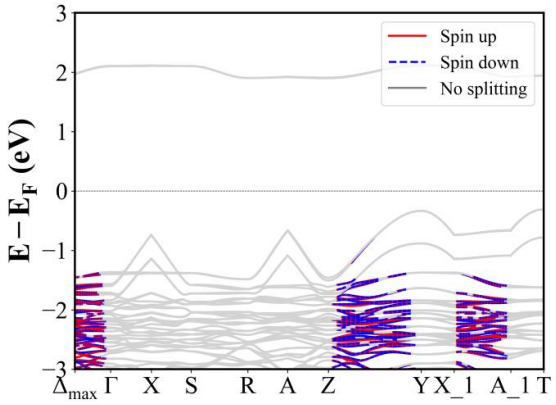


BaCuF4 (Cmc2_1) | Band Gap = 2.208 eV

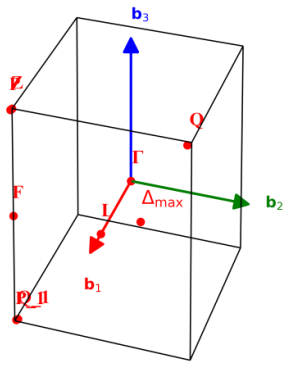


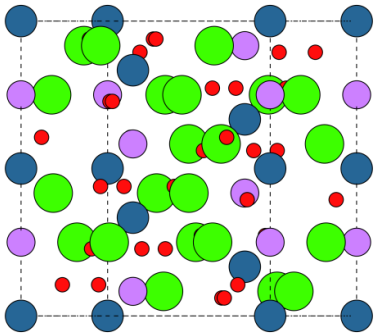


Δ_{max}: (0.000, 0.250, 0.300)

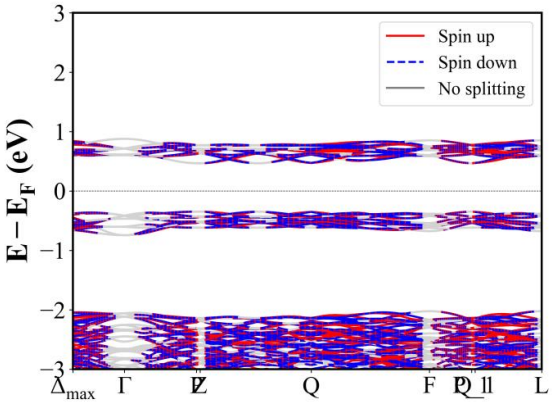


LiCa3OsO6 (R-3c) | Band Gap = 0.813 eV

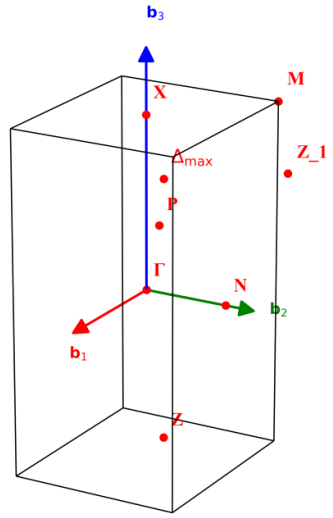




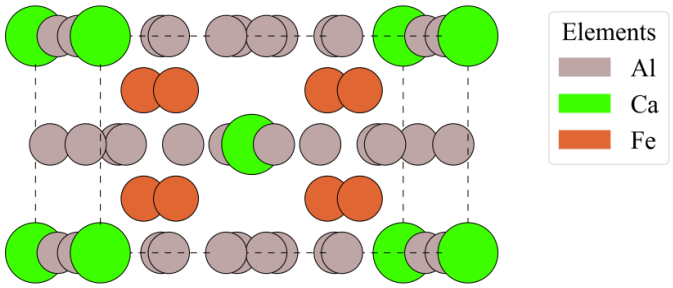
Δ_{max}: (0.333, 0.167, 0.000)

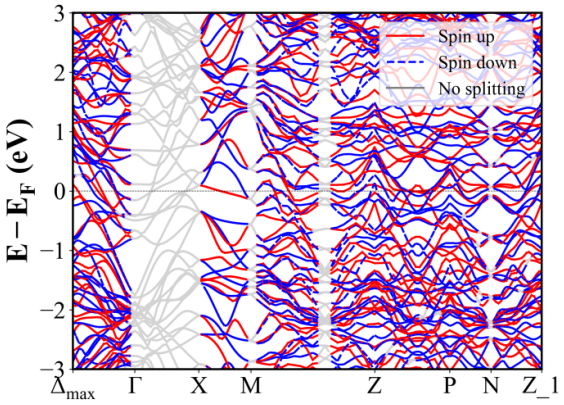


Ca(Al2Fe)4 (I4/mmm) | Band Gap = 0.000 eV

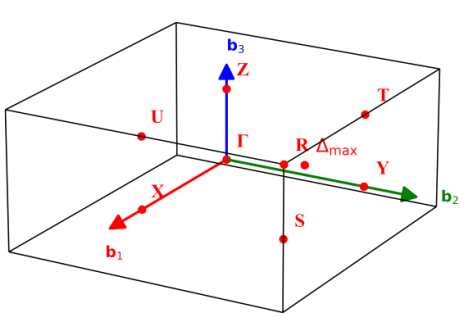


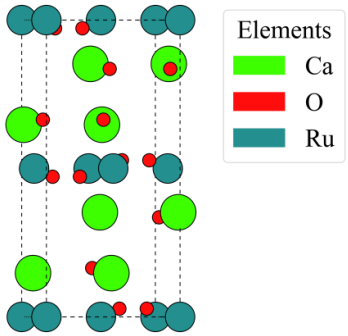
Δ_{max}: (0.333, 0.333, 0.400)



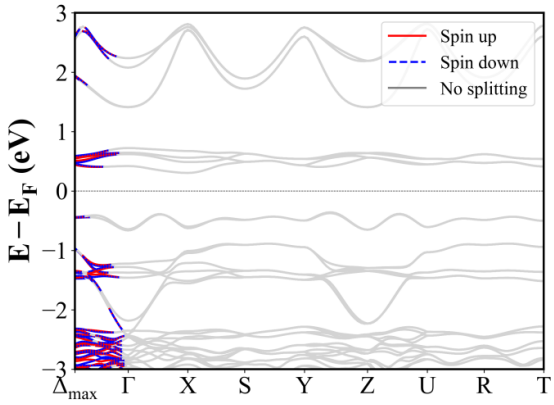


Ca2RuO4 (Pbca) | Band Gap = 0.664 eV

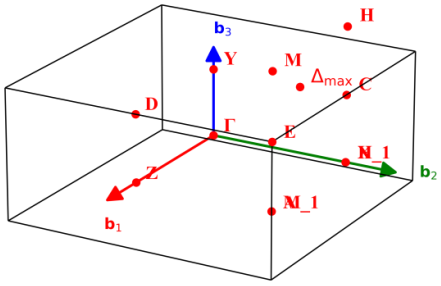


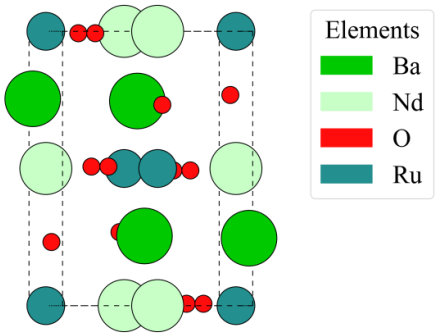


Δ_{max}: (0.200, 0.400, 0.250)

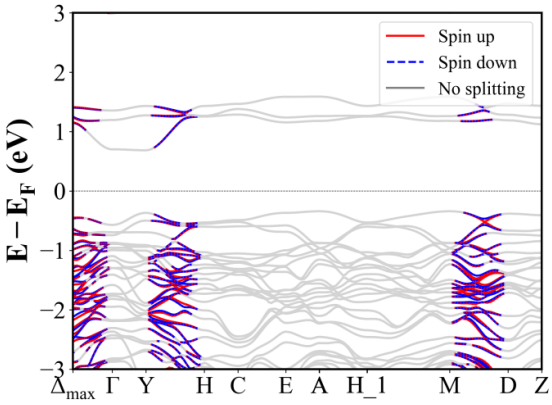


Ba2NdRuO6 (P2_1/c) | Band Gap = 1.026 eV

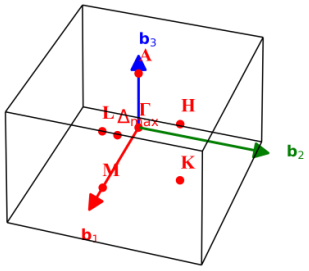


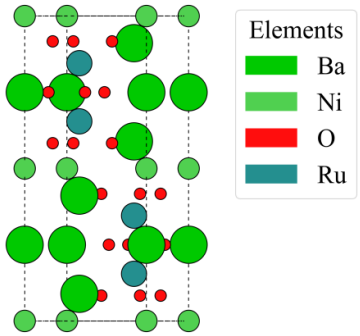


Δ_{max}: (-0.375, 0.125, 0.167)

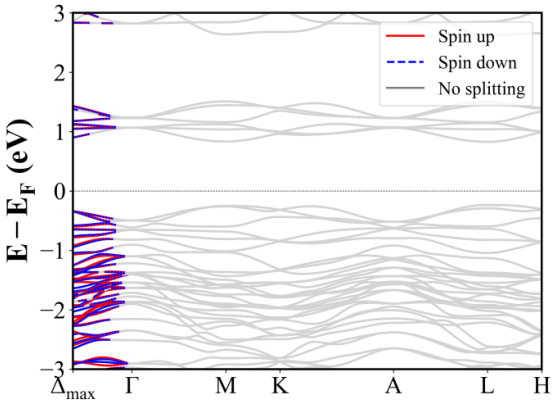


Ba3NiRu2O9 (P6_3/mmc) | Band Gap = 1.062 eV

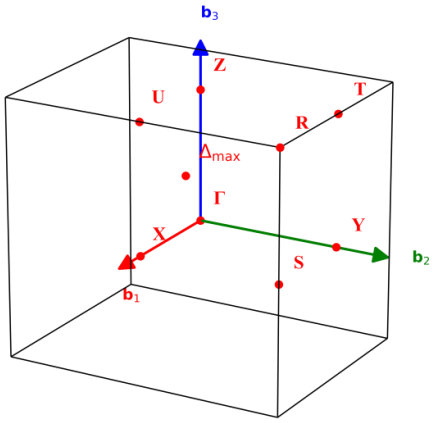


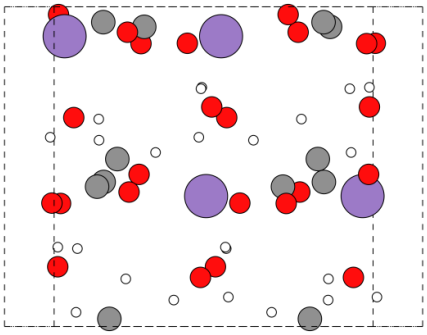


Δ_{max}: (0.300, 0.000, 0.250)

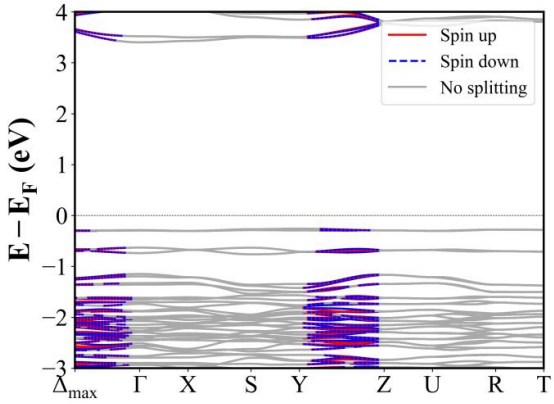


MnH6(CO2)3 (Pca2_1)

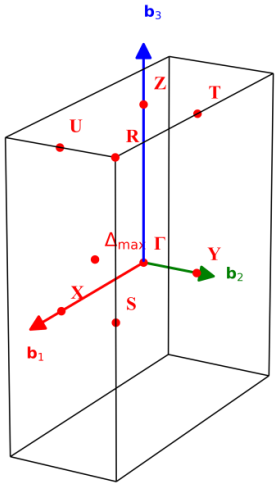




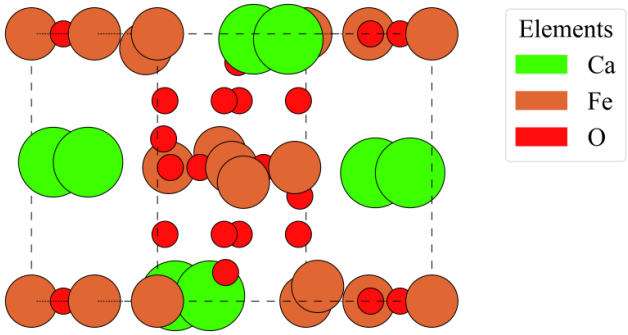
Δ_{max}: (0.500, 0.167, 0.333)

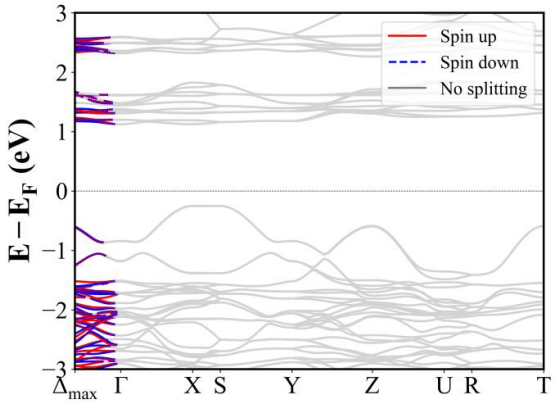


Ca2Fe2O5 (Pnma) | Band Gap = 1.373 eV

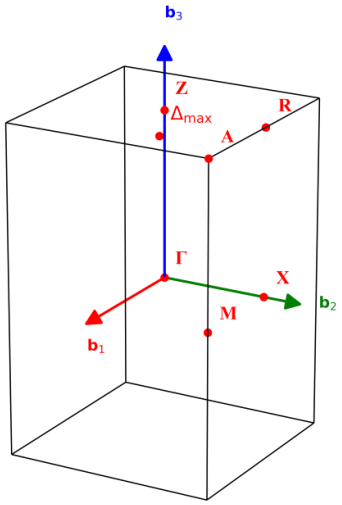


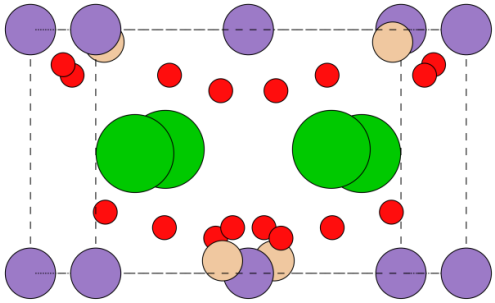
Δ_{max}: (0.300, 0.000, 0.100)



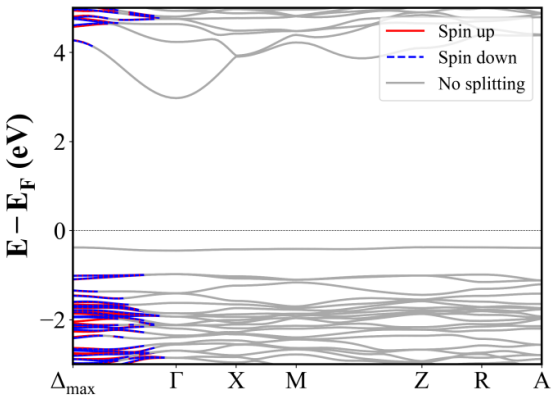


Ba2MnSi2O7 (P-42_1m) | Band Gap = 3.349 eV

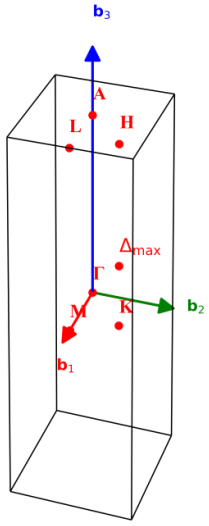




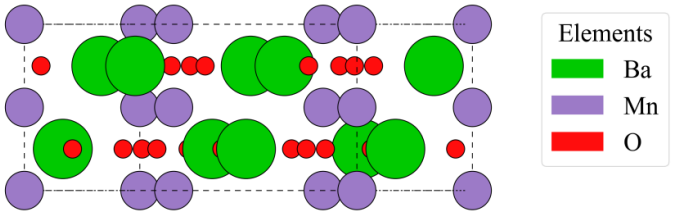
Δ_{max}: (0.333, 0.167, 0.500)

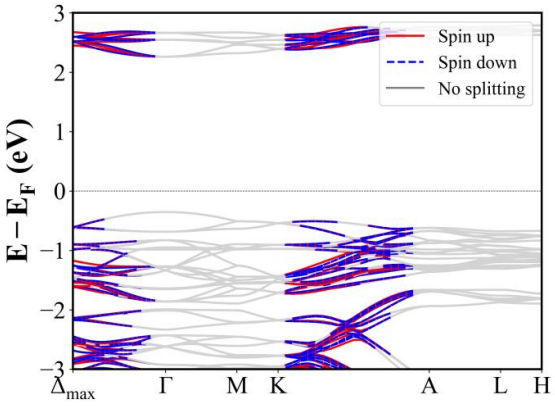


BaMnO3 (P6_3/mmc) | Band Gap = 2.613 eV

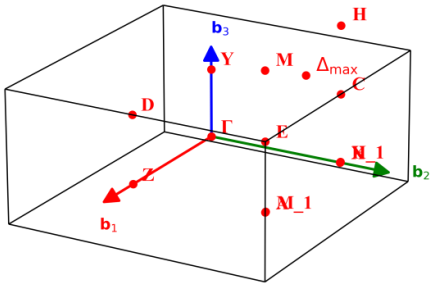


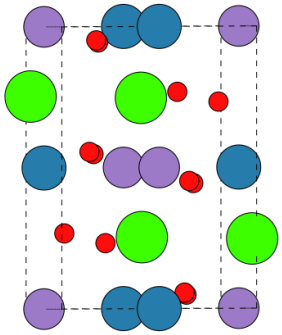
Δ_{max}: (0.333, 0.333, 0.167)

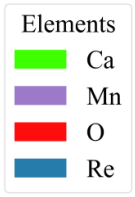




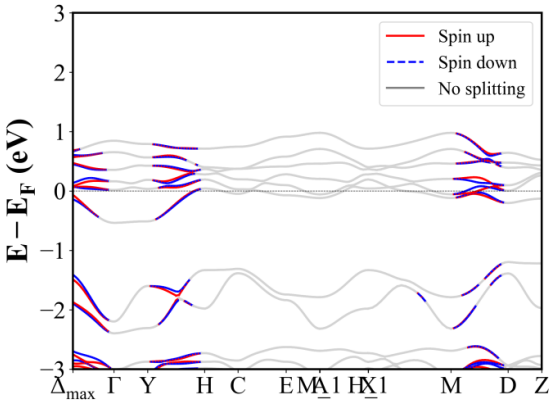
Ca2MnReO6 (P2_1/c) | Band Gap = 0.000 eV



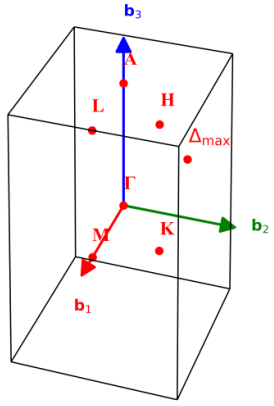


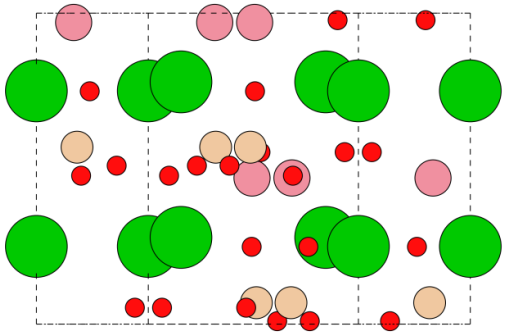


Δ_{max}: (-0.300, 0.200, 0.333)

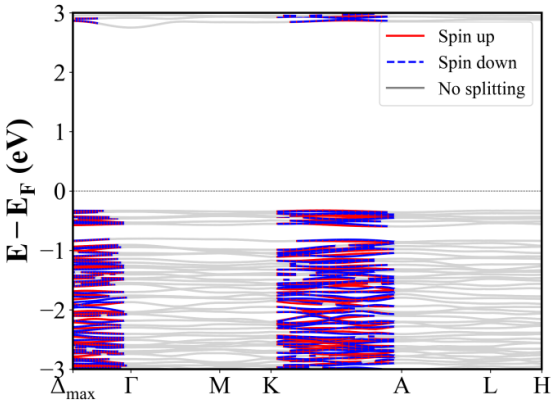


BaCoSiO4 (P6_3) | Band Gap = 3.079 eV

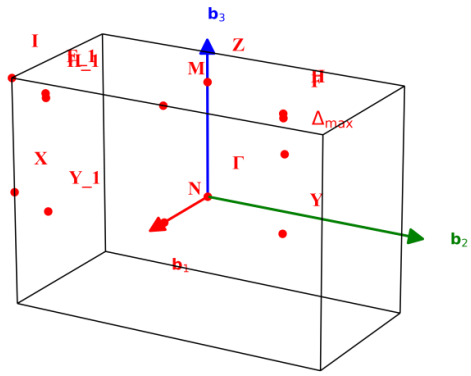


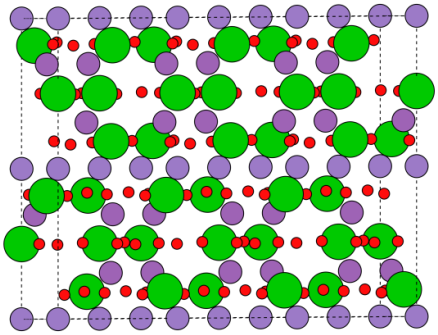


Δ_{max}: (-0.167, 0.333, 0.167)



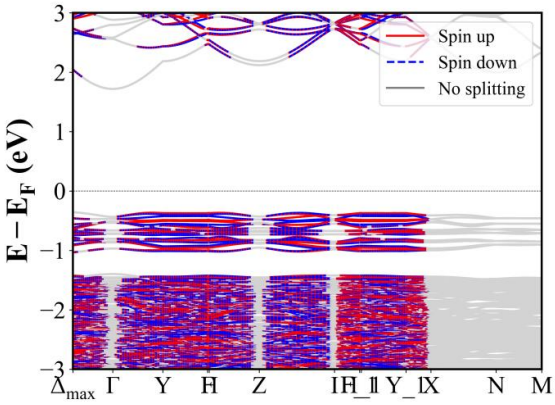
Ba3MnSb2O9 (C2/c) | Band Gap = 2.075 eV



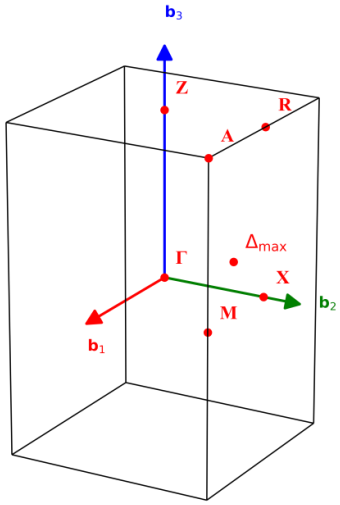


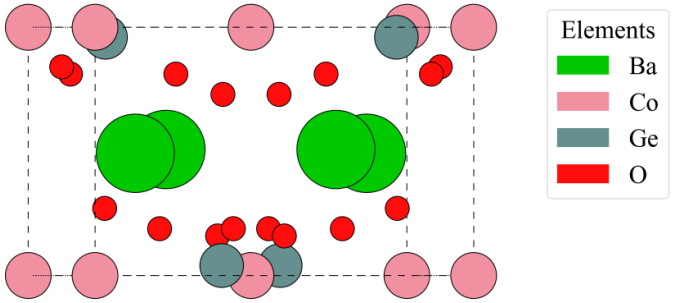


Δ_{max}: (0.000, 0.250, 0.250)

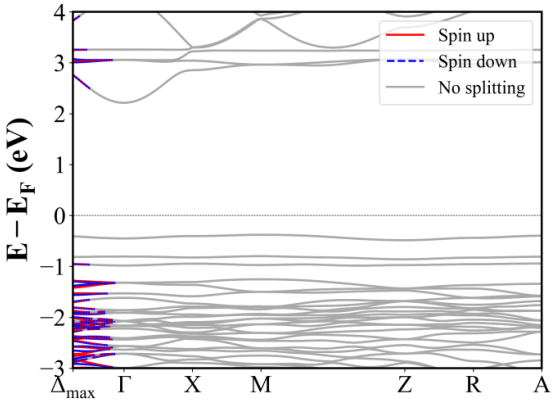


Ba2CoGe2O7 (P-42_1m) | Band Gap = 2.592 eV

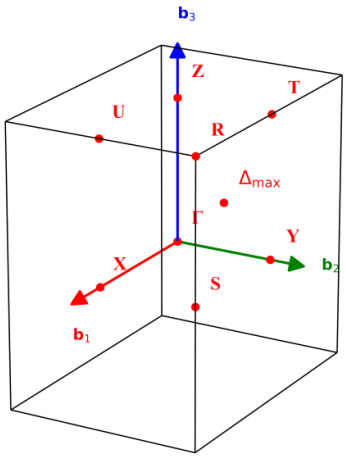


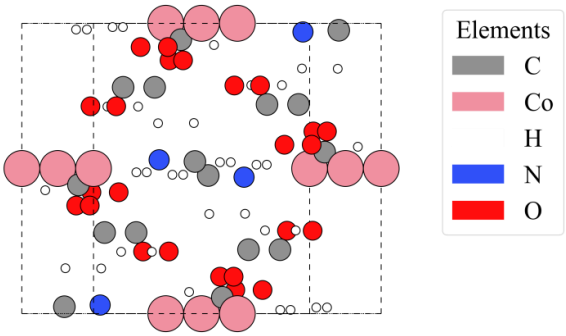


Δ_{max}: (-0.333, 0.167, 0.000)

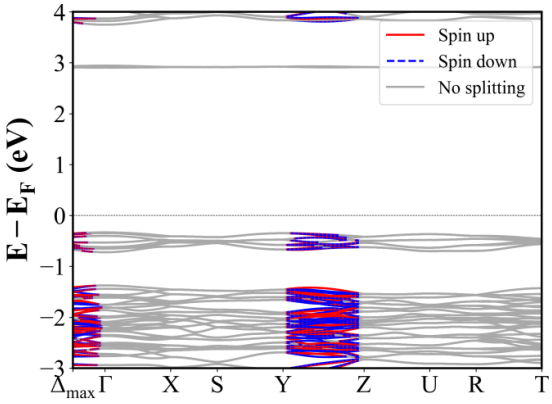


CoH9C4NO6 (Pnma) | Band Gap = 3.236 eV

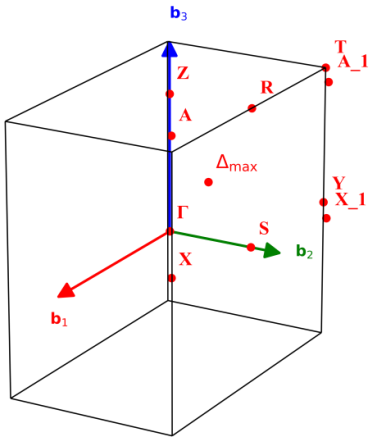


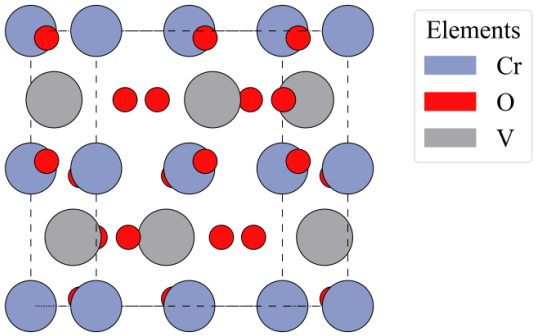


Δ_{max}: (0.000, 0.250, 0.167)

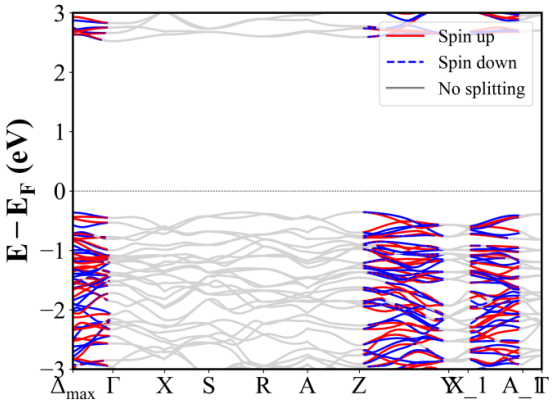


VCrO4 (Cmcm) | Band Gap = 2.877 eV

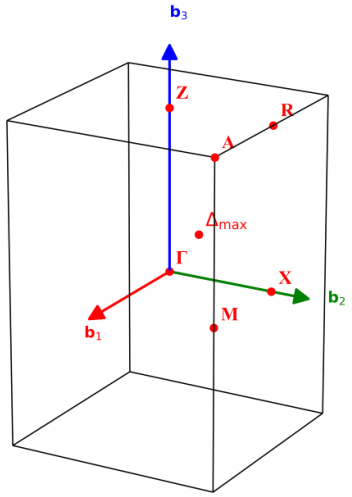


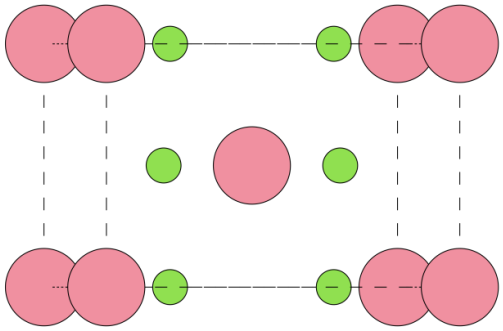


Δ_{max}: (0.100, 0.333, 0.250)

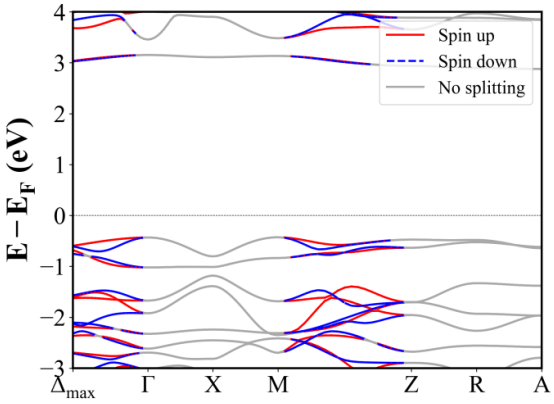


CoF2 (P4_2/mnm) | Band Gap = 3.306 eV

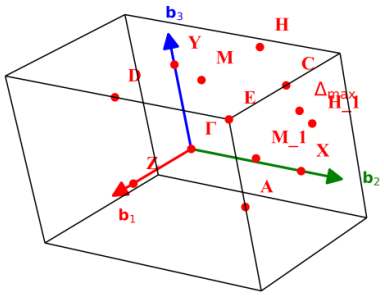


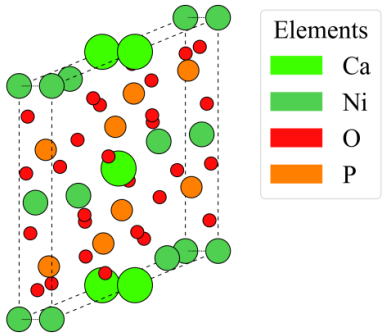


Δ_{max}: (0.333, 0.333, 0.222)

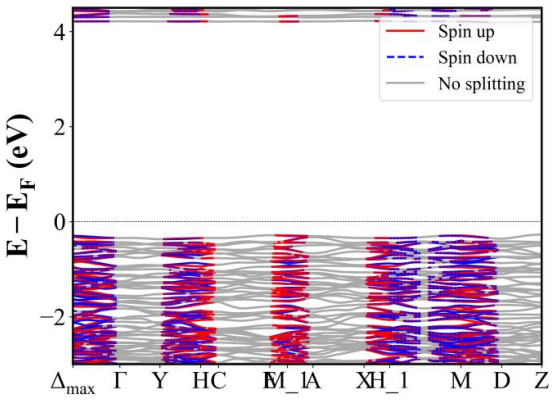


CaNi3(P2O7)2 (P2_1/c) | Band Gap = 4.464 eV

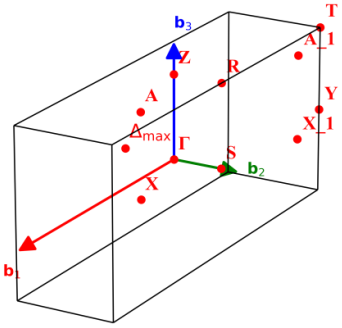


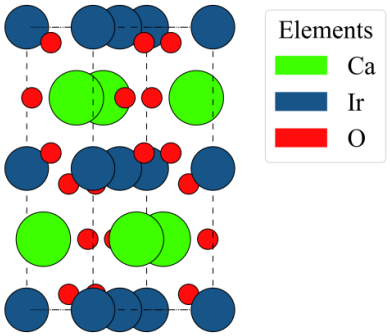


Δ_{max}: (-0.375, 0.333, 0.167)

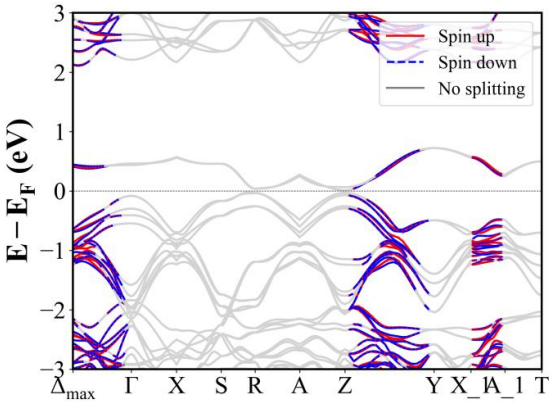


CaIrO3 (Cmcm) | Band Gap = 0.038 eV

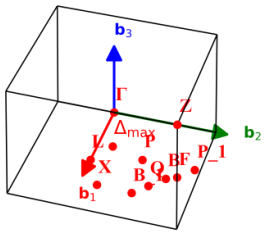


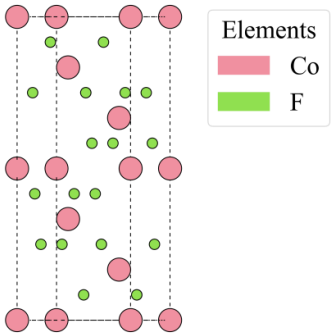


Δ_{max}: (0.333, 0.250, 0.333)

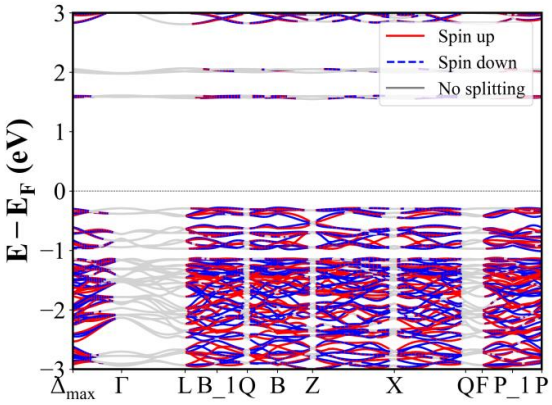


CoF3 (R-3c) | Band Gap = 1.825 eV

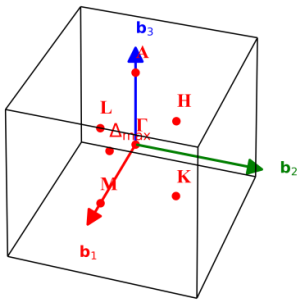


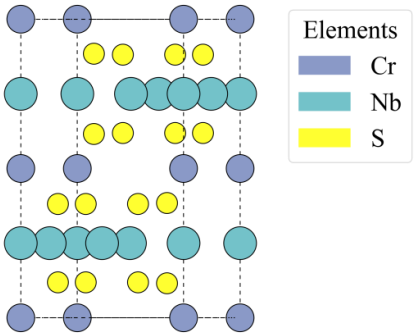


Δ_{max}: (0.333, 0.083, 0.000)

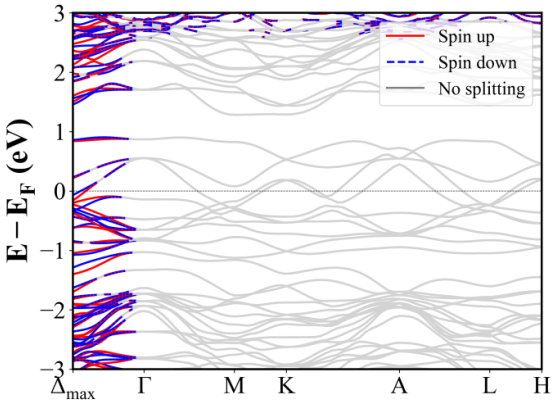


Nb4CrS8 (P6_3/mmc) | Band Gap = 0.000 eV

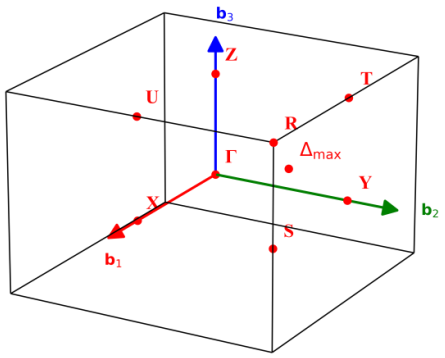


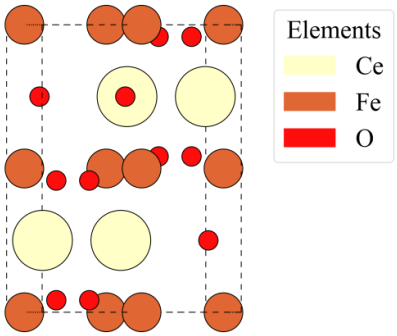


Δ_{max}: (0.375, 0.000, 0.250)

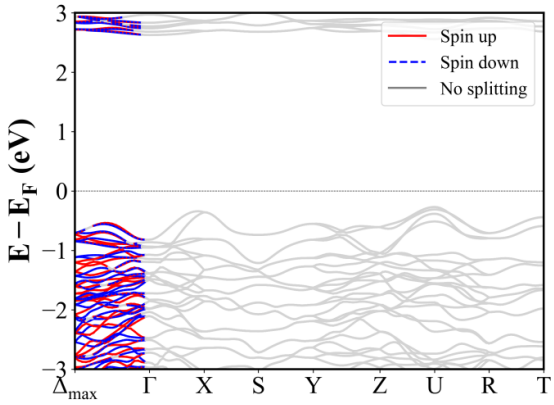


CeFeO3 (Pnma) | Band Gap = 2.825 eV

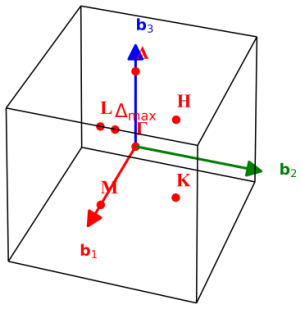


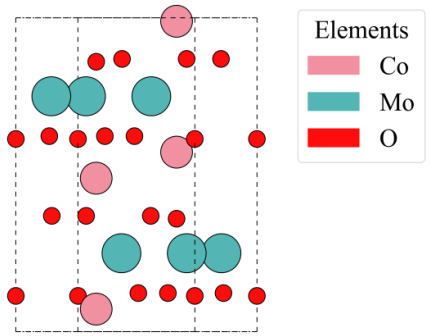


Δ_{max}: (0.400, 0.500, 0.333)

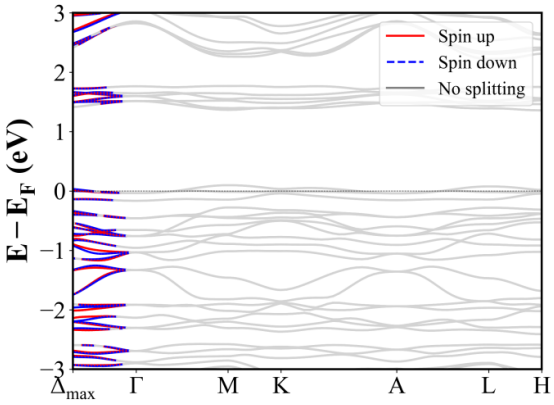


Co2Mo3O8 (P6_3mc) | Band Gap = 0.000 eV

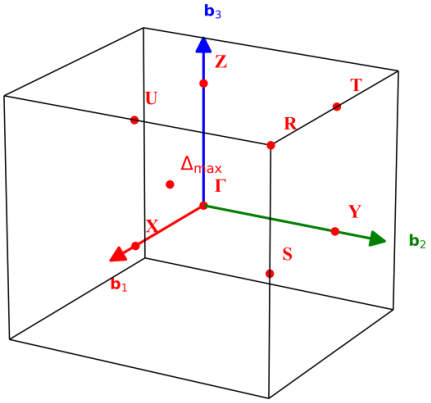


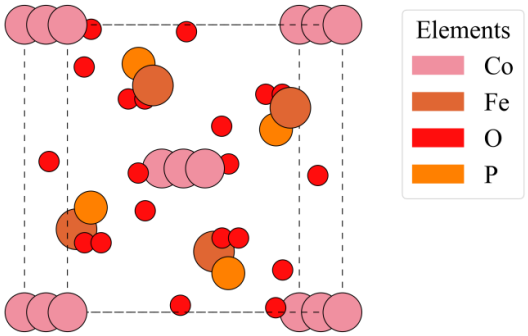


Δ_{max}: (0.300, 0.000, 0.333)

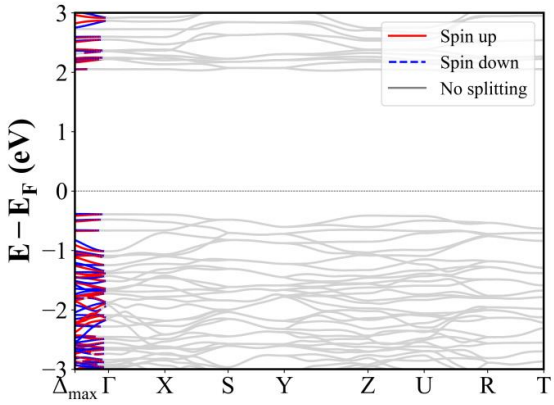


FeCoPO5 (Pnma) | Band Gap = 2.399 eV

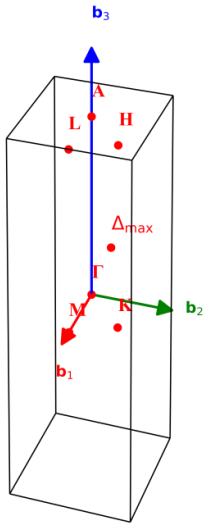




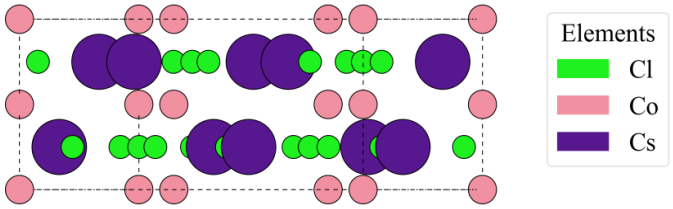
Δ_{max}: (0.250, 0.000, 0.167)

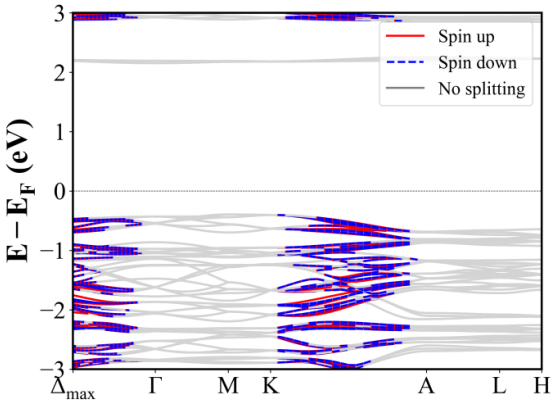


CsCoCl3 (P6_3/mmc) | Band Gap = 2.546 eV

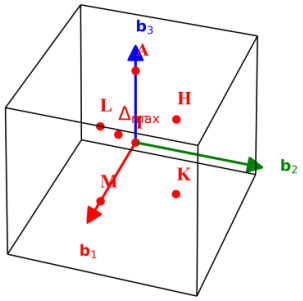


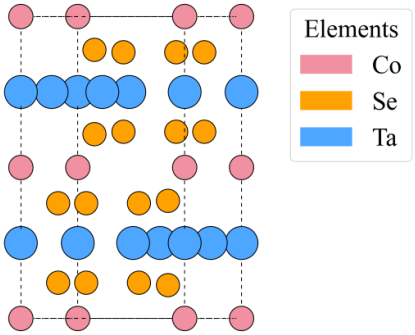
Δ_{max}: (0.250, 0.250, 0.200)



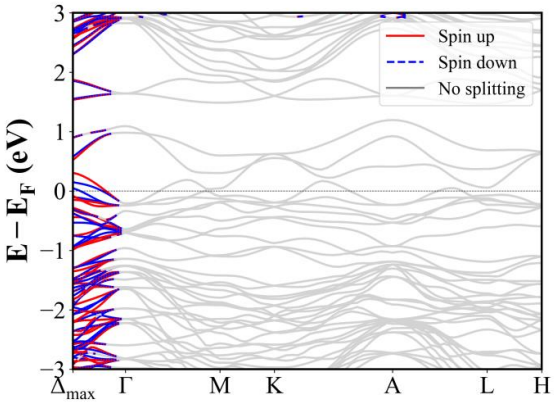


Ta4CoSe8 (P6_3/mmc) | Band Gap = 0.000 eV

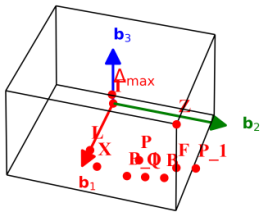


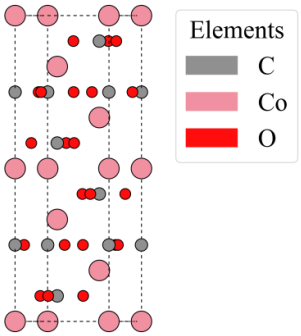


Δ_{max}: (0.250, 0.000, 0.250)

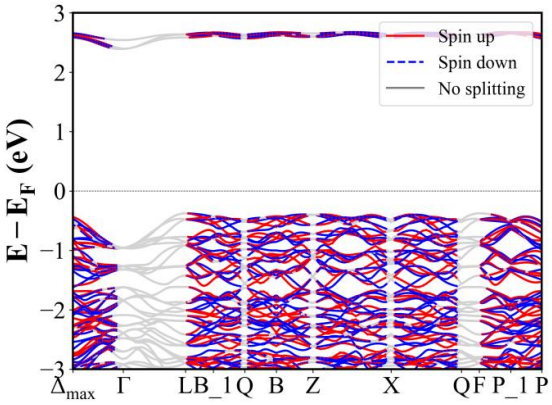


CoCO3 (R-3c) | Band Gap = 2.766 eV

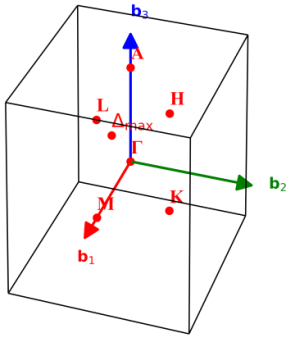


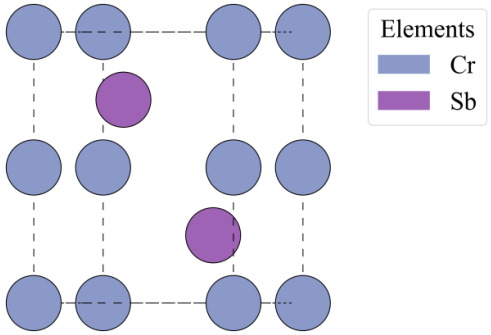


Δ_{max}: (0.333, 0.083, 0.500)

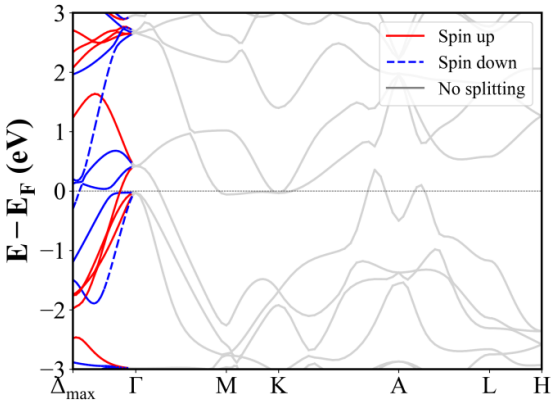


CrSb (P6_3/mmc) | Band Gap = 0.000 eV

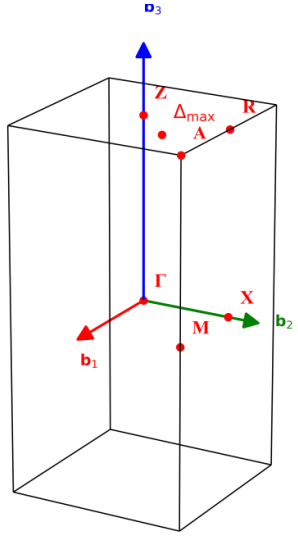




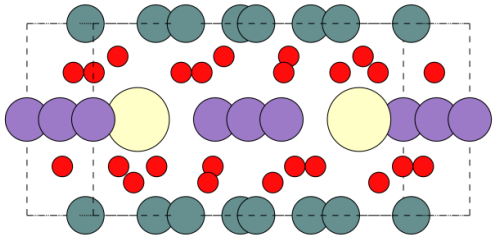
Δ_{max}: (0.286, 0.000, 0.300)

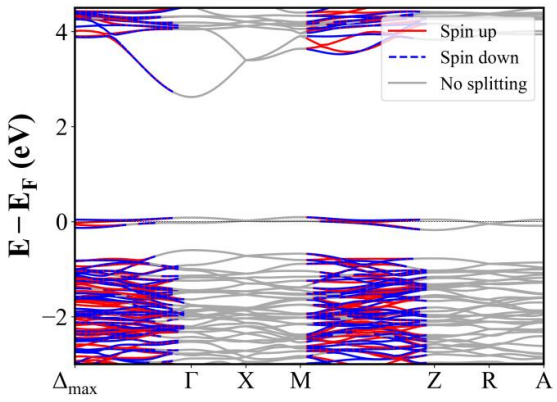


CeMn2(GeO3)4 (P4/nbm) | Band Gap = 0.000 eV

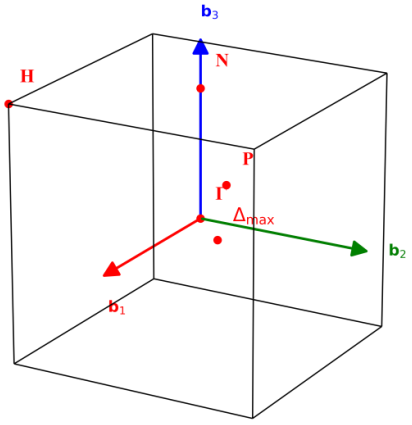


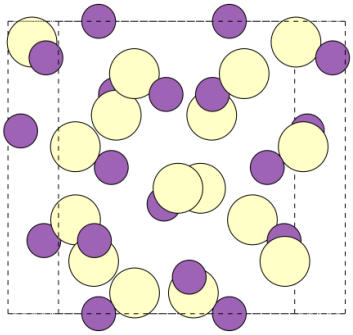
Δ_{max}: (0.250, 0.250, 0.500)



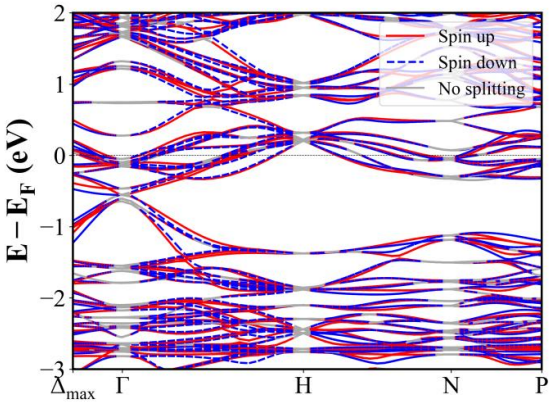


Ce4Sb3 (I-43d) | Band Gap = 0.000 eV

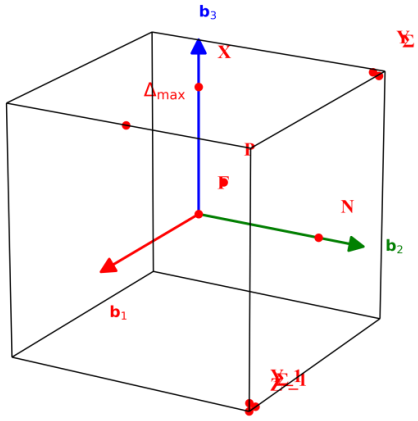


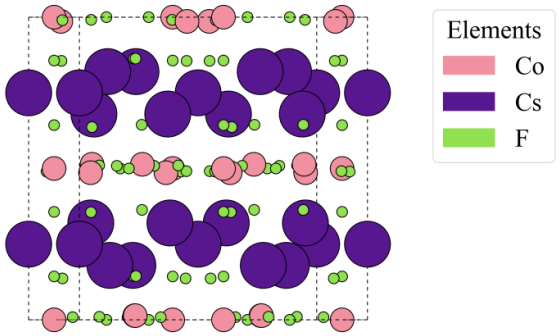


Δ_{max}: (0.167, 0.167, 0.000)

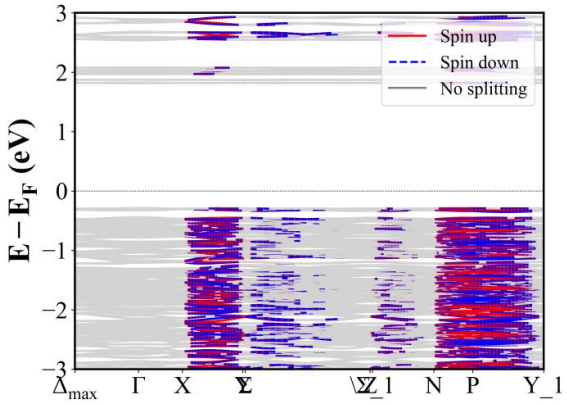


CsCoF4 (I-4c2) | Band Gap = 2.099 eV

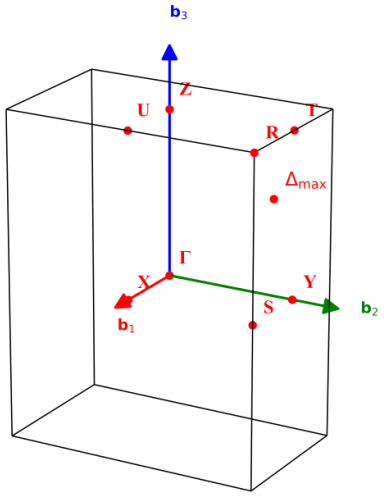


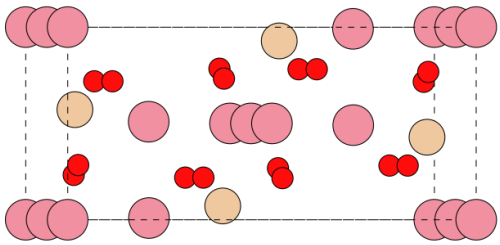


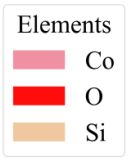
Δ_{max}: (0.500, 0.000, 0.500)



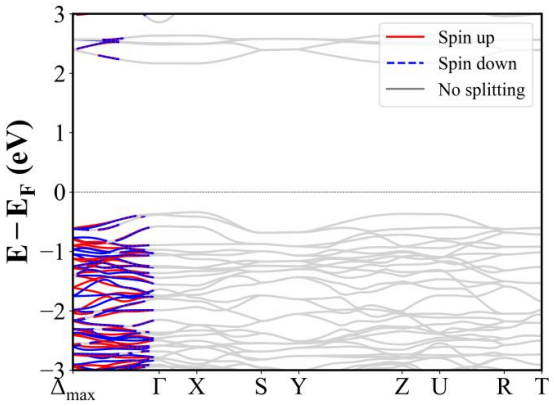
Co2SiO4 (Pnma) | Band Gap = 2.505 eV



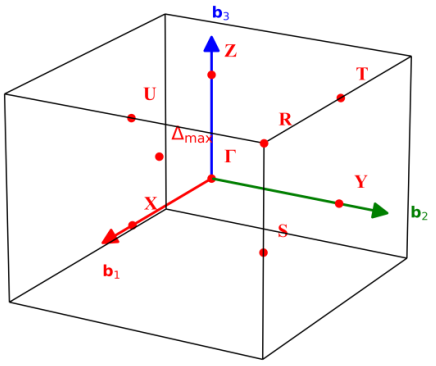


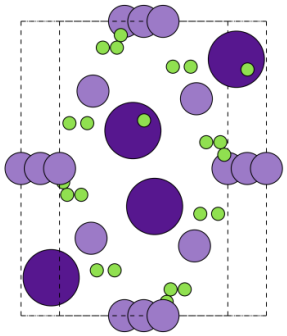


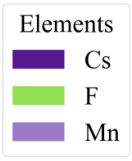
Δ_{max}: (0.250, 0.500, 0.333)



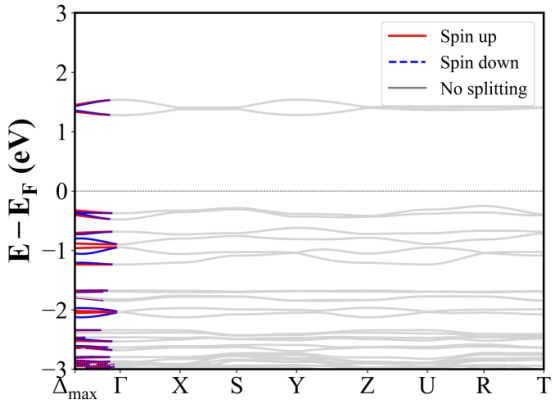
CsMn2F6 (Pnma) | Band Gap = 1.529 eV



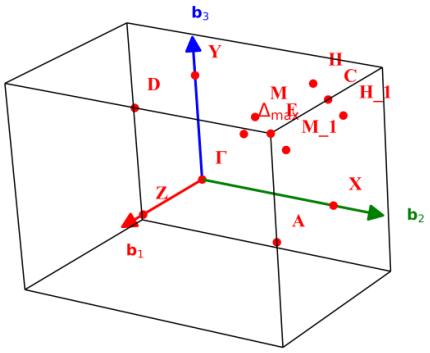


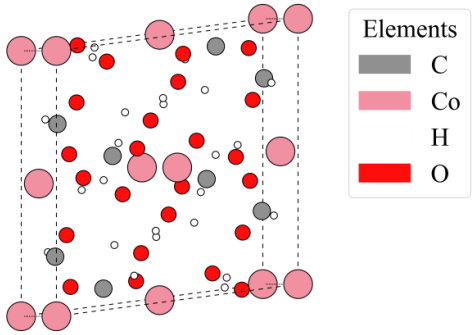


Δ_{max}: (0.333, 0.000, 0.250)

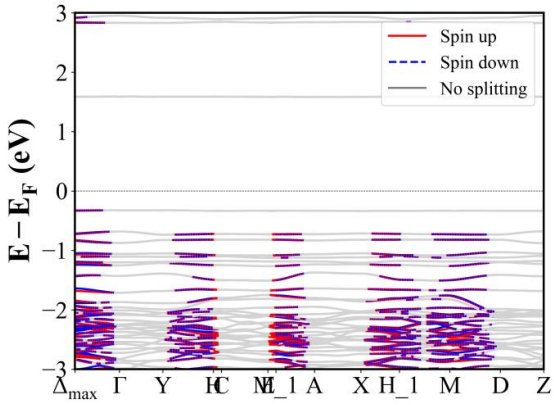


CoH6(CO3)2 (P2_1/c) | Band Gap = 1.908 eV

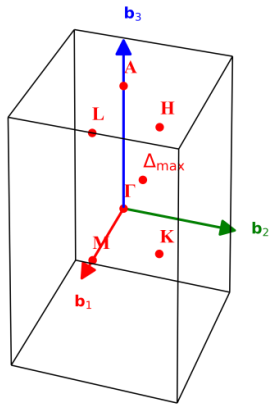


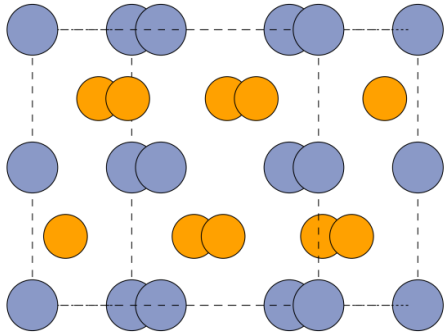


Δ_{max}: (0.167, 0.250, 0.333)

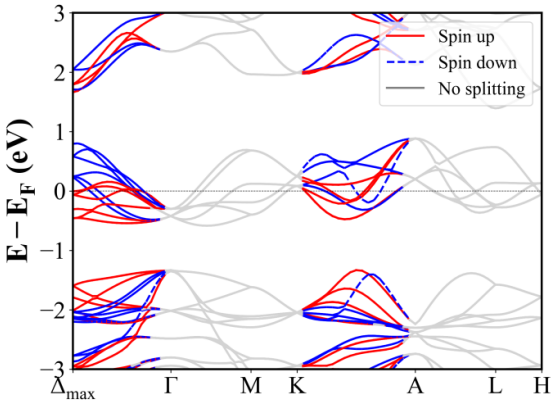


CrSe (P6_3/mmc) | Band Gap = 0.000 eV

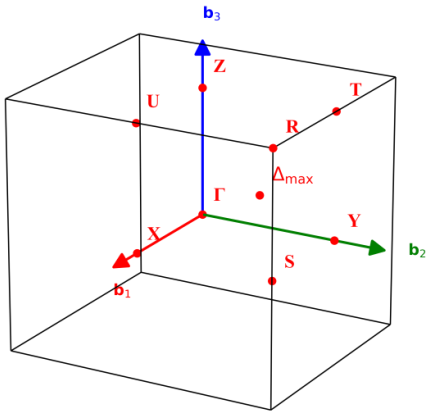


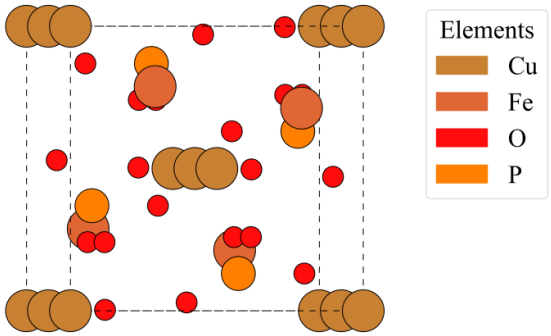


Δ_{max}: (0.375, 0.250, 0.300)

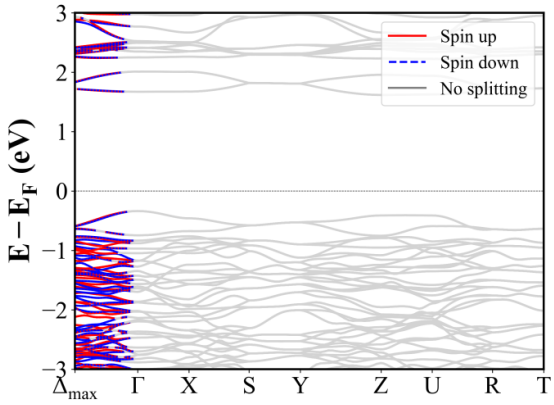


FeCuPO5 (Pnma) | Band Gap = 1.955 eV

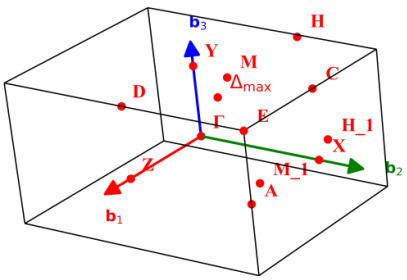


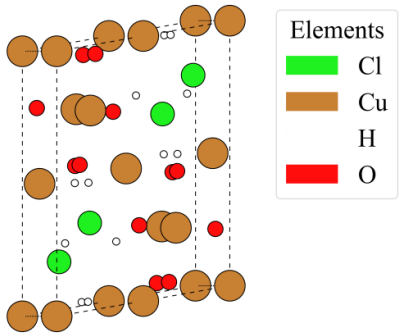


Δ_{max}: (0.333, 0.375, 0.250)

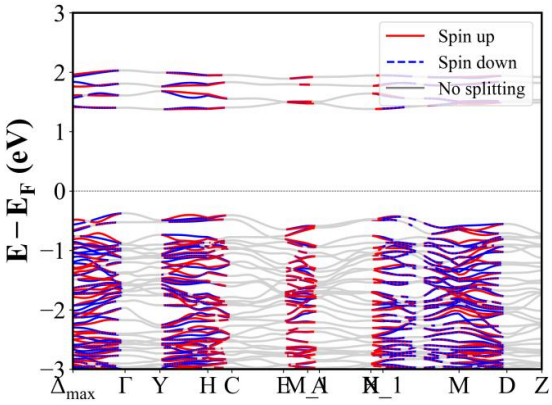


Cu2H3ClO3 (P2_1/c) | Band Gap = 1.749 eV

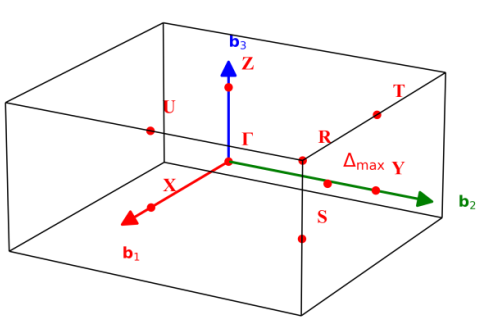


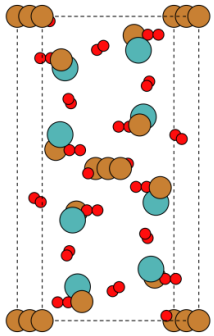


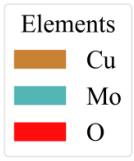
Δ_{max}: (0.250, 0.250, 0.500)



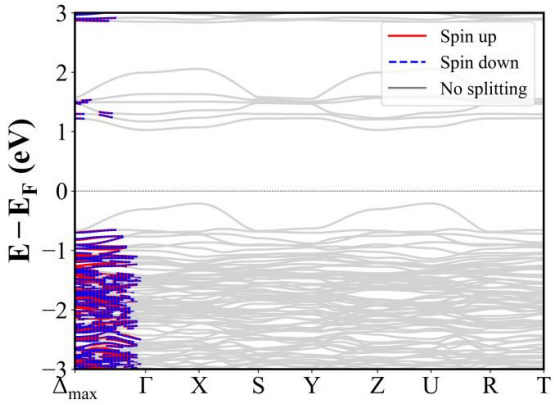
Cu3Mo2O9 (Pnma) | Band Gap = 1.236 eV



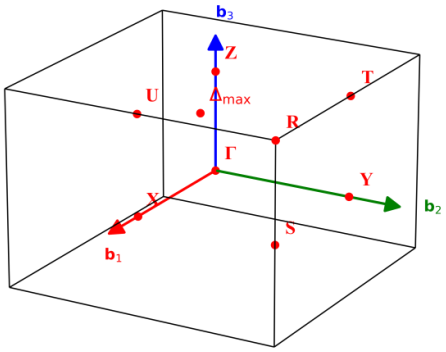


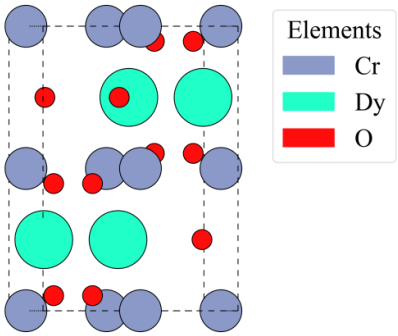


Δ_{max}: (0.333, 0.500, 0.250)

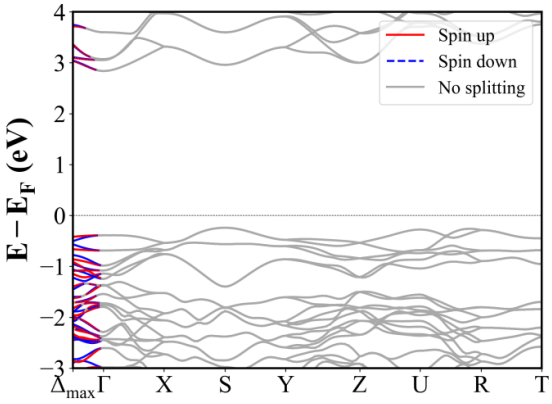


DyCrO3 (Pnma) | Band Gap = 3.079 eV

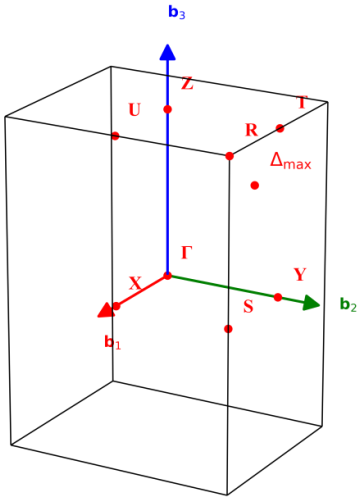


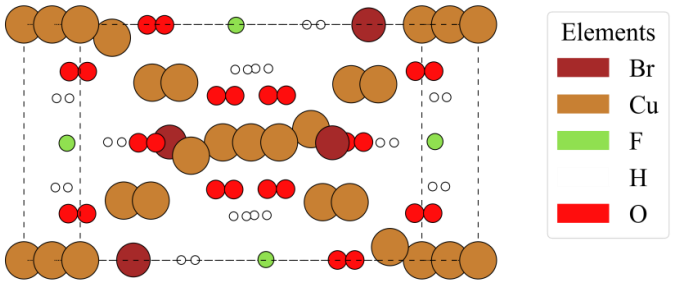


Δ_{max}: (0.100, 0.000, 0.333)

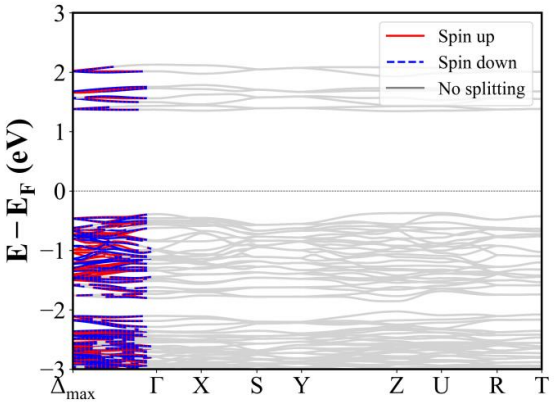


Cu4H6BrO6F (Pnma) | Band Gap = 1.714 eV

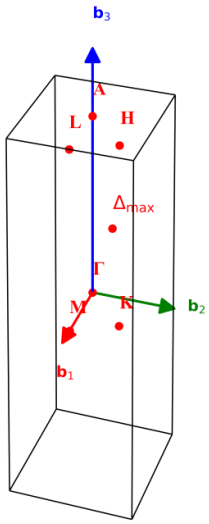




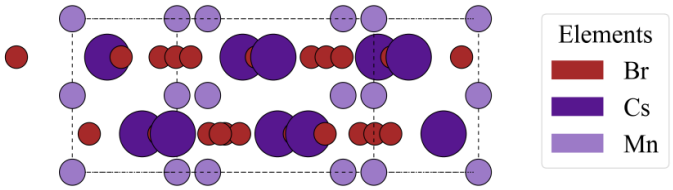
Δ_{max}: (0.250, 0.500, 0.375)

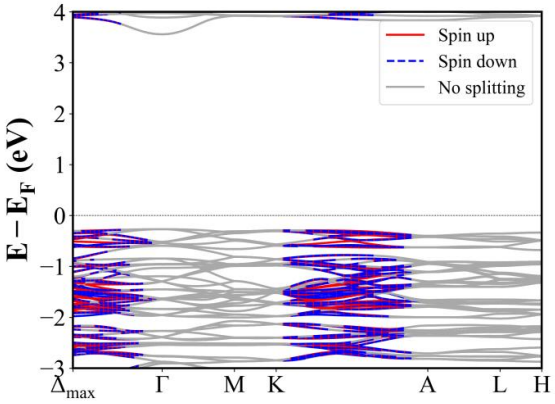


CsMnBr3 (P6_3/mmc) | Band Gap = 3.828 eV

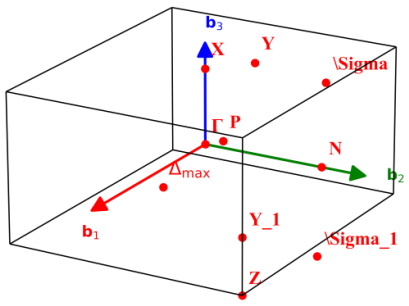


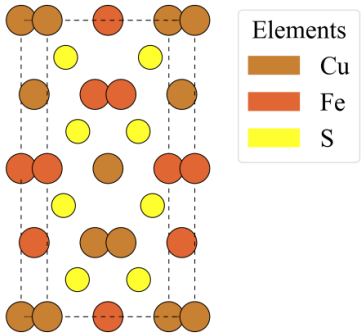
Δ_{max}: (0.250, 0.250, 0.250)



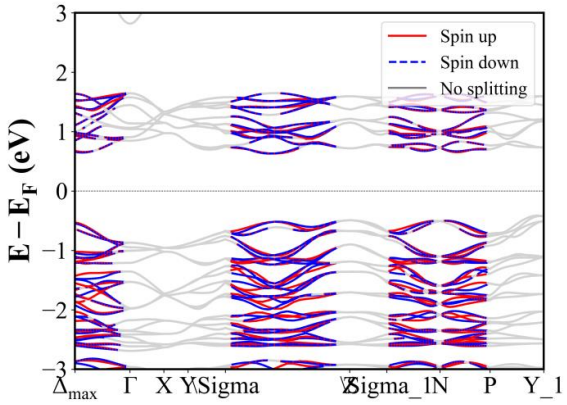


FeCuS2 (I-42d) | Band Gap = 1.043 eV

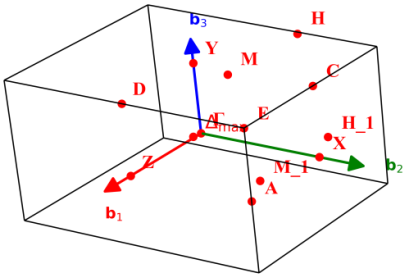


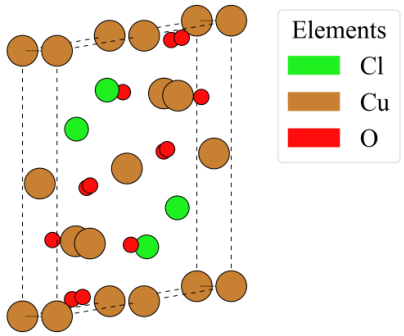


Δ_{max}: (0.400, 0.100, 0.000)

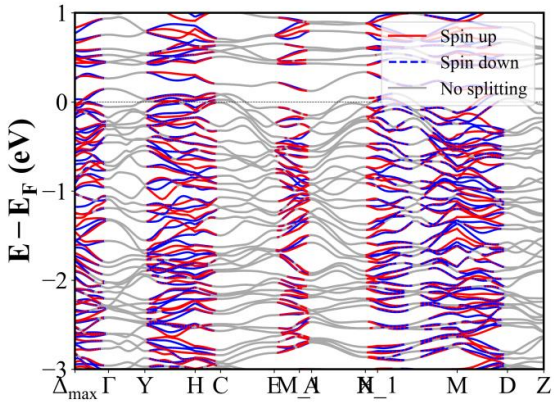


Cu2ClO3 (P2_1/c) | Band Gap = 0.000 eV

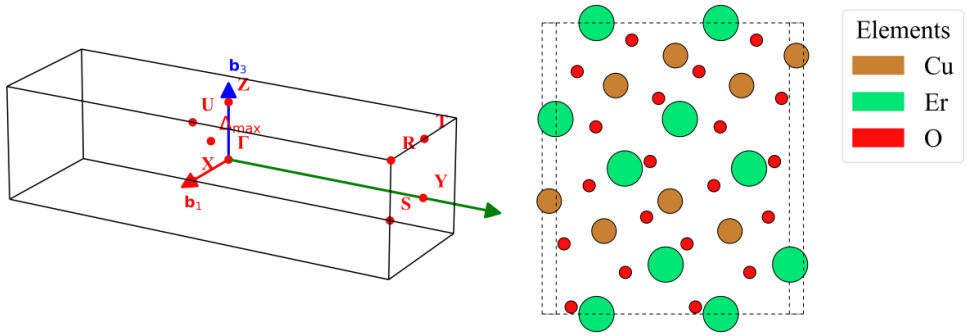




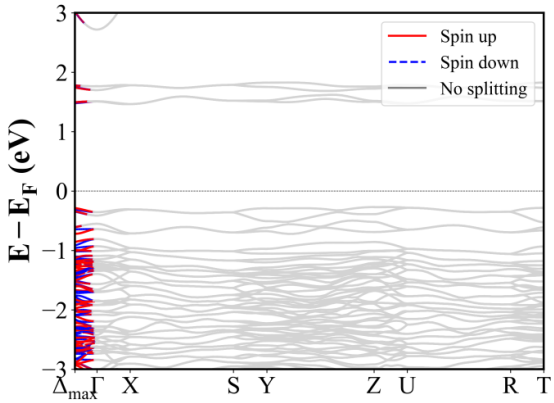
Δ_{max}: (0.250, 0.125, 0.167)



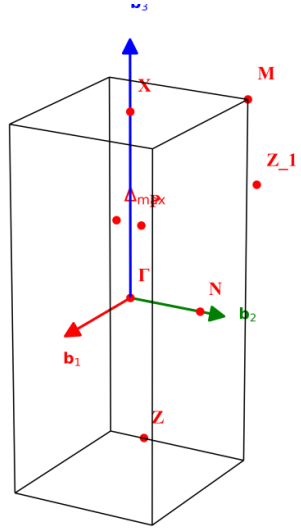
Er2Cu2O5 (Pna2_1) | Band Gap = 1.732 eV



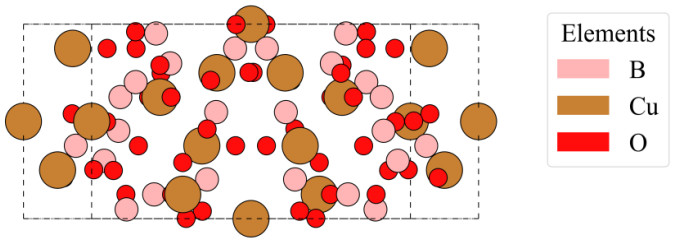
Δ_{max}: (0.250, 0.000, 0.250)

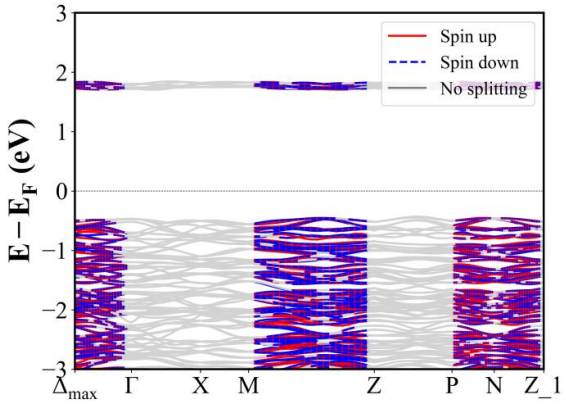


Cu(BO2)2 (I-42d) | Band Gap = 2.137 eV

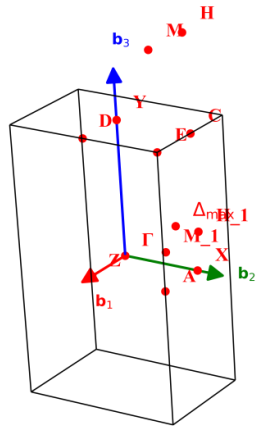


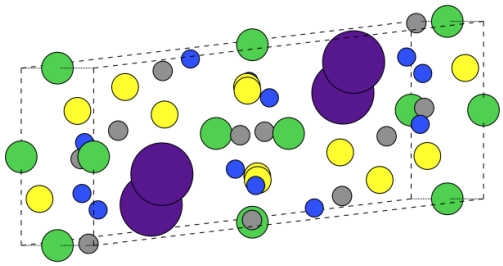
Δ_{max}: (0.500, 0.250, 0.300)

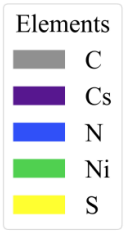




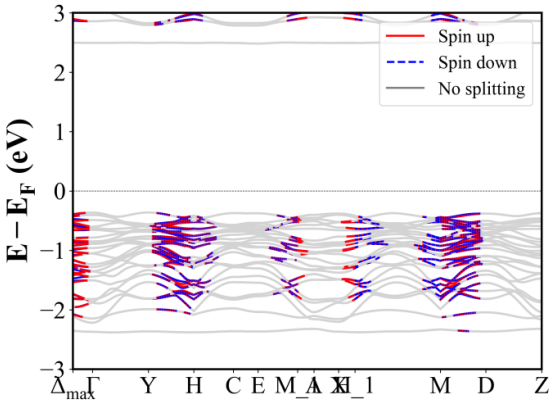
CsNiC3(SN)3 (P2_1/c) | Band Gap = 2.843 eV



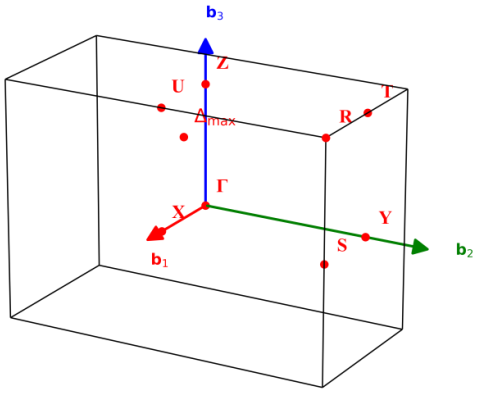


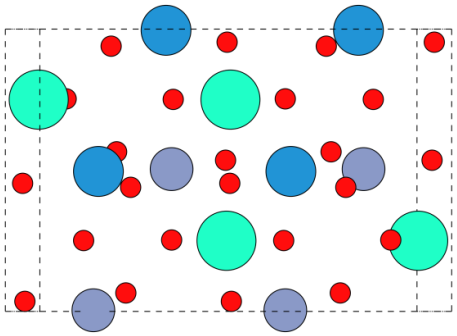


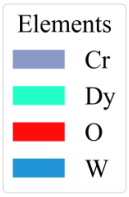
Δ_{max}: (-0.250, 0.250, 0.100)



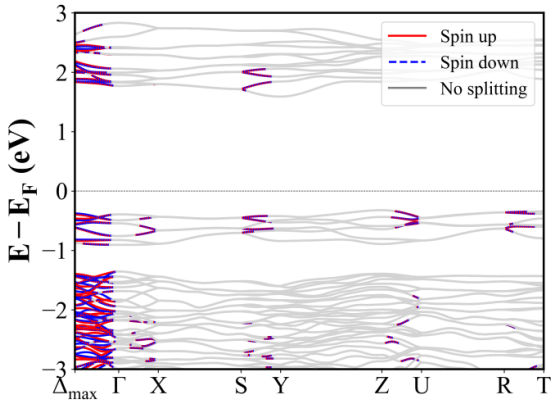
DyCrWO6 (Pna2_1) | Band Gap = 1.912 eV



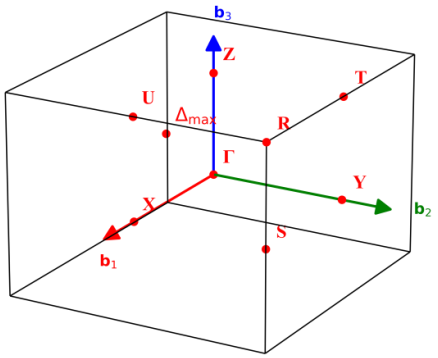


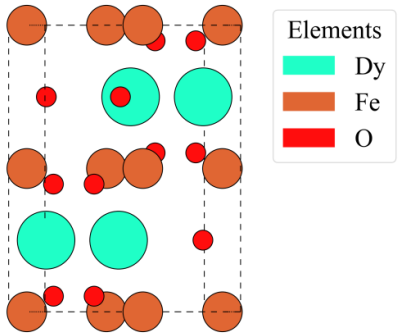


Δ_{max}: (0.250, 0.000, 0.333)

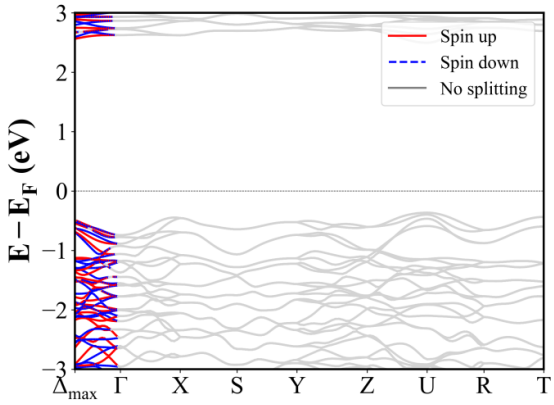


DyFeO3 (Pnma) | Band Gap = 2.861 eV

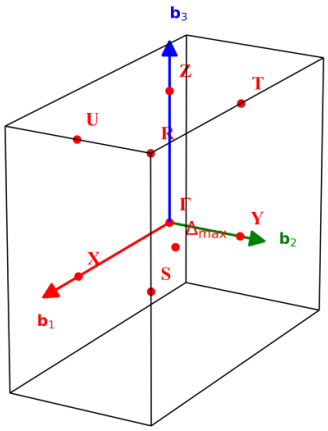


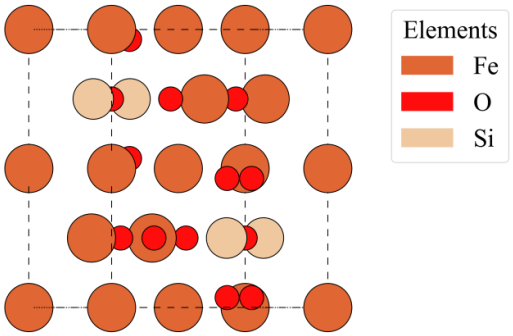


Δ_{max}: (0.300, 0.000, 0.333)

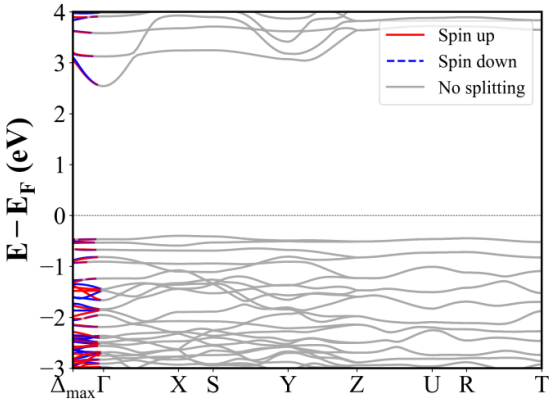


Fe2SiO4 (Pnma) | Band Gap = 2.940 eV

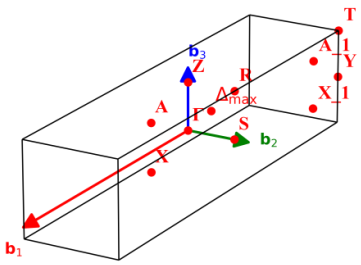


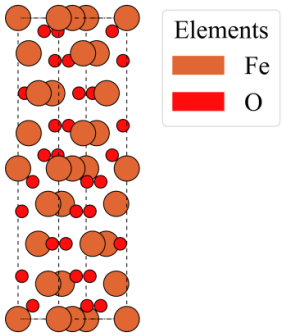


Δ_{max}: (0.167, 0.250, 0.000)

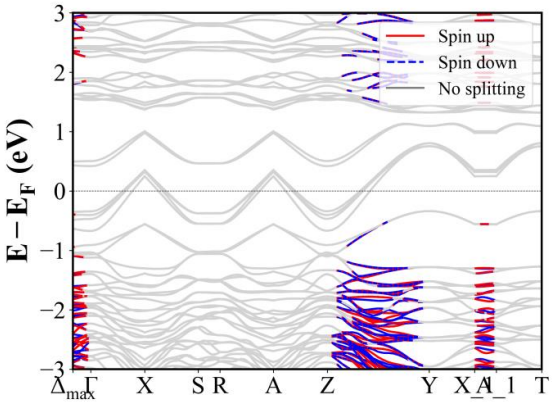


Fe4O5 (Cmcm) | Band Gap = 0.000 eV

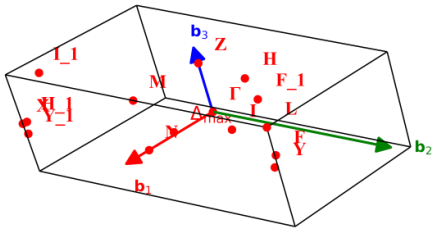


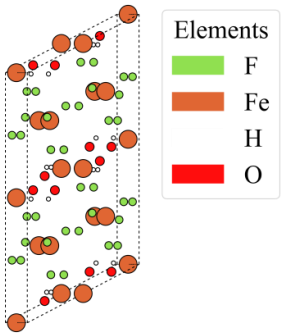


Δ_{max}: (0.000, 0.250, 0.250)

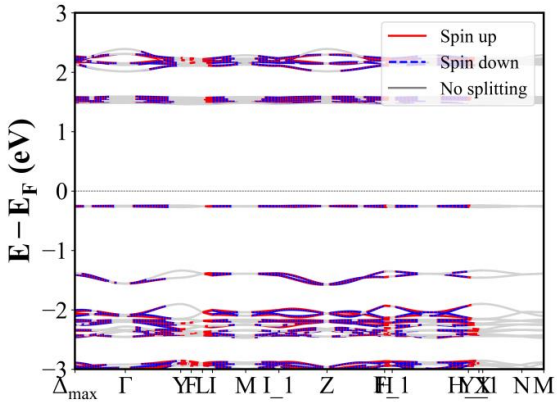


Fe3H4(OF4)2 (C2/m) | Band Gap = 1.706 eV

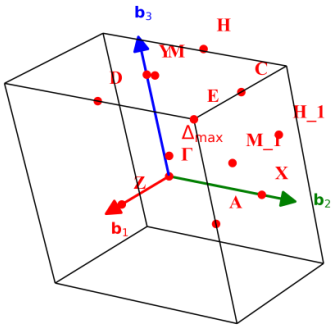


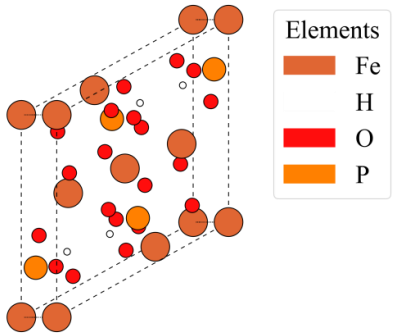


Δ_{max}: (0.500, 0.125, 0.250)

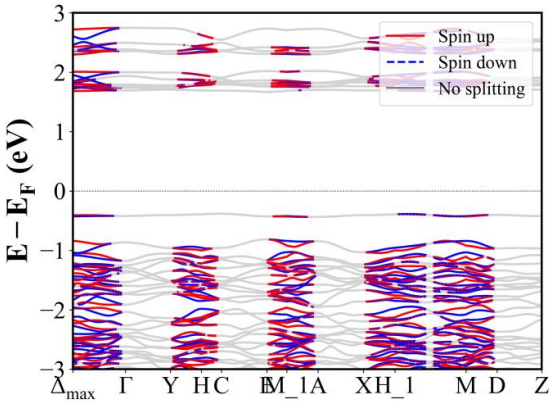


Fe3P2(HO5)2 (P2_1/c) | Band Gap = 2.051 eV

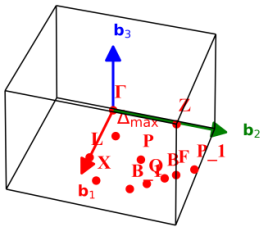


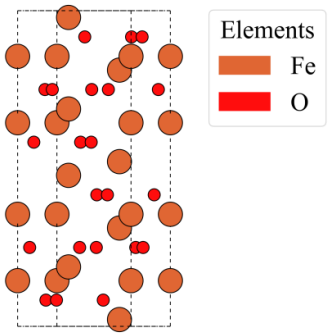


Δ_{max}: (0.375, 0.250, 0.250)

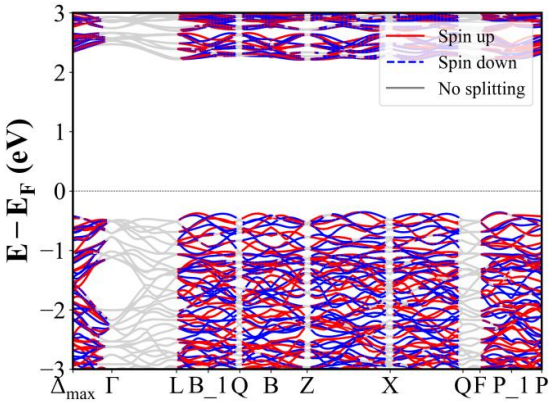


Fe2O3 (R-3c) | Band Gap = 2.566 eV

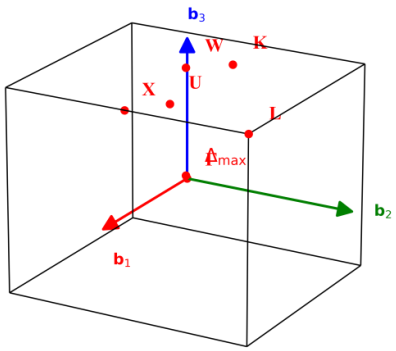


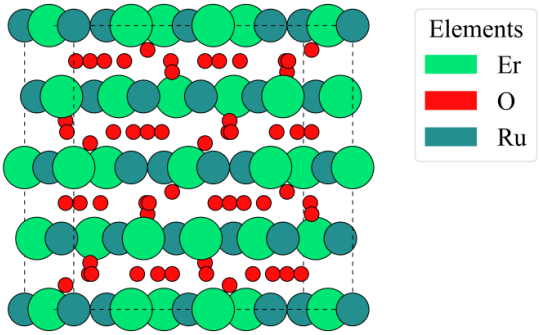


Δ_{max}: (0.250, 0.083, 0.000)

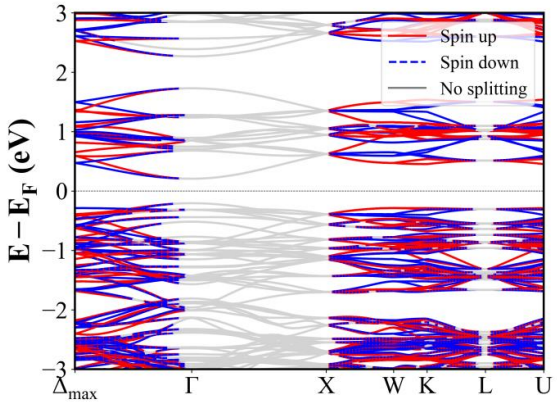


Er2Ru2O7 (Fd-3m) | Band Gap = 0.412 eV

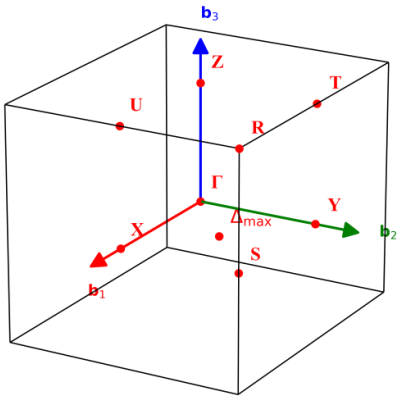


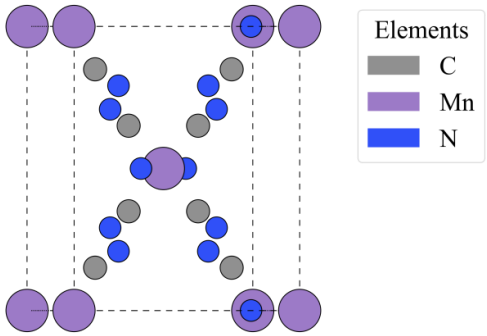


Δ_{max}: (0.500, 0.250, 0.250)

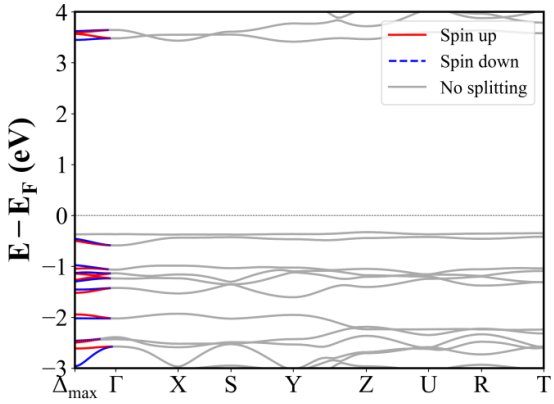


Mn(C2N3)2 (Pnnm) | Band Gap = 3.742 eV

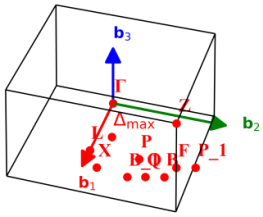


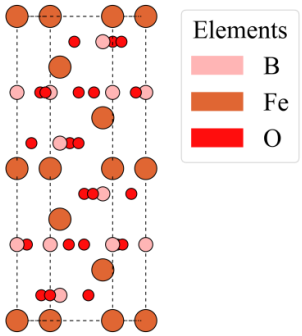


Δ_{max}: (0.250, 0.250, 0.000)

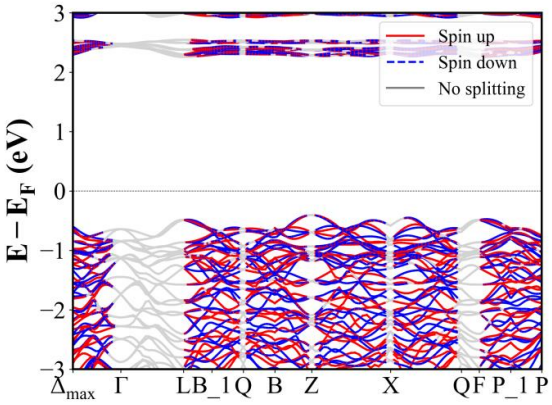


FeBO3 (R-3c) | Band Gap = 2.660 eV

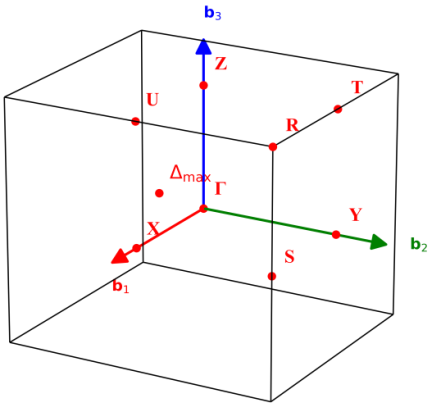


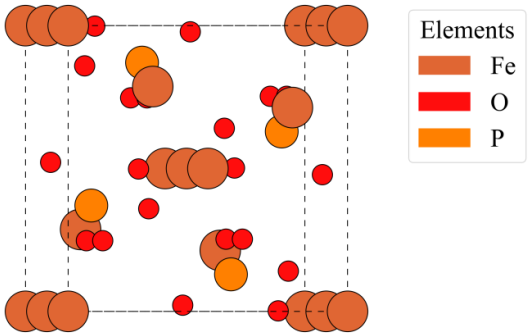


Δ_{max}: (0.333, 0.083, 0.000)

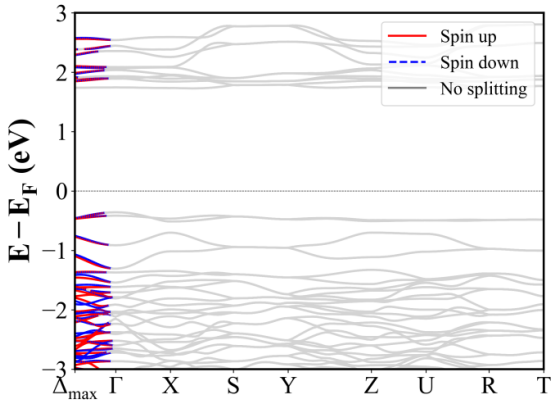


Fe2PO5 (Pnma) | Band Gap = 2.086 eV

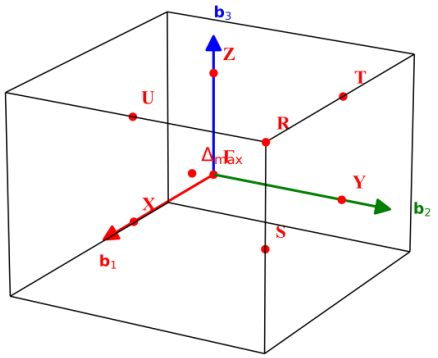


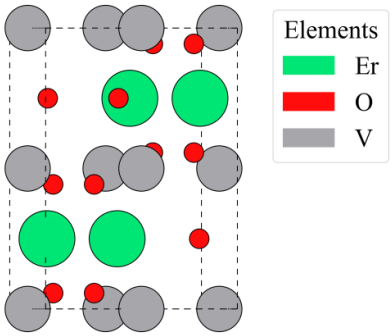


Δ_{max}: (0.333, 0.000, 0.167)

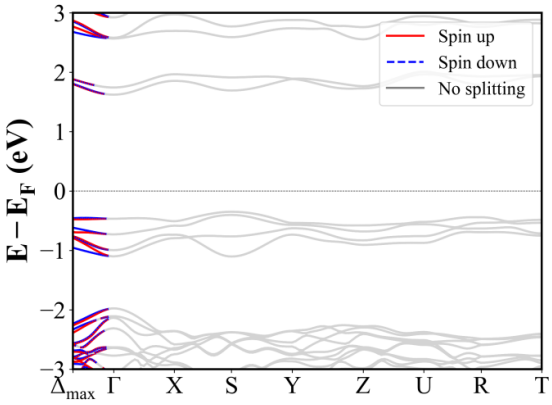


ErVO3 (Pnma) | Band Gap = 1.971 eV

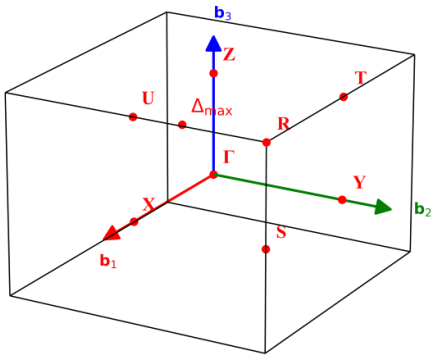


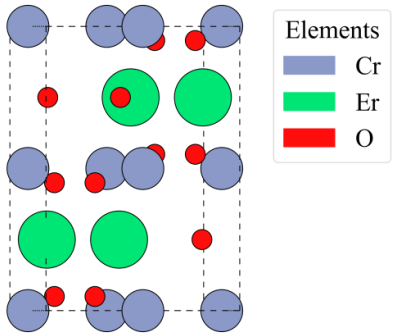


Δ_{max}: (0.300, 0.100, 0.167)

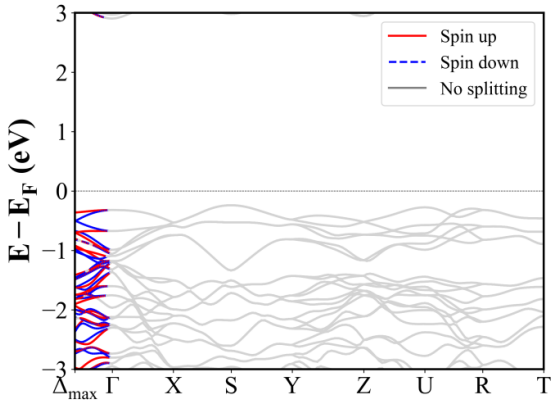


ErCrO3 (Pnma) | Band Gap = 3.143 eV

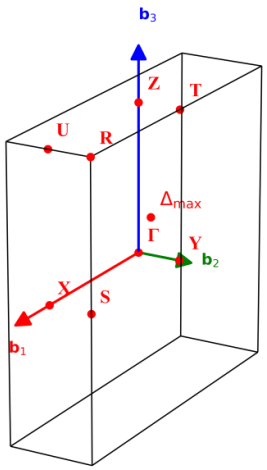


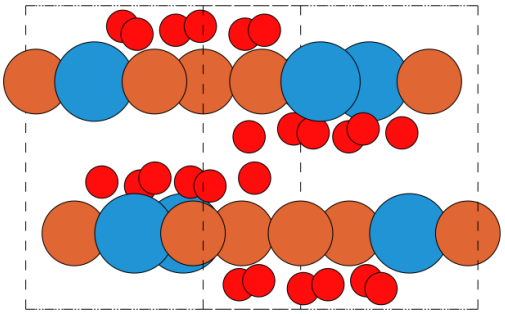


Δ_{max}: (0.200, 0.000, 0.333)

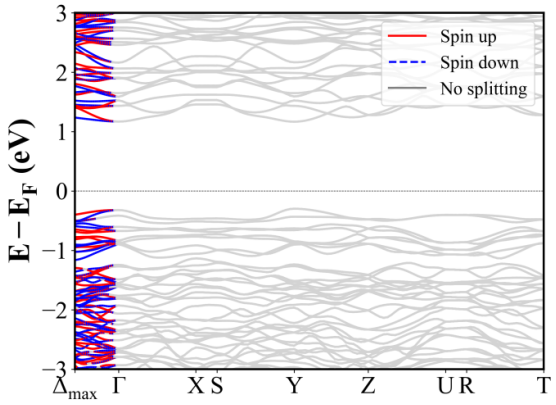


Fe2WO6 (Pbcn) | Band Gap = 1.465 eV

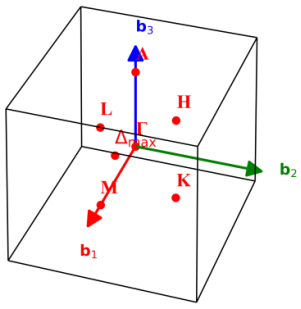


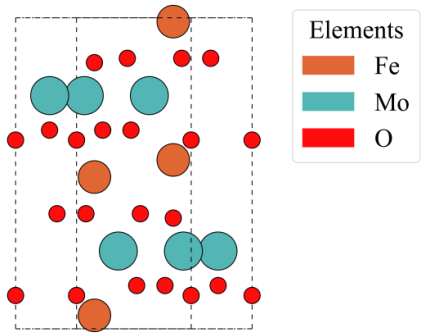


Δ_{max}: (0.167, 0.500, 0.200)

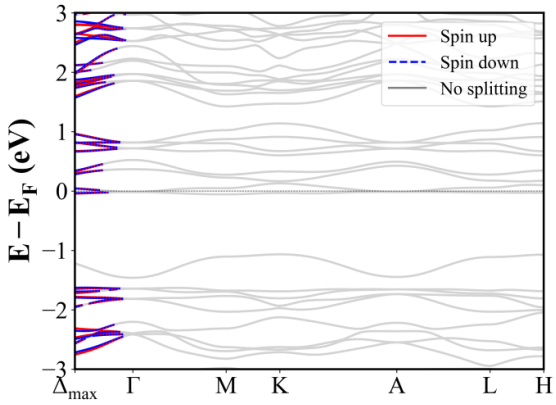


Fe2Mo3O8 (P6_3mc) | Band Gap = 0.000 eV

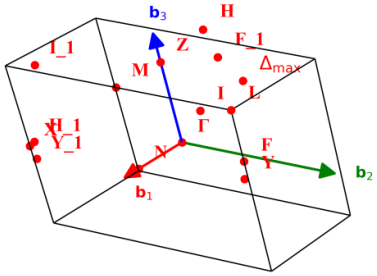


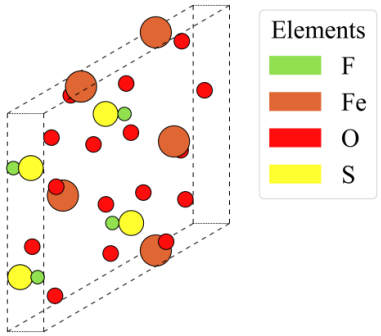


Δ_{max}: (0.300, 0.000, 0.167)

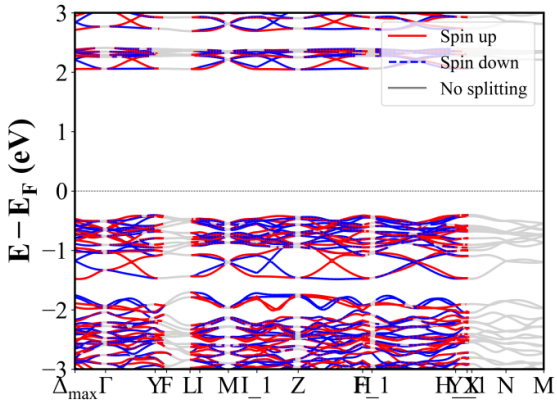


FeSO4F (C2/c) | Band Gap = 2.451 eV

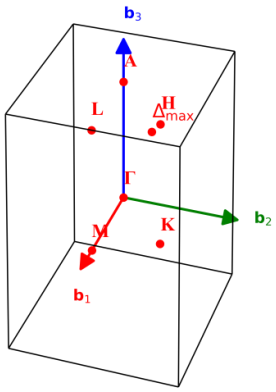


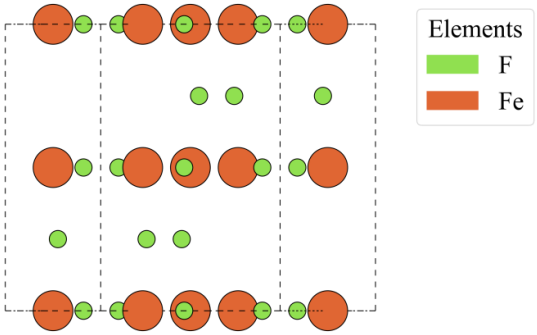


Δ_{max}: (-0.250, 0.250, 0.375)

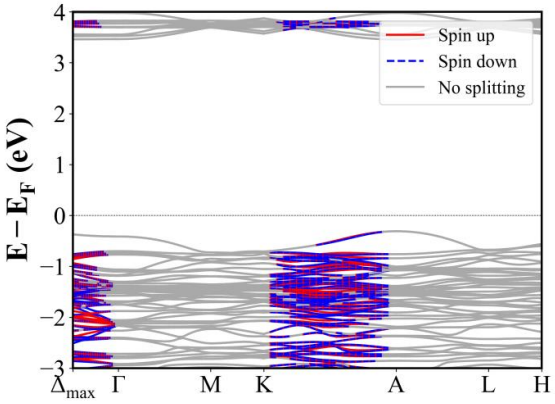


FeF3 (P6_3/m) | Band Gap = 3.764 eV

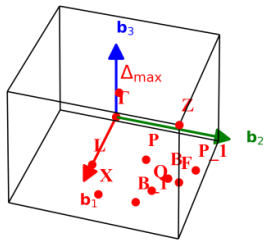


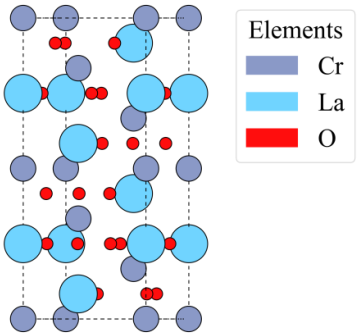


Δ_{max}: (-0.125, 0.125, 0.250)

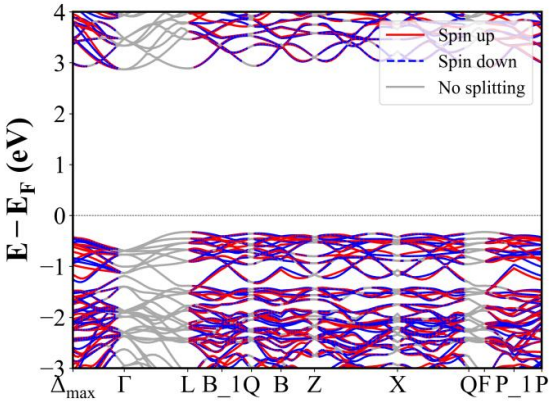


LaCrO3 (R-3c) | Band Gap = 3.194 eV

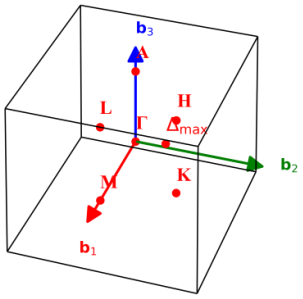


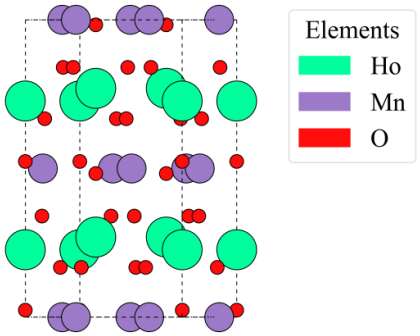


Δ_{max}: (0.300, 0.100, 0.500)

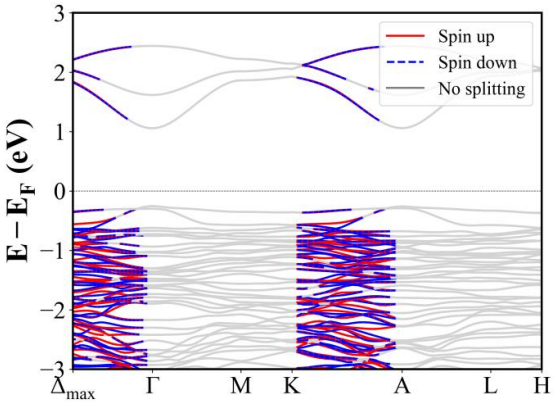


HoMnO3 (P6_3cm) | Band Gap = 1.310 eV

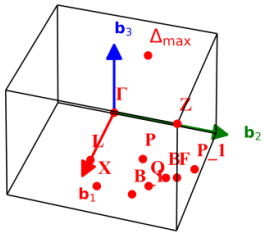


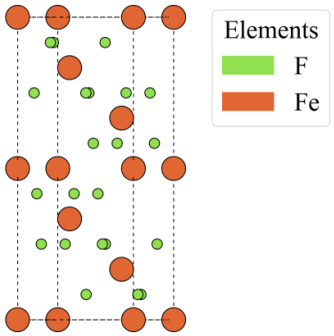


Δ_{max}: (0.250, 0.250, 0.250)

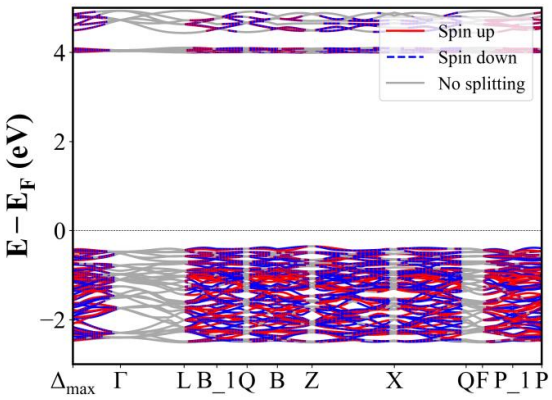


FeF3 (R-3c) | Band Gap = 4.342 eV

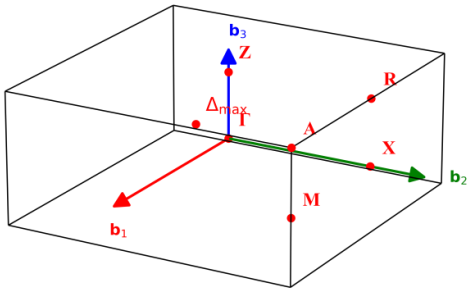


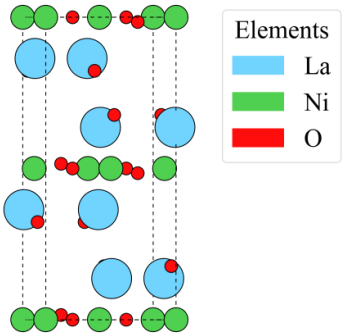


Δ_{max}: (-0.400, 0.100, 0.250)

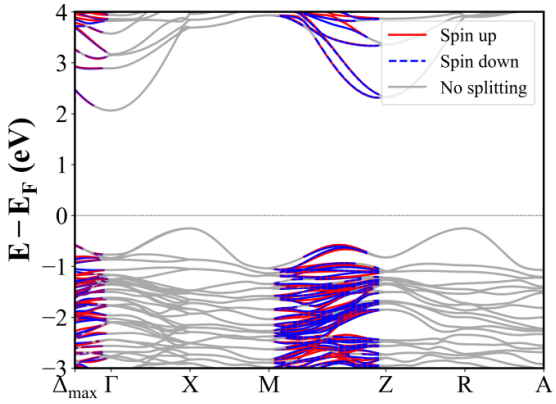


La2NiO4 (P4_2/ncm) | Band Gap = 2.313 eV

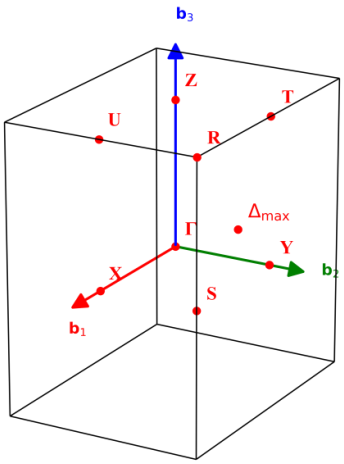


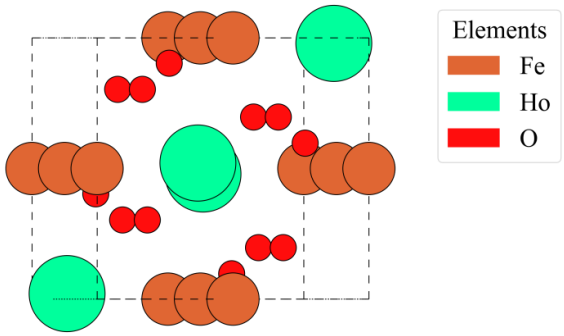


Δ_{max}: (0.200, 0.000, 0.250)

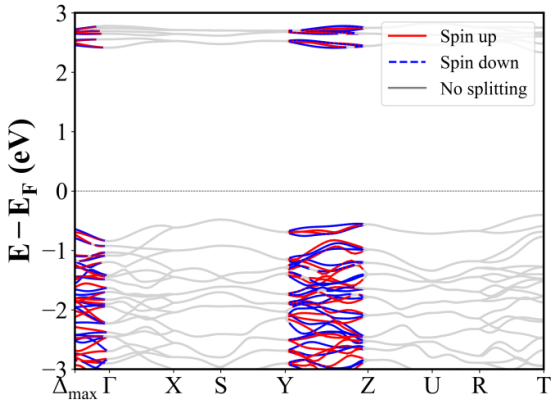


HoFeO3 (Pnma) | Band Gap = 2.735 eV

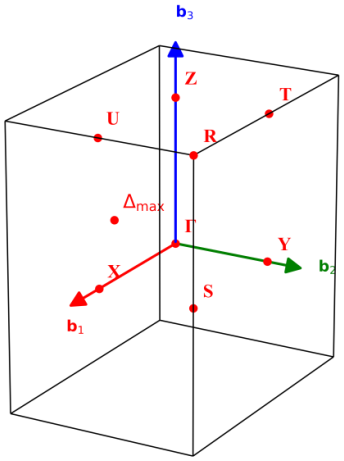


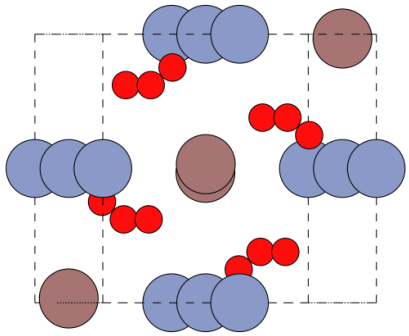


Δ_{max}: (0.000, 0.333, 0.100)

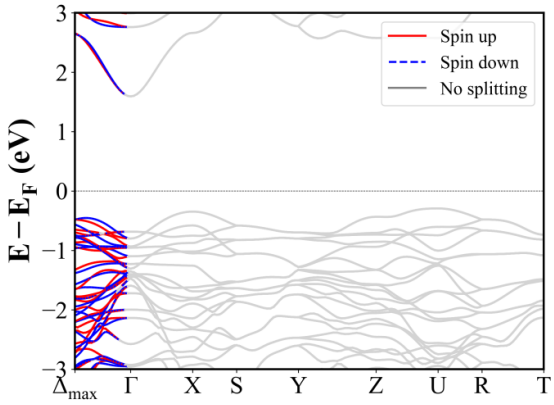


CrInO3 (Pnma) | Band Gap = 1.886 eV

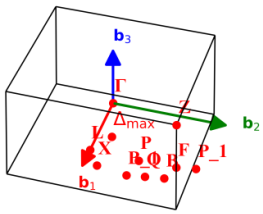


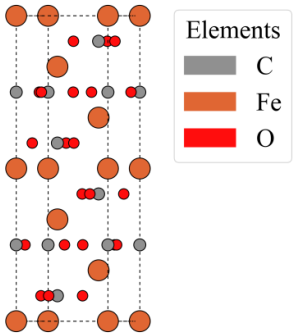


Δ_{max}: (0.400, 0.000, 0.200)

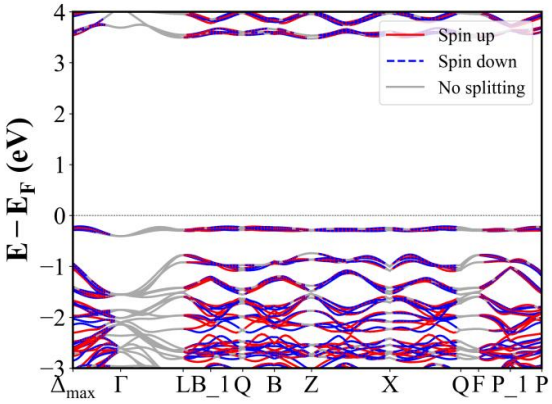


FeCO3 (R-3c) | Band Gap = 3.688 eV

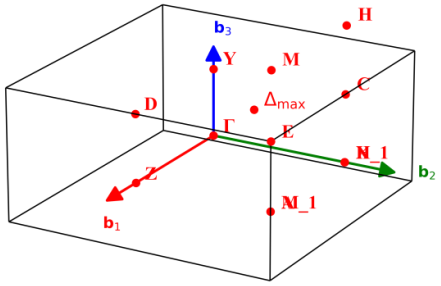


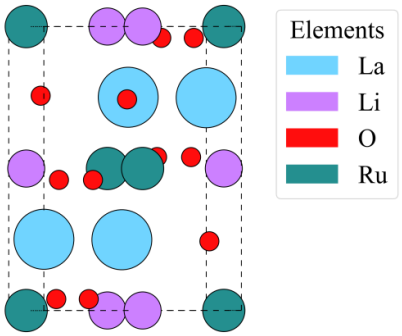


Δ_{max}: (0.333, 0.083, 0.000)

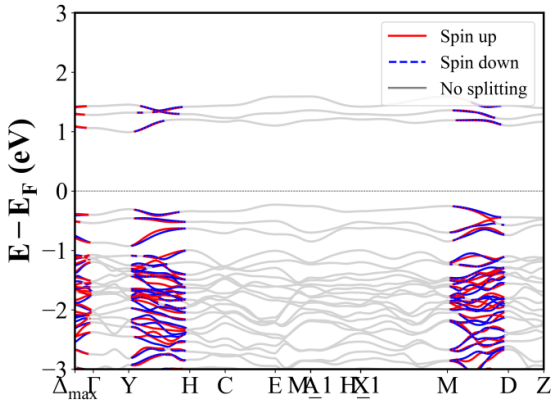


LiLa2RuO6 (P2_1/c) | Band Gap = 1.220 eV

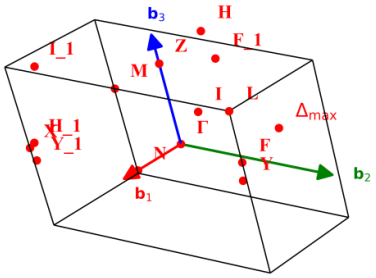


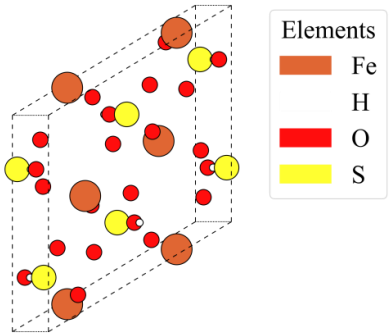


Δ_{max}: (-0.100, 0.100, 0.167)

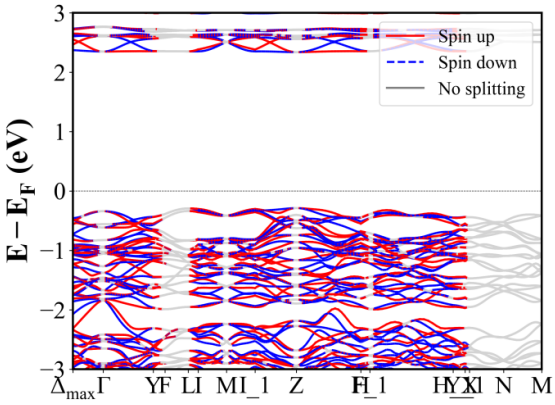


FeHSO5 (C2/c) | Band Gap = 2.625 eV

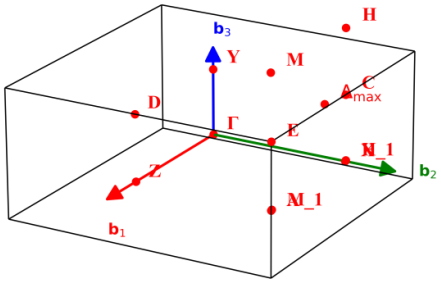


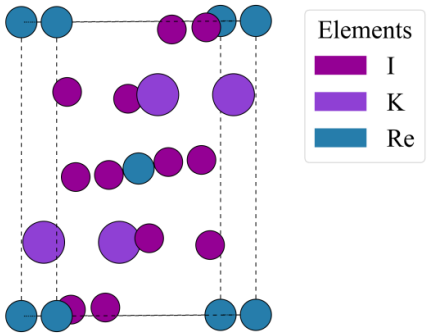


Δ_{max}: (-0.250, 0.375, 0.125)

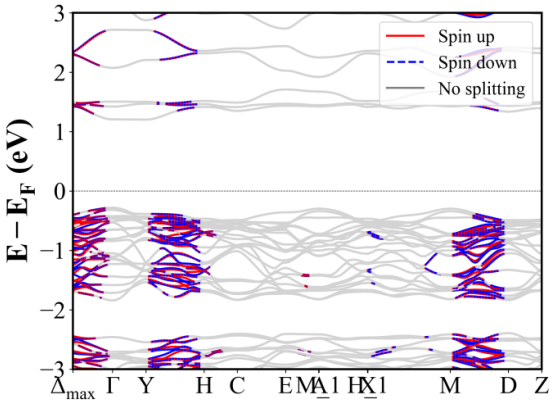


K2ReI6 (P2_1/c) | Band Gap = 1.483 eV

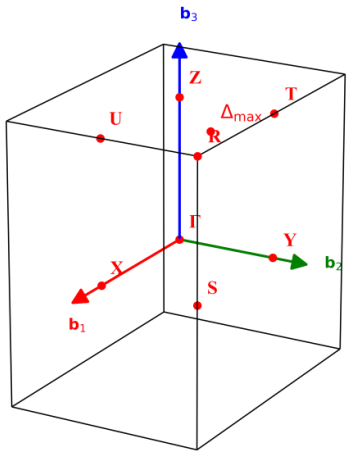


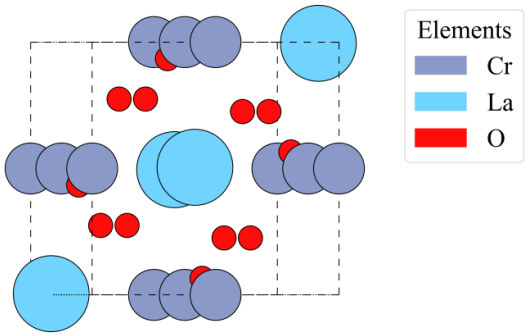


Δ_{max}: (-0.167, 0.333, 0.250)

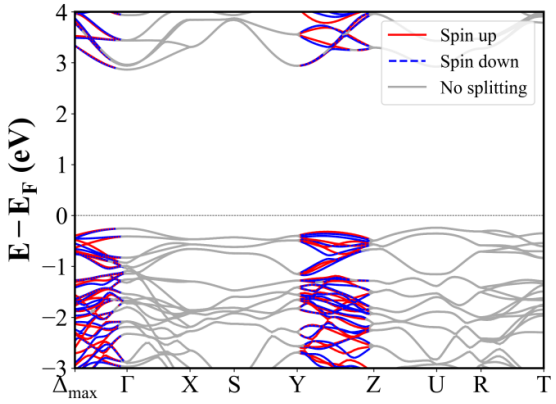


LaCrO3 (Pnma) | Band Gap = 3.105 eV

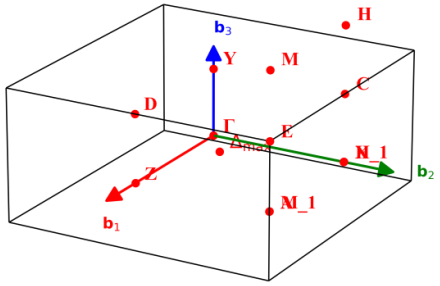


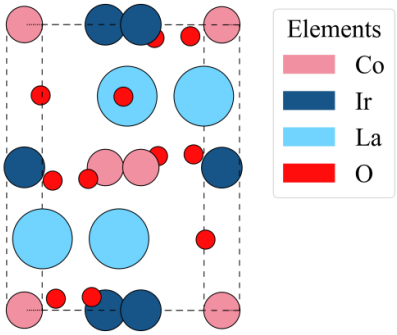


Δ_{max}: (0.000, 0.167, 0.400)

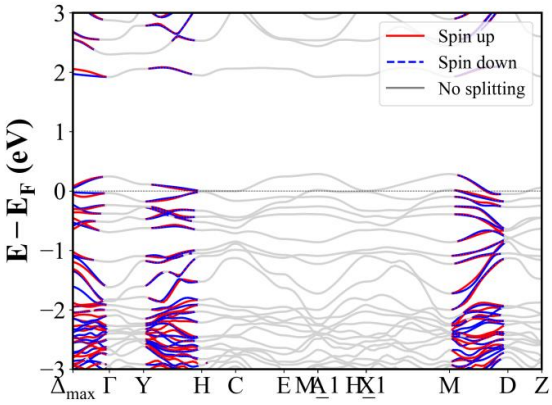


La2CoIrO6 (P2_1/c) | Band Gap = 0.000 eV

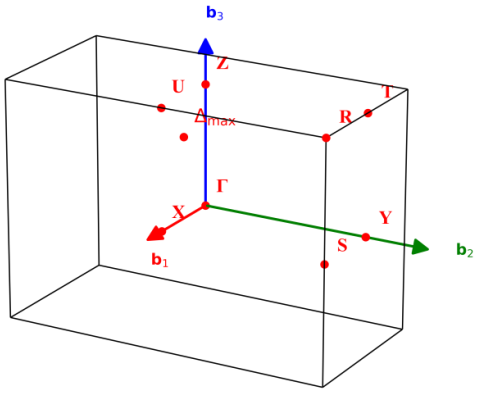


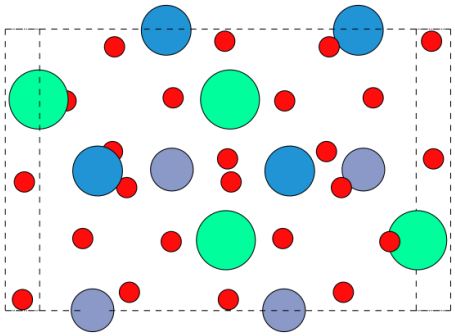


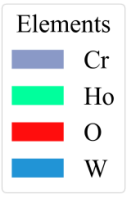
Δ_{max}: (0.300, 0.200, 0.167)



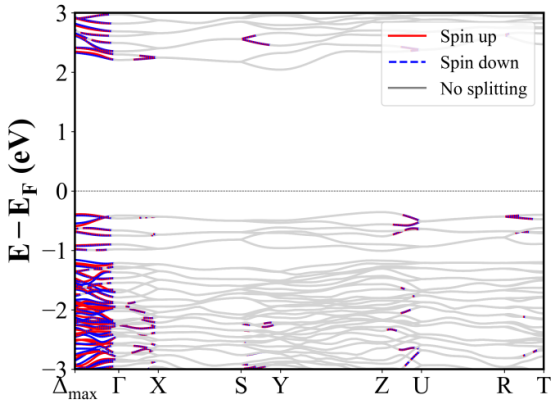
HoCrWO6 (Pna2_1) | Band Gap = 2.398 eV



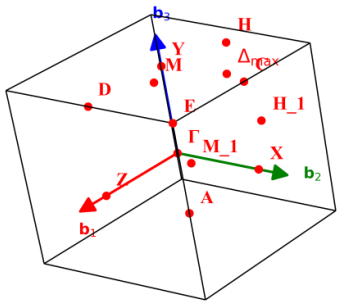


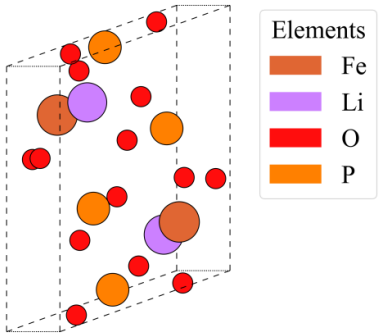


Δ_{max}: (0.250, 0.000, 0.333)

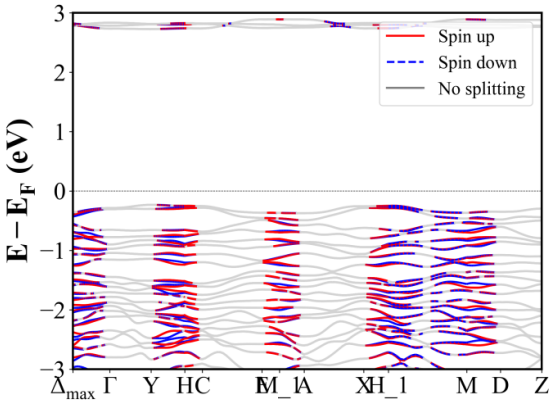


LiFeP2O7 (P2_1) | Band Gap = 2.958 eV

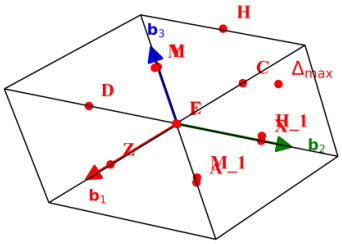


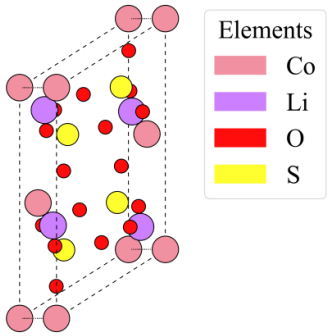


Δ_{max}: (-0.250, 0.167, 0.375)

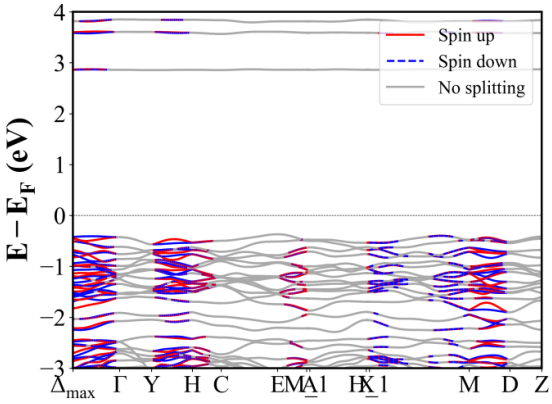


Li2Co(SO4)2 (P2_1/c) | Band Gap = 3.224 eV

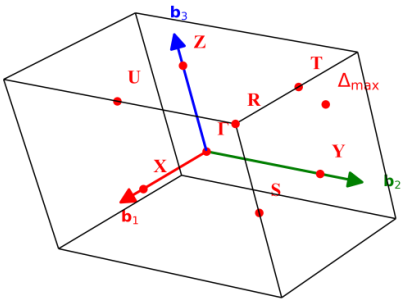


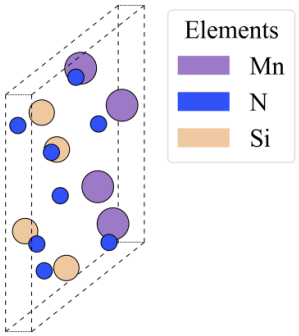


Δ_{max}: (-0.417, 0.333, 0.167)

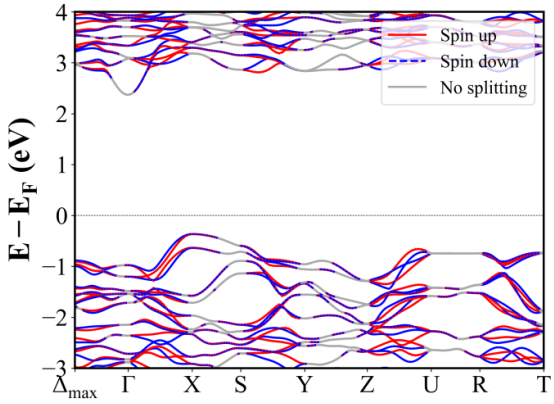


MnSiN2 (Pna2_1) | Band Gap = 2.733 eV

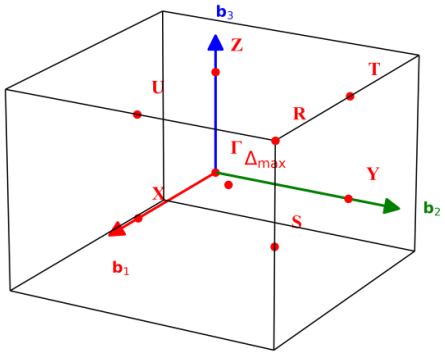


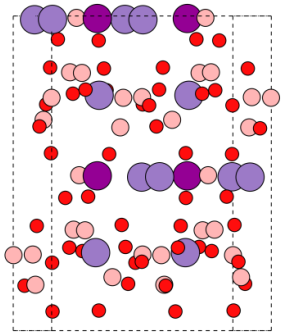


Δ_{max}: (-0.167, 0.500, 0.333)



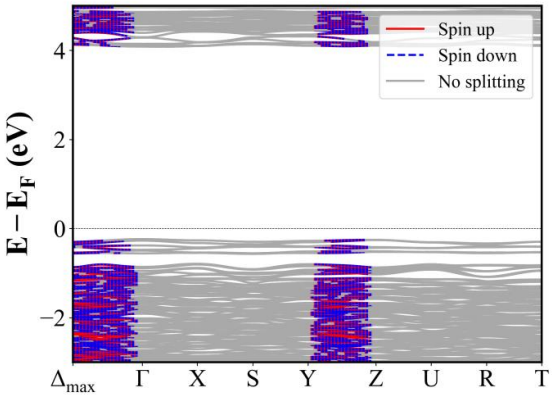
Mn3B7IO13 (Pca2_1)



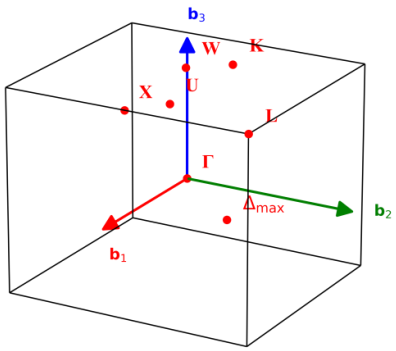


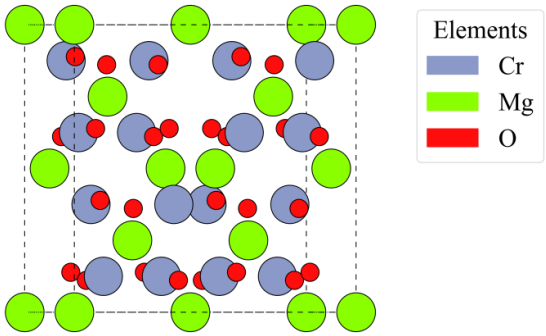


Δ_{max}: (0.500, 0.333, 0.250)

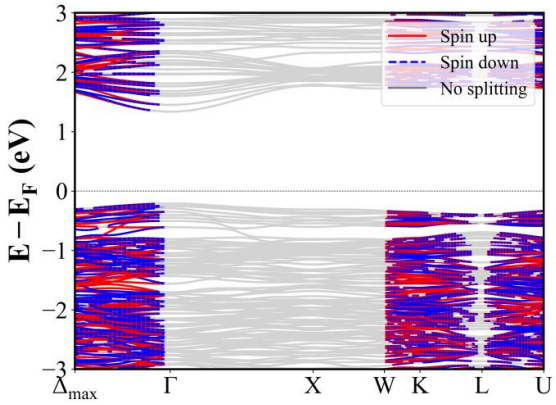


MgCr2O4 (Fd-3m) | Band Gap = 1.545 eV

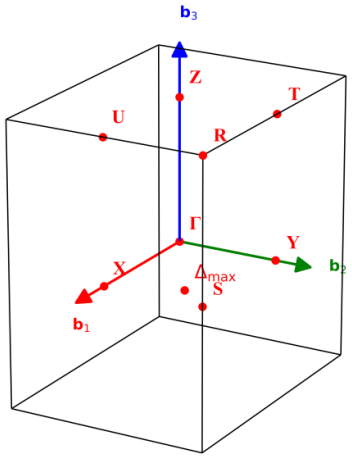


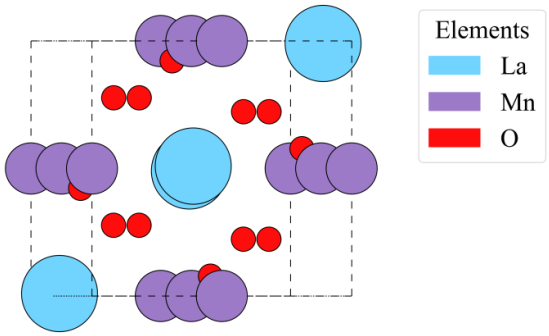


Δ_{max}: (0.333, 0.333, 0.000)

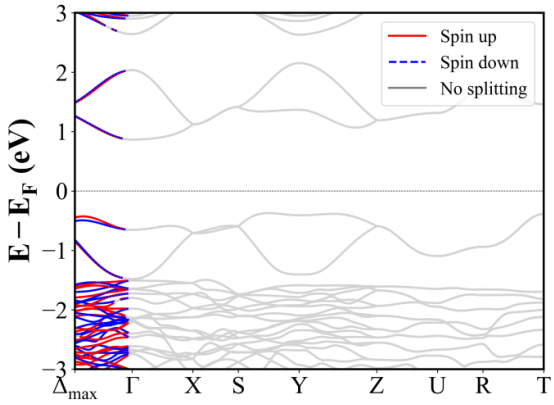


LaMnO3 (Pnma) | Band Gap = 1.237 eV

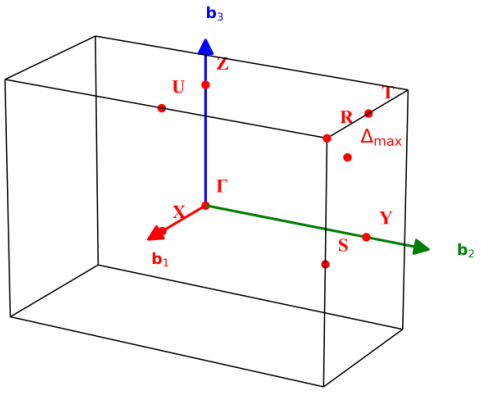


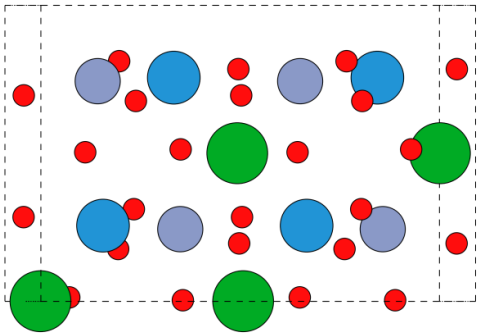


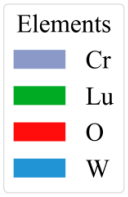
Δ_{max}: (0.400, 0.333, 0.000)



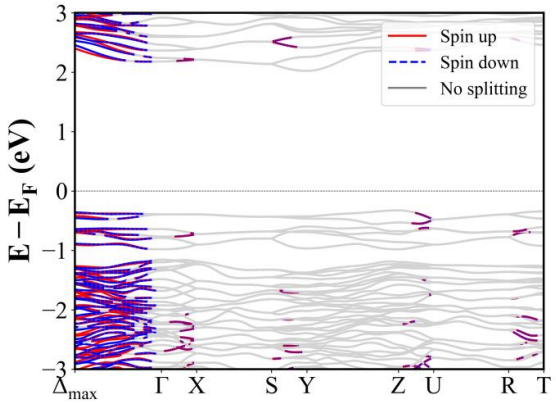
LuCrWO6 (Pna2_1) | Band Gap = 2.347 eV



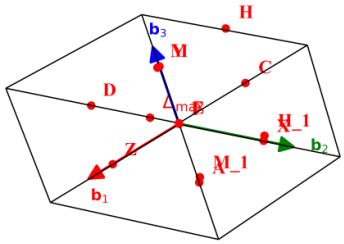


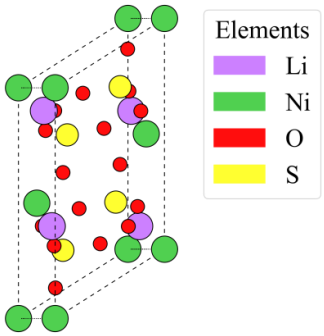


Δ_{max}: (0.250, 0.500, 0.375)

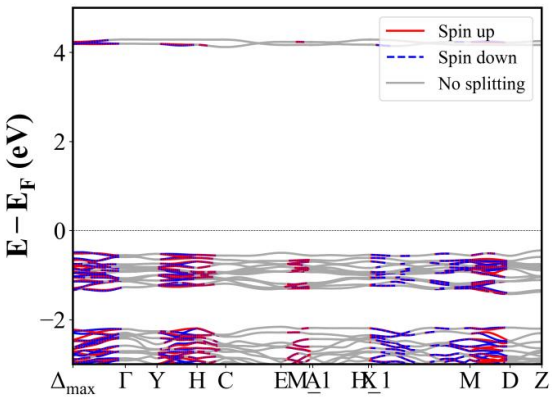


Li2Ni(SO4)2 (P2_1/c) | Band Gap = 4.565 eV

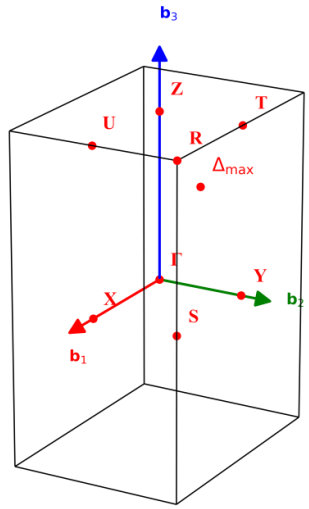




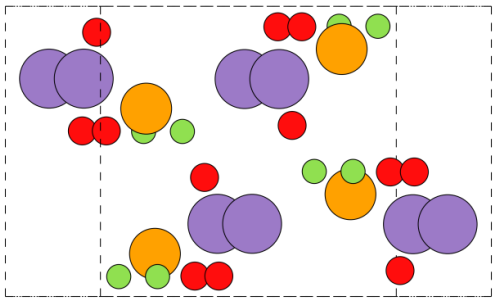
Δ_{max}: (0.333, 0.167, 0.333)



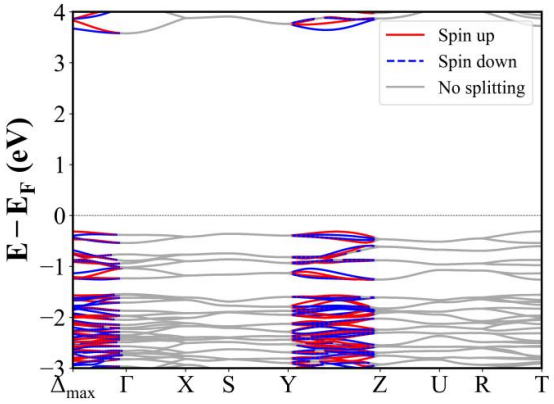
Mn2SeO3F2 (Pnma) | Band Gap = 3.889 eV



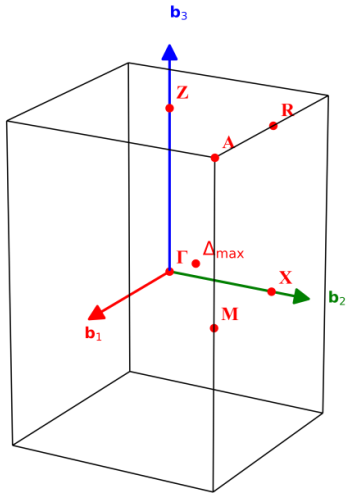
Δ_{max}: (0.000, 0.250, 0.300)

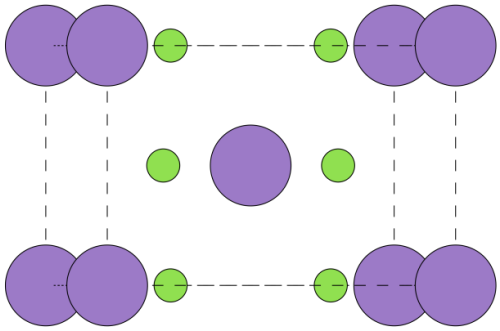




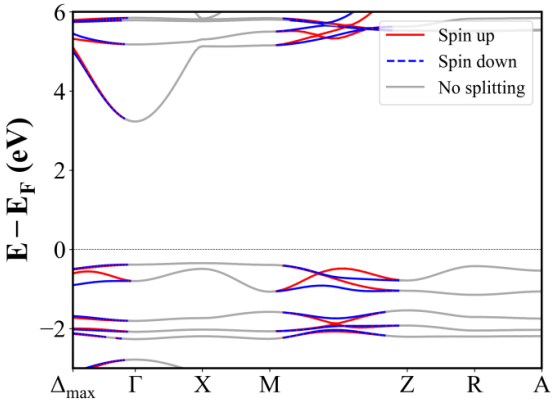


MnF2 (P4_2/mnm) | Band Gap = 3.575 eV

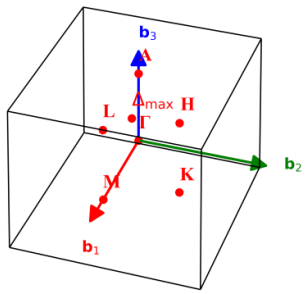


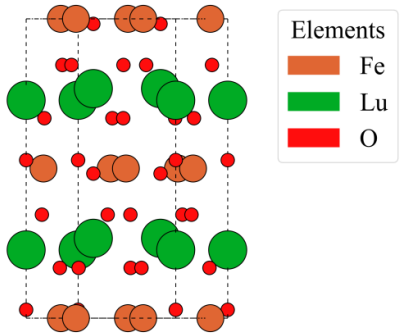


Δ_{max}: (0.300, 0.300, 0.125)

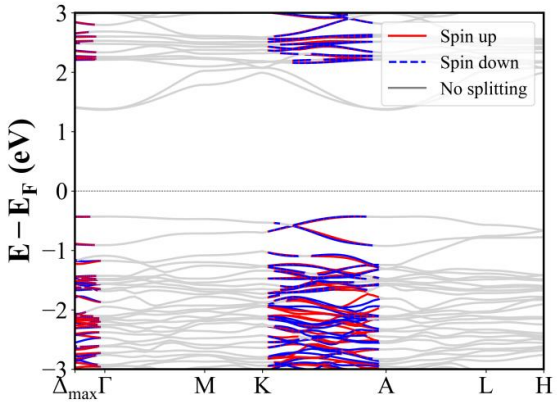


LuFeO3 (P6_3cm) | Band Gap = 1.795 eV

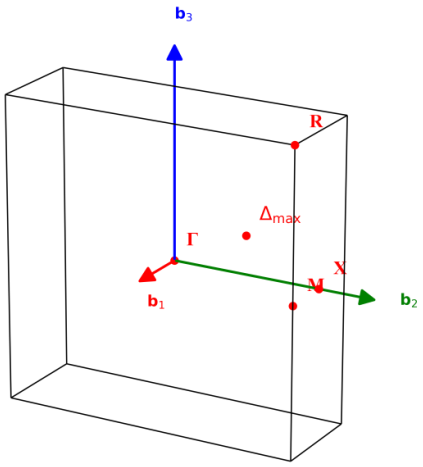


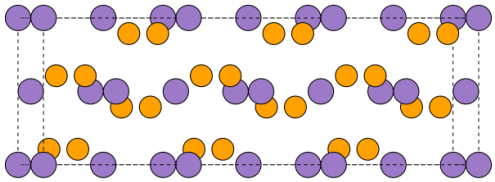


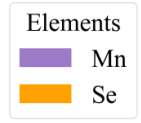
Δ_{max}: (0.100, 0.000, 0.250)



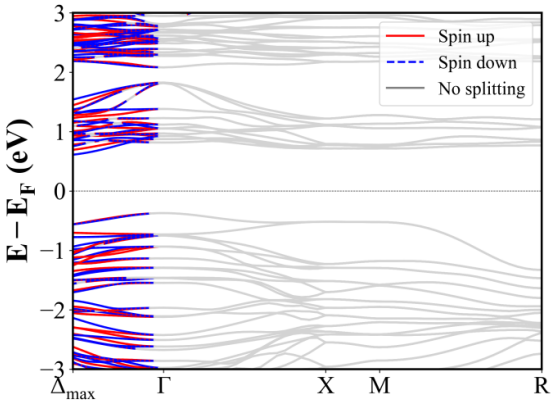
MnSe2 (Pa-3) | Band Gap = 0.983 eV



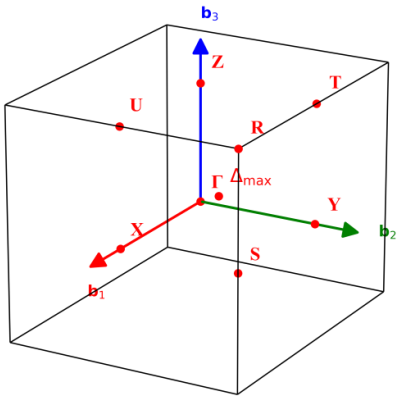


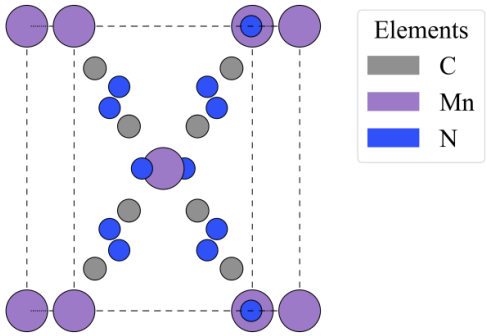


Δ_{max}: (0.000, 0.250, 0.125)

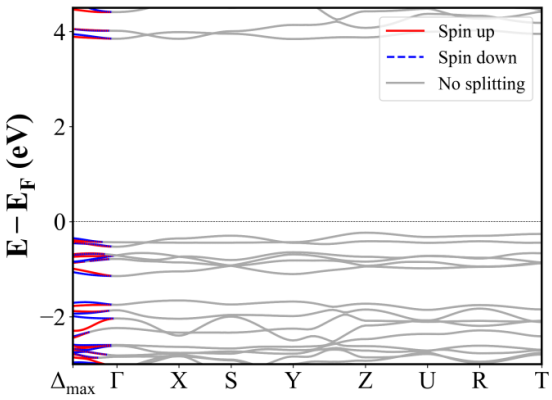


Mn(C2N3)2 (Pnnm) | Band Gap = 4.076 eV

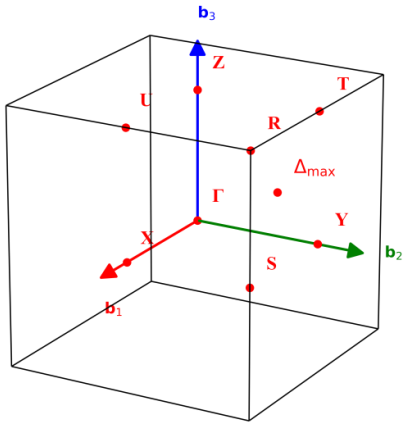


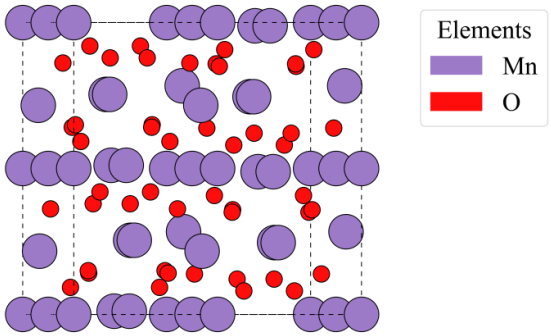


Δ_{max}: (0.250, 0.250, 0.167)

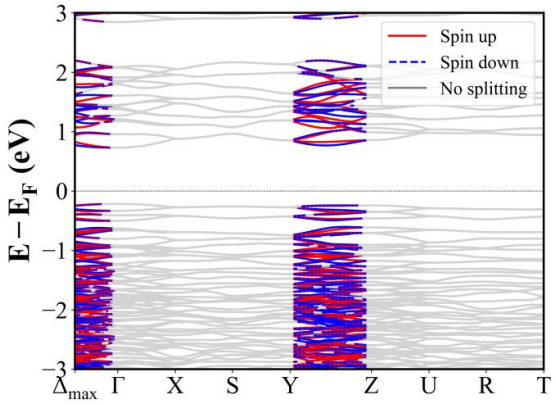


Mn2O3 (Pbca) | Band Gap = 0.946 eV

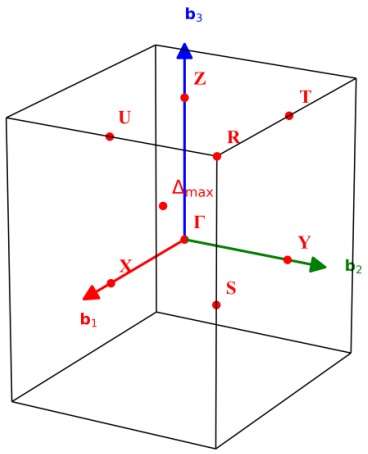


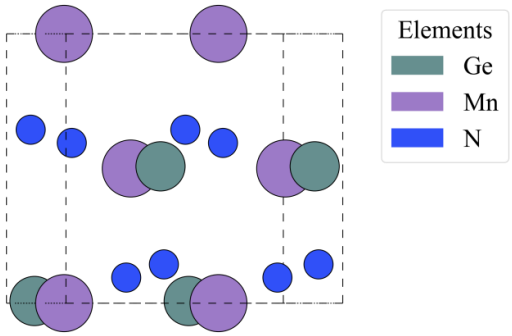


Δ_{max}: (0.000, 0.333, 0.167)

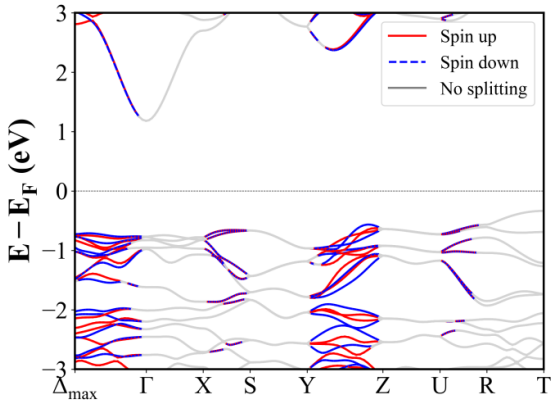


MnGeN2 (Pna2_1) | Band Gap = 1.516 eV

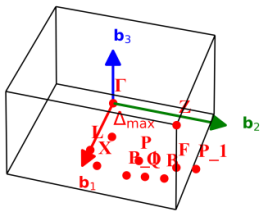


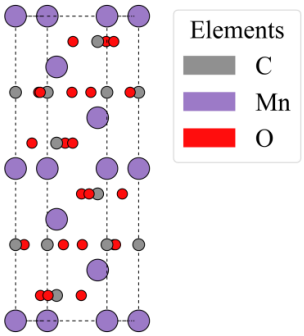


Δ_{max}: (0.500, 0.250, 0.300)

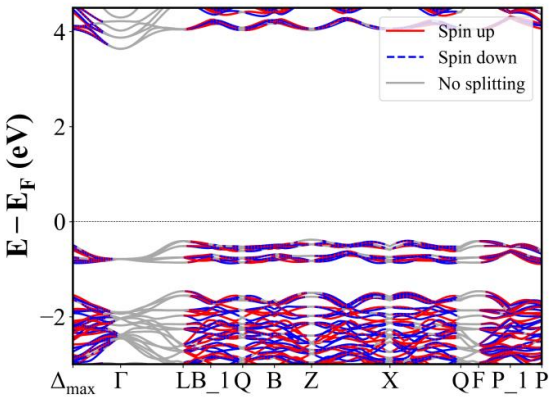


MnCO3 (R-3c) | Band Gap = 4.015 eV

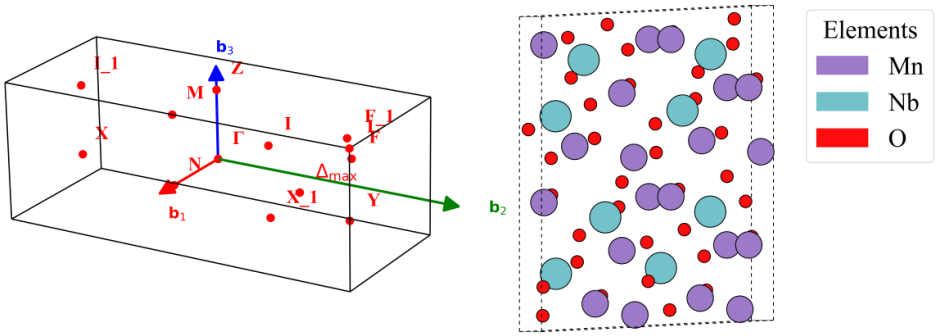




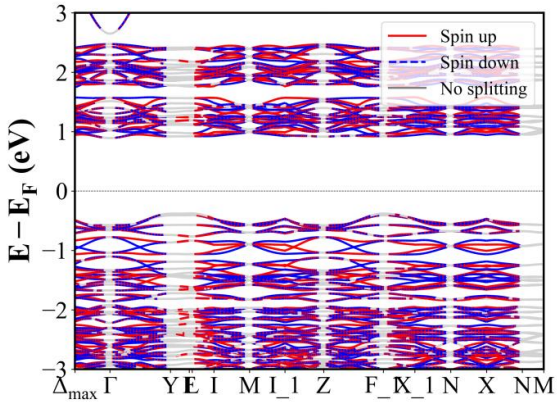
Δ_{max}: (0.333, 0.083, 0.000)



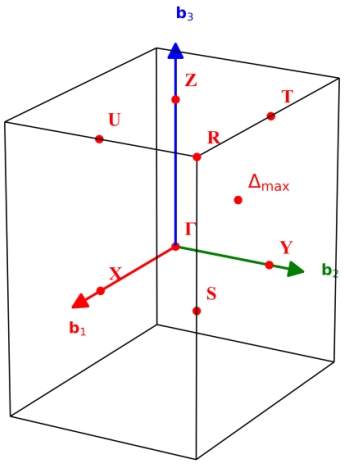
Mn4Nb2O9 (Cc) | Band Gap = 1.270 eV

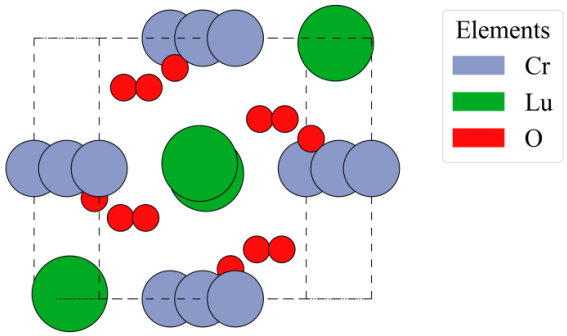


Δ_{max}: (0.250, 0.300, 0.000)

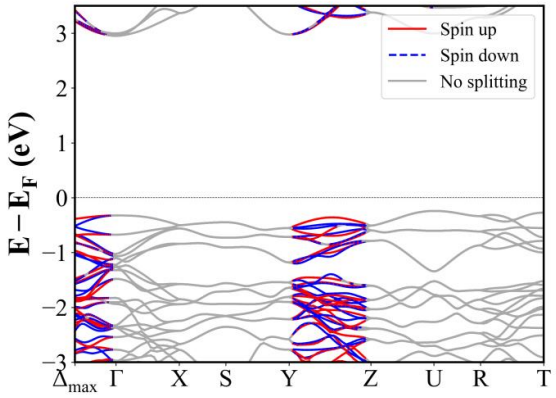


LuCrO3 (Pnma) | Band Gap = 3.192 eV

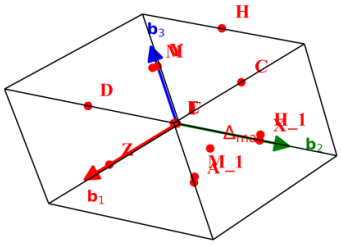


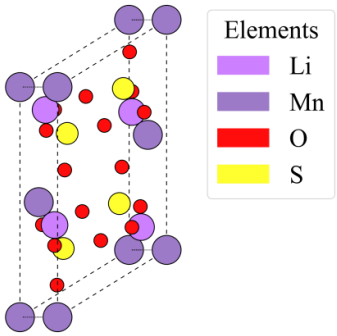


Δ_{max}: (0.000, 0.333, 0.200)

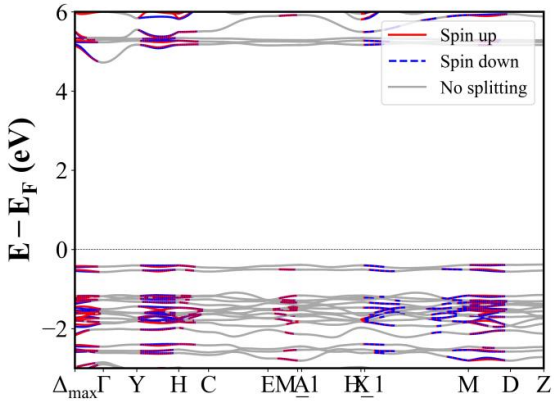


Li2Mn(SO4)2 (P2_1/c) | Band Gap = 5.101 eV

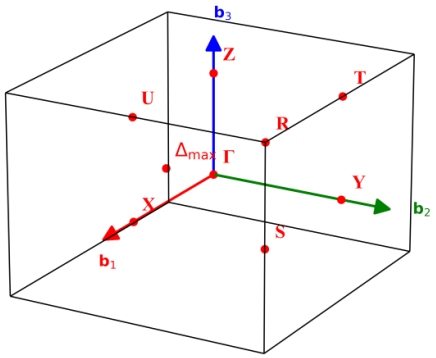


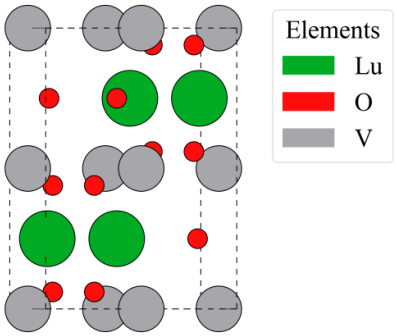


Δ_{max}: (0.167, 0.333, 0.000)

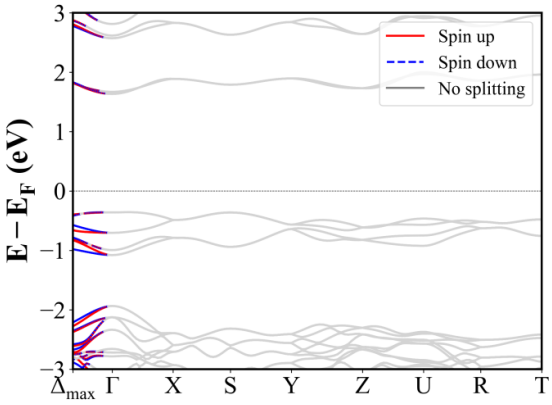


LuVO3 (Pnma) | Band Gap = 1.991 eV

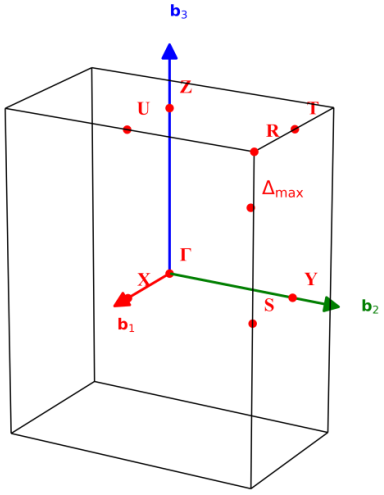


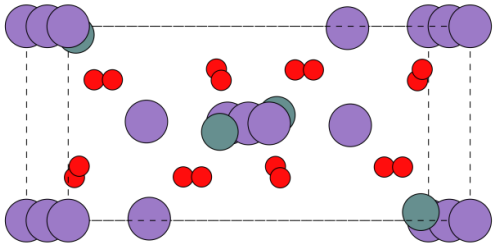


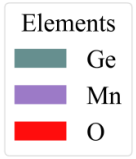
Δ_{max}: (0.300, 0.000, 0.167)



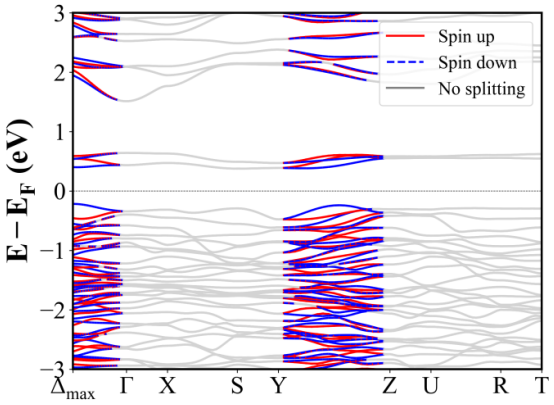
Mn2GeO4 (Pnma) | Band Gap = 0.594 eV



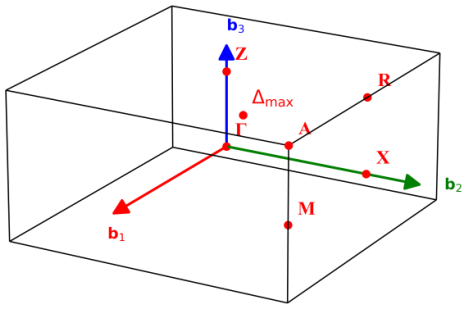


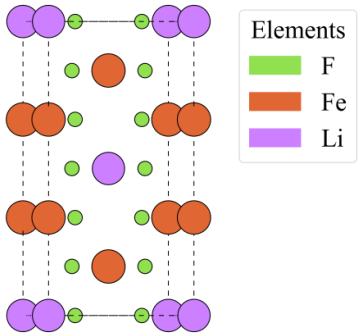


Δ_{max}: (-0.250, 0.250, 0.200)

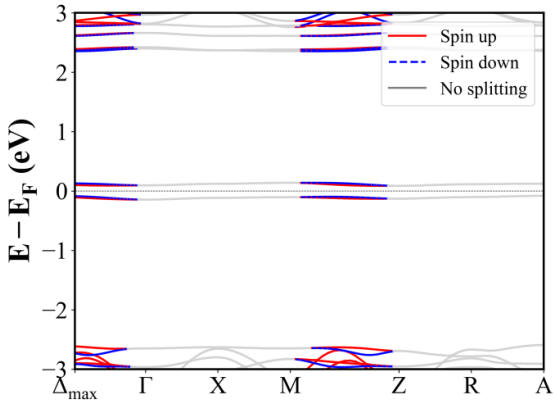


LiFe2F6 (P4_2/mnm) | Band Gap = 0.168 eV

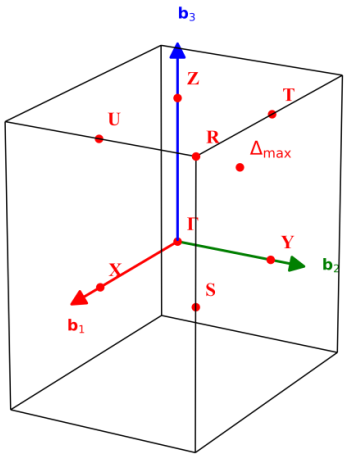


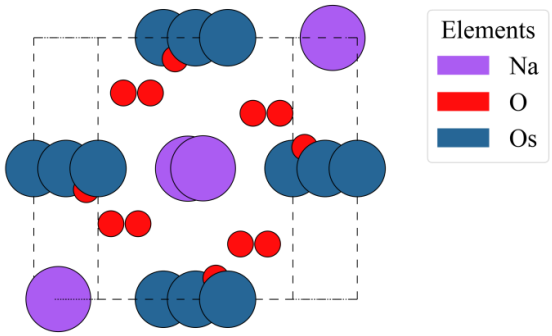


Δ_{max}: (0.333, 0.250, 0.500)

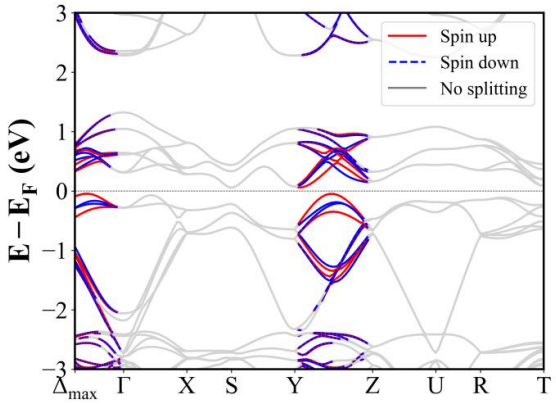


NaOsO3 (Pnma) | Band Gap = 0.103 eV

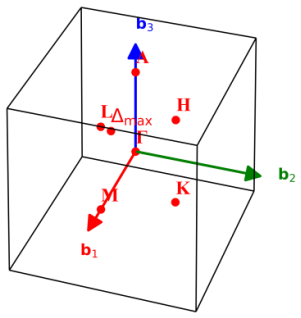


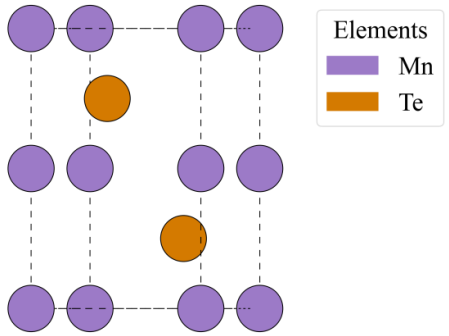


Δ_{max}: (0.000, 0.333, 0.300)

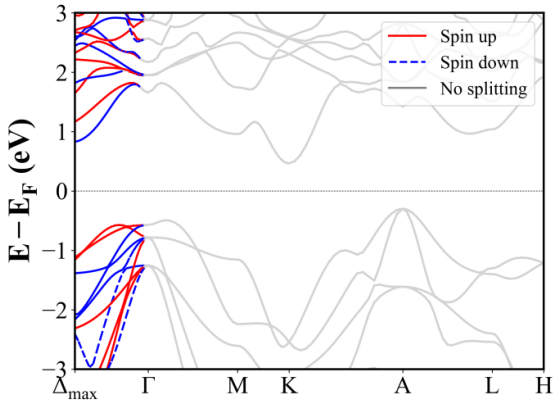


MnTe (P6_3/mmc) | Band Gap = 0.764 eV

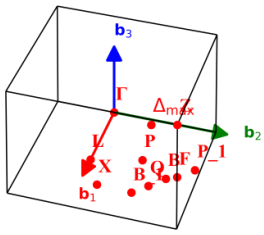


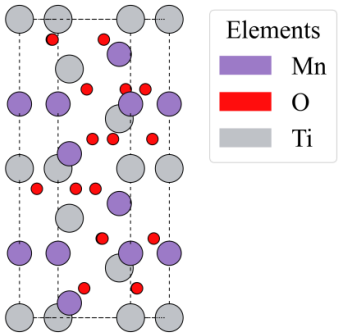


Δ_{max}: (0.357, 0.000, 0.375)

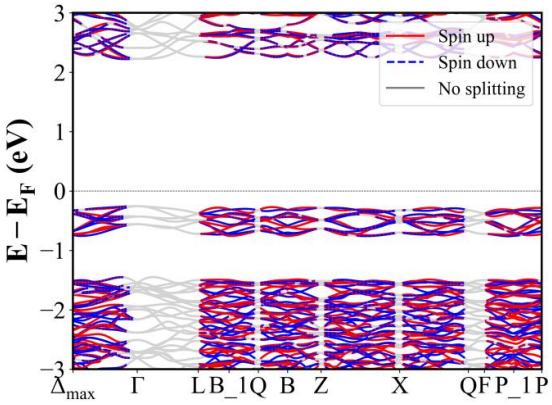


TiMnO3 (R3c) | Band Gap = 2.475 eV

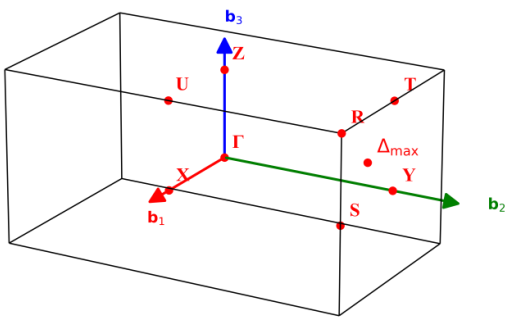


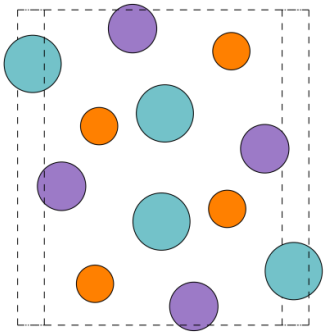


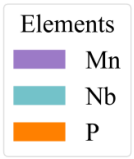
Δ_{max}: (0.300, 0.300, 0.250)



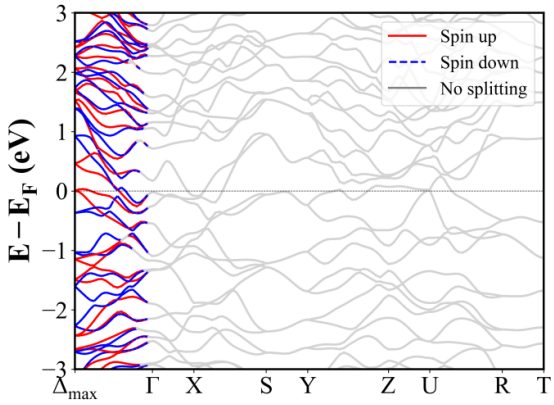
MnNbP (Pnma) | Band Gap = 0.000 eV



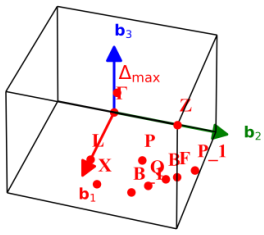


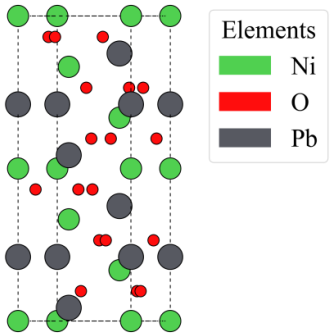


Δ_{max}: (0.250, 0.500, 0.250)

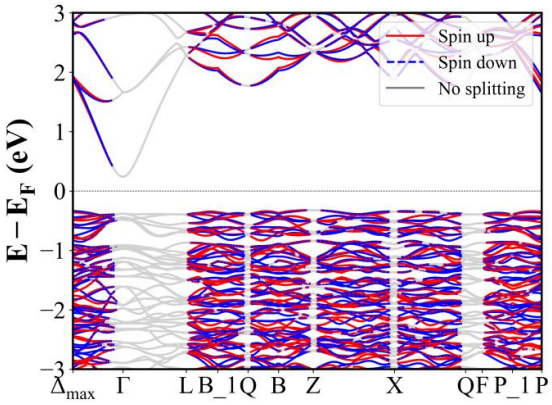


NiPbO3 (R3c) | Band Gap = 0.561 eV

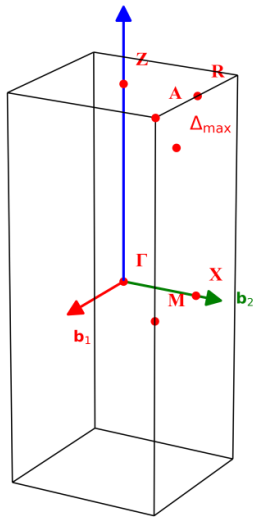




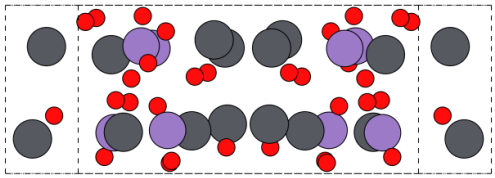
Δ_{max}: (0.300, 0.100, 0.500)

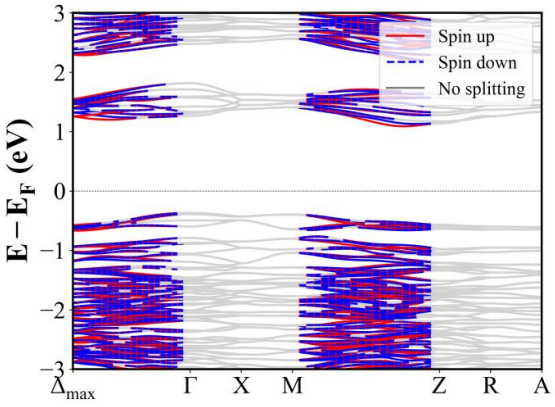


Mn(PbO2)2 (P-42_1c) | Band Gap = 1.458 eV

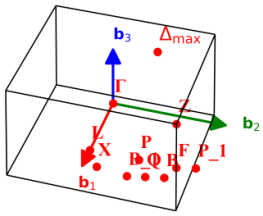


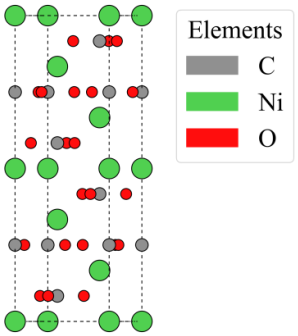
Δ_{max}: (0.250, 0.500, 0.400)



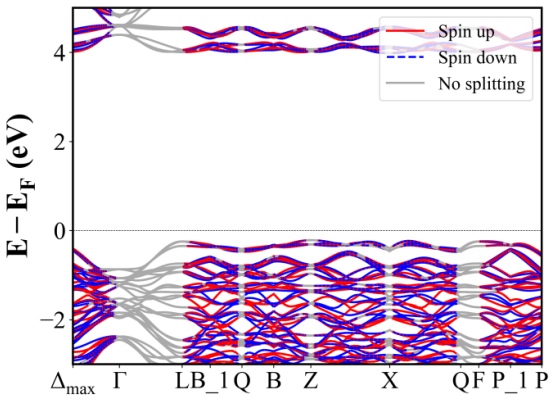


NiCO3 (R-3c) | Band Gap = 4.197 eV

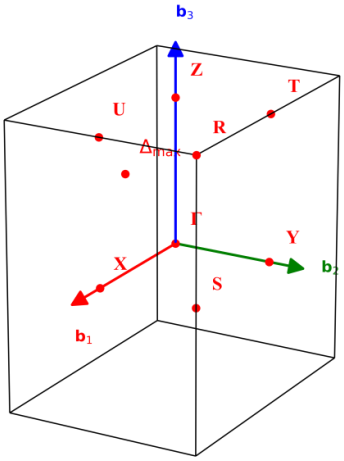


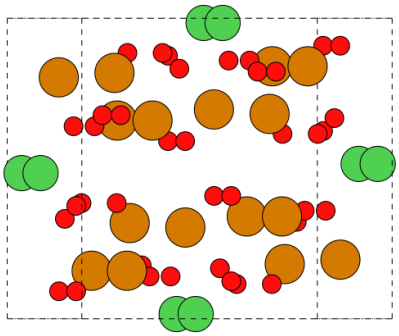


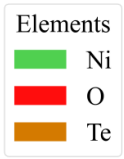
Δ_{max}: (-0.417, 0.167, 0.250)



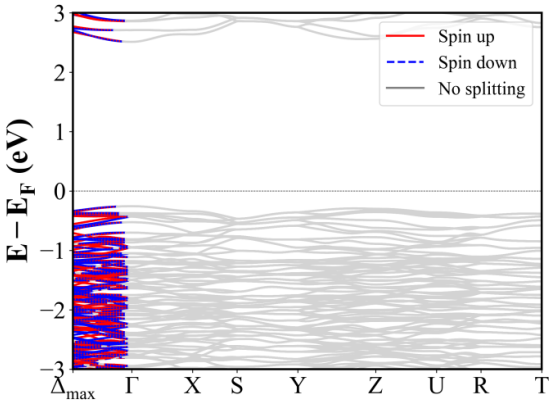
NiTe2O5 (Pnma) | Band Gap = 2.766 eV



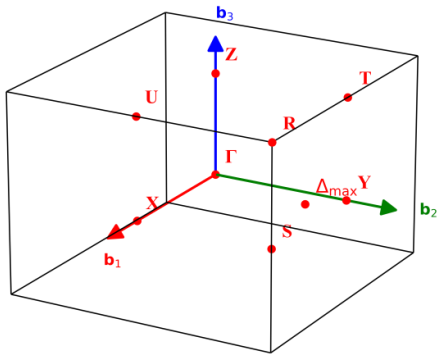


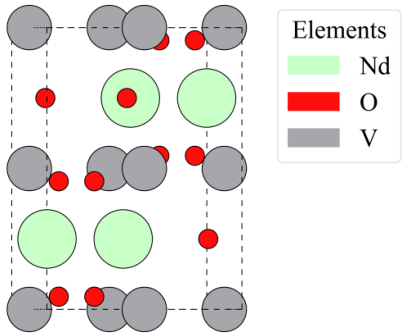


Δ_{max}: (0.333, 0.000, 0.333)

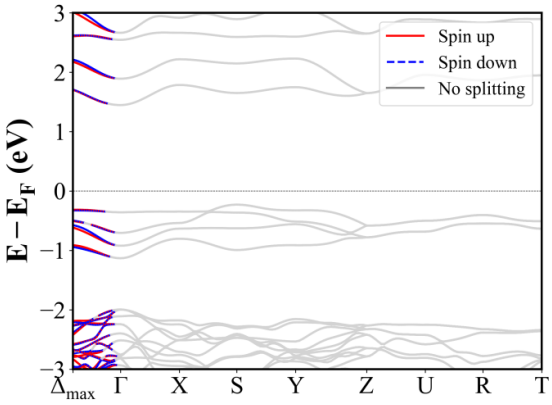


NdVO3 (Pnma) | Band Gap = 1.676 eV

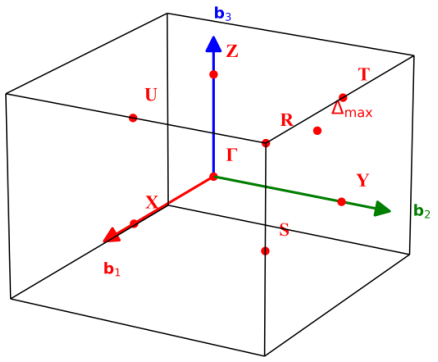


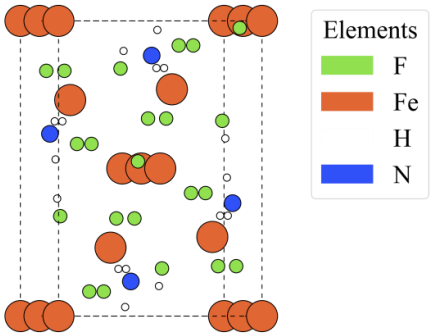


Δ_{max}: (0.100, 0.400, 0.000)

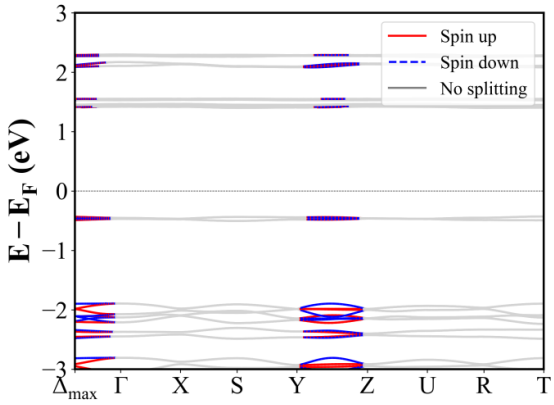


Fe2H4NF6 (Pnma) | Band Gap = 1.828 eV

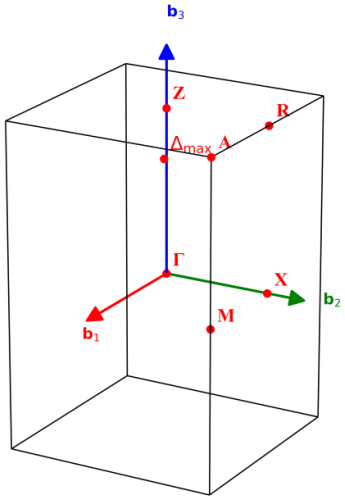


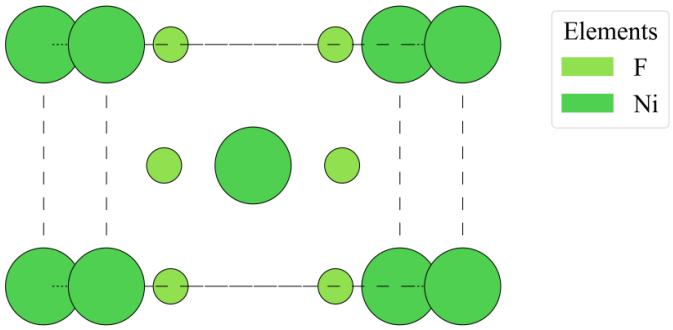


Δ_{max}: (-0.125, 0.333, 0.250)

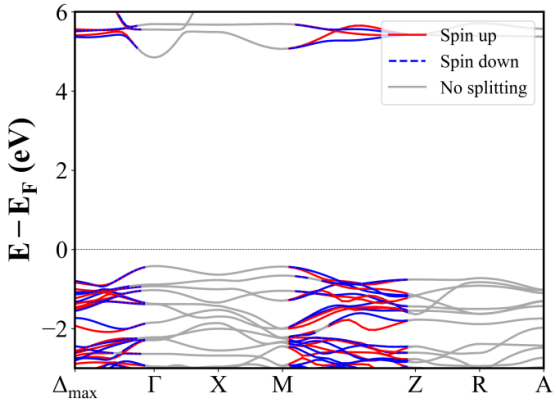


NiF2 (P4_2/mnm) | Band Gap = 5.268 eV

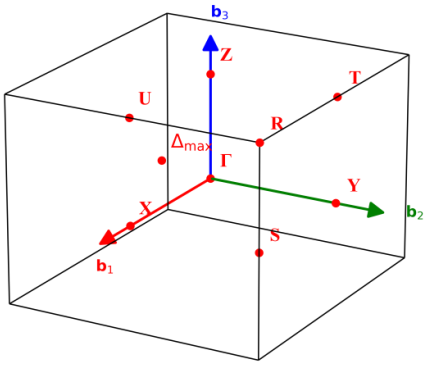


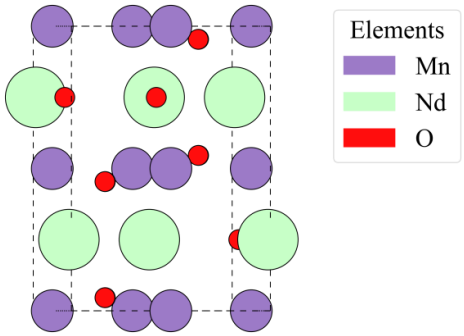


Δ_{max}: (0.167, 0.083, 0.389)

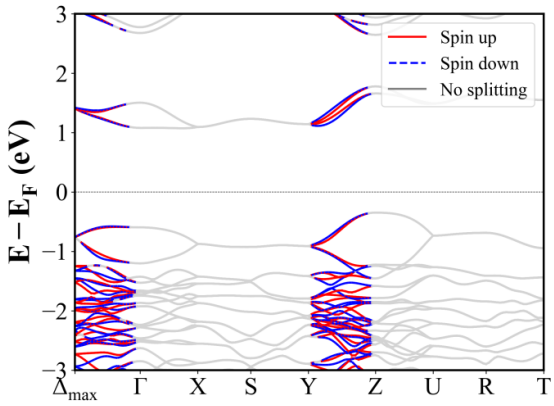


NdMnO3 (Pnma) | Band Gap = 1.420 eV

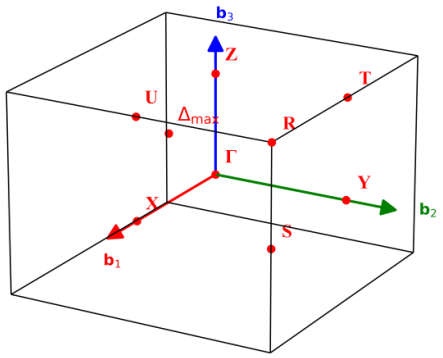


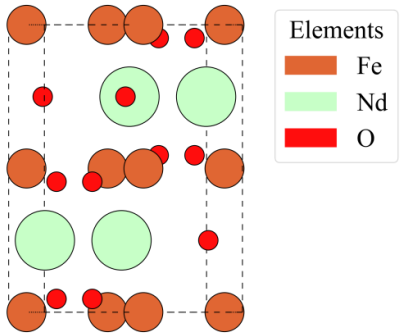


Δ_{max}: (0.500, 0.125, 0.333)

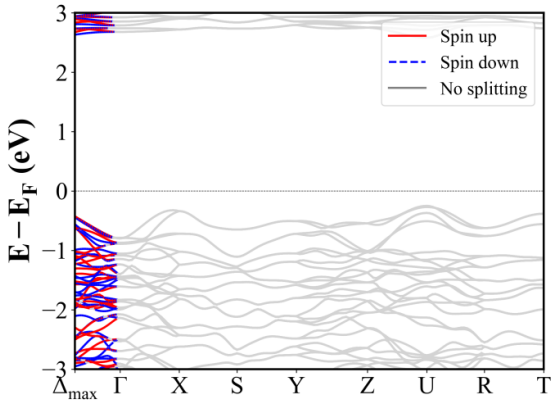


NdFeO3 (Pnma) | Band Gap = 2.833 eV

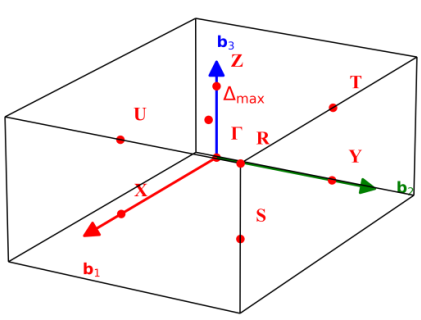


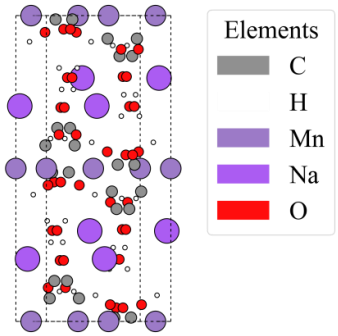


Δ_{max}: (0.300, 0.000, 0.333)

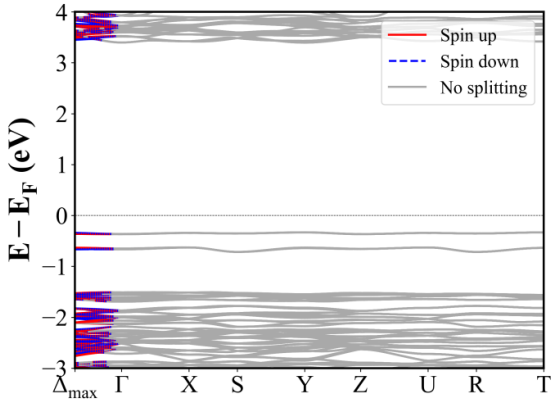


Na2MnH8(C3O5)2 (Pbca)

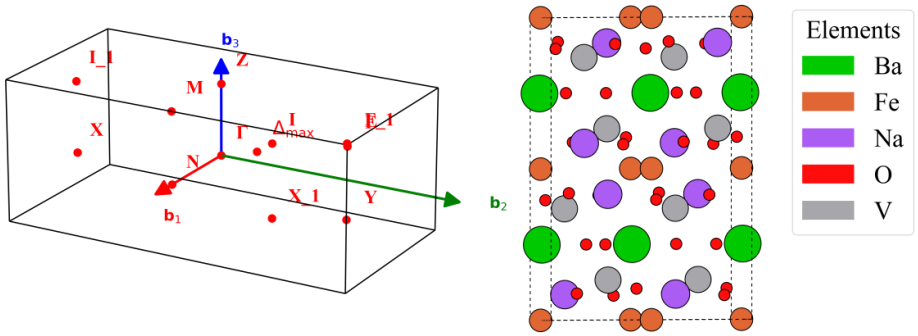




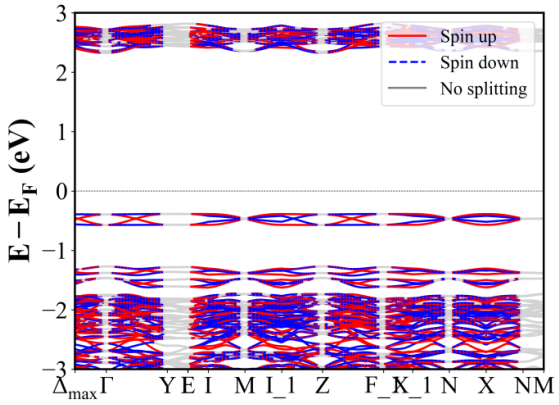
Δ_{max}: (0.250, 0.167, 0.500)



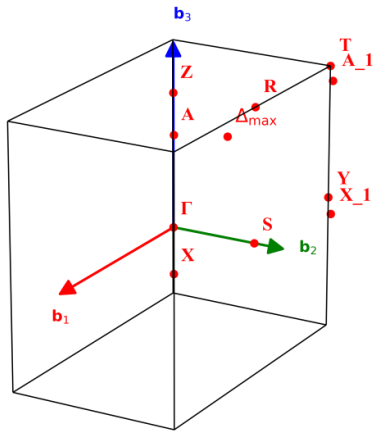
BaNa2V2FeO8 (C2/c) | Band Gap = 2.710 eV

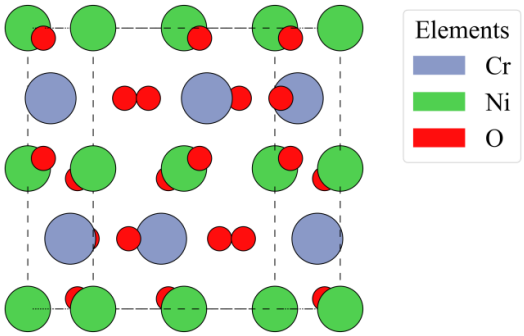


Δ_{max}: (0.333, 0.200, 0.250)

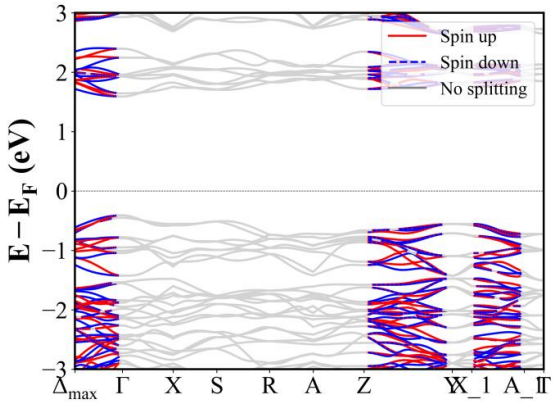


CrNiO4 (Cmcm) | Band Gap = 2.000 eV

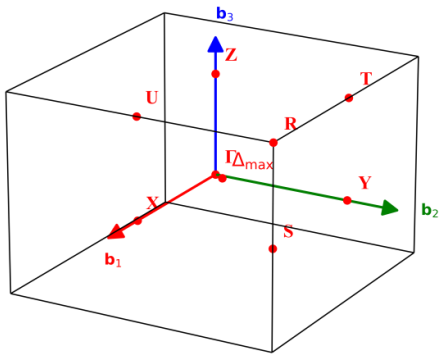


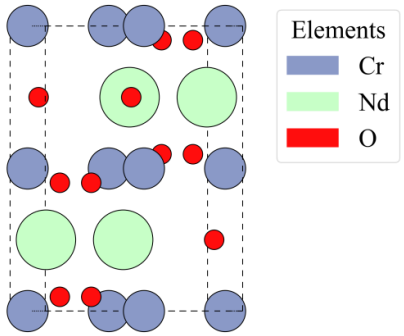


Δ_{max}: (0.000, 0.333, 0.375)

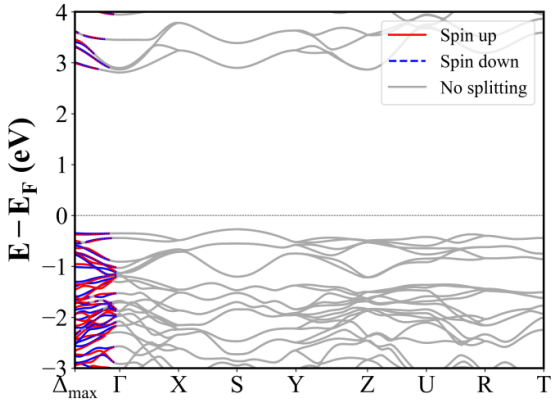


NdCrO3 (Pnma) | Band Gap = 3.079 eV

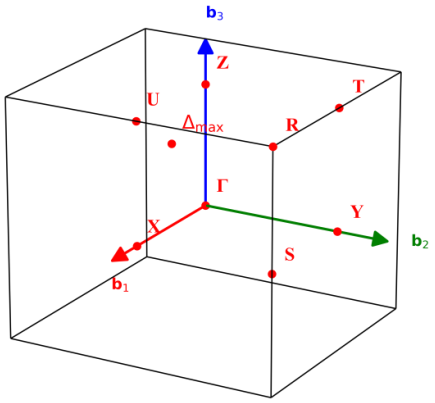


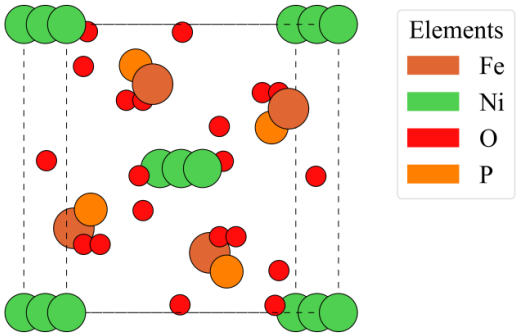


Δ_{max}: (0.300, 0.200, 0.167)

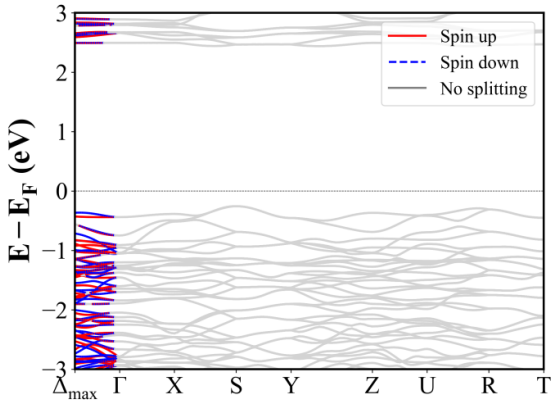


FeNiPO5 (Pnma) | Band Gap = 2.694 eV

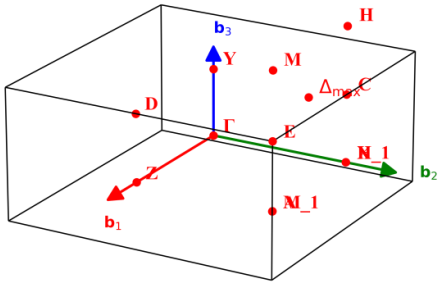


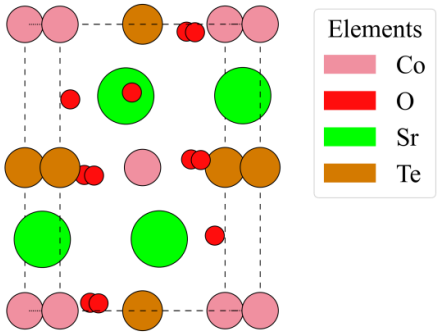


Δ_{max}: (0.250, 0.000, 0.333)

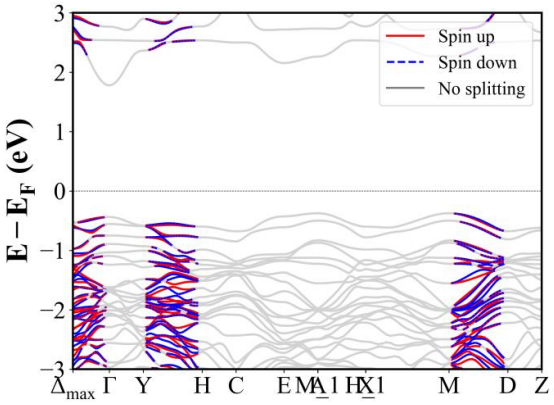


Sr2CoTeO6 (P2_1/c) | Band Gap = 2.154 eV

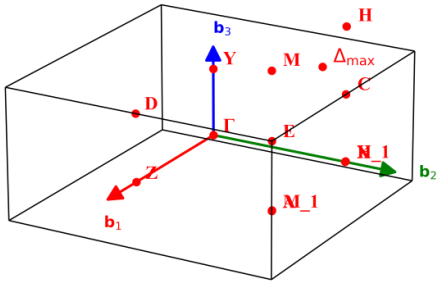


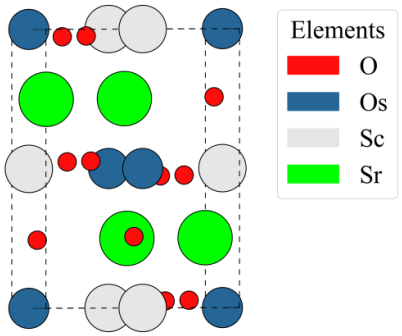


Δ_{max}: (-0.300, 0.200, 0.167)

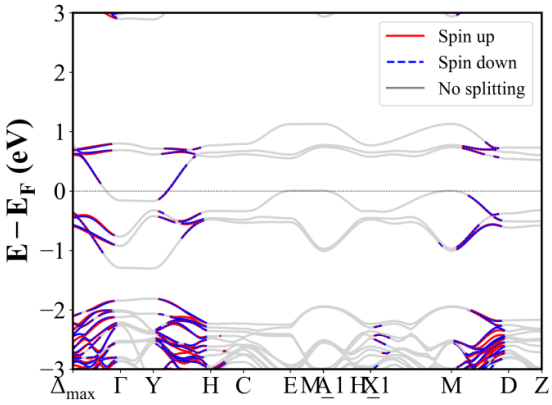


Sr2ScOsO6 (P2_1/c) | Band Gap = 0.000 eV

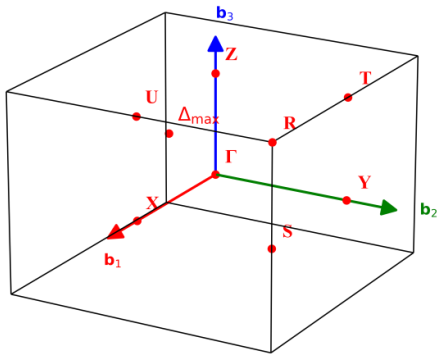


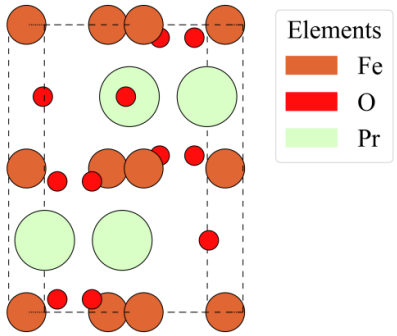


Δ_{max}: (-0.400, 0.200, 0.333)

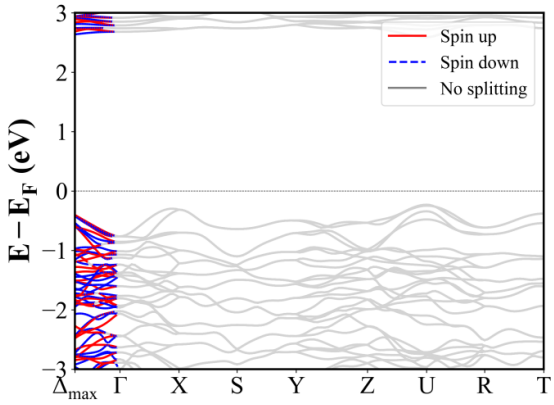


PrFeO3 (Pnma) | Band Gap = 2.822 eV

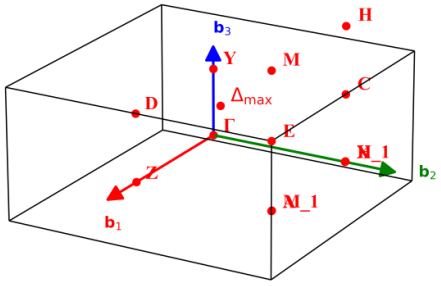


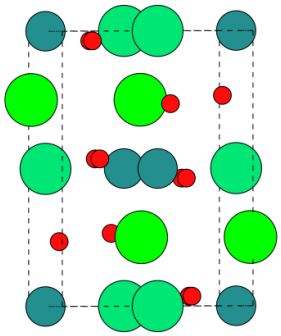


Δ_{max}: (0.300, 0.000, 0.333)



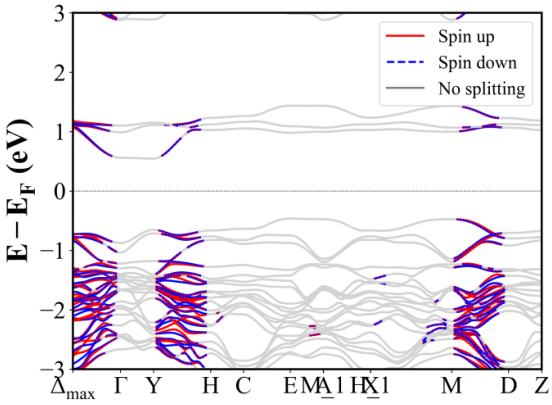
Sr2ErRuO6 (P2_1/c) | Band Gap = 1.009 eV



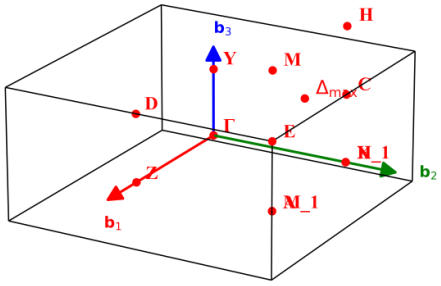


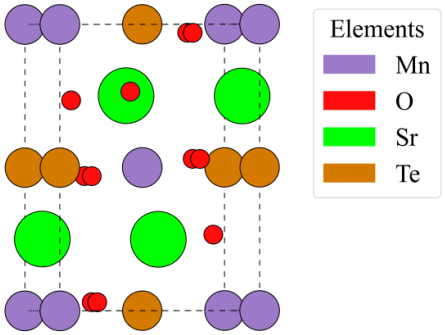


Δ_{max}: (0.300, 0.200, 0.500)

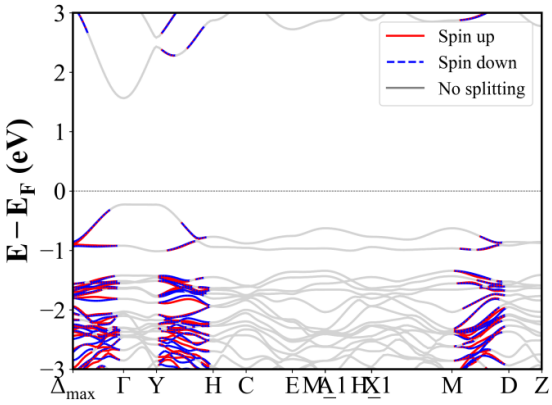


Sr2MnTeO6 (P2_1/c) | Band Gap = 1.792 eV

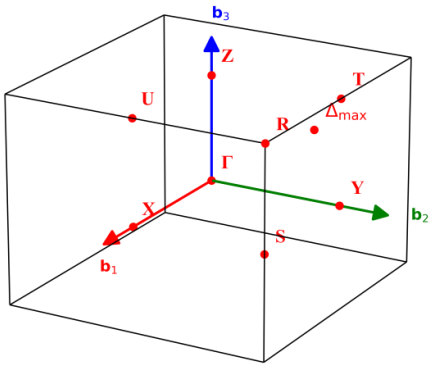


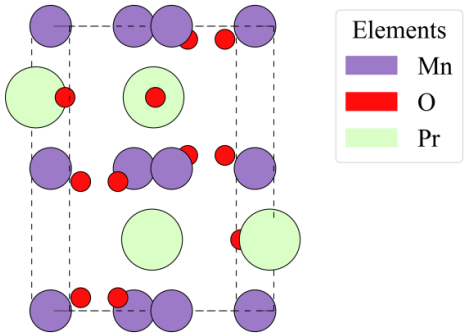


Δ_{max}: (0.100, 0.400, 0.500)

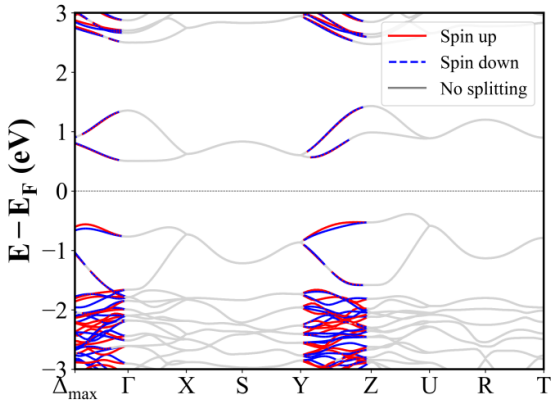


PrMnO3 (Pnma) | Band Gap = 0.892 eV

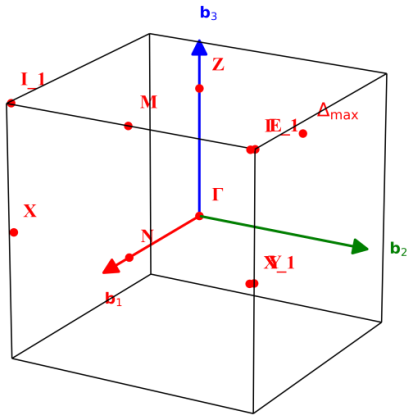


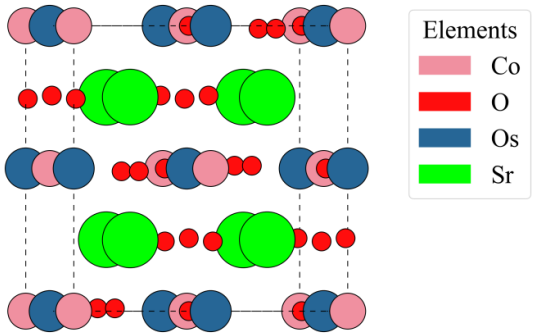


Δ_{max}: (0.000, 0.400, 0.333)

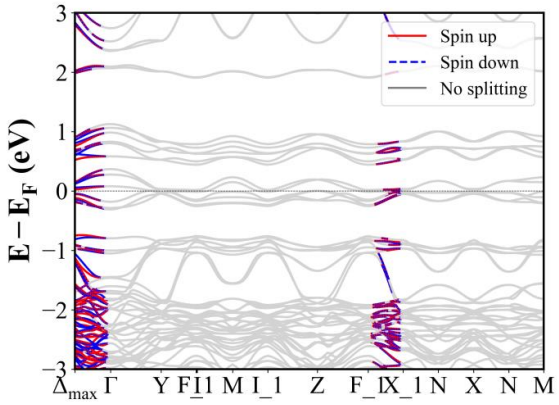


Sr2CoOsO6 (C2/c) | Band Gap = 0.000 eV

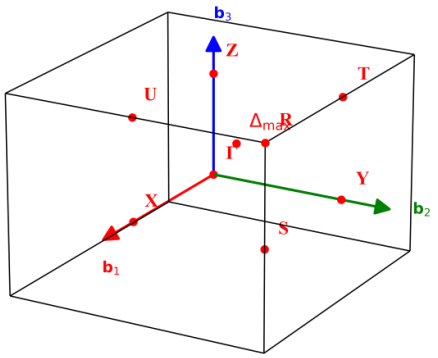


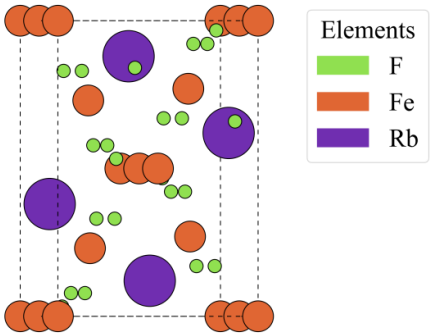


Δ_{max}: (-0.167, 0.333, 0.333)

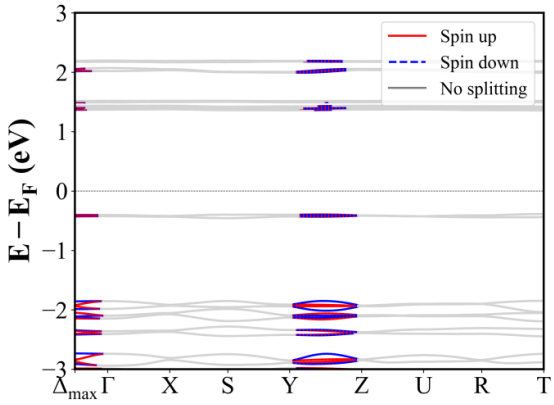


RbFe2F6 (Pnma) | Band Gap = 1.744 eV

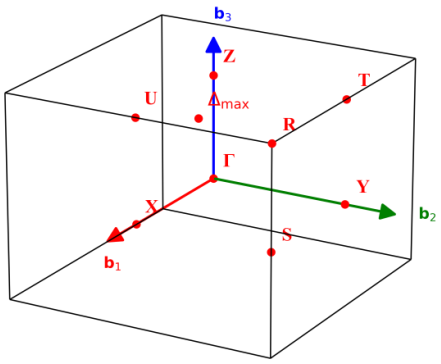


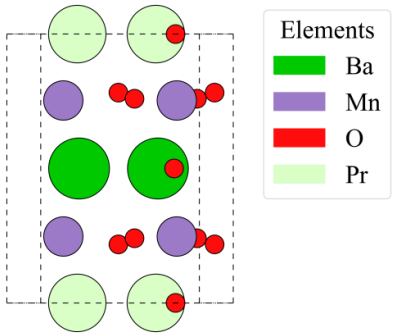


Δ_{max}: (0.125, 0.167, 0.250)

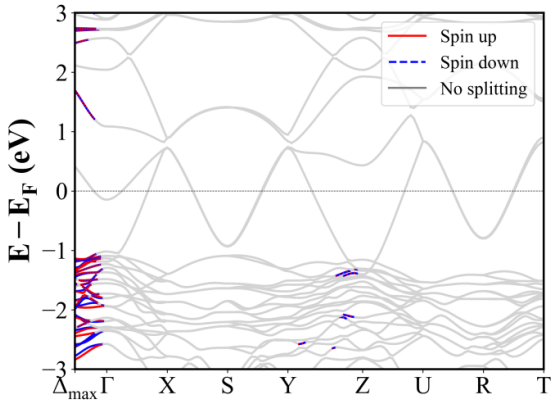


BaPrMn2O6 (Pmc2_1) | Band Gap = 0.000 eV

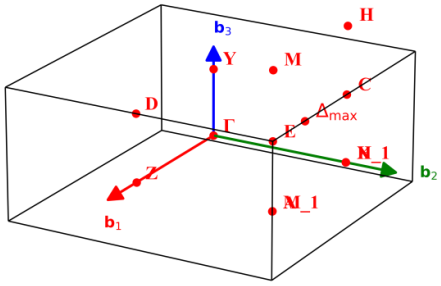


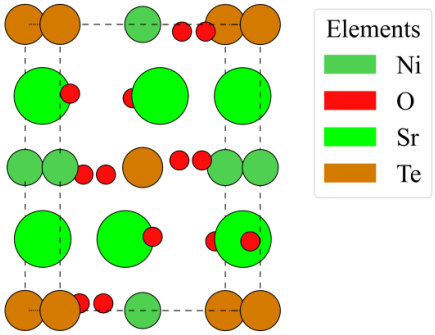


Δ_{max}: (0.100, 0.000, 0.333)

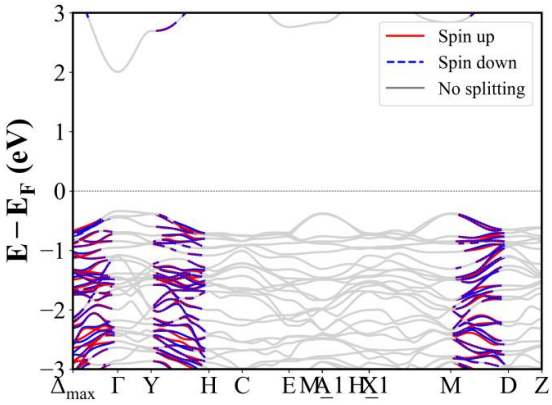


Sr2NiTeO6 (P2_1/c) | Band Gap = 2.343 eV

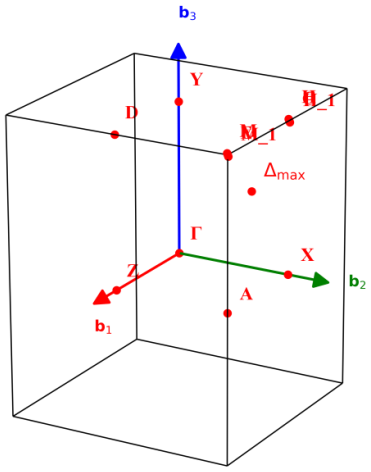


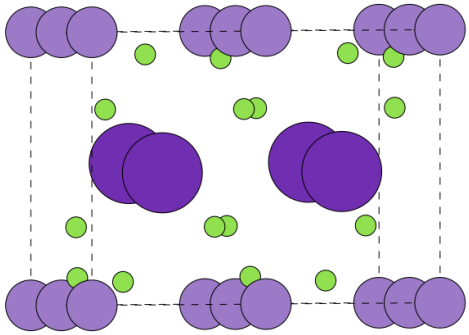


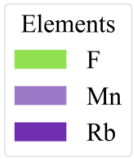
Δ_{max}: (0.100, 0.400, 0.333)



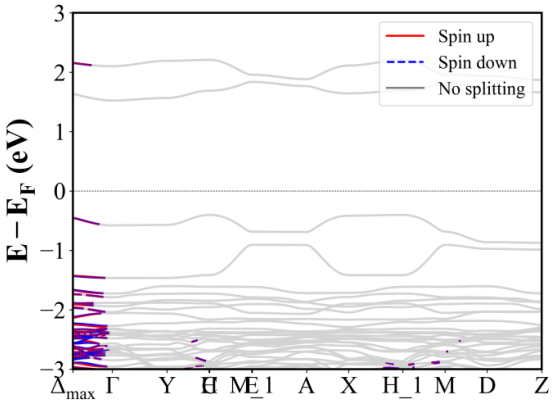
RbMnF4 (P2_1/c) | Band Gap = 1.926 eV



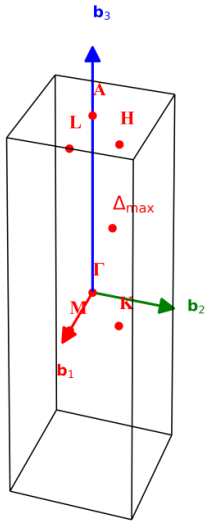




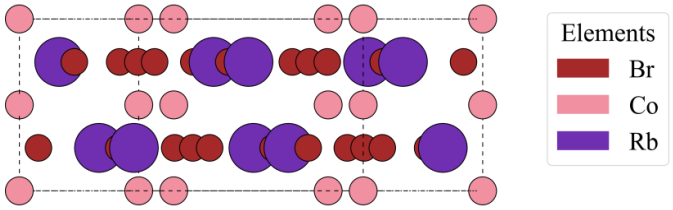
Δ_{max}: (0.000, 0.333, 0.250)

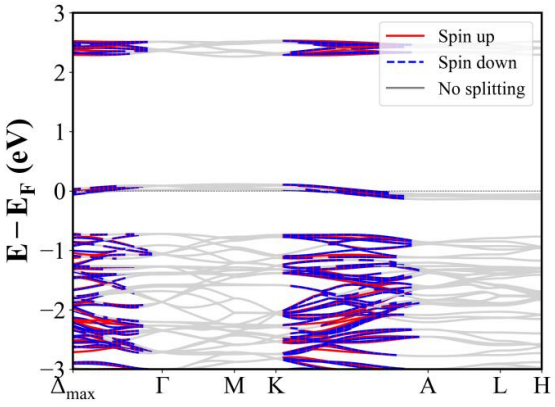


RbCoBr3 (P6_3/mmc) | Band Gap = 0.000 eV

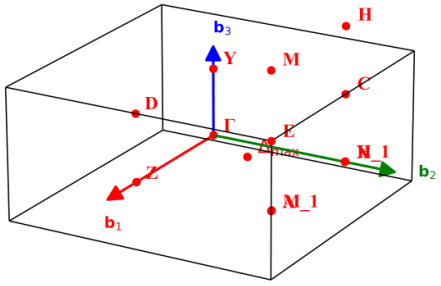


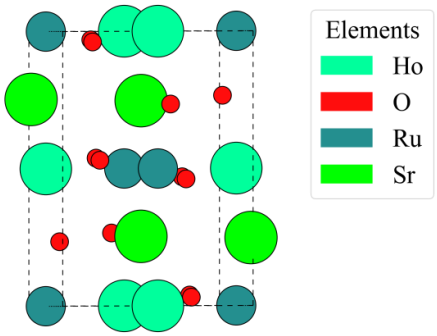
Δ_{max}: (0.250, 0.250, 0.250)



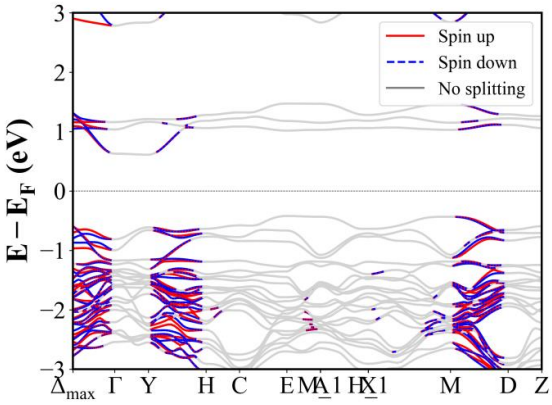


Sr2HoRuO6 (P2_1/c) | Band Gap = 1.031 eV

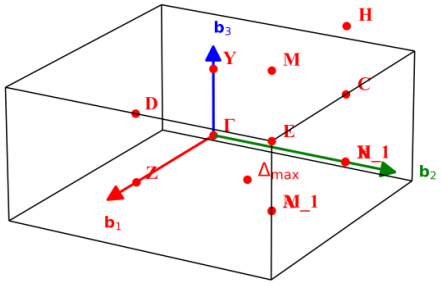


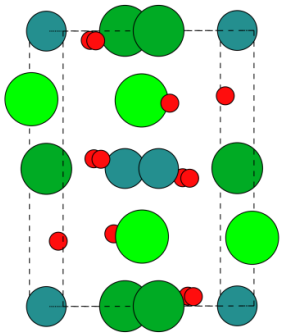


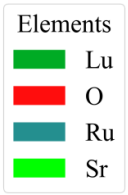
Δ_{max}: (0.300, 0.300, 0.167)



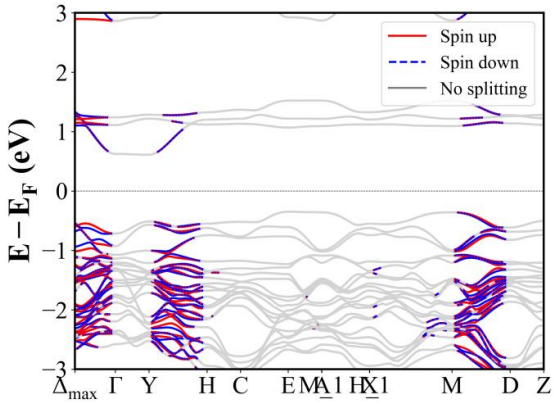
Sr2LuRuO6 (P2_1/c) | Band Gap = 0.958 eV



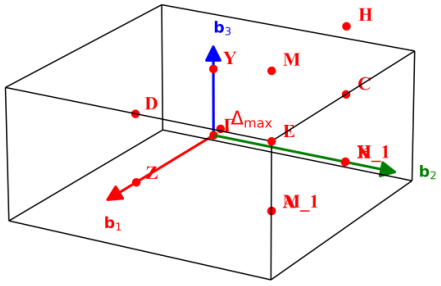


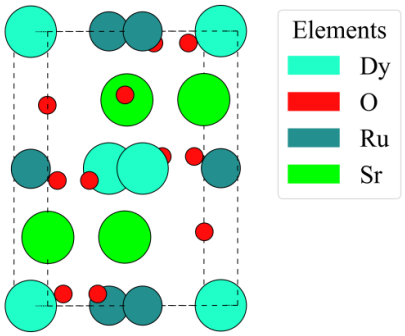


Δ_{max}: (0.300, 0.300, 0.000)

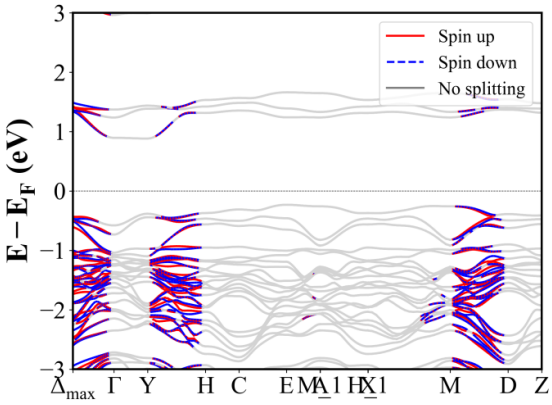


Sr2DyRuO6 (P2_1/c) | Band Gap = 1.114 eV

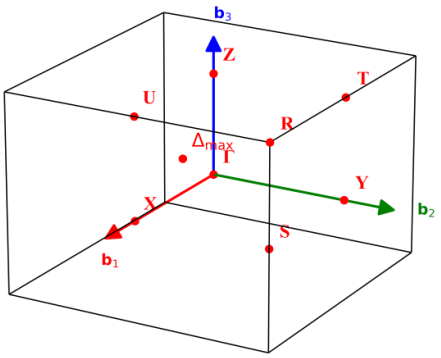


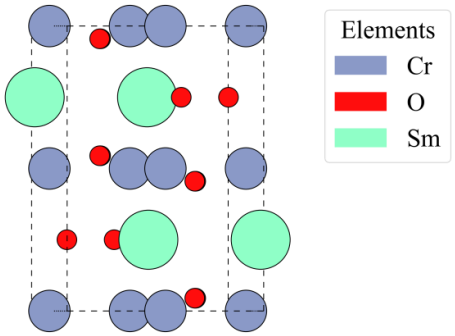


Δ_{max}: (0.300, 0.200, 0.333)

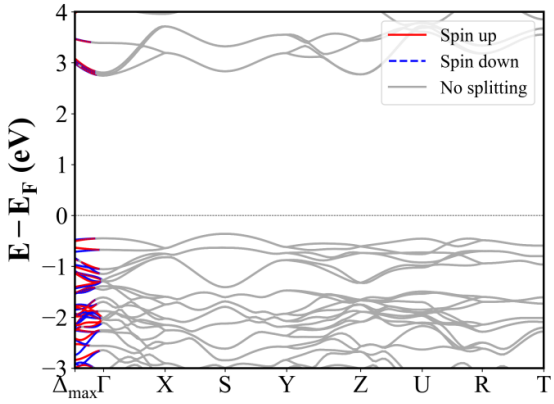


SmCrO3 (Pnma) | Band Gap = 3.106 eV

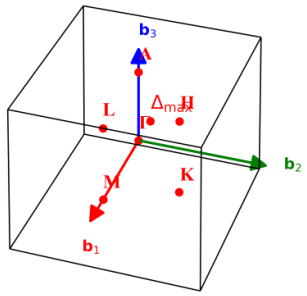


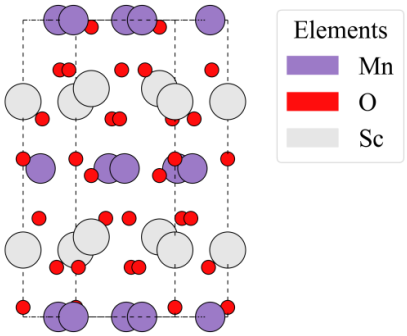


Δ_{max}: (0.200, 0.000, 0.167)

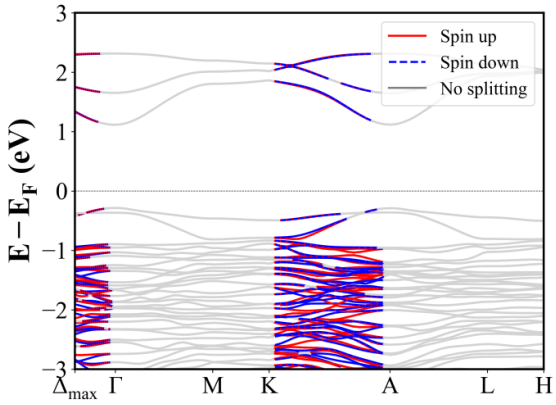


ScMnO3 (P6_3cm) | Band Gap = 1.400 eV

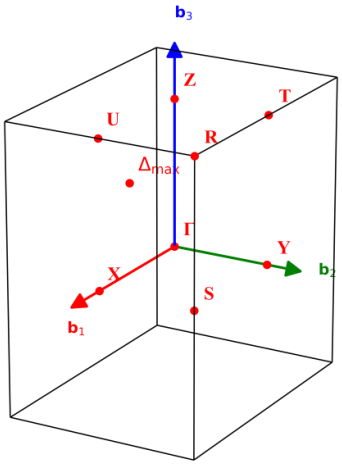


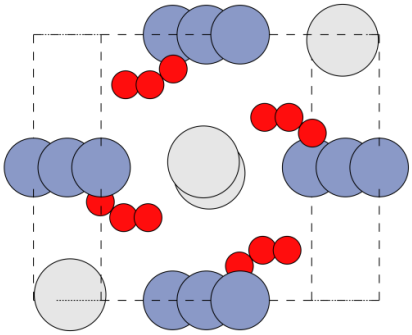


Δ_{max}: (0.100, 0.100, 0.250)

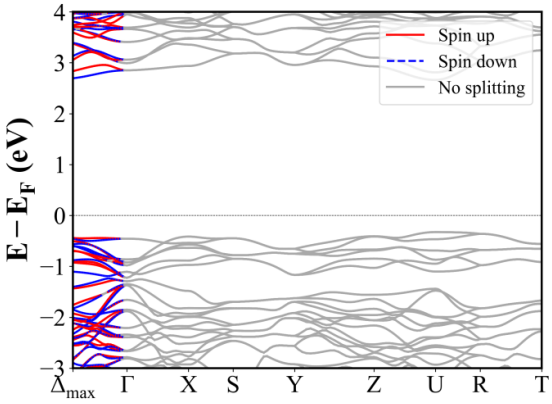


ScCrO3 (Pnma) | Band Gap = 2.987 eV

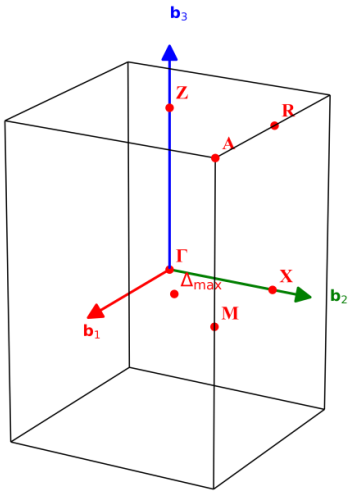


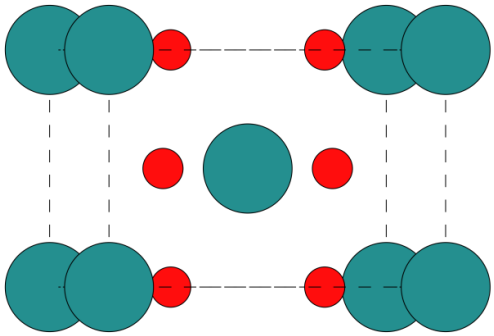


Δ_{max}: (0.300, 0.000, 0.300)

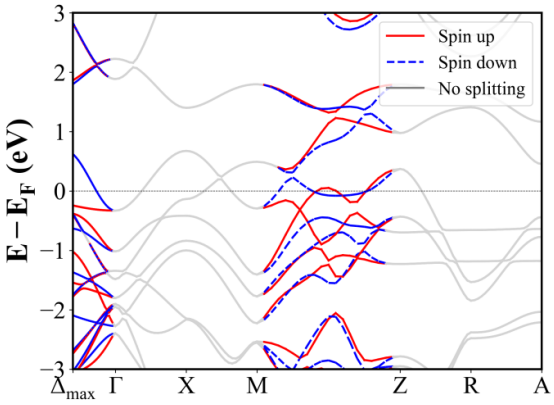


RuO2 (P4_2/mnm) | Band Gap = 0.000 eV

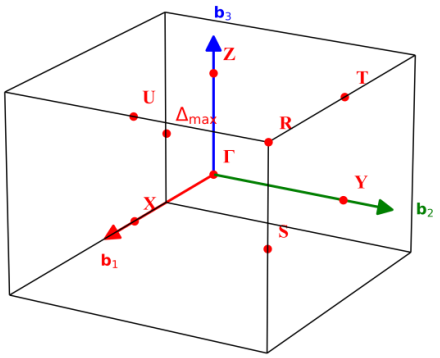


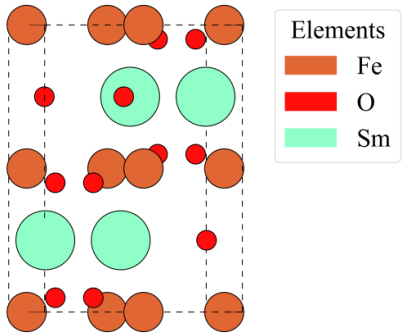


Δ_{max}: (0.250, 0.167, 0.000)

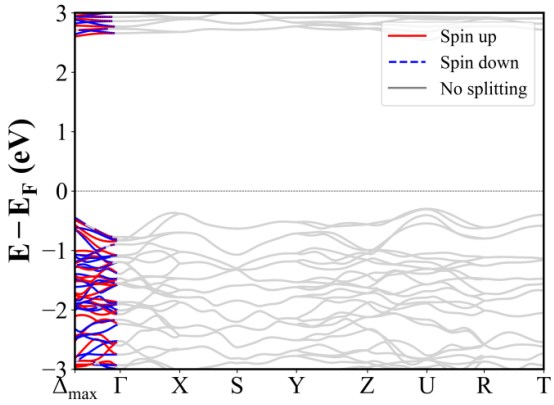


SmFeO3 (Pnma) | Band Gap = 2.843 eV

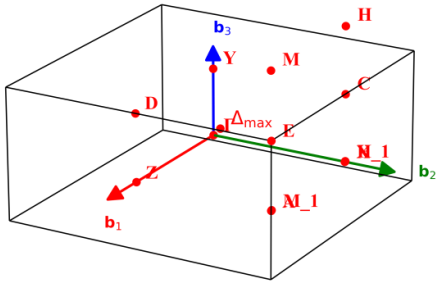


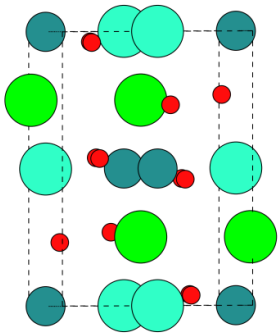


Δ_{max}: (0.300, 0.000, 0.333)



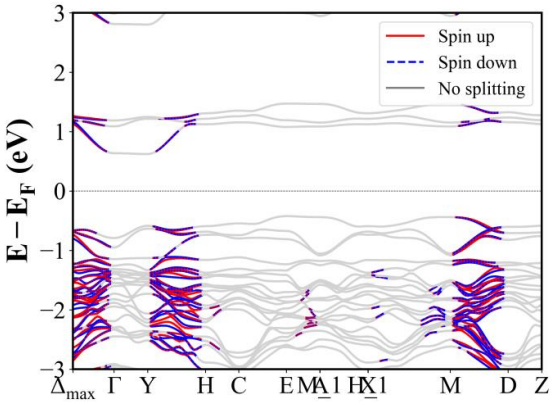
Sr2TbRuO6 (P2_1/c) | Band Gap = 1.044 eV



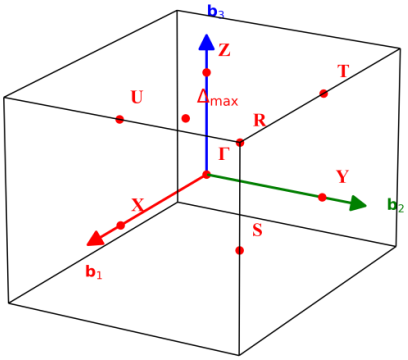


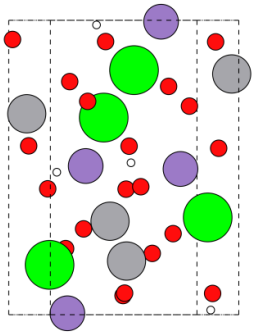


Δ_{max}: (0.300, 0.200, 0.333)



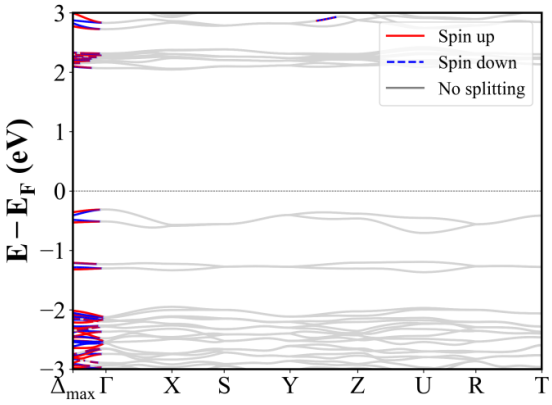
SrMnVHO5 (P2_12_12_1) | Band Gap = 2.356 eV



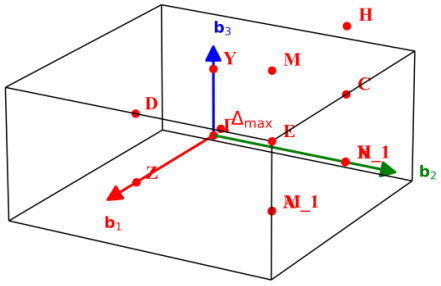


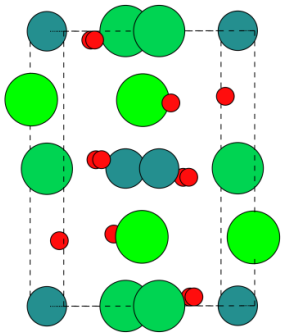


Δ_{max}: (0.125, 0.000, 0.333)



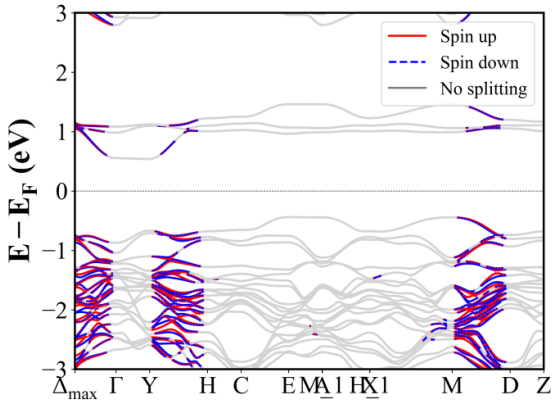
Sr2TmRuO6 (P2_1/c) | Band Gap = 0.978 eV



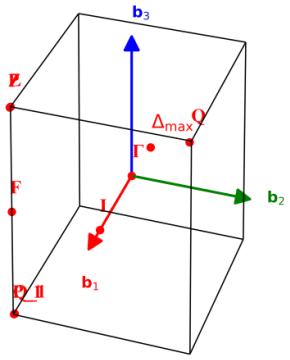


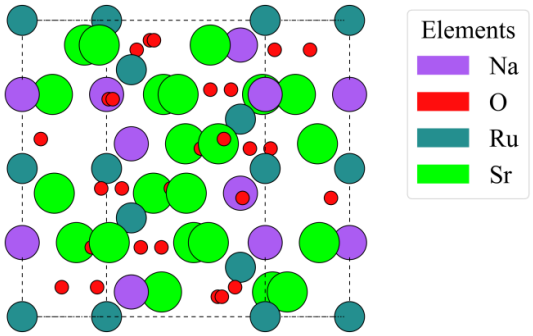


Δ_{max}: (0.300, 0.200, 0.333)

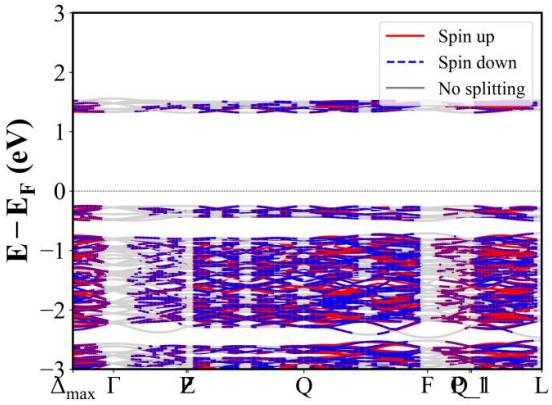


NaSr3RuO6 (R-3c) | Band Gap = 1.568 eV

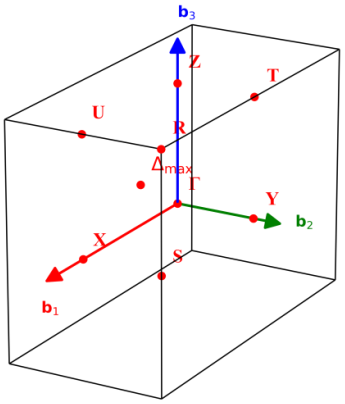


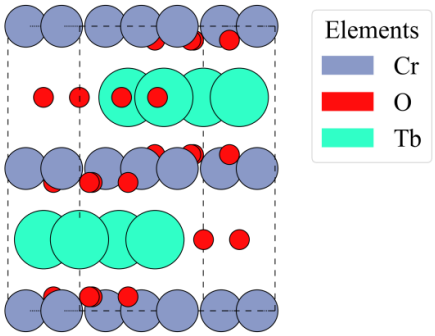


Δ_{max}: (0.167, 0.167, 0.250)

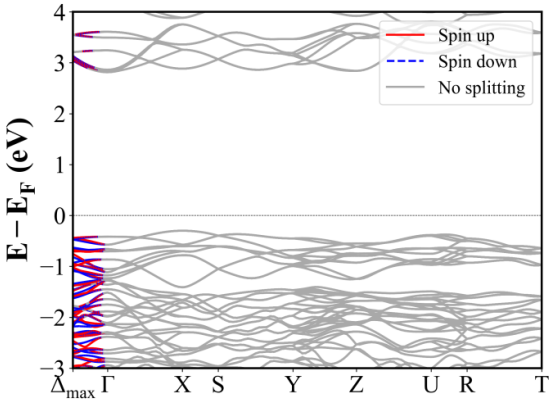


TbCrO3 (Pnma) | Band Gap = 3.114 eV

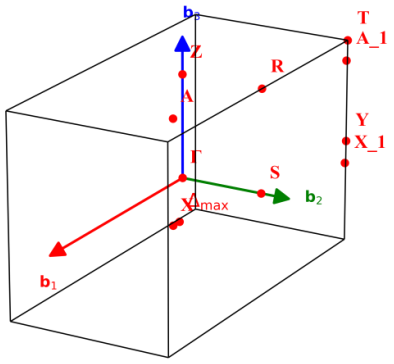


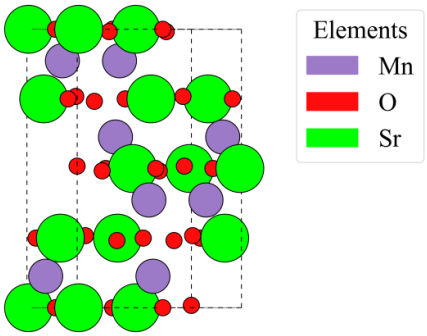


Δ_{max}: (0.200, 0.000, 0.167)

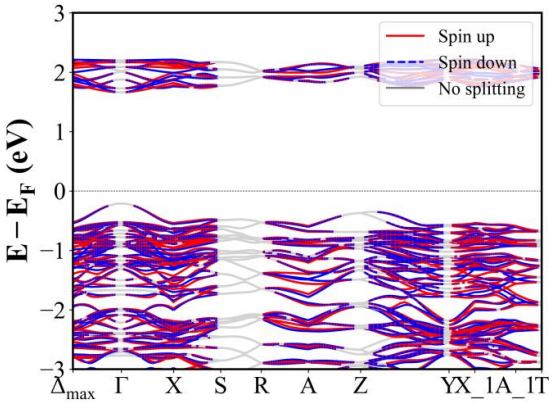


SrMnO3 (C222_1) | Band Gap = 1.873 eV

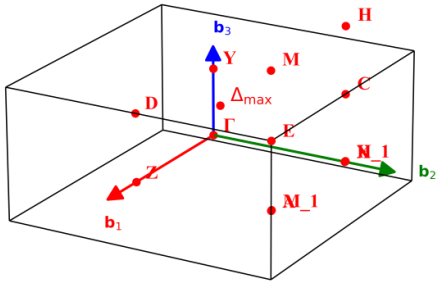


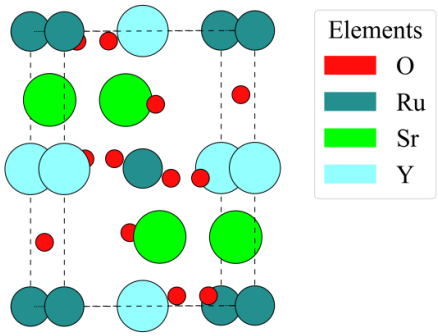


Δ_{max}: (0.300, 0.333, 0.000)

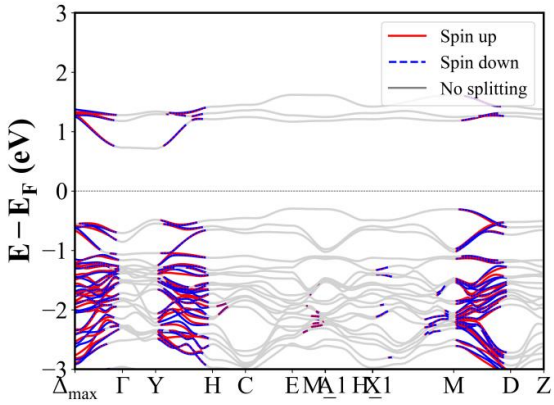


Sr2YRuO6 (P2_1/c) | Band Gap = 1.012 eV

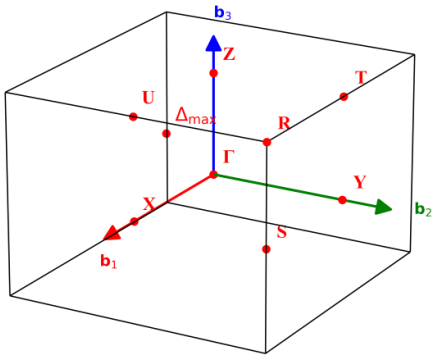


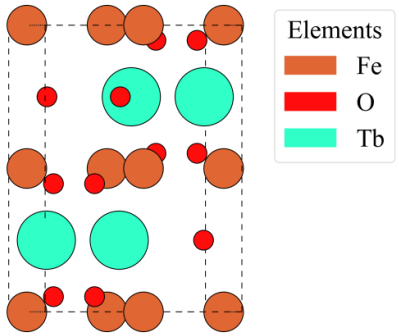


Δ_{max}: (0.300, 0.200, 0.500)

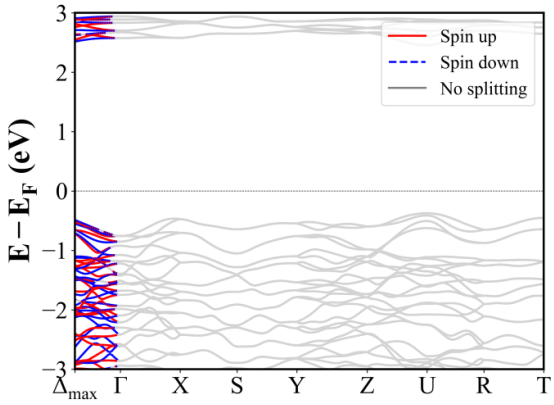


TbFeO3 (Pnma) | Band Gap = 2.826 eV

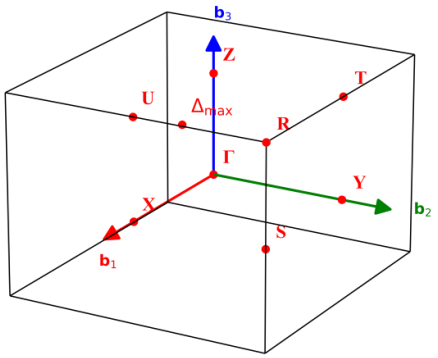


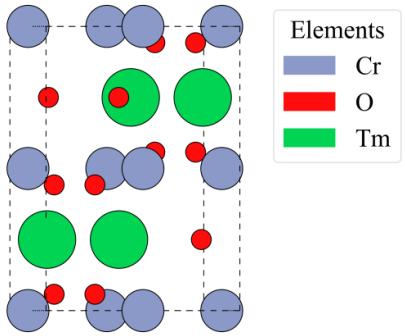


Δ_{max}: (0.300, 0.000, 0.333)

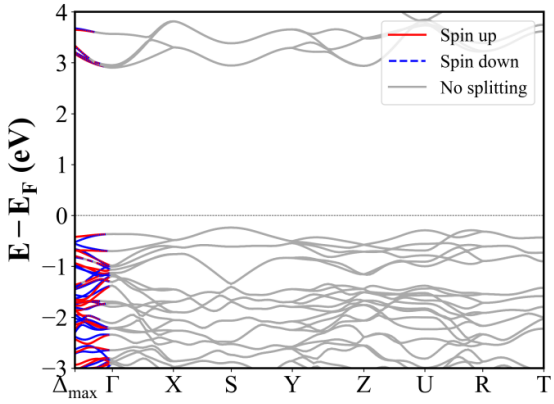


TmCrO3 (Pnma) | Band Gap = 3.141 eV

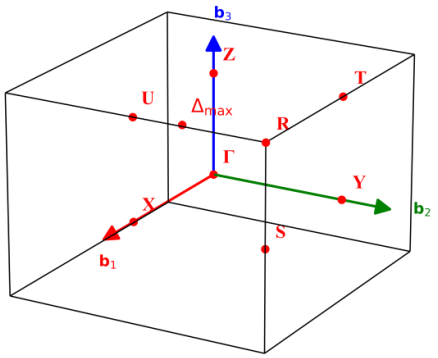


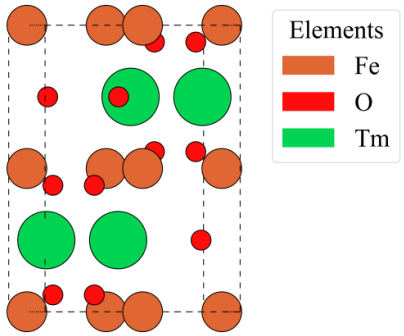


Δ_{max}: (0.200, 0.000, 0.333)

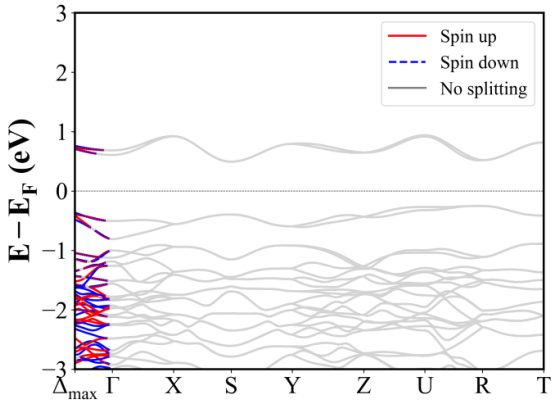


TmFeO3 (Pnma) | Band Gap = 0.745 eV

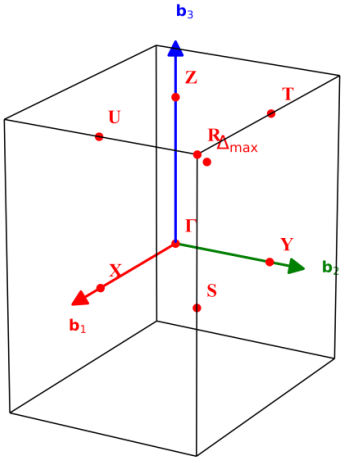


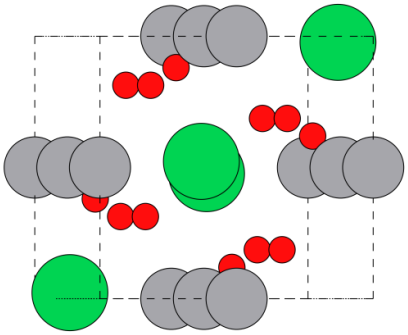


Δ_{max}: (0.200, 0.000, 0.333)

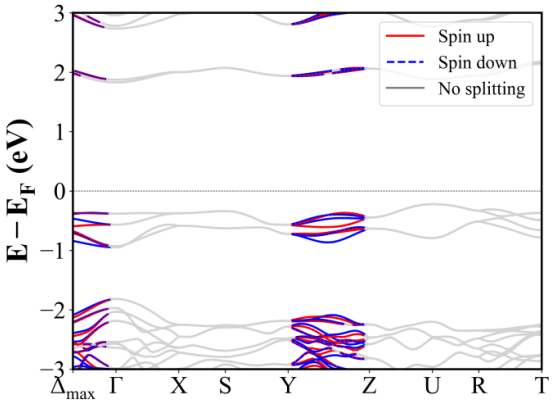


TmVO3 (Pnma) | Band Gap = 2.050 eV

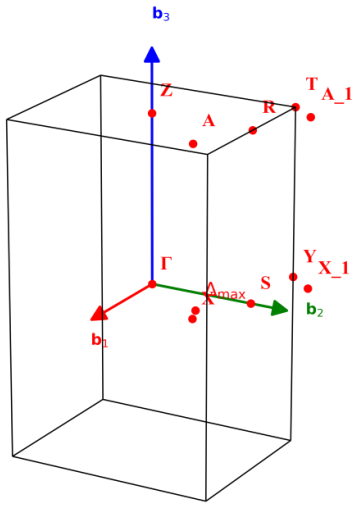


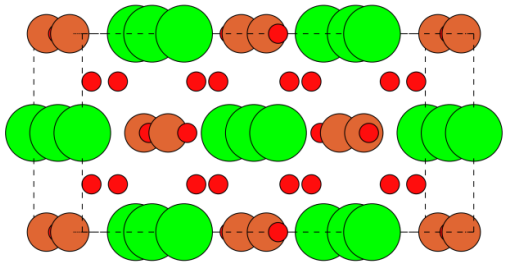


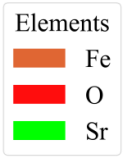
Δ_{max}: (0.000, 0.167, 0.300)



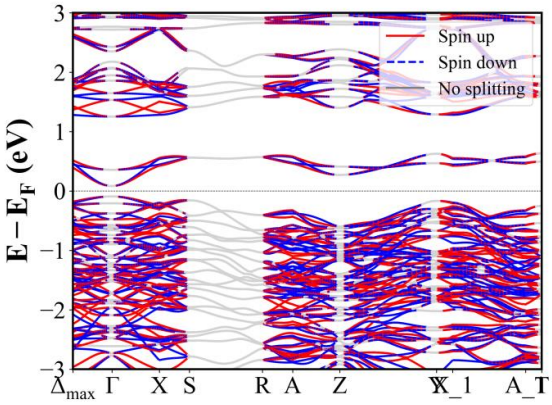
Sr4Fe4O11 (Cmmm) | Band Gap = 0.176 eV



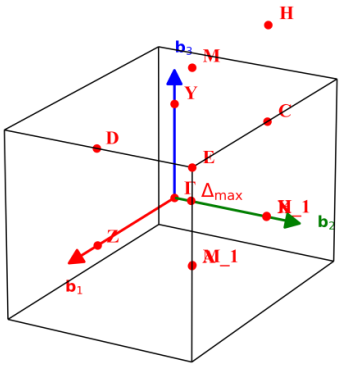


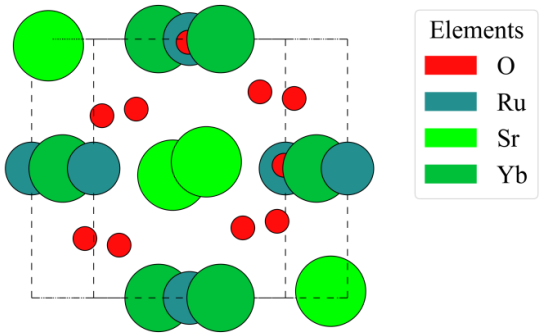


Δ_{max}: (0.250, 0.333, 0.000)

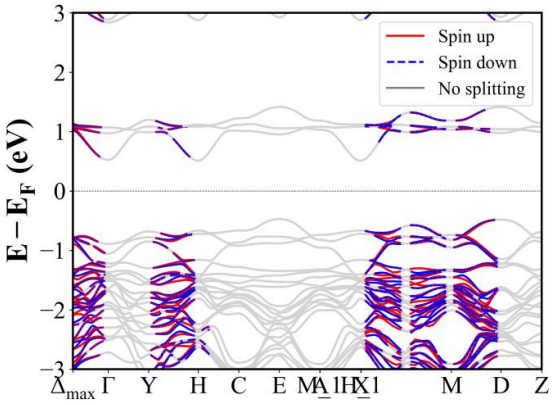


Sr2YbRuO6 (P2_1/c) | Band Gap = 0.981 eV

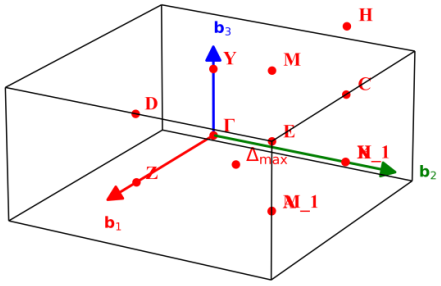


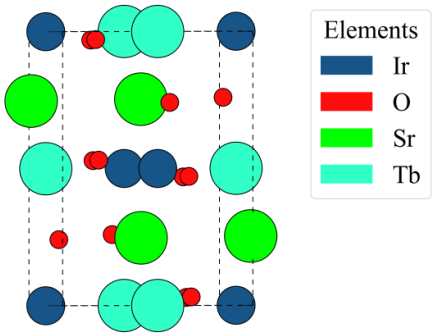


Δ_{max}: (0.300, 0.333, 0.200)

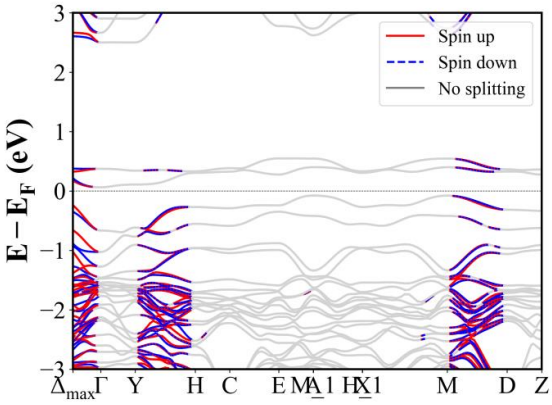


Sr2TbIrO6 (P2_1/c) | Band Gap = 0.139 eV

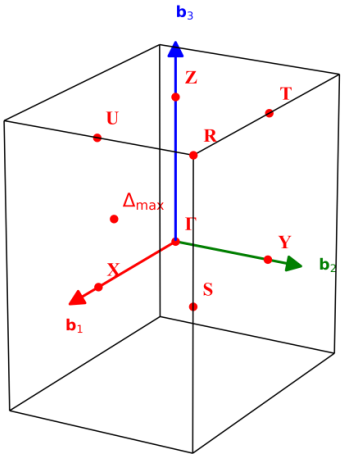


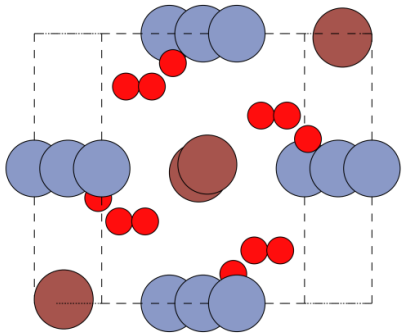


Δ_{max}: (0.200, 0.200, 0.000)

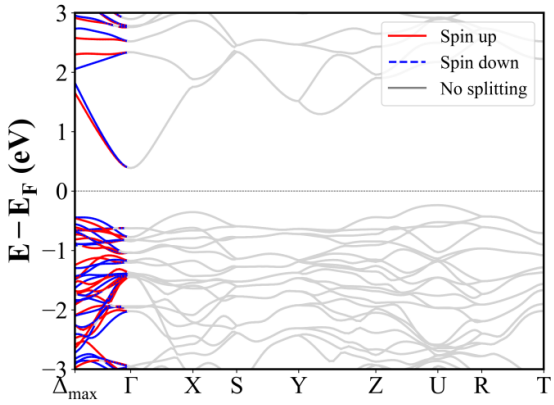


TlCrO3 (Pnma) | Band Gap = 0.625 eV

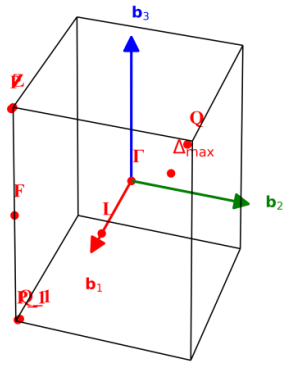


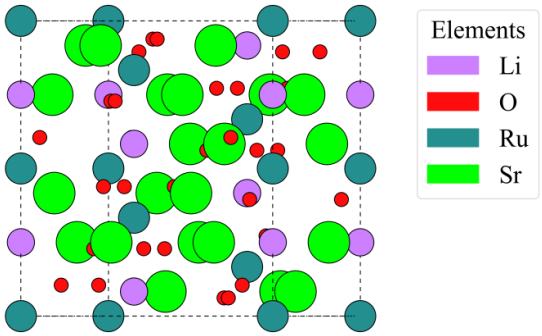


Δ_{max}: (0.400, 0.000, 0.200)

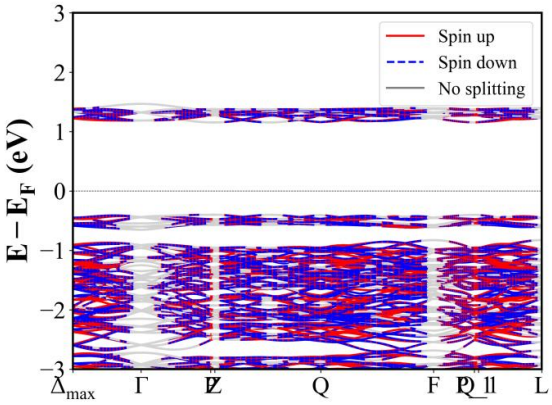


Sr3LiRuO6 (R-3c) | Band Gap = 1.553 eV

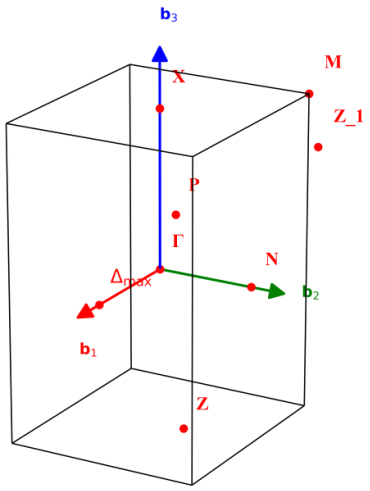


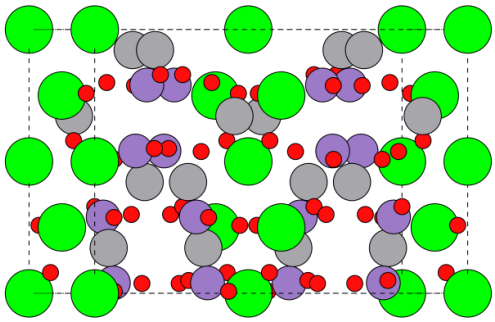


Δ_{max}: (0.333, 0.333, 0.250)



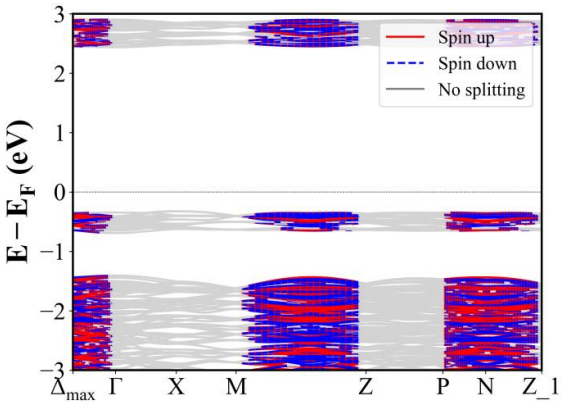
SrMn2V2O8 (I4_1cd) | Band Gap = 2.760 eV



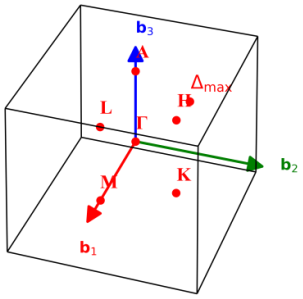


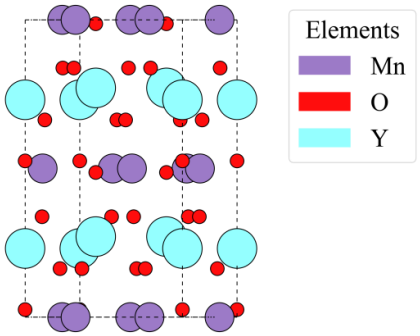


Δ_{max}: (0.500, 0.000, 0.000)

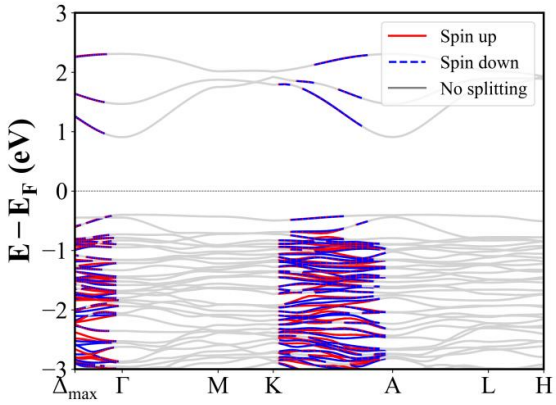


YMnO3 (P6_3cm) | Band Gap = 1.304 eV

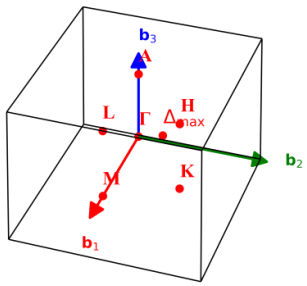


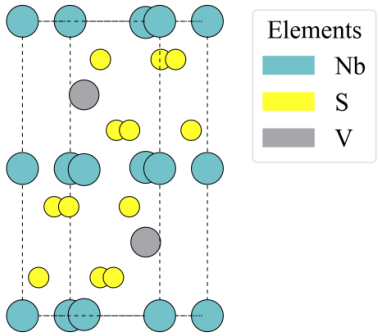


Δ_{max}: (-0.125, 0.250, 0.250)

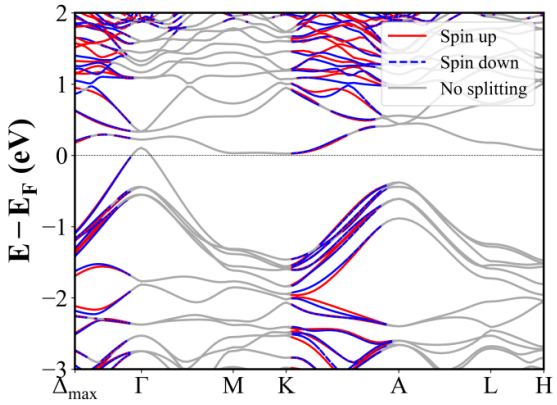


Nb3VS6 (P6_322) | Band Gap = 0.000 eV

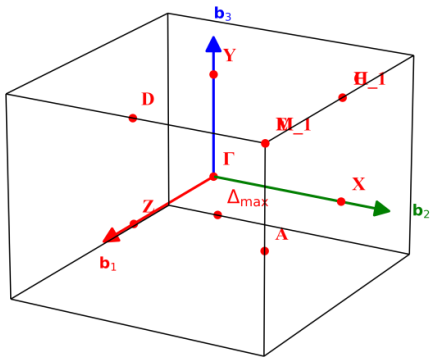


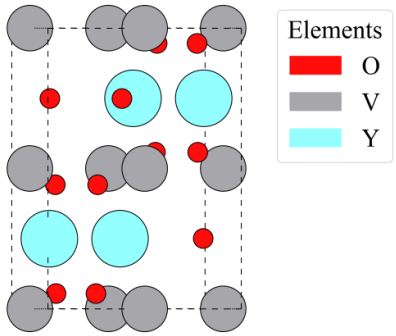


Δ_{max}: (0.200, 0.200, 0.250)

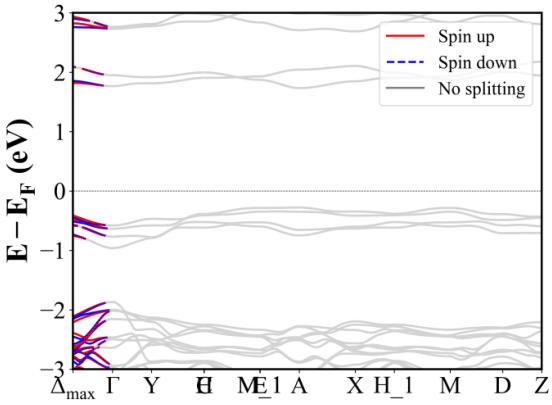


YVO3 (P2_1/c) | Band Gap = 2.012 eV

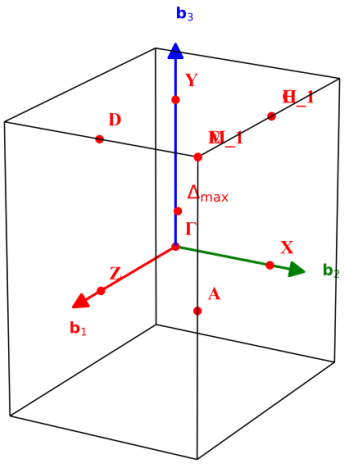


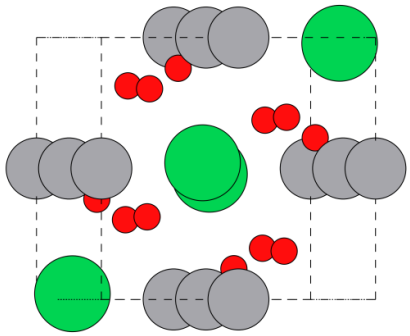


Δ_{max}: (0.300, 0.200, 0.000)

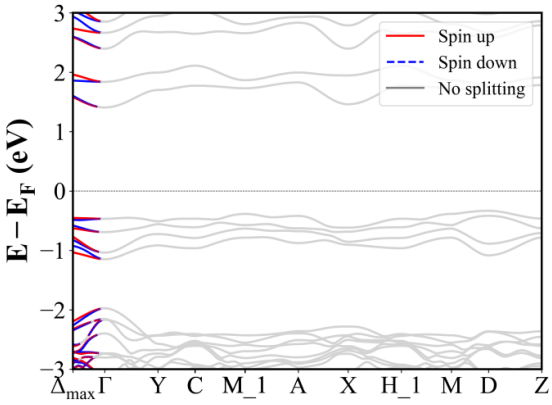


TmVO3 (P2_1/c) | Band Gap = 1.739 eV

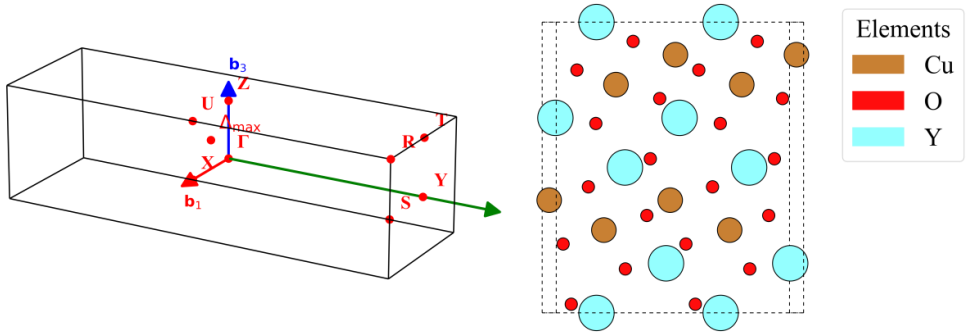




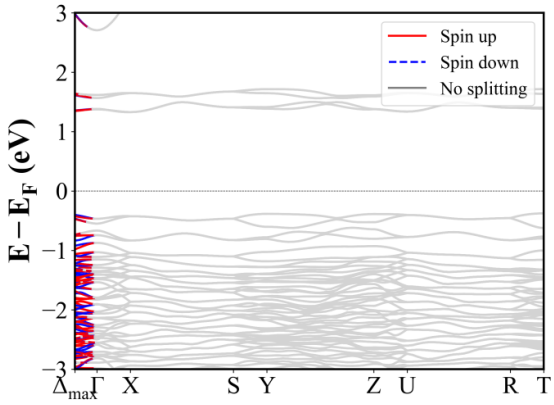
Δ_{max}: (0.200, 0.167, 0.200)



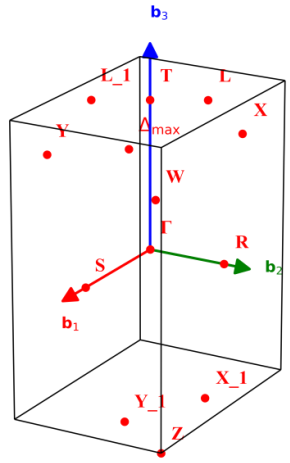
Y2Cu2O5 (Pna2_1) | Band Gap = 1.704 eV

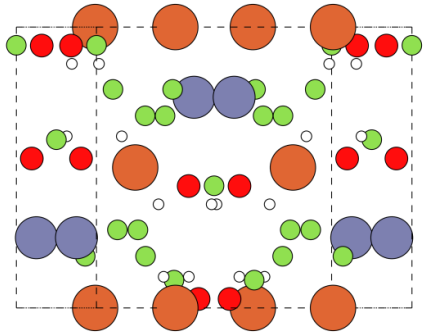


Δ_{max}: (0.250, 0.000, 0.250)

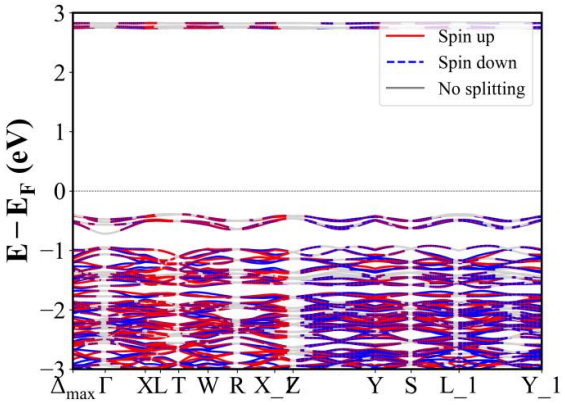


ZnFeH4O2F5 (Imm2) | Band Gap = 3.124 eV

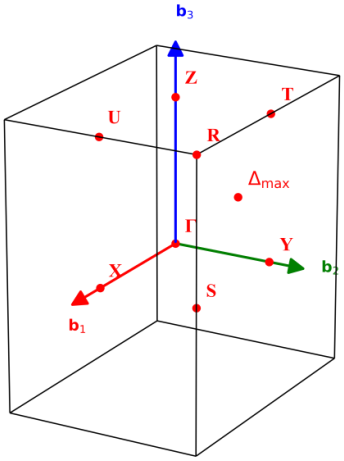


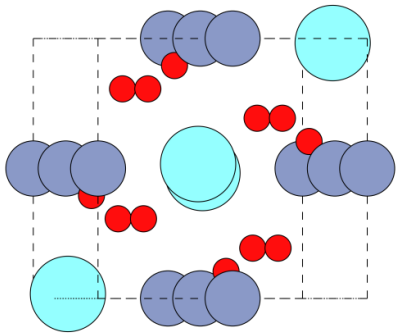


Δ_{max}: (0.167, 0.000, 0.375)

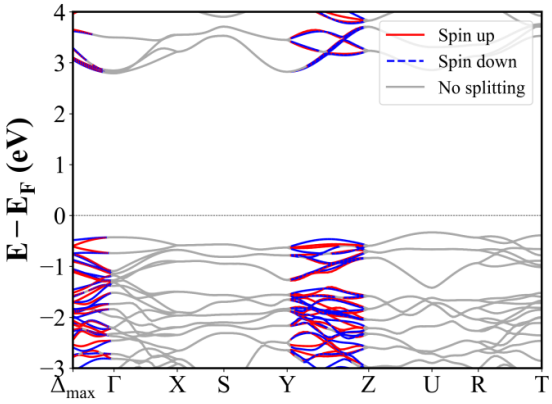


YCrO3 (Pnma) | Band Gap = 3.124 eV

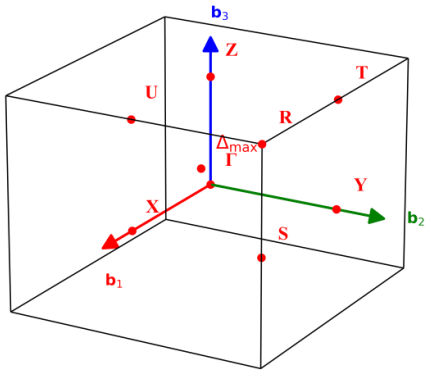


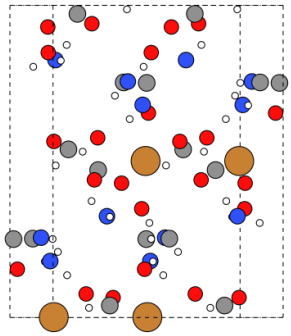


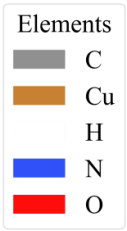
Δ_{max}: (0.000, 0.333, 0.200)



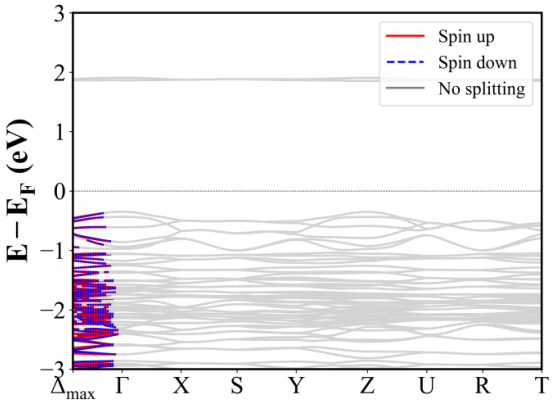
CuH9C4(NO2)3 (Pna2_1) | Band Gap = 2.201 eV



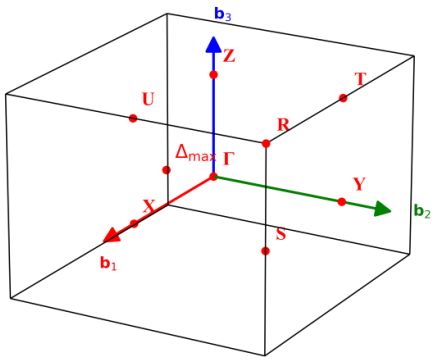


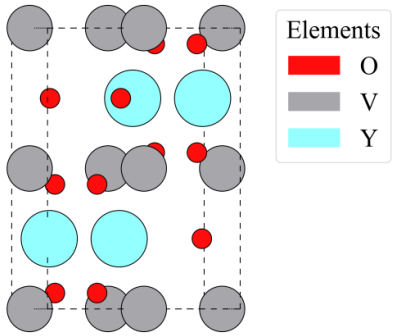


Δ_{max}: (0.333, 0.167, 0.250)

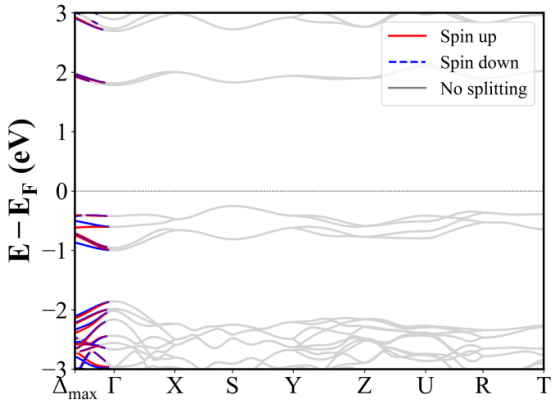


YVO3 (Pnma) | Band Gap = 2.037 eV

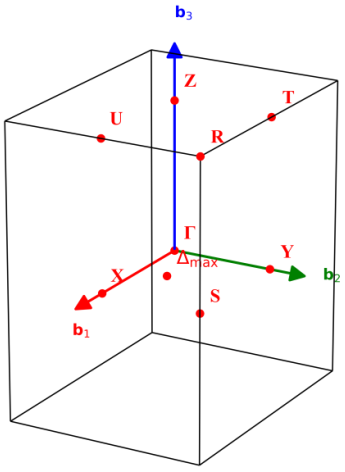


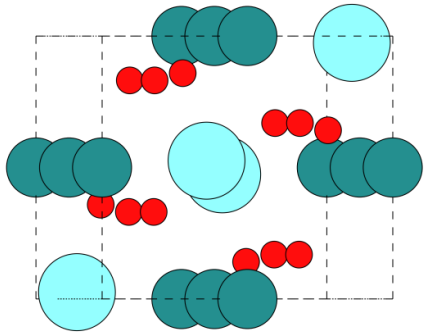


Δ_{max}: (0.300, 0.000, 0.167)

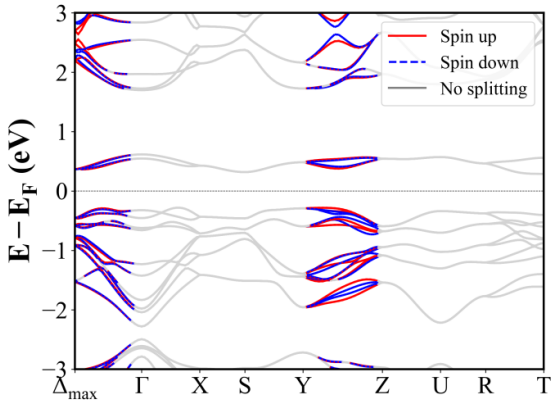


YRuO3 (Pnma) | Band Gap = 0.569 eV

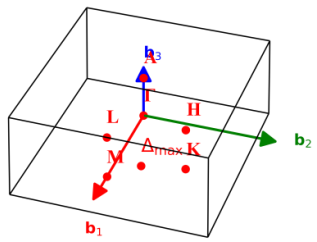


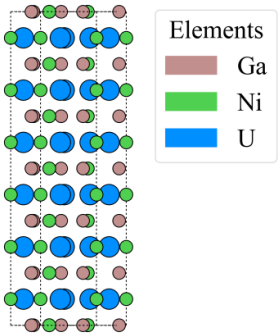


Δ_{max}: (0.500, 0.333, 0.100)

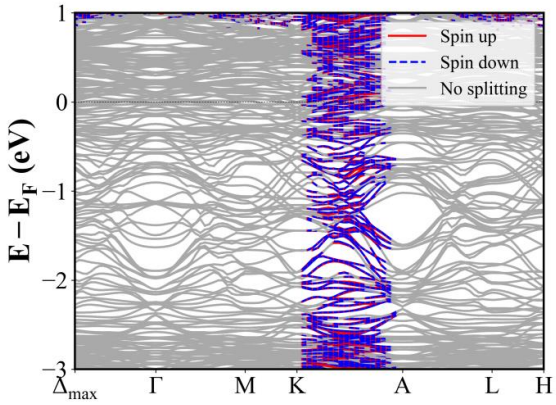


UGaNi (P-62m)

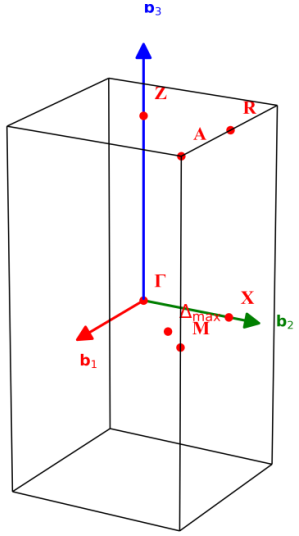




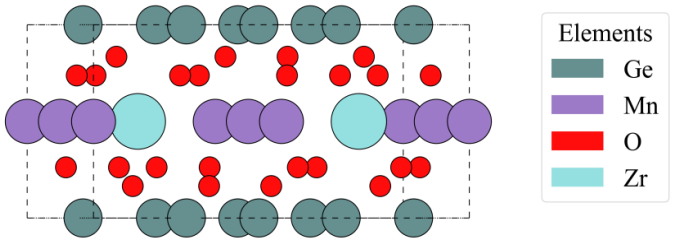
Δ_{max}: (0.375, 0.125, 0.000)

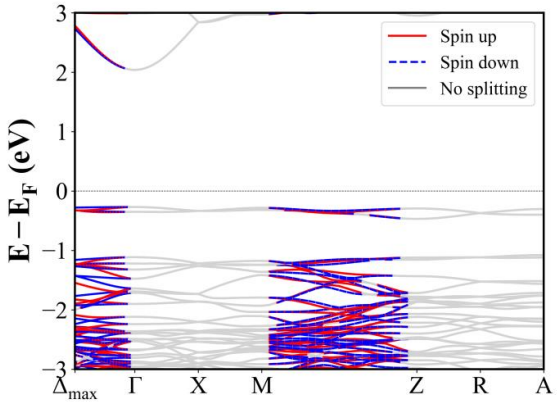


ZrMn2(GeO3)4 (P4/nbm) | Band Gap = 2.309 eV

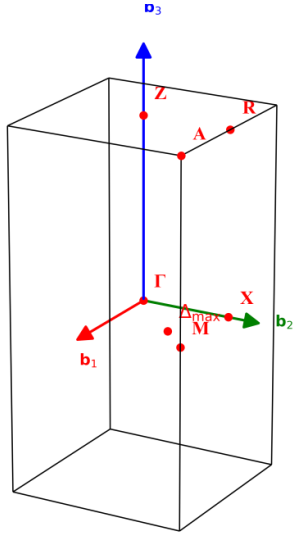


Δ_{max}: (0.333, 0.333, 0.000)

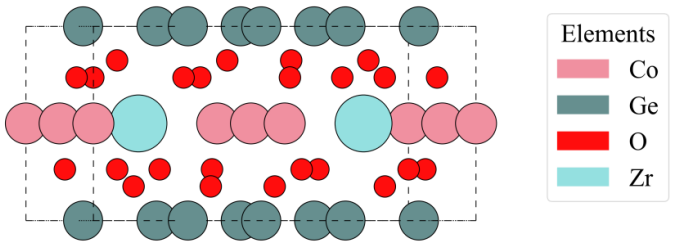


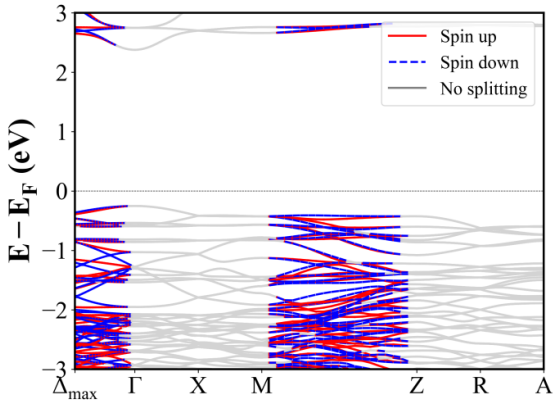


ZrCo2(GeO3)4 (P4/nbm) | Band Gap = 2.628 eV

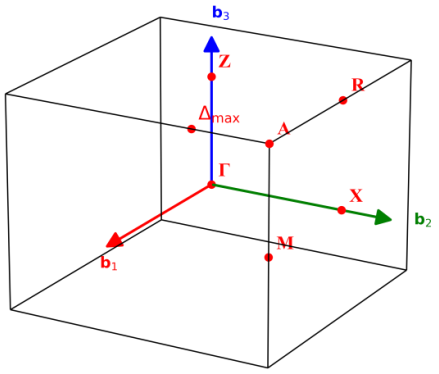


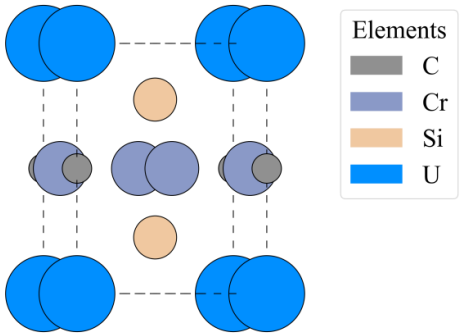
Δ_{max}: (0.333, 0.333, 0.000)



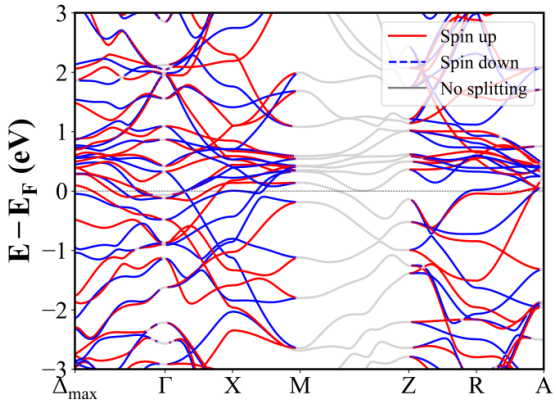


UCr2Si2C (P4/mmm) | Band Gap = 0.000 eV

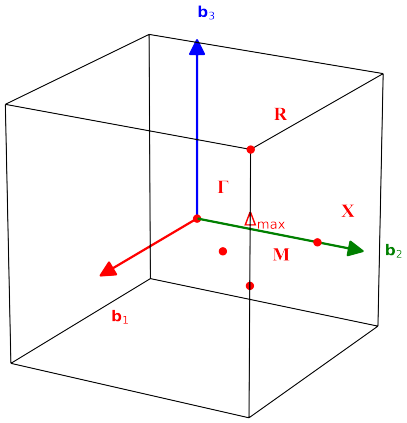


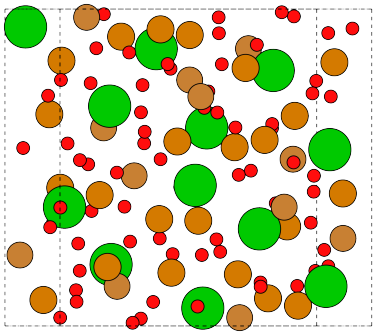


Δ_{max}: (0.500, 0.214, 0.500)

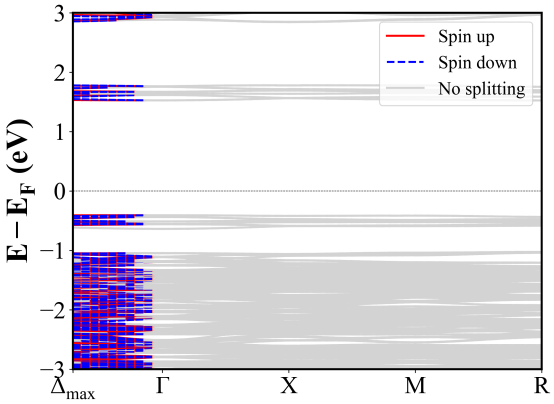


BaCu(TeO3)2 (P4_132) | Band Gap = 1.933 eV

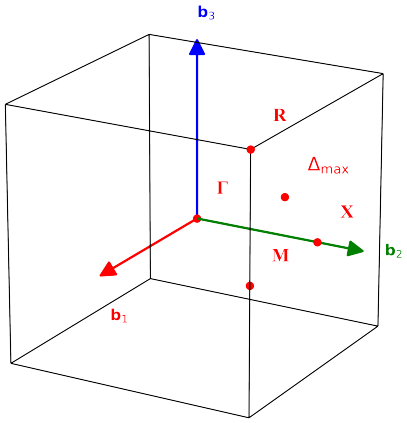


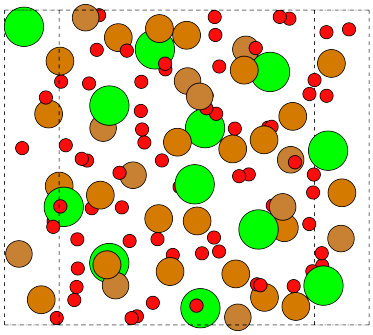


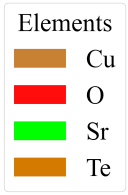
Δ_{max}: (0.250, 0.250, 0.000)



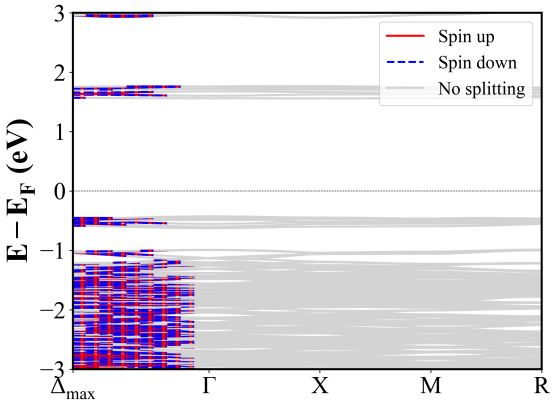
SrCu(TeO3)2 (P4_132) | Band Gap = 1.985 eV



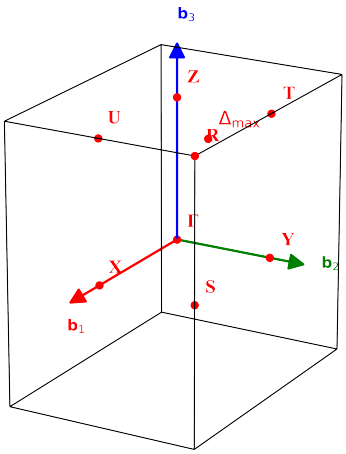


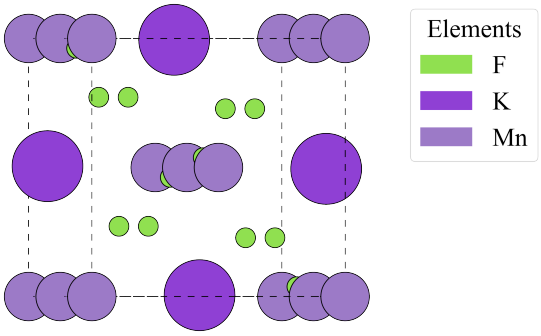


Δ_{max}: (0.250, 0.500, 0.250)

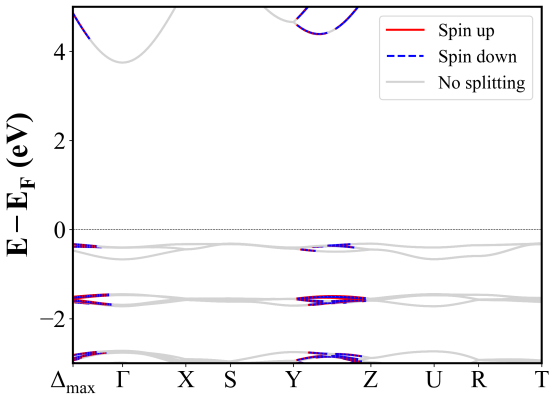


KMnF3 (Pnma) | Band Gap = 4.057 eV

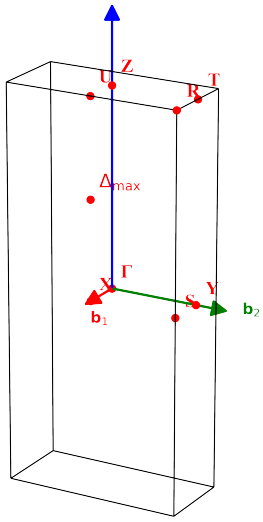


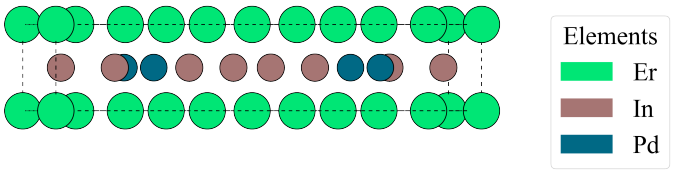


Δ_{max}: (0.000, 0.167, 0.375)

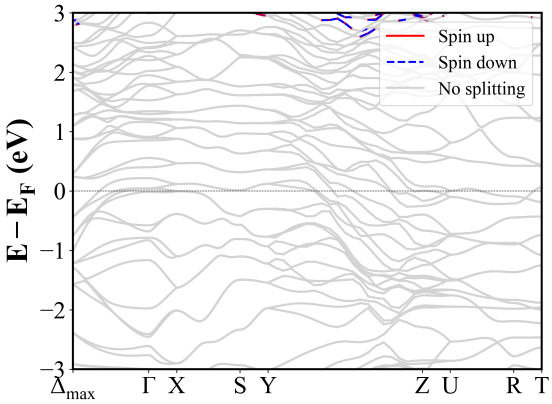


Er5(In2Pd)2 (Pbam) | Band Gap = 0.000 eV

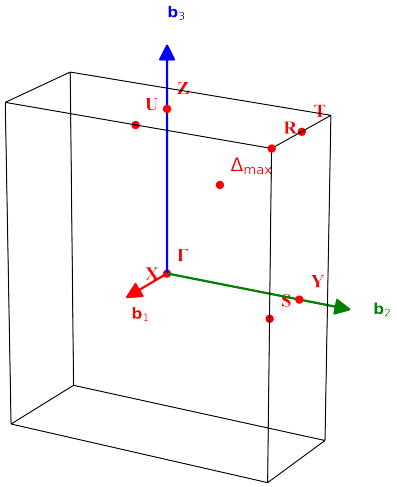


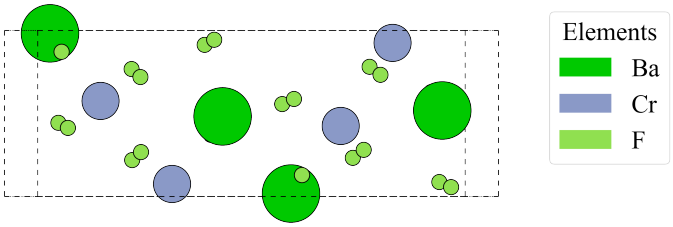


Δ_{max}: (0.500, 0.000, 0.250)

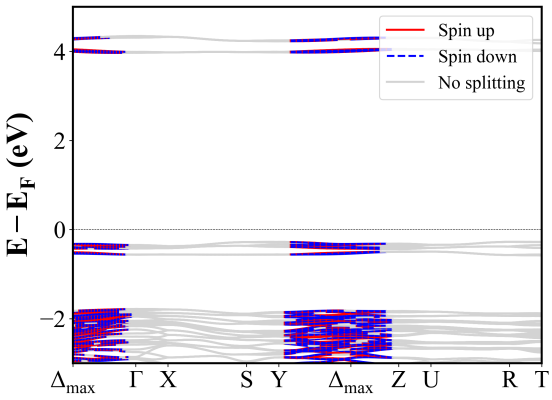


BaCrF5 (P2_12_12_1) | Band Gap = 4.241 eV

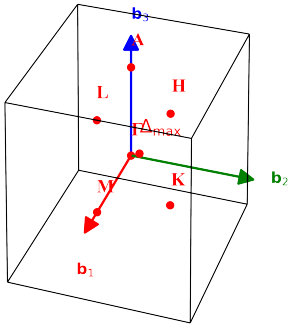


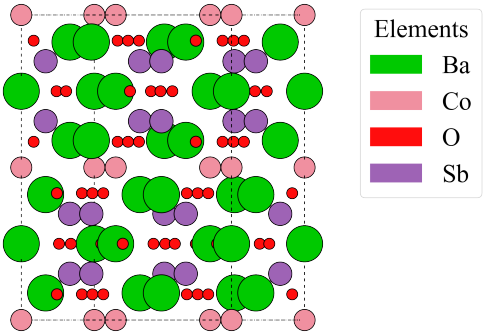


Δ_{max}: (0.000, 0.200, 0.300)

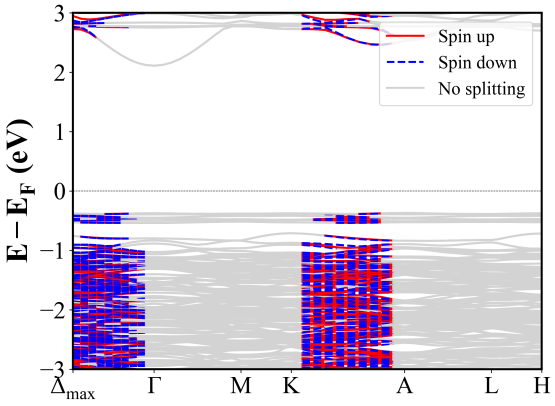


Ba3CoSb2O9 (P6_3/mmc) | Band Gap = 2.479 eV

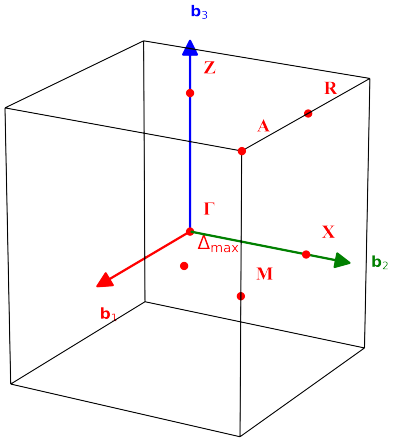


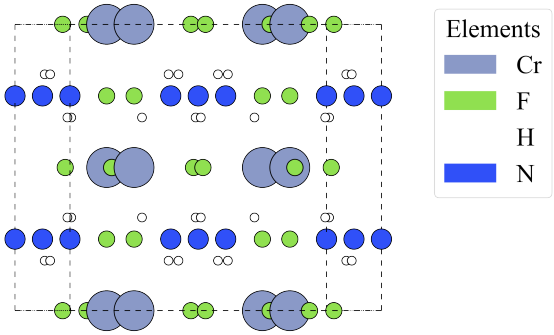


Δ_{max}: (0.333, 0.167, 0.250)

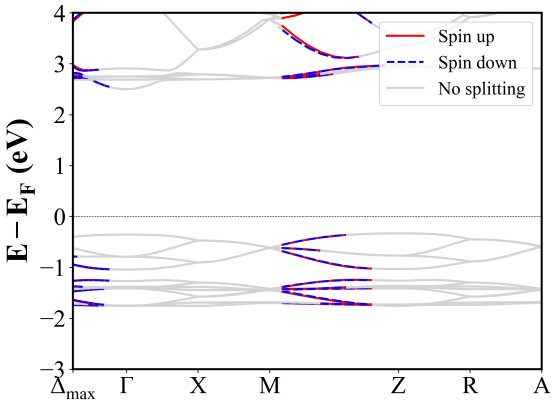


CrH4NF3 (P4_2/mbc) | Band Gap = 2.831 eV

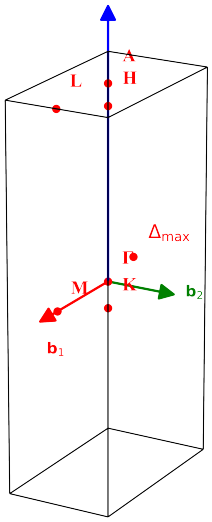




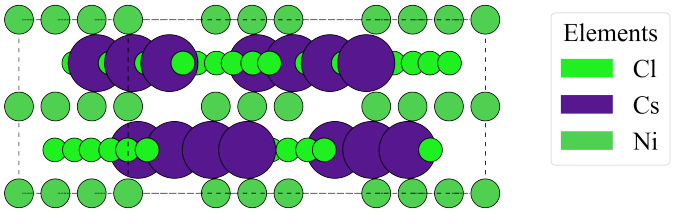
Δ_{max}: (0.333, 0.167, 0.000)

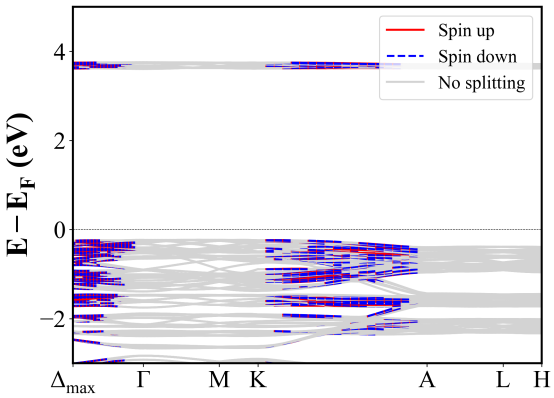


CsNiCl3 (P6_3/mmc) | Band Gap = 3.837 eV

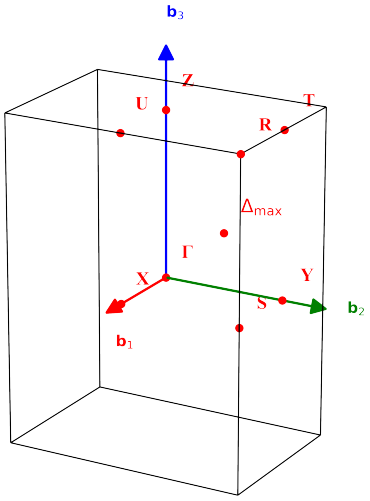


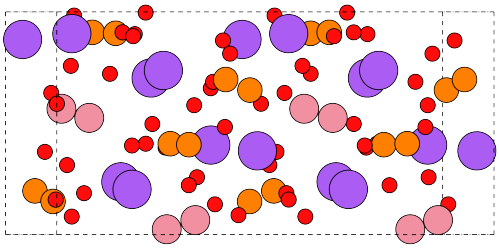
Δ_{max}: (0.250, 0.500, 0.125)

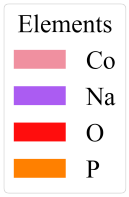




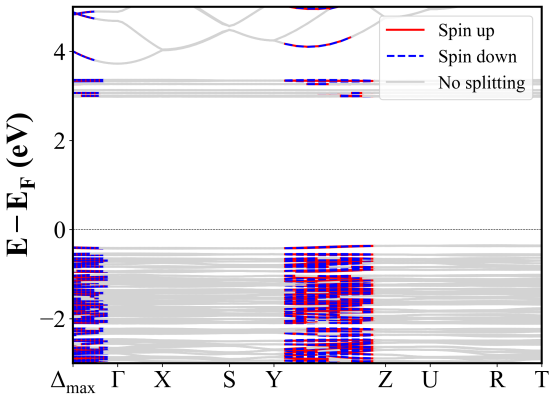
Na2CoP2O7 (Pna2_1) | Band Gap = 3.332 eV



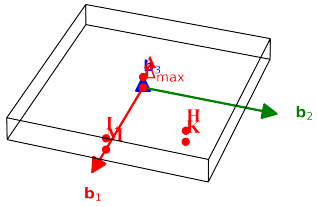


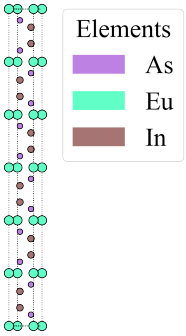


Δ_{max}: (0.000, 0.250, 0.167)



Eu(InAs)2 (P6_3/mmc) | Band Gap = 0.000 eV





Δ_{max}: (0.000, 0.000, 0.000)

